Nano-Metal Oxides For Elemental Mercury Removal from Natural Gas

Anastasios Chalkidis

MSc (Pet Eng), Heriot-Watt University, UK, 2014
Dipl Ing (Chem Eng), University of Patras, Greece, 2012

A Thesis Submitted in Fulfilment of the Requirements
for the Degree of Doctor of Philosophy

School of Science
College of Science, Engineering and Health
RMIT University

Melbourne, November 2019

Declaration Statement

I, **Anastasios Chalkidis**, certify that except where due acknowledgement has been made, the work is that of the author alone; the work has not been submitted previously, in whole or in part, to qualify for any other academic award; the content of the thesis is the result of work which has been carried out since the official commencement date of the approved research program; any editorial work, paid or unpaid, carried out by a third party is acknowledged; and, ethics procedures and guidelines have been followed. Also, I acknowledge the support I have received for my research through the provision of an Australian Government Research Training Program Scholarship.

Anastasios Chalkidis
November 18, 2019

Acknowledgments

The present thesis is written in accordance with the requirements for the award of doctoral (PhD) degree at RMIT University. The research project, which was co-funded by CSIRO, was carried out between March 2016 and August 2019 at the Centre for Advanced Materials and Industrial Chemistry (CAMIC) in the School of Science of RMIT. The supervisory team comprised of Professor Suresh Bhargava, Dr Patrick Hartley (CSIRO), Dr Ylias Sabri and Dr Jampaiah Deshetti. I would like to thank all my supervisors for their valuable input, guidance and continuing support to carry out a project comprising of significant experimental challenges to address a global issue with substantial socio-medical and economic impact. Dr Ahmad Kandjani is gratefully acknowledged for his assistance in the Mercury Lab, as well as Dr Edwin Mayes for his help with the material's characterization at RMIT Microscopy and Microanalysis Facility (RMMF). Moreover, I would like to thank Dr Maciej Mazur from RMIT's Advanced Manufacturing Precinct (AMP) for providing the 3D-printed sorbent supports, as well as Dr Selvakannan Periasamy for his helpful comments on their application for mercury capture. The contribution of Dr Lathe Jones is also greatly appreciated, especially with respect to procedural issues. My thanks are further extended to the academic, technical and administrative staff for the fruitful collaboration, as well as to my colleagues for their patience and encouragement.

Research Output

Journal Publications Included in Thesis

Chalkidis, A**., Jampaiah, D., Hartley, P.G., Sabri, Y.M., Bhargava, S.K. Mercury in Natural Gas Streams: A Review of Materials and Processes for Abatement and Remediation. **Journal of Hazardous Materials** 2020, 382, 121036 (doi.org/10.1016/j.jhazmat.2019.121036) **(Chapters 1 & 2)

Chalkidis, A**., Jampaiah, D., Hartley, P.G., Sabri, Y.M., Bhargava, S.K. "Regenerable α-MnO_2 Nanotubes for Elemental Mercury Removal from Natural Gas". **Fuel Processing Technology** 2019**,** 193, 317-327 (doi.org/10.1016/j.fuproc.2019.05.034) **(Chapter 4)

Chalkidis, A**., Jampaiah, D., Amin M.H., Hartley, P.G., Sabri, Y.M., Bhargava, S.K. "CeO_2-Decorated α-MnO_2 Nanotubes: A Highly Efficient and Regenerable Sorbent for Elemental Mercury Removal from Natural Gas". **Langmuir** 2019, 35, 8246-8256 (doi.org/10.1021/acs.langmuir.9b00835) **(Chapter 5)

Additional Relevant Journal Publications

***Chalkidis, A**., Jampaiah, D., Hartley, P.G., Sabri, Y.M., Bhargava, S.K. "Mercury-Bearing Wastes: Sources, Policies and Treatment Technologies for Mercury Recovery and Safe Disposal". **Chemosphere** (Under review)*

*Jampaiah, D., **Chalkidis, A**., Sabri, Y.M., Mayes, E.L.H., Reddy, B.M., Bhargava, S.K. "Low-Temperature Elemental Mercury Removal over TiO_2 Nanorods-Supported MnO_x-FeO_x-CrO_x". **Catalysis Today** 2019, 324, 174-182 (doi.org/10.1016/j.cattod.2018.11.049)*

*Jampaiah, D., **Chalkidis, A**., Sabri, Y.M., Bhargava, S.K. "Role of Ceria in the Design of Composite Materials for Elemental Mercury Removal". **The Chemical Record** 2019, 19, 1407-1419 (doi.org/10.1002/tcr.201800161)*

Other Journal Publications

*Jampaiah, D., Devaiah, D., **Chalkidis**, **A**., Venkataswamy, P., Bhargava, S.K, Reddy, B.M. "MOF-derived ceria-zirconia supported Co_3O_4 catalysts with enhanced activity in CO_2 methanation". **Catalysis Today** (Under review)*

*Jampaiah, D., Devaiah, D., **Chalkidis, A**., Singh, M., Sabri, Y.M., Mayes, E.L.H., Bansal, V., Bhargava, S.K. "MOF-Derived Noble-Metal-Free Cu/CeO_2 with High Porosity for Efficient Water-Gas Shift Reaction at Low Temperatures". **Catalysis Science & Technology** 2019, 9, 4226-4231 (doi.org/10.1039/C9CY01114E)*

*Reddy, V.G., Jampaiah, D., **Chalkidis, A**., Sabri, Y.M., Mayes, E.L.H., Bhargava, S.K. "Highly Dispersed Cobalt Oxide Nanoparticles on Manganese Oxide Nanotubes for Aerobic Oxidation of Benzyl Alcohol". **Catalysis Communications** 2019, 130, 105763 (doi.org/10.1016/j.catcom.2019.105763)*

Abstract

Undoubtedly mercury pollution poses detrimental threats to the human health and environment. Global initiatives such as the Minamata Convention on Mercury (2017) and the United Nations Environment Programme (2018) have emphatically addressed the necessity to undertake drastic actions to reduce anthropogenic emissions. At the same time, the role of natural gas in mitigating greenhouse gas emissions and advancing renewable energy integration is certainly critical. It accounts for less than 25% of the world fuel consumption, with liquified natural gas (LNG) comprising around 10% of global gas trade. The intensive exploitation of low-cost shallow hydrocarbon reservoirs has directed exploration to deeper geological basins. However, drilling into deeper and hotter reservoirs increases the possibility of mercury contamination. This impacts on the industry sustainability from health and safety risk aspects due to corrosion and contamination of equipment, to catalyst poisoning and toxicity through emissions to the environment. In the past, catastrophic industrial events, such as the one occurred in Skikda LNG plant, Algeria in 1973 or the most recent 2004 New Year's Day Moomba gas plant explosion in South Australia, were attributed to mercury-induced corrosion.

Elemental mercury (Hg^0) is the prevalent species in natural gas streams and it is characterized by its low water solubility and high mobility in the atmosphere. According to the industry practice, the mercury concentration of the gas stream entering the cryogenic section, must be reduced to fewer than 10 $ng \cdot m^{-3}$. Thus, fixed-beds of non-regenerative and regenerative materials, such as sulfur-impregnated carbons, supported metal sulfides/oxides and silver-impregnated zeolites, are utilized to remove mercury by means of amalgamation, chemical or physical adsorption as well as reactive absorption. Since the 1970's, when the effect of mercury on natural gas cryogenic processing plants was realized, numerous patents have been published. Nevertheless, the conventional materials are often problematic and alternative ones, are currently under research. These need to be efficient at ambient temperatures, regenerable at low temperatures, and effective at high-mercury concentration streams and reducing atmospheres. Given the extremely low mercury concentration specifications in LNG plants, the target efficiencies may as high as 99.9%, and when the efficiency drops below 99%, the sorbent may need to be replaced.

Metal oxides possess high adsorption capacity, strong metal ion affinity and the ability to remove heavy metal traces with the possibility of recovery and reuse. Among them, manganese oxides are low cost, environmentally friendly and have been tested as

sorbents/catalysts for the elimination of various gaseous pollutants including Hg^0 vapor. A particular crystal phase of MnO_2, α-MnO_2, consists of 2x2 (4.6x4.6 Å) tunnels constructed from double chains of octahedra [MnO_6] with a variety of stabilizing cations (e.g. K^+, Ba^{2+}) being situated inside its tunnels. Its distinctive properties which are related to the tunnel cavity, moderately acidic sites and easy release of lattice oxygen have rendered it promising for sorption and catalytic applications. Furthermore, various studies have involved the incorporation of CeO_2 into sorbent/catalyst compositions with the aim of enhancing the Hg^0 removal activity, usually at temperatures over 150 °C. This is due to its unique properties, which are related to the reversible Ce^{3+}/Ce^{4+} redox pair, the surface acid-base properties, and the defects that primarily consist of oxygen vacancies.

The target of this study was to develop a regenerable Hg^0 vapor composite sorbent based on nanostructured manganese and cerium oxides, for Hg^0 removal from natural gas streams at ambient conditions. The experimental work was divided into three parts. In the first part, different nanomorphologies (nanotubes, nanorods and nanowires) of α-MnO_2 were hydrothermally synthesized and evaluated for Hg^0 capture at CH_4/N_2 mixtures containing both CO_2 and H_2S. α-MnO_2 nanotubes manifested the highest uptake (1 wt%) and could be regenerated at only 250 °C. The enhanced activity of nanotubes was ascribed to the presence of abundant surface adsorbed oxygen species, that are believed to facilitate Hg^0 adsorption. In the next part the aim was to improve the removal capacity of α-MnO_2 nanotubes by sustaining at the same time its regeneration ability. To achieve this, α-MnO_2 nanotubes were decorated with CeO_2 nanoparticles via a low-temperature hydrothermal method. The CeO_2-saturated nanosorbent, which had a relative Ce/Mn atomic weight ratio of around 35%, exhibited a maximum Hg^0 uptake capacity exceeding 2 wt%, as determined from measurements of mercury breakthrough which corresponded to 99.5% Hg^0 removal efficiency. Its impressive activity was speculated to be related with the facile oxygen vacancy formation at α-MnO_2 NTs as a result of CeO_2 incorporation. Finally in the third part, the potential industrial application of the developed nanosorbent was demonstrated by coating a 3D-printed Ti-based support structure with the developed Mn-Ce nanocomposite. Engineered honeycomb-like structures are advantageous in gas separations because they can provide substantially uniform flow paths which reduce the pressure drop. The structured support was manufactured by a 3D-printing process (SLM) using as material source a titanium alloy, Ti-6Al-4V powder, which is attractive for application in oil and gas industry due to its corrosion resistance and high strength to weight ratio. Despite the fact that the active phase, which was loaded on its surface by a simple dip-coating process, constituted less than 5 wt% of the total mass, the coated structure captured almost 100% Hg^0 vapor in the preliminary 7-h test. The future research plans concern the optimization of the coating process, the examination of alternatives synthetic routes to produce the developed Mn-Ce nanocomposite as well as the investigation of its tolerance against water vapor.

Table of Contents

List of Figures

List of Tables

Nomenclature

Chemical Compounds

Ag^0	*Elemental silver*
$AgNO_3$	*Silver nitrate*
Ag_2O	*Silver(I) oxide*
Al_2O_3	*Aluminium(III) oxide (alumina)*
$Al(OH)_3$	*Aluminum hydroxide*
$AlO(OH)$	*Aluminium hydroxide oxide*
AsH_3	*Arsenic trihydride (arsine)*
$BaSO_4$	*Barium sulfate (barite)*
$C_8H_{15}ClN_2$	*1-butyl-3-mehtylimidazolium chloride ([Bmim]Cl)*
$C_8H_{15}N_2$	*1-butyl-3-methyl-1H-imidazol-3-ium ([Bmim]$^+$)*
$Ca_{10}(PO_4)_6(OH)_2$	*Hydroxyapatite*
$CaSO_4$	*Calcium sulfate*
CdS	*Cadmium(II) sulfide*
$Ce(NO_3)_3\cdot 6H_2O$	*Cerium(III) nitrate hexahydrate*
CeO_2	*Cerium(IV) oxide (ceria)*
CH_4	*Methane*
CH_3CH_2OH	*Ethanol*
CH_3CO_2Ag	*Silver acetate*
$C_6H_4(CO_2H)_2$	*Benzene 1,4-dicarboxylic acid (terephthalic acid)*
$C_{17}H_{35}CO_2H$	*Octadecanoic acid (stearic acid)*
CH_3Hg^+	*Monomethylmercury*
$(CH_3)_2Hg$	*Dimethylmercury*
CH_3HgCl	*Methylmercury chloride*
$CH_3N(C_2H_4OH)_2$	*2,2'-(ethylazanediyl)di(ethan-1-ol) (methyl diethanolamine; MDEA)*
$C_5H_{11}NS_2$	*Diethyl[sulfanyl(carbonothioyl)]amine (diethyldithiocarbamic acid)*
$(CH_2OH)_2$	*1,2-ethanediol (monoethylene glycol; MEG)*
CH_3OH	*Methanol*
$(CH_3)_3SiCl$	*Trimethylsilyl chloride (chlorotrimethylsilane; TMSCI)*
CO_2	*Carbon dioxide*
$CoCl_2$	*Cobalt(II) chloride*
$CO(NH_2)_2$	*Carbonyl diamide (urea)*
COS	*Carbonyl sulfide*
CoS	*Cobalt(II) sulfide*
Co_3S_4	*Tricobalt tetrasulfide*
CS_2	*Carbon disulfide*
$CuCl_2$	*Copper(II) chloride*
$CuCO_3$	*Copper(II) carbonate*
$Cu(NO_3)_2$	*Copper(II) nitrate*
CuO	*Copper(II) oxide*
$Cu_2(OH)_2CO_3$	*Copper(II) carbonate hydroxide (basic copper carbonate)*
CuS	*Copper(II) sulfide*
Cu_2S	*Copper(I) sulfide*
$CuSO_4$	*Copper(II) sulfate*
Fe_2O_3	*Iron(III) oxide*
FeS	*Iron(II) sulfide*
HCl	*Hydrogen chloride*

$HOCH_2(CH_2CH_2O)_2CH_2OH$	*(2,2'-[ethane-1,2 diylbis(oxy)]di(ethan-1-ol) (triethylene glycol; TEG)*
$HN(CH_2CH_2OH)_2$	*2,2'-iminodiethanol (diethanolamine; DEA)*
$H_2N(CH_2)_3Si(OC_2H_5)_3$	*(3-aminopropyl)triethoxysilane (APTES)*
H_2O_2	*Hydrogen peroxide*
$HOCH_2CH_2NH_2$	*2-aminoethan-1-ol (ethanolamine; MEA)*
H_2S	*Hydrogen sulfide*
H_2SO_4	*Sulfuric acid*
Hg^0	*Elemental mercury*
Hg^0_{in}	*Inlet elemental mercury*
Hg^0_{out}	*Outlet elemental mercury*
Hg_2^{2+}	*Mercurous mercury*
Hg^{2+}	*Mercuric mercury*
Hg_p	*Particulate-bound mercury*
Hg_{tot}	*Total mercury*
$HgCl_2$	*Mercury(II) chloride (mercuric chloride)*
Hg_2Cl_2	*Mercury(I) chloride (mercurous chloride)*
$Hg(NO_3)_2$	*Mercury(I) nitrate (mercuric nitrate)*
HgO	*Mercury(II) oxide*
$Hg(SR)_2$	*Mercury thiolates*
HgS	*Mercury sulfide*
HgS_xH, HgS_x^{-2}	*Soluble mercury-sulfur complexes*
HNO_3	*Nitric acid*
$HSCH_2CO_2H$	*Sulfanylacetic acid (thioglycolic acid)*
KCl	*Potassium chloride*
K_2CO_3	*Potassium carbonate*
$KHSO_5$	*Potassium peroxysulfate*
$KHSO_4$	*Potassium hydrogen sulfate (potassium bisulfate)*
$KMnO_4$	*Potassium permangate*
MnO_2	*Manganese(IV) oxide*
MnO_x	*Manganese oxides*
MnS	*Manganese(II) sulfide*
$MnSO_4{\cdot}H_2O$	*Manganese(II) sulfate monohydrate*
MoS_2	*Molybdenum(IV) sulfide*
$NaBH_4$	*Sodium borohydride*
$NaCl$	*Sodium chloride*
$NaNO_3$	*Sodium nitrate*
$NaOH$	*Sodium hydroxide*
Na_2S	*Sodium sulfide*
Na_2S_x	*Sodium polysulfide*
$Na_2S_2O_3$	*Sodium thiosulfate*
NH_4Cl	*Ammonium chloride*
$(NH_4)_2S_x$	*Ammonium polysulfides*
O_a	*Lattice oxygen*
O_b	*Surface adsorbed oxygen*
O_c	*Oxygen from water and/or carbonates*
PbO	*Lead(II) oxide*
R	*Alkyl group* (C_nH_{2n+1})
RSH	*Thiols (R=alkyl group)*
SiH_4	*Silicon tetrahydride (silane)*
SiO_2	*Silicon(IV) oxide (silica)*
S_2	*Disulfur*
S_8	*Octasulfur*
$SnCl_2$	*Tin(II) chloride*

SnO_2	*Tin(IV) oxide*
SnS	*Tin(II) sulfide*
SO_2	*Sulfur dioxide*
TiO_2	*Titanium(IV) oxide (titania)*
$ZnCO_3$	*Zinc carbonate*
ZnO	*Zinc oxide*
ZnS	*Zinc sulfide*
$ZnSO_4$	*Zinc sulfate*
$ZrCl_4$	*Zirconium(IV) chloride*

Abbreviations and Acronyms

3DTi	*3D-printed titanium-based support structure*
AAS	*spectroscopy*
AC	*Activated carbon*
AFS	*Atomic fluorescence spectroscopy*
BCC	*Body centered cubic*
BET	*Brunauer-Emmett-Teller*
C-3DTi	*3D-printed titanium-based support structure coated with MnCe35*
CVAFS	*Cold vapor atomic fluorescence spectroscopy*
DFT	*Density functional theory*
EDS	*Energy dispersive X-ray spectroscopy*
E-R	*Eley-Rideal*
FCC	*Face centered cubic*
GHSV	*Gas hourly space velocity*
HCP	*Hexagonal closest packed*
Hg-TPD	*Mercury temperature programmed desorption*
HRTEM	*High resolution transmission electron microscopy*
L-H	*Langmuir-Hinshelwood*
ICDD-PDF	*International center for diffraction data-Power diffraction file*
IL	*Ionic liquid*
IUPAC	*International Union of Pure and Applied Chemistry*
LNG	*Liquified natural gas*
LME	*Liquid metal embrittlement*
MMSCFD	*Million standard cubic feet per day*
MnCe10	CeO_2*-decorated* α-MnO_2 *nanotubes with 10% Ce/Mn atomic weight ratio*
MnCe25	CeO_2*-decorated* α-MnO_2 *nanotubes with 25% Ce/Mn atomic weight ratio*
MnCe35	CeO_2*-decorated* α-MnO_2 *nanotubes with 35% Ce/Mn atomic weight ratio*
MOF	*Metal-organic framework*
MPAES	*Microwave plasma atomic emission spectroscopy*
MRU	*Mercury removal unit*
NRs	*Nanorods*
NTs	*Nanotubes*
NWs	*Nanowires*
SAED	*Selected area electron diffraction*
SEM	*Scanning electron microscopy*
SILP	*Supported ionic liquid-phase*
SLM	*Selective laser melting*

STP	*Standard temperature and pressure*
TCLP	*Toxicity characteristic leaching procedure*
TEM	*Transmission electron microscopy*
TG	*Thermogravimetry*
Ti-6Al-4V	*Alpha-beta titanium alloy*
UNEP	*United Nations Environment Programme*
US EPA	*United States Environment Protection Agency*
XPS	*X-ray photoelectron spectroscopy*
XRD	*X-ray diffraction*

Chapter 1. Introduction: Mercury’s Detrimental Impact

1.1. Chapter Overview

The introductory chapter is subdivided into three sections. In the first section the significance of mercury’s pollution at a global scale is addressed, by presenting the fundamental physicochemical properties of mercury compounds as well as their source and their biogeochemical circle. The second section provides an overview of the problems caused by mercury’s presence in the natural gas industry. This will help the reader understand why the provision of effective abatement and mitigation treatment is required. The subjects discussed include health and safety issues, equipment’s corrosion and contamination, mercury’s occurrence and geographic variability as well as the available detection, sampling and measurement methods. Recent studies regarding the speciation and solubility of mercury compounds are also reviewed. Most importantly, the gas treatment operations along with the conventional mercury removal systems are evaluated. Finally, taking into consideration the aforementioned, the objective if the thesis is justified and its structure is outlined.

---

* Part of the work presented in this chapter has been published in:
Chalkidis, A.*, Jampaiah, D., Hartley, P.G., Sabri, Y.M., Bhargava, S.K. "Mercury in Natural Gas Streams: A Review of Materials and Processes for Abatement and Remediation".* ***Journal of Hazardous Materials*** *2020, 382, 121036 (doi.org/10.1016/j.jhazmat.2019.121036)*

1.2. Mercury Pollution

1.2.1. Physicochemical Properties of Mercury

Mercury is the only metal that is liquid at room temperature. It has a glistering silver color and forms amalgams with other metals (Kozin and Hansen, 2013a; c). Its low melting temperature is attributed to its electronic structure ([Xe] $4f^{14}5d^{10}6s^2$), the lanthanide contraction and relativistic effects (Gonzalez-Raymat et al., 2017). In its gaseous state, it is a colorless vapor and below its melting point it is a white solid. It is also relative stable and dense, exhibiting high surface tension and volatility. Its electric conductivity is fair, but its heat conductivity is rather poor (Table 1.1) (Beckers and

Rinklebe, 2017). It has a strong affinity for the organic matter, therefore it concentrates in black shales and coal as well as in petroleum and natural gas deposits (Hazen et al., 2012). Apart from the mercuriferous belts and anthropogenically contaminated areas, its terrestrial abundance is in the order of 50 ppb, mainly in the form of cinnabar (HgS) (Adriano, 2001).

Mercury may be present in three oxidation states: elemental or metallic mercury (Hg^0), monovalent or mercurous mercury (Hg_2^{2+}), and divalent or mercuric mercury (Hg^{2+}). Its properties and chemical behaviour depend on the oxidation state, with Hg^0 and Hg^{2+} being the two most prevalent (Kozin and Hansen, 2013b). Since it is monomeric in the gas phase, it tends to form covalent instead of ionic bonds (e.g. $Hg^+–Hg^+$, Hg–C). Hg_2^{2+} is not stable under typical environmental conditions and it rapidly disproportionates into Hg^0 and Hg^{2+}. Both Hg_2^{2+} and Hg^{+2} form numerous inorganic and organic chemical compounds with varying properties. The species' abundance varies between different environmental compartments with more than 95% of the mercury encountered in the atmosphere being Hg^0 (Pandey et al., 2011). Most of the mercury in water, soils, and sediments is present as Hg^{2+} (Lin et al., 2011b), while organic mercury compounds like monomethylmercury (CH_3Hg^+) and dimethylmercury ($(CH_3)_2Hg$) are dominant in biota (Kidd et al., 2011).

***Table 1. 1**. Properties of selected mercury compounds (US EPA, 2007; Beckers and Rinklebe, 2017).*

Compound	***Molecular weight ($g \cdot mol^{-1}$)***	***Density ($g \cdot cm^{-3}$)***	***Melting point (°C)***	***Boiling point (°C)***	***Decomp. temperature (°C)***	***Aqueous solubility, 25 °C ($g \cdot L^{-1}$)***
Hg^0	200.59	13.534	-38.8	356.7	n/a	5.6×10^{-7}
HgO	216.59	11.14	n/a	356	500	Insoluble
HgS	232.66	8.1	n/a	446-583	580	Insoluble
$HgSO_4$	296.66	6.47	n/a	n/a	450	Decomposes
$HgCl_2$	271.50	5.43	277	302	n/a	28.6
Hg_2Cl_2	472.09	7.15	525	n/a	383	0.002
$(CH_3)_2Hg$	230.66	2.96	-43	93	n/a	1 (21 °C)
CH_3HgCl	251.1	4.063	170	n/a	n/a	0.1 (21 °C)

1.2.2. Emissions and Biogeochemical Cycle

The 92 current parties of the Minamata Convention on Mercury, which entered into force in 2017, have committed to undertake decisive actions to reduce mercury pollution (Budnik and Casteleyn, 2018; Chen et al., 2018; Selin, 2018). As the comprehensive report compiled by the United Nations Environment Programme (UNEP, 2018) has recently shown, human activities have resulted in an increase of total atmospheric mercury concentrations by about 450% above natural levels. Small (Esdaile and Chalker, 2018) (>37.5%) and large-scale gold production (>3.5%), non-ferrous metal (e.g. zinc, copper, lead, aluminium) (Staun et al., 2018) (>10%) and ferrous metal production (Fukuda et al., 2011) (~2%), cement production (Zheng et al., 2012) (>10%), waste disposal (>7%) (Svoboda et al., 2016), as well as combustion of fossil fuels (mainly coal-fired power stations) (>23%) (Pavlish et al., 2010; Pavlish et al., 2003; Pudasainee et al., 2017; Srivastava et al., 2006; Wang et al., 2017a; Wilcox et al., 2012; Zhao et al., 2019) comprise the majority of around 2220 t mercury releases into the environment. This accounts for about 30% of mercury emitted annually to the atmosphere. A further 60% results mostly form recycling of anthropogenic mercury previously deposited to soils and water, and around 10% comes from natural sources such as volcanoes.

The natural biogeochemical cycle of mercury relates to its atmospheric transport, deposition to land and ocean, and revolatilization (Selin, 2009). Ultimately a portion deposits at a low rate in deep-ocean sediments (Zaferani et al., 2018). Hg^0 is emitted from geological sources as well as from land and ocean surfaces. Hg^0 is also emitted by anthropogenic sources, such as coal-fired power plants (Galbreath and Zygarlicke, 1996; 2000; Shah et al., 2010). Hg^{2+} and particulate mercury (Hg_p) are also emitted from anthropogenic sources (Hower et al., 2010; Zhang et al., 2016a). Hg^0 is the most abundant species in the atmosphere with an atmospheric residence time of about 0.8-1.7 years, with oxidized and particulate-bound mercury (Hg_p) having a much shorter lifetime (days to weeks). Hg^{2+} and Hg_p are more water-soluble than Hg^0, therefore they can accumulate in ecosystems through wet and dry deposition (Ariya et al., 2015).

As a result of the significant atmospheric lifetime of Hg^0, large-scale patterns of oxidation and reduction control its conversion to Hg^{2+} and subsequent deposition (Driscoll et al., 2013; Obrist et al., 2018). Mercury is brought to the terrestrial surface by wet and dry deposition and a portion of it rapidly revolatilizes to the atmosphere, while the remainder is incorporated into the soil. It may return to the atmosphere by reduction to Hg^0 and subsequent diffusion or mass transport through the soil and into the atmosphere (Gustin, 2011). Wet and dry deposition to watersheds and lake surfaces, as in terrestrial systems, occurs predominantly in the form of Hg^{2+}, which can then reduce to Hg^0, and volatilize to the atmosphere (Zhu et al., 2018b). A portion of Hg^{2+} may convert to the more toxic form of CH_3Hg^+ through methylation, which is a biologically mediated process facilitated by sulfate- and iron-reducing bacteria. Wetlands and lake sediments are the most common environments for methylation (Regnell and Watras, 2018). CH_3Hg^+ can bio-concentrate in living organisms and further bio-magnify up the food chain (Lin et al., 2011a). In the oceans (Gworek et al., 2016; Qureshi et al., 2011), similar to processes in freshwater systems, Hg^{2+} is deposited by dry and wet deposition, and Hg^0 by dry deposition. Hg^{2+} deposited to the ocean may reduce to Hg^0, adsorb onto particles (Liu et al., 2011) or undergo methylation. The reduction from $Hg^{2+}_{(aq)}$ to Hg^0 can be both biologically and photochemically (Vost et al., 2011) facilitated, and the oxidation processes might as well be significant.

1.3. Mercury in Natural Gas Streams

1.3.1. Implications of Mercury's Presence

The role of natural gas (Faramawy et al., 2016) in mitigating greenhouse gas emissions and advancing renewable energy integration is undoubtedly critical (Mac Kinnon et al., 2018). It accounts for less than 25% of the world fuel consumption (BP plc, 2018), with liquefied natural gas (LNG) (Lim et al., 2013) comprising around 10% of global gas trade (International Gas Union, 2018). As hydrocarbon exploration technology advances and as most of the oil-gas reservoirs in shallow layers have been explored, drilling into deeper and hotter reservoirs (Pang et al., 2015) has become an inevitable choice. However, this results in increased probability of encountering mercury in produced fluids, which impacts on the industry from health and safety risks, due to corrosion and contamination of equipment, to catalyst poisoning and toxicity through emissions to the environment (Wilhelm and Bloom, 2000).

Mercury associated with hydrocarbon production (Cousins et al., 2012) may be released through drilling waste (Candler et al., 1992), co-produced water (Lothongkum et al., 2011), production operations and processing waste (Sompongchaiyakul et al., 2018), as well as offshore energy production and gas flaring. For instance, $BaSO_4$ is known to be the main source of mercury in drilling discharges (Trefry and Smith, 2003; Trefry et al., 2003). However, there has been no evidence that mercury is available to marine organisms (Neff, 2008; Parker and Smith, 2004). Likewise, further investigation is required to elucidate the potential impact of unconventional natural gas extraction (Mikos-Szymanska et al., 2018; Xu et al., 2018a), especially with respect to mercury contamination of aquatic ecosystems (Grant et al., 2015; Silva et al., 2017; Vengosh et al., 2014).

The amount of mercury remaining in refined products (Mojammal et al., 2019; Wilhelm, 2001) may be released into the atmosphere during combustion. Although the mercury emissions from oil and gas industry are a negligible contributor (Doll et al., 2012) to the global atmospheric mercury cycle (Ariya et al., 2015; Streets et al., 2017), studies conducted near oil and gas processing facilities (El-Feky et al., 2018; Kirk et al., 2014; Lan et al., 2015; Špirić and Mashyanov, 2000) have reported local increases in mercury concentrations of ambient air. Since the 1970's, when the effect of mercury on natural gas cryogenic processing plants was first realized (Phannenstiel et al., 1976), numerous patents have been published on mercury abatement and remediation. Figure 1.1a shows that in the last decade the patents in the United States, which are related to mercury's presence in natural gas streams, account for almost half of the total patents published in the last 40 years, thereby indicating the increasing interest of energy industry in this issue. This also the case for the journal and conference publications (Figure 1.1b) regarding mercury's presence in oil and gas industry, suggesting the need for further research on this subject.

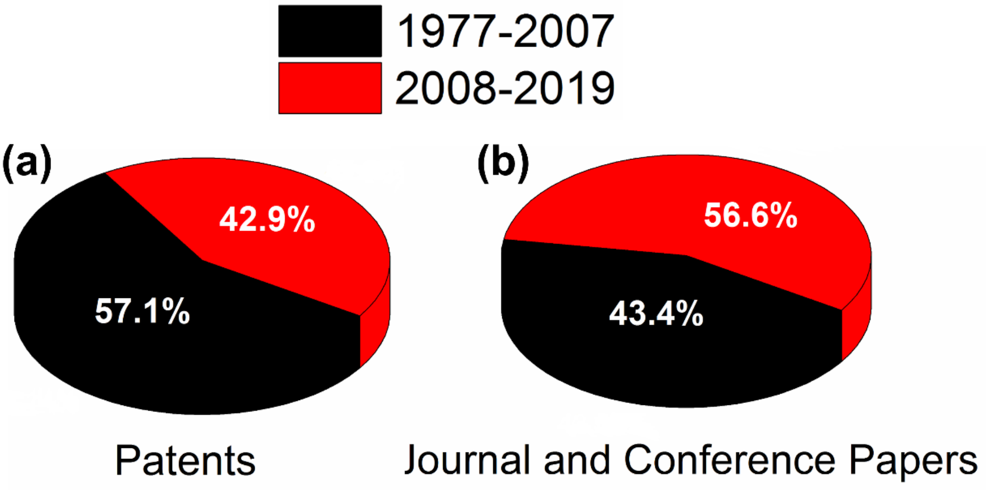

Figure 1. 1*. a) Published patents in the United States with respect to mercury's management in natural gas streams, b) Journal and conference papers regarding mercury's presence in oil and gas industry.*

1.3.2. Corrosion and Equipment Contamination

Corrosion phenomena have been frequently reported in production facilities at the top side wellhead and downhole materials made from carbon/stainless steel. When the protecting chromium oxide film is disturbed under reducing or neutral conditions, corrosion results by Hg^0 forming an amalgam with iron, chromium or nickel and interacting with the liquid water or aqueous acidic phase (Nengkoda and Al-Hinai, 2009). Chloride ions and carbon dioxide have been reported to enhance mercury corrosion of carbon/stainless steel (Pojtanabuntoeng et al., 2011). During production, mercury may be scavenged by carbon/stainless steel by adsorbing into interfacial surfaces and complexing into the scale/metal grain boundaries. Trace quantities of H_2S, which is very common in natural gas streams, catalyze the reaction of mercury with the iron oxide from the pipes (Chanvanichskul et al., 2017).

Most importantly, mercury's presence is associated with the corrosion of aluminum-brazed heat exchangers that are broadly used in LNG facilities (Leeper, 1980; Phannenstiel et al., 1976). This may occur by a combination of physical (amalgamation) and electrochemical corrosion (amalgam corrosion), which can be stress-assisted (LME) (Coade and Coldham, 2006; Wilhelm, 2009). Galvanic corrosion may also occur when Hg^{2+} ions are brought in contact with metallic aluminum in an aqueous solution environment (Bessone, 2006). In the past, catastrophic industrial events, such as the one occurred in Skikda LNG plant, Algeria in 1973 or the more recent 2004 New Year's Day Moomba gas plant explosion in South Australia, have been linked to mercury's presence (Bingham, 1991; Harfoushian, 2013).

The condensation of gaseous Hg^0 or the precipitation of dissolved mercury in liquid hydrocarbons leads to the formation of mercury deposits in cryogenic heat exchangers. The cooling of the heat exchanger or the external cooling from a Joule-Thomson valve or turbo-expander results in phase transitions. Therefore, solid mercury deposits will turn into the liquid phase when the heat exchangers warm-up in shutdowns or during maintenance (Wilhelm, 2009). Amalgamation involves the mercury adsorption on bare aluminum, which induces the localized reduction in the strength of the atomic bonds as a result of the diffusion through the Hg-Al interface. When mercury and aluminum amalgamate in the presence of moisture, amalgam corrosion takes place. After amalgamation, electrochemical oxidation of aluminum and H_2O reduction occurs, leading to the production of $Al_2O_3{\cdot}3H_2O$, hydrogen and free mercury (Equations 1.1-1.3) (Bessone, 2006; Coade and Coldham, 2006).

$$Hg + Al \rightarrow Hg(Al) \tag{1.1}$$

$$Hg(Al) + 6H_2O \rightarrow Al_2O_3{\cdot}3H_2O + H_2 + Hg \tag{1.2}$$

$$Hg(Al) \rightarrow Hg + Al \tag{1.3}$$

Lynch (1981, 2008) explained that LME (Figures 1.2a and 1.2b) concerns the adsorption of mercury atoms at stressed surfaces and crack tips along grain boundaries, leading to the weakening of interatomic bonds at the substrate. Even at low stresses, once cracks are initiated, subcritical cracking can occur rapidly. However, the degradation process may occur on the condition that the Al_2O_3 layer, which protects aluminum alloys from direct contact with mercury, is breached. Clegg (2010) found that the protective nature of the oxide film on aluminum is dependent on the moisture content of air. Nonetheless, in cryogenic heat exchangers the moisture and oxygen content are very low, consequently the formation of the oxide film would potentially be slow.

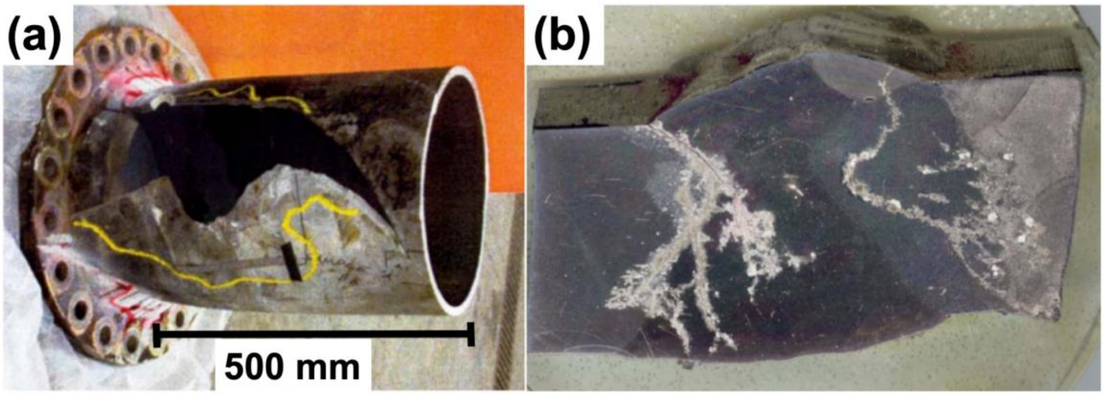

Figure 1. 2. *a) Macroscopic view of a ruptured 5083-0 Al-Mg alloy inlet nozzle of a heat exchanger (Lynch, 2008), b) LME failure on a brazed aluminum heat exchanger (Carnell and Row, 2007).*

The Al_2O_3 film may be damaged by chemical processes, such as corrosion by plastic deformation of the aluminum or mechanical processes such as abrasion or scribing. Also, the differential thermal expansion between the alumina oxide and the aluminum substrate when the heat exchanger is warmed, has been suggested to cause the oxide to crack (Coade and Coldham, 2006; Wilhelm, 2009). Nelson (1994) stated that the locations of all leaks in heat exchangers have been spotted in the corners of headers or in circumferential welds that join the nozzle of the heat exchanger to the piping. In these areas mercury was trapped and held against the aluminum by weld backing strips and unit design, with grain boundary precipitation being also present in aluminum. To detect active LME in contaminated equipment, acoustic emission technique (Wilhelm et al., 1993) has been proposed as a viable method, however the placement of the acoustic transducers is critical to its success.

1.3.3. Health and Safety Issues

Mercury compounds are neurotoxins and in the human body, they accumulate in the liver, kidney, brain and blood (Kim et al., 2016; Syversen and Kaur, 2012). Mercury exposure takes place via inhalation, ingestion and dermal absorption, with various mercury species (elemental, inorganic and organic compounds) differing in the way they interact with biological processes (Clarkson et al., 2003). For instance, Hg^0 is absorbed mainly through inhalation in the body and its rate of absorption via the digestive system is very limited in comparison to CH_3Hg^+.

Until the early 1990's, mercury was used as a displacement fluid in pressure-volume-temperature measurements on hydrocarbon reservoir fluids (Berdugo et al., 2005). According to Wilhelm (1999a) the health and safety considerations of workers in oil and gas processing, include the exposure to Hg^0 vapor (Calabrese et al., 2018; Fields et al., 2017) as well as the dermal absorption of dialkyl mercury (e.g. $(CH_3)_2Hg$). Separators and heat exchangers are the most common locations for mercury accumulation, while inadvertent mercury contamination may occur by pipe leaks and spillages. This is often experienced by offshore workers at platform shutdowns (Ling and Kasim, 2017). Therefore, a careful cleaning and inspection of equipment are necessary (ASTM International, 2017b), since mercury accumulates and concentrates in vessels through adsorption on equipment surfaces and dissolution in sludge, potentially producing interior vapor concentrations that can be much higher than those in process streams.

Blood test measures all three types for mercury (remains in bloodstream for 2-4 days), urine test identifies exposure to elemental and inorganic species (peaks in 2-3 weeks after exposure) (Junio-Ramirez, 2004), while the amount of mercury in hair (Branco et al., 2017) reflects its incorporation via the methylated form. According to the guidelines of the Norwegian Oil and Gas Association (2016), the biological exposure of total inorganic mercury in urine is 30 μg per gram of creatinine, and the permissible exposure limit (time-weighted average-8 h) is 20 $\mu g \cdot m^{-3}$. The guidelines on mercury management in oil and gas by the Malaysian Ministry of Human Resources (2011), specify the total inorganic mercury limit in blood at 15 $\mu g \cdot L^{-1}$.

1.3.4. Occurrence and Geographical Variability

Mercury is present in several hydrocarbon fields globally (Figure 1.3), such as in North (Environment Canada, 2007; Lewis, 1995; Lund, 1996) and South America (Salva and Gallup, 2010), Europe (Hrncevic et al., 2010; Rhodes et al., 1999; Zettlitzer et al., 1997), North Africa (Abu El Ela et al., 2007; Chemrak et al., 2018), Middle East (Al-Sawafi and Al-Jabri, 2017; Baageel, 2010), China (Liu, 2013) and Southeast Asia (Charoensawadpong et al., 2018; Oekon and Suyanto, 1985; Sainal et al., 2007b) including Australia (Chevron Australia, 2015). Its concentration may vary considerably from below 0.01 μg·m^{-3} to well above 1,000 μg·m^{-3} (O'Rear and Thompson, 2017), depending on the geological conditions.

As stated in the first section, mercury has a strong affinity for organic matter (Miedaner et al., 2005) and concentrates in coal as well as in hydrocarbon deposits, with the most abundant mercury compound being HgS (Hazen et al., 2012; Krupp, 1988). In natural gas the mercury formations are of organic (from hydrocarbon source rocks) and inorganic origin (from deep earth's ore-forming fluid) (Yan et al., 2017). The basins where mercury is encountered are often associated with the earth's tectonic and volcanic belts. In fact the mercury concentration in natural gases is determined by factors like the gas genesis, the depositional environment of source rocks as well as the tectonic and volcanic activity (Liu, 2013). According to Gallup et al. (2017), fields producing hydrocarbons and water with elevated mercury concentration are characterized by low H_2S, elevated CO_2, abnormally high geothermal gradients, and may be associated with coaly or I-type tin granite or carbonate source rocks. O'Rear et al. (2016a, b) additionally claimed that Hg^0 reacts in the reservoir with some of the sulfur compounds (e.g. mercaptans, disulfides, hydrogen sulfide), but does not react with thiophenes or some aromatic sulfur compounds.

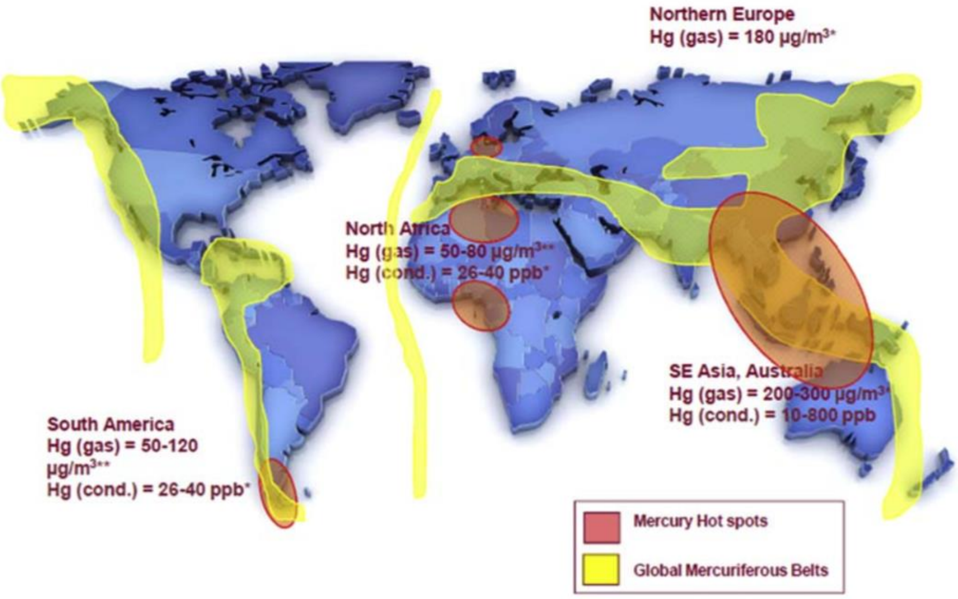

Figure 1. 3. *Mercuriferous belts and hot spots globally (Row, 2012).*

Significant cost overruns have been experienced due to mercury's occurrence in hydrocarbon fluids well into commercial development after processes and equipment are in place to handle production. In the design phase of production facilities, the specification of the mercury removal unit (MRU) is based on the mercury concentration in production fluids collected. However, the mercury concentration (Sainal et al., 2007b) and chemical form (Yamada et al., 2017) of mercury species may be unstable and different from those in the stable production phase. In fact, long-term variability of mercury concentration has been observed even in individual gas wells (Ryzhov et al., 2003). This may be attributed to the deposit's regional-tectonic position and geologic structural features, the storage of hydrocarbons and operating conditions as well as the region's seismic activity. In conclusion, it can be argued that an effective mercury mitigation plan could be provided if mercury's presence in the production fluids could be predicted (Nengkoda et al., 2014; O'Rear et al., 2016a).

1.3.5. Detection, Sampling and Measurement

Regardless of the sample container metallurgy, when sampling mercury some adsorption will always take place (ASTM International, 2017b; Lewis, 1995). In fact, Larsson et al. (2007) showed that the temperature and the type of materials in tubing and valves of the apparatus used for the collection of Hg^0 vapor through amalgamation, in natural gases high H_2S content, may significantly affect the accuracy of results obtained. According to Harfoushian (2013) mercury content quantification is conventionally carried out by wireline formation testers or while drillstem testing a well. However, during drillstem testing mercury can be lost due to adsorption to the string (Yamada et al., 2017) or to the metal surfaces of the sample chambers and sampling tools. Besides, small amounts of drilling fluids or mud filtrate may compromise the sampling process, and if the downhole flow pressure falls below the dew point, the two-phase flow will be present, resulting in unrepresentative samples with larger amounts of heavier constituents. As a consequence, the sampling process must be conducted in single-phase conditions and the sample must be free of contaminants and contained in an inert receptacle. The optimum gas sampling method is with wireline formation testers. To isolate the gas sample (Harfoushian, 2013), a silicon coating (Figure 1.4) is applied via chemical vapor deposition to all metal surfaces that could potentially come in contact with. This coating is specifically designed to improve mercury inertness of steel, stainless steel and alloys.

Nevertheless, the application of the above in gas fields that require hundreds of wells for their development is costly. Currently a major part of mercury sensing research (Kabir et al., 2017a), in which our group has contributed a great deal, is focused on microscale mercury sensors such as quartz crystal microbalance (Mohibul Kabir et al., 2019), surface acoustic wave (Kabir et al., 2017b) and conductometric devices (Griffin et al., 2016).

Their working principle is based on mercury amalgamation with the sensitive material, which induces alterations in certain properties (e.g. frequency, resistance, capacitance) of the sensors. Surface acoustic wave technology has been proved to be capable of detecting and speciating organic and inorganic mercury compounds in hydrocarbon fluids (Thomas et al., 2017). The integrated sensor assembly can be placed at the sampling location (wellhead platform of processing plant) and left to run independently under continuous or near-continuous mode. Its temperature and pressure operating conditions range between 60-300 °C and 140-850 bar, respectively, while its quantification limit in gas is 1 $\mu g \cdot m^{-3}$.

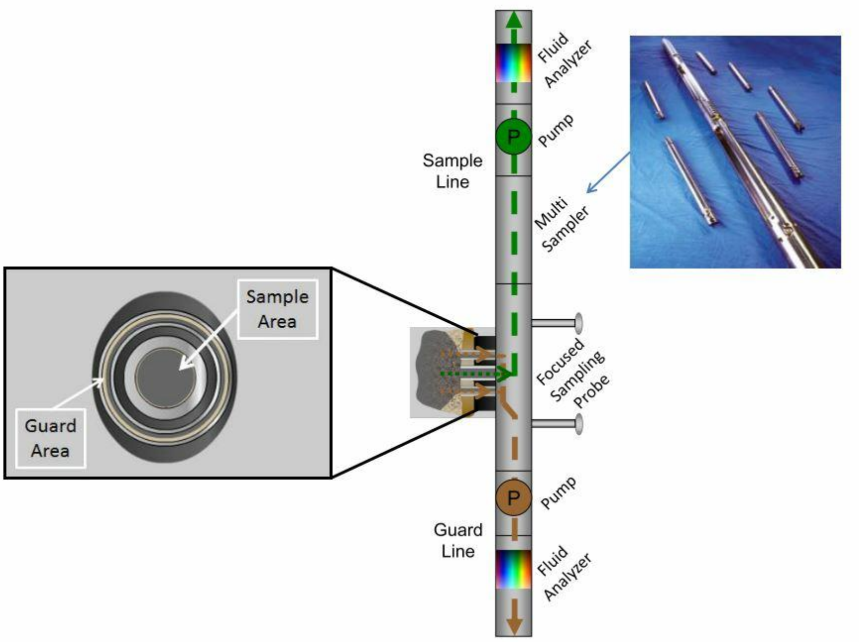

Figure 1. 4*. Wireline formation tester toolstring with focused sampling probe and a multisampler containing six silicon-coated sample receptacles (Harfoushian, 2013).*

Mercury concentration may vary over time as it is not produced at constant concentration, but rather in the form of plugs and slugs, therefore continuous monitoring is required. In a recent patent (Van Hal et al., 2018), a technique was developed according to which, a liquid phase reagent solution, including suspended nanoparticles with affinity to mercury, is mixed with the hydrocarbon fluid in a microfluidic device that produces a slug flow, which is then subjected to optical analysis for mercury detection. Gas chromatography and ultraviolet photometric detection (Gras et al., 2015) have also been combined to achieve direct Hg^0 detection without pre-concentration, requiring less than 2 min sample analysis time and 2 ml sample volume. Measuring mercury content in-situ a gas production line and in continuous mode, has been succeeded by a method based on infrared spectroscopy (Guieze et al., 2010), while more recently, a high-pressure bubbling sampler (Cachia et al., 2017) has been developed to sample and concentrate metals directly in a natural gas network, designed to work up to 100 bar and 40 $L \cdot min^{-1}$. Further, a mercury-in-gas sampling system was claimed by Laine et al. (2018), in which the pressure of the sample gas stream upstream of the critical orifice in the pressure reduction section, is up to 100 bar, while the gas stream pressure downstream the orifice is less than 1 bar.

In practice, the low mercury concentrations in hydrocarbons, the high volatility of mercury and the sample matrix complexity, make mercury's determination difficult (Grice and Vanorman, 2008). This dictates the need for either a highly sensitive detector or a large sample volume, or even both. Total mercury in natural gas (Frech et al., 1995) is commonly measured by atomic absorption (AAS) (ASTM International, 2014a) and fluorescence spectroscopy (AFS) (ASTM International, 2014b). Compared to other measurement methods (Table 1.2), AFS can achieve greater sensitivity because of the very low background of fluorescence signals. The operation of cold vapor atomic fluorescence spectroscopy (CVAFS) (Sánchez-Rodas et al., 2010) is explained in detail in Chapter 3. As far as sampling is considered, the Ontario Hydro method (ASTM International, 2016) has been traditionally employed for the determination of elemental, oxidized, and particle-bound mercury in the flue gases generated from coal-fired stationary sources. Recently, Brombach and Pichler (2019) developed a modified method for trapping mercury from gases with high H_2S content. Apart from acidified $KMnO_4$ traps, this method also makes use of NaOH to remove H_2S and $NaBH_4$ to maintain reducing conditions,.

Table 1. 2*. Analytical techniques for total mercury determination in natural gas and condensates (Sainal et al., 2007a).*

Method	***Detection limit (ng)***
X-Ray fluorescence	10
Neutron activation	2
Gold film	0.5
Differential pulse voltammetry	0.04
Cold-vapor atomic absorption	0.01
Cold-vapor atomic fluorescence	0.0001
Inductively coupled plasma mass spectrometry	0.001
Inductively coupled plasma mass spectrometry	50 ng·mL

1.3.6. Speciation and Solubility

In natural gas mercury almost exclusively exists as Hg^0 (Ezzeldin et al., 2016; Wilhelm and Bloom, 2000) at concentrations far below saturation suggesting that no liquid mercury phase exists in most reservoirs. In gas condensate and crude oil (US EPA, 2001) apart from dissolved Hg^0, other forms (see Table 1.1) may be present: inorganic mercury (Hg^{2+} such as $HgCl_2$, HgO), dissolved organic mercury (RHgR′ where R=CH_3, C_2H_5, etc. and R′= CH_3, C_2H_5, Cl, etc.), mercury-sulfur complexes (HgK where K=organic sulfide, thiol, thiophene, mercaptan), as well as suspended/particulate Hg_p (e.g. HgS). Speciation consists of the analysis of various mercury species to fulfill the requirements of the mass balance (Ruhland et al., 2018) described by Equation 1.4:

$$Hg_{tot} = Hg^0 + R_2Hg + RHg^+ + Hg^{2+} + Hg_p \tag{1.4}$$

Nevertheless, uncertainties arise for mercury species found in most liquid hydrocarbon fractions, due to their different physicochemical properties and instability over time, as well as the inadequate validation of the employed speciation methods (Bouyssiere et al., 2000, 2002; Frech et al., 1996; Gaulier et al., 2015; Shafawi et al., 1999; Snell et al., 1996; Tao et al., 1998). The speciation and solubility of mercury in hydrocarbons is necessary to understand its partitioning and distribution in various phases during processing, transport and storage. It is also essential for the provision of effective mitigation treatment. A demonstration of the latter was the evaluation of sorbent-based mercury removal systems for gas condensate by Shafawi et al. (2000).

Mercury in crudes (Wilhelm et al., 2006) and condensates (Bloom, 2000) is mostly particle-associated. Recently, Avellan et al. (2018) highlighted the presence of HgS nanoparticles on solid petroleum residues. Also, Ruhland et al. (2018) reported the presence of HgS nanoparticles of various size in the condensate. Gajdosechova et al. (2015) had already suggested that mercury particles in petroleum products are reactive at low temperature during Grignard alkylation, explaining in this way the random variation in Hg^{2+} species concentration in a given crude oil sample. Physical filtration (Charoensawadpong et al., 2018) along with centrifuge technology (Manelius and Aguedach, 2018), have been practiced for Hg_p removal from condensate.

Hg^0 exerts high vapor pressures at ambient conditions and easily amalgamates with most metals, but it does not dissolve well in polar solvents such as H_2O. In general, the solubility of Hg^0 is higher in aromatics than alkanes and increases with the temperature (Marsh et al., 2016). For pure polar solvents used in natural gas treatment operations, its solubility follows the order: alcohols > triethylene glycol (TEG) > monoethylene glycol (MEG) > amines > H_2O (Gallup, 2018; Gallup et al., 2017). Several successful attempts have been made to predict mercury’s solubility in hydrocarbons and polar solvents by developing thermodynamic models based on the use of modified equations of state

(Khalifa and Lue, 2017; Koulocheris et al., 2018; Polishuk et al., 2016, 2017; Smit et al., 2004). Changes in temperature and pressure during the migration of fluids to the surface and downstream the wellhead may re-distribute mercury in the phases. As discussed earlier it may adsorb and accumulate on the drill strings, production tubes and equipment. Generally, organic mercury species (if present) preferentially partition to the heavy liquid fraction (condensate) and ionic compounds escape to water, while Hg^0, due to its low solubility and high volatility, equilibrates between the liquid and gas fraction (Ezzeldin et al., 2016).

1.3.7. Gas Treatment Operations

Chemical treatment processes such as gas hydrate control (Bomba et al., 2018) using methanol or MEG, as well as acid gas removal (Rufford et al., 2012; Shah et al., 2017; Yeo et al., 2012) and dehydration (Kong et al., 2018) (Figure 1.5) are potentially affected by the presence and partition of mercury species. H_2S and/or CO_2 are very often present in natural gas and their removal is usually carried out by amine treatment (e.g. DEA, MDEA), while the dehydration process usually involves the use of glycols (e.g. MEG, TEG) or molecular-sieves (Alcheikhhamdon and Hoorfar, 2016).

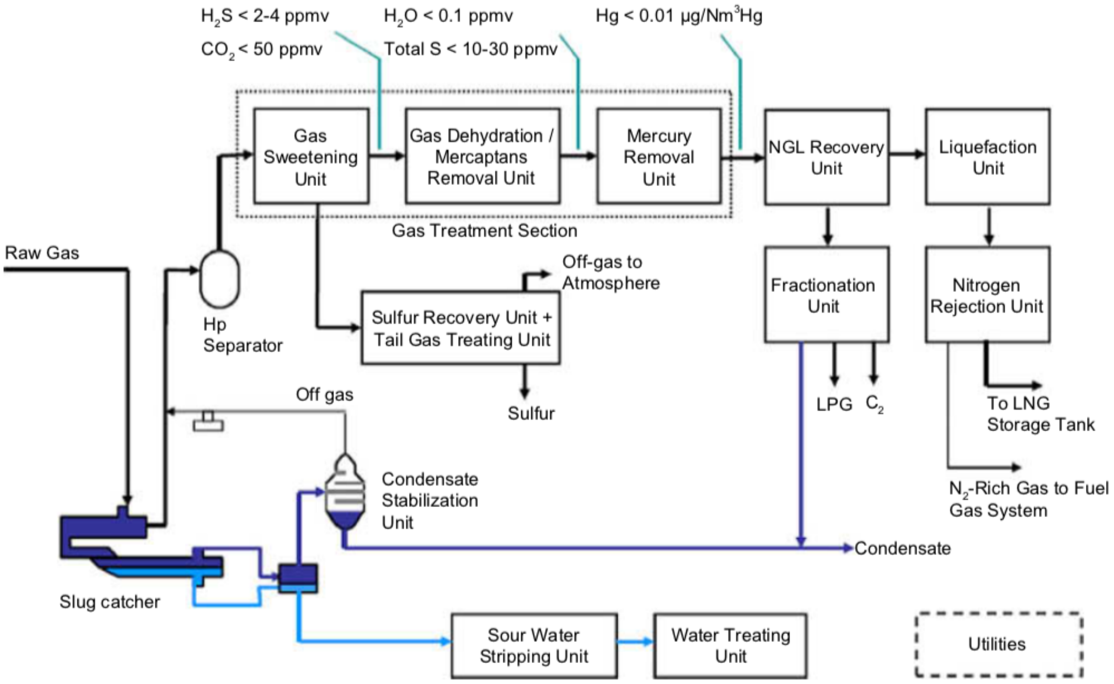

Figure 1. 5*. Illustration of a typical LNG plant: Unit operations and concentration requirements (Mokhatab et al., 2014).*

Mercury is partially removed in these processes (Carnell and Openshaw, 2004) and if no MRU is installed upstream of the units, its distribution may resemble to that illustrated in Figure 1.6. It may exit either in the water vapor from the glycol unit or in the acid gas from an amine unit. It may as well be present in the regeneration off-gas from these units, or it can end up as a stable form in the treating solution from these processes. Also, it can accumulate in tanks, filters, pipelines, metal equipment surfaces, as well as wastewater treatment by-products and sludges.

Given the range of conditions in these compartments, mercury potentially exists as Hg^0 vapor, various oxidized organic forms and particulate forms. In high-pH amine solutions, mercury is probably in the form of HgS_2H^- and HgS_2^{-2}, while in glycol dehydrators $Hg(SR)_2$ is predominant among other species (Avellan et al., 2018). Gallup (2018) showed that the concentrations of elemental and ionic mercury are very small compared to particulate mercury. This is in line with Avellan et al. (2018), who reported high concentrations of solids collected from MEG dehydrators in the form of HgS and mercury thiolates. It is worth mentioning at this point that centrifugal separation by use of disc stack centrifuges (Manelius and Aguedach, 2018) offers a powerful alternative technology to filtration for Hg_p removal in MEG streams.

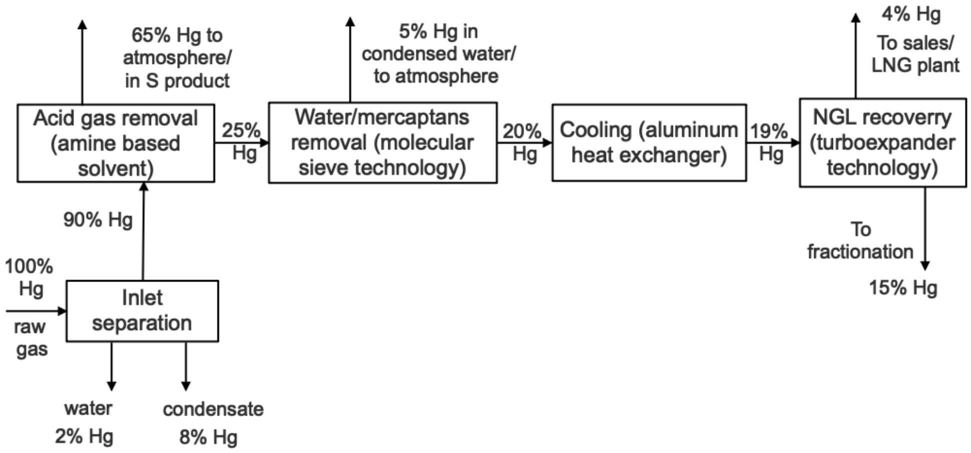

Figure 1. 6. *Indicative mercury distribution on a gas processing plant lacking a mercury removal unit (Row and Humphrys, 2011).*

1.3.8. Mercury Removal Systems

Fixed-bed reactors (MRUs) like that shown in Figure 1.7, are typically deployed in regenerative or non-regenerative modes (Markovs and Clark, 2005) to reduce the gas stream mercury concentration to fewer than 10 $ng \cdot m^{-3}$ (1.0 ng $Hg \cdot g^{-1}$ in liquid streams). The conventional systems comprise of materials (see Table 1.3) such as sulfur-impregnated activated carbons, metal sulfides and silver-impregnated molecular sieves, which remove mercury by amalgamation, physical or chemical adsorption and reactive absorption (Table 1.4) (Abai et al., 2015; Warrag et al., 2018). Adsorption (Tagliabue et al., 2009) has been considered as a superior method due to its comparatively low cost, design simplicity, easy operation, low-harmful secondary products and facile sorbent regeneration. Although MRUs remove the majority of mercury species from gas streams, environmentally appreciable amounts can still be emitted due to the vast quantities of gas processed at some facilities (Washburn et al., 2018).

A variety of sorbents (Granite et al., 2000; Liu et al., 2010; Xu et al., 2018b; Yang et al., 2007) has been proposed for the removal of mercury from flue gases generated in coal-fired power stations (Zhao et al., 2019). For example, our research group (Jampaiah et al., 2015a; 2016; 2013; 2015b) has comprehensively investigated the synergistic effect of CeO_2 and MnO_x in the design of catalysts for Hg^0 oxidation at flue gas environments. It is true, however, that many of the reported materials are not deemed as suitable for mercury removal under natural gas processing conditions.

Table 1. 3. *Manufacturers of commercial mercury removal systems.*

Manufacturer	***Commercial product***	***Material/System***
Honeywell UOP	UOP GB	Alumina-supported copper sulfide
	UOP HgSIV	Silver-impregnated molecular sieves
Johnson Matthey	PURASPEC	Alumina-supported copper sulfide/copper carbonate with zinc sulfide/zinc carbonate
Axens	AxTrap 200 Series	Alumina-supported copper sulfide
Calgon Carbon	HGR	Sulfur-impregnated activated carbon
Cabot Corporation	NORIT RBHG	Sulfur-impregnated activated carbon
Nucon International	MERSORB	Sulfur-impregnated activated carbon
Schlumberger	SELECT Hg	Mixed metal sulfide-based
BASF	Durasorb HG	Alumina-supported copper sulfide
Pall Corporation	SepraSol Plus, Medallion HP	Liquid/gas coalescers (upstream of the adsorption bed)
	MCC1401	Gas particle filter (downstream of the adsorption bed)

Such conditions (Table 1.5) require high removal efficiency at ambient temperatures, high-mercury concentration gas streams and reducing atmospheres, as well as tolerance against the commonly present acid gases, H_2S and CO_2. High sorption capacity at low Hg^0 breakthrough tolerance, as well as reusability are the two essential properties for the mercury sorbents in natural gas treatment operations. Additionally, it is desirable that the sorbents possess large pore volume with specifically engineered pore size distribution, highly dispersed active phase on a substrate with large surface area, as well as crushing strength and attrition resistance to ensure low and stable pressure drop with plug flow, no channeling, and no powder formation (Eckersley, 2013; Jubin, 2017). Of course, the manufacturing cost is a defining factor and the utilization of waste materials is highly advantageous (Worthington et al., 2017).

Table 1. 4. *Mercury removal systems for natural gas (Abai et al., 2015; Bingham, 1991).*

Active compounds	***Support/ Medium***	***Mercury fate***	***Advantages/ Disadvantages***	***Indicative range of operating conditions***
Sulfur	Carbon	HgS	Most used, cheap, disposal problems	Temperature:0-120 °C, Pressure:0.1-70 bar, Contacting time at 25 °C and 1 bar:0.2-20s (Nishino et al., 1985)
Silver	Zeolite	Ag-Hg amalgam	High investment cost, simultaneous dehydration	Temperature:16-60 °C, Pressure:1.4-175 bar, GHSV:10,000-100,000 h^{-1}, Regeneration: 200-350 °C (Rastelli et al., 2015)
Metal oxide/ metal sulfide	Metal oxide	HgO/HgS	Regeneration ability, high removal capacity	Temperature:20-100 °C, Pressure:10-200 bar, GHSV:4,000-20,000 h^{-1}, humidity:10-90% (Porcheron et al., 2015)
Thiol/oxidizing agent/chelating agent	Scavenger Solution	Soluble Hg^{2+} compound	Corrosivity, system contamination, regeneration issues	Temperature:20-90 °C, Pressure:1-70 bar, Superficial gas velocity: 2-30 $\text{cm}\cdot\text{s}^{-1}$ (O'Rear et al., 2013)

Figure 1. 7. *Parallel fixed-bed reactors (MRUs) utilizing mercury sorbents at the PTT GSP-5 gas plant at Map Ta Phut in Rayong, Thailand (Eckersley, 2010).*

The MRUs can be installed in different locations within the gas plant (Table 1.6) (Mokhatab et al., 2019). Traditionally, the location downstream the acid gas removal and dehydration unit (Figure 1.5) prevents mercury migration (Ikealumba and Wu, 2014; Rios et al., 1998) to the liquefaction unit. Retrograde condensation is avoided, the gas is already dried and cleaned, and consequently the removal process is more effective. However, mercury contaminates all upstream equipment and fluid streams.

In the last years, there is a rising trend to place a simple in both construction and operation, MRU at the wellhead or close to the front of the process plant. An example of this was presented by Al-Sawafi and Al-Jabri (2017). At this location, mercury emissions to the atmosphere and contamination of plant equipment are prevented, but larger volumes of sorbent may be required due to the large volumetric flow of feed gas (Sayed et al., 2017). Also, the gas is always wet, and if sulfur-impregnated carbon is utilized, the mercury removal process will be compromised by the adsorption of moisture into the microporous carbon substructure.

Table 1. 5*. Specifications of MRU installed at Salam gas processing facility in Egypt (Abu El Ela et al., 2007).*

Catalyst Information		***Operational Conditions***	
Type	PURASPEC 1156	No. of trains	2
Weight	19 t	Flow rate per train	120 MMSCFD
Density	1000 kg·m^{-3}	Turn-down ratio	50%
Diameter	2.8-4.75 mm	Pressure	63.1 barg (normal) 70 barg (design)
Form	Spherical granules	Temperature	61 °C (normal) 100 °C (design)
Composition (mol %)		Hg^0_{in}	170 μg·Sm^{-3}
N_2	1	Hg^0_{out}	< 0.1 μg·Sm^{-3}
CO_2	6.59	***Bed Information***	
C_1	73.91	Volume	19 m^3
C_2	10.85	Diameter	3 m
C_3	5.31	Height	2.7 m
i-C_4	0.73	Pressure drop	< 0.5 bar
n-C_4	0.97	Life	5 years
i-C_5	0.25		
n-C_5	0.15		
C_{6+}	0.24		
SG	0.764		
MW	22.13		

Installing the MRU downstream of the sweetening unit and upstream of the dehydration unit, reduces the size of the bed, since the gas volume after acid gas treatment is reduced. However, the solvent in sweetening process may be contaminated and further treatment may be required for the contaminated regeneration stream. Water and mercury can be simultaneously removed in a single bed by employing regenerable silver-impregnated molecular sieves. In this case, unnecessary increases in pressure drop are avoided and mercury does not accumulate on the sorbent, overcoming the issue of spent sorbent disposal. Nevertheless, mercury may be present in the regeneration gaseous stream and condensed water, requiring further treatment. Besides, the regeneration system and the additional size requirements may potentially pose additional capital costs (Ruddy et al., 2007). In conclusion, it should be stated that when the MRU malfunctions or operates inefficiently, the residual mercury may need to be removed before the gas stream enters the LNG plant by using additional beds (Al-Faqeer, 2007; Audeh and Hoffman, 1992a, b; Audeh and Kirker, 1993; Gammie and Yan, 1991; Yan, 1990a, 1991b).

Table 1. 6*. Assessment of mercury removal processes depending on the installation location of MRU in the gas plant.*

MRU location	***Advantages***	***Disadvantages***
At the wellhead or close to the front of the plant	Protection of all downstream equipment, simple in both construction and operation	Larger volumes of sorbent, gas is always wet
Downstream of the acid removal and dehydration unit	Retrograde condensation is avoided, gas is already dried and cleaned	Contamination of all upstream equipment and fluid streams
Downstream of the acid removal unit and upstream of the dehydration unit	The size of the bed is reduced	The solvent in sweetening process may be contaminated, the regeneration stream needs further treatment
Simultaneous dehydration using regenerable silver-impregnated molecular sieves	Unnecessary increases in pressure drop are avoided, mercury does not accumulate on the sorbent	Mercury present in the regeneration stream and condensed water, further treatment required, additional capital costs

1.4. Thesis Objective and Outline

The scope of this research work relates to the investigation of low-cost, selective and regenerable sorbents that are efficient for Hg^0 vapor removal from methane gas mixtures at ambient temperatures. Metal oxides possess high adsorption capacity, strong metal ion affinity, as well as regeneration capacity. Among them, manganese and cerium oxides have been successfully utilized in the design of composite catalysts for the adsorption/oxidation of Hg^0 in flue gas environments at higher temperatures (>150 °C). Therefore, the question that arises is how the synergistic effect of these active metal oxides can be exploited at the conditions pertaining to natural gas processing operations. With the advent of nanoscience it has been realized that the activity of a metal oxide-based sorbent/catalyst may be affected by the size and/or shape of its nanoparticles. Hence, the research focus in this study was placed on the examination these parameters, with the aim of elucidating the mechanism of low-temperature Hg^0 removal process and establishing correlations between the sorbent's properties and its performance under certain reaction conditions. Of course, from the industrial perspective the major question concerns the feasibility of employing the developed nanomaterials at full scale, for which certain criteria must be fulfilled (e.g. low increase in pressure drop of fixed bed). Hence, this study is completed by utilizing additive manufacturing technology (i.e. 3D-printing) to propose a viable transition to production-scale operation, by making use of metal-based (i.e. titanium) support structures that offer advantageous properties in comparison to the commonly used pellets, granules and extrudates.

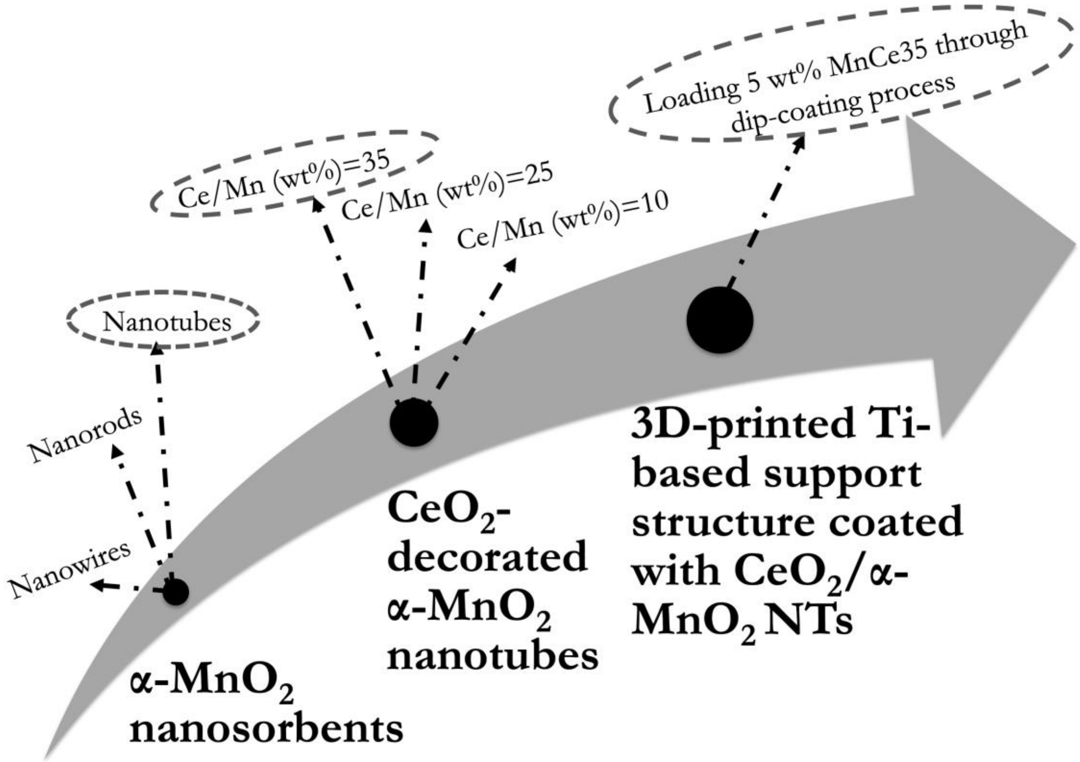

Figure 1. 8*. Schematic representation of the thesis experimental outline.*

To meet the above discussed objectives, the thesis is organized as follows:

- Chapter 1 provides a general introduction to the issues related to mercury's presence in industry. Before this, the mercury's pollution global impact is addressed by presenting the latest data with respect to its sources and fate in the environment.

- Chapter 2 presents a literature review of the materials and processes utilized for abatement and remediation in natural gas industry. For the first time the patents, as well as the journal and conference papers on this subject are critically discussed to pinpoint areas that require further research.
- Chapter 3 analyses the experimental methods regarding the synthesis of materials and their characterization. It also explains in detail the experimental configuration and procedure for the conduction of mercury removal and sorbent regeneration tests.
- Chapter 4 evaluates the suitability of a particular crystal phase of MnO_2, α-MnO_2, as an efficient and regenerable mercury sorbent at conditions pertaining to natural gas processing operations. It also includes the attempt to elucidate the morphology effect at nanoscale, through the comprehensive characterization of the prepared materials.
- Chapter 5 describes the effort to exploit the synergistic effect of nanostructured manganese and cerium oxides at room temperature. CeO_2 nanoparticles are incorporated by a low-temperature hydrothermal method to the superior α-MnO_2 nanomorphology with aim the of enhancing its activity towards Hg^0 vapor removal as well as improving its tolerance against acid gases (e.g. H_2S).
- Chapter 6 displays a viable way to deploy the developed nanocomposite at full scale. The nanomaterial is coated on a 3D-printed Ti-based support structure, which manifests a promising performance. In relation to this, the future challenges are discussed and general conclusions are drawn.

Chapter 2. Literature Review: Materials and Processes for Abatement and Remediation

2.1. Chapter Overview

Based on the introduction (first chapter), the second chapter reviews the materials and processes for mercury abatement and remediation in the natural gas industry. This entails the evaluation of all critical areas from production to processing, where mercury is present and poses threats to both the human health and facilities. In the first section the conventional materials used in fixed beds, such as activated carbons, metal sulfides, metal oxides and molecular sieves are compared. Furthermore, recent proposed alternative materials such as ionic liquids and metal-organic frameworks are assessed. In the second section processes such as complexation and scrubbing, simultaneous Hg and H_2S removal, glycol and molecular sieve dehydration, as well as recent subsurface methods in conjunction with hydrates treatment are discussed. Finally, a brief overview of the facilities clean up and waste disposal practices is given. This is the first thorough review on this challenging industrial problem and aims to help readers understand that tackling mercury contamination during natural gas treatment is a complex task.

---

* Part of the work presented in this chapter has been published in:
Chalkidis, A., *Jampaiah, D., Hartley, P.G., Sabri, Y.M., Bhargava, S.K. "Mercury in Natural Gas Streams: A Review of Materials and Processes for Abatement and Remediation".* ***Journal of Hazardous Materials*** *2020, 382, 121036 (doi.org/10.1016/j.jhazmat.2019.121036)*

2.2. Materials

2.2.1. Activated Carbons

Activated carbons (ACs) due to their high specific area, pore volume and wide pore size distribution, have been extensively utilized for Hg^0 removal via physical and chemical sorption. In physisorption, Hg^0 vapor is essentially condensed on AC’s surface, reflecting a weak bond that is sensitive to temperature changes. The process is exothermic and the adsorption capacity decreases with temperature increase (Suresh Kumar Reddy et al., 2014a). Chemisorption, on the other hand, occurs on porous AC’s active surface sites, resulting in the formation of non-volatile species. Dejong and Vos (1980) proposed the use of chlorine-modified activated carbon. Sulfur has also been suggested for impregnating ACs (Equation 2.1) (Nishino et al., 1985; Otani et al., 1988). Interestingly, carbon molecular sieves impregnated with sulfur were found to be less adversely affected by water and temperature (Matviya et al., 1987).

$$Hg_{(g)} + 1/8S_8 \rightarrow HgS \tag{2.1}$$

Li et al. (2003) argued that the lactonic and carbonyl groups present on porous ACs are favorable sites for Hg^0 adsorption, whereas phenolic groups play an adverse role. Carbons with mesoporous and macroporous structure may exhibit better performance due to the improved access to internal surface-active sites (Wdowin et al., 2014). The impregnation with sulfur adds on active sites, and HgS formation acts as the driving force for improved Hg^0 removal efficiency (Lee and Park, 2003; Liu et al., 1998). A mechanism (Figure 2.1b) proposed by Yao et al. (2014) first involves Hg^0 oxidation to Hg^{2+} by forming a double bond with sulfur with the use of two pairs of shared electrons. Then, one electron transfers from Hg=S double bond to C–S single bond, leaving reactive electrons of the mercury and carbon to form a single bond. Subsequently the bond, which originally connected carbon and sulfur, breaks creating a lone pair of electrons.

Suresh Kumar Reddy et al. (2014b) explained that the increase in Hg^0 adsorption capacity of sulfur-impregnated carbon (SIC) with the raise in temperature up to 140 °C, may be attributed to the chemisorption process due to the reaction of mercury with sulfur. Also, they argued, in agreement with earlier studies (Guijarro et al., 1994; Korpiel and Vidic, 1997), that the sulfur-embodiment process affects the sulfur distribution and bondage, which in turn impacts greater the Hg^0 removal efficiency than the percentage of sulfur loading itself. Therefore, they attempted to incorporate sulfur during AC's manufacturing process, rather than impregnating it externally (Kumar Reddy et al., 2016). The AC (SC-600) exhibited at 50 ºC a higher mercury uptake (~5.5 $mg \cdot g^{-1}$) than the commercial sulfur-impregnated carbons (Table 2.1). Despite its relatively lower surface area and sulfur loading, the higher adsorption capacity was attributed to the presence of $-SO_3H$ functional group attached to graphitized rings with high density of acid sites.

In a more recent study of the same group (Achazhiyath Edathil et al., 2018), bio-derived porous carbon (PC-900) was prepared by pyrolyzing at 900 °C alginate biomass containing calcium salts. This was found to be superior to other bio-based and sulfur-impregnated carbons at 50 °C. The bigger average pore radius and pore volume allowed easy access to the surface oxygen functional groups (lactone, carbonyl or carboxyl), which facilitated the electron process transfer, as they acted as surface-active centers for Hg^0, causing its oxidation to Hg^{2+} on AC's surface (Figure 2.1a).

Table 2. 1*. Properties of sulfur-impregnated activated carbons (Kumar Reddy et al., 2016, 2014b).*

Adsorbent	***Sulfur content (%)***	***Surface area ($m^2 \cdot g^{-1}$)***	***Average pore diameter (nm)***
Calgon-HGR	5.21	573	2.48
Calgon-SGL	0.23	900	2.52
UOP	1.7	–	–
Norit-3	19.08	612	2.39
SIC	12.32	780	2.45
SC-600	2.19	510	3.1

In general, the effect of N_2, O_2 and H_2S is promotional, H_2O inhibits the Hg^0 removal process, while CO_2 has been reported to have either neutral or inhibiting role (Diamantopoulou et al., 2010; Liu et al., 2000; Lopez-Anton et al., 2015; Wei et al., 2015). Impregnation temperature also plays a key role in the Hg^0 removal efficiency of the prepared sorbent. 400-600 °C has been reported to be the optimum temperature range to produce effective sorbents. It has been also argued that the sulfurization process is associated with the decomposition of surface functionalities, which creates active sites for sulfur bonding (Feng et al., 2006a, b). Below 300 °C, sulfur adheres to porous AC in the form of clusters, blocking the pores, while at higher temperatures it distributes evenly (Suresh Kumar Reddy et al., 2014a).

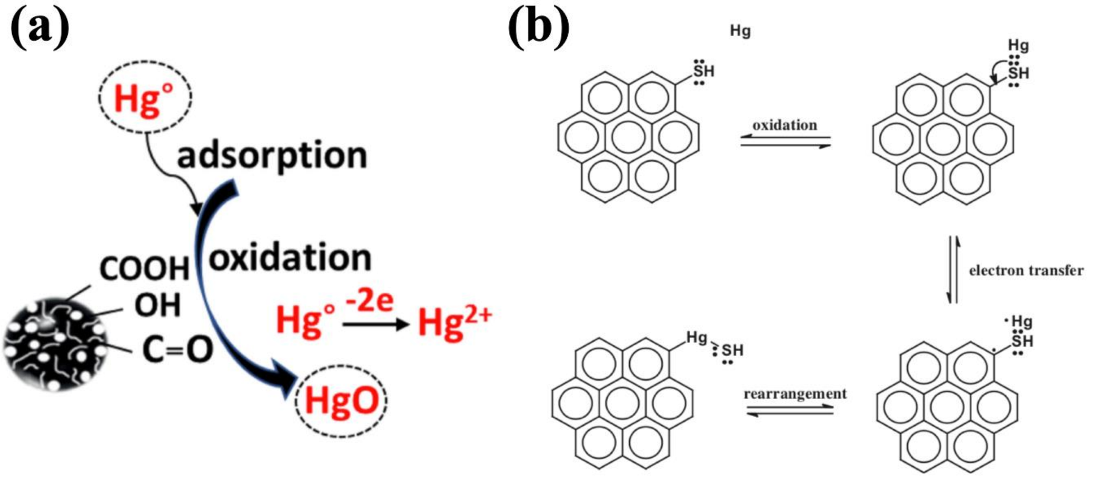

Figure 2. 1*. a) Mechanism of Hg^0 sorption and oxidation on bio-derived porous carbon (Achazhiyath Edathil et al., 2018), b) Mechanism of Hg^0 adsorption by a sulfide group (Yao et al., 2014).*

Sulfur-impregnated carbons are broadly utilized for demercuration in natural gas industry, however, serious drawbacks have been reported in practice. ACs are rarely regenerated due to the high temperature regeneration requirements (600 °C) (Li et al., 2018c). Also, in wet gas streams, ACs are prone to sulfur dissolution (Kumar Reddy et al., 2015) and suffer from capillary condensation because of the extensive microporous nature of their structure. This may lead to sulfur slips, damages to downstream equipment and reduction in mercury removal capacity. Consequently, beds comprising of ACs are located downstream of the molecular sieve dryers, even if the pressure drop is introduced into the final stages of processing (Jubin and Ducreux, 2014). A potential solution might be the incorporation of metal sulfides on porous carbon matrix (Reddy et al., 2018), combining in this way the inertness of metal sulfides to sulfur leaching and the higher crushing strength of ACs. In any case, the disposal of the mercury-containing sulfur-impregnated carbons constitutes a serious environmental problem (Wang et al., 2012), given that landfill is the most relied method of disposal (Wilhelm, 1999b).

2.2.2. Metal Sulfides

Metal sulfides such as CoS/Co_3S_4 (Quan et al., 2019), CuS (Liu et al., 2019a; Yang et al., 2018c), ZnS (Li et al., 2016a; Liao et al., 2019; Zhao et al., 2018b), MoS_2 (Zhao et al., 2018a), FeS/FeS_2 (Li et al., 2018b; Wu et al., 2007), and sulfide-modified Cu-Fe (Makkuni et al., 2007), have been tested for Hg^0 removal from flue gases, although in many cases a reduction in efficiency has been observed at temperatures above 150 °C (Couling et al., 2012). In natural gas processing, to overcome the drawbacks of activated carbons, metal sulfides produced by solid-state fusion, spray pyrolysis and precipitation techniques, have been proposed as an alternative solution. The reactive metal is incorporated in the inorganic support and the sorbent is supplied with the reactive sulfide already present, or formed in situ by reaction with H_2S in the hydrocarbon stream to be treated (Abbott and Openshaw, 2002; Han et al., 2016). The chemical reaction is non-reversible (Equation 2.2) and the process has now been established as the industry's norm (Jubin and Ducreux, 2014).

$$Hg_{(g)} + M_xS_y \rightarrow M_xS_{y-1} + HgS \qquad (2.2)$$

Metal sulfides can be used on both wet and dry gases since the reactive species and the support have mesoporous structures with little affinity for liquid hydrocarbons. Also, there is little risk of capillary condensation even at very high pressures, and no risk of sulfur migration by sublimation or dissolution. Additionally, the spent mercury sorbent can be recycled through metal smelters, when the inorganic support is compatible with smelting processes (Pornsakulsak and Soponkanabhorn, 2007). Most interestingly, it has been reported that organic mercury compounds can also be removed (Abbott and Openshaw, 2002).

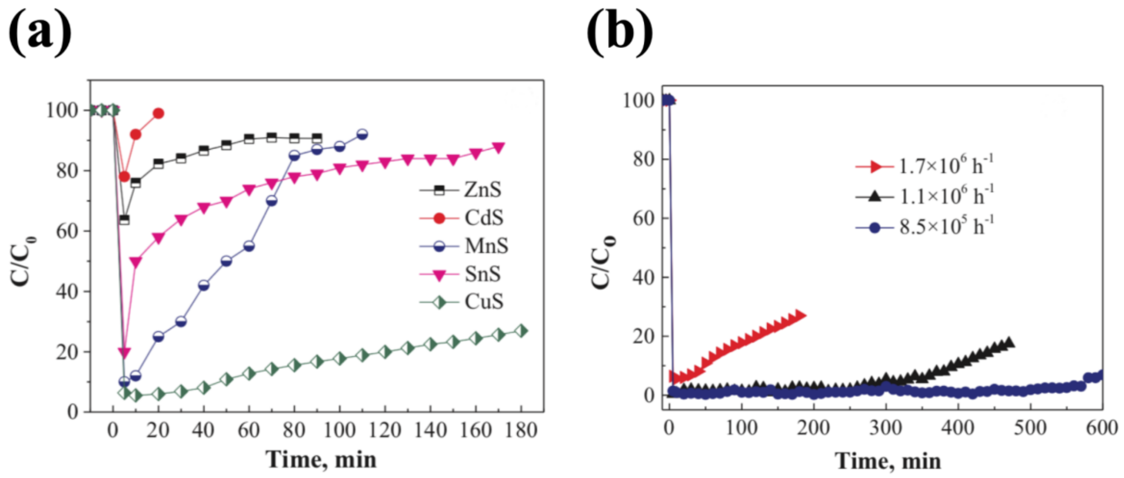

Figure 2. 2*. a) Hg^0 removal efficiency of different metal sulfides, b) Effect of space velocity over CuS. Experimental conditions: T=50 °C, Hg$^0_{in}$=1300 μg·m^{-3}, flow rate=800 mL·min^{-1}, gas mix=5% O_2 (Liu et al., 2019a).*

Recently, (Liu et al., 2019a) synthesized different metal sulfides by precipitation method, and tested them for Hg^0 removal from non-ferrous metal smelting gas, at temperatures similar to those utilized in natural gas processing. As depicted in Figure 2.2a, CuS possessed the largest Hg^0 uptake at 50 °C, followed by MnS, SnS, ZnS and CdS. The Hg^0 removal efficiency of CuS increased with lowering the space velocity (Figure 2.2b). The influence of O_2 and H_2 was negligible with XPS and Hg-TPD suggesting that mercury existed as HgS on material’s surface. The mercury removal mechanism (Equation 2.3) involves Hg^0 oxidation to Hg^{2+} under the action of Cu^{2+}, with Cu^{2+} being reduced to CuS_2 at the same time.

$$Hg_{(g)} + 2CuS \rightarrow HgS + Cu_2S \tag{2.3}$$

Jubin and Ducreux (2014) argued that the liming factor for this mechanism is rather the mercury diffusion than the thermodynamics or reaction kinetics. Different diffusion types are involved in the process: diffusion of mercury to the sorbent external surface, then diffusion through the gas film around the sorbent particle, and finally diffusion inside the sorbent particle. The sorbent particle shape and size can be both tuned to enhance the mercury external diffusion (Figure 2.3a), and the carrier porosity can also be tailored to optimize the mercury sorption efficiency, by preventing capillary condensation (Nédez et al., 1996) and enhancing the access of mercury to the active sites.

Camargo et al. (2014, 2015) used phenomenological modelling to investigate Hg^0 removal by $Ca_{10}(PO_4)_6(OH)_2$ modified with CuS/Cu_2S. In their first model the active sites associated with Hg^0 removal mechanism, were located on the surface and inside the sorbent crystalline matrix (spherical crystallites), whilst in the second model they were located on the surface of Cu_xS_y-segregated particles (mesoporous spherical grains). In their most recent study (Camargo et al., 2018), their updated model of adsorption and transport processes was based on the experimental findings that Hg^0 migrates by diffusion into the mesopores of the sorbent, where it is chemisorbed in two active sites (CuS and Cu_2S) located on the crystalline phase (Figure 2.3b).

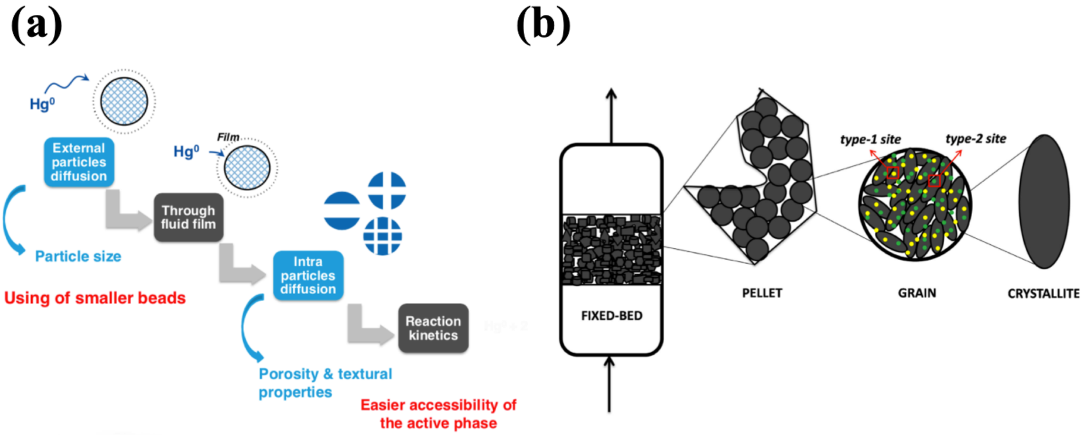

***Figure 2. 3**. a) Mercury diffusion to active sites of Al_2O_3-supported CuS (Jubin, 2017), b) Conceptual model of mercury dynamic adsorption on $Ca_{10}(PO_4)_6(OH)_2$ modified with CuS/Cu_2S (Camargo et al., 2018).*

In fact, as early as in 1978 a patent by Sugier and Villa (1978) related to Al_2O_3-based CuS for Hg^0 removal from hydrocarbons streams. Later, Yan (1989) claimed the use of a sulfur-impregnated alumina containing at least one noble metal to catalyze the removal reaction. Actually, the sulfidation process affects the mercury sorbent's activity and the materials undergo considerable physicochemical changes when treated with sulfur compounds to form metal sulfides. It was experienced that CuS-based sorbents which had been sulfided prior to use and stored under contact with air, resulted in the formation of $CuSO_4$ which was less effective than CuS. Therefore, Denny (1991) prepared CuS by contacting in situ a precursor comprising a copper compound with a stream containing H_2S. Another method (Cameron et al., 1993) involved the incorporation of at least one copper compound, other than sulfide, like an aqueous solution of $Cu(NO_3)_2$, into Al_2O_3. Recently Cousins (2012) tested different combinations of binders and supports, with the aim of increasing the strength, whilst at the same time maintaining attrition resistance. According to his invention, a metal precursor such as copper from $Cu_2(OH)_2CO_3$ with zinc as promoter, was combined with γ-Al_2O_3, a first binder (e.g. calcium aluminate cement) and a second, high aspect ratio binder (e.g. aluminum-magnesium silicate clay) in the presence of little amount of water to form a particulate precursor which was then dried and calcined. The sulfidation step with H_2S was performed either ex-situ or in the fixed bed and the final product was in the form or tablet, extrudate or granule with a particle size between 1-10 mm and sulfur loading up to 10 wt%.

Nevertheless, metal sulfates, such as $ZnSO_4$, formed by the oxidation of metal sulfides other than CuS, can cause agglomeration of the sorbent because of dissolution and re-deposition of the metal sulfate by water in the fluid stream (e.g. regeneration gases from dehydration units), leading to increase in pressure drop, and rendering the sorbent discharge from the vessel difficult and lengthy. Thus, Cousins et al. (2012) suggested a similar to previous method for the production of a granule sorbent comprising of particulate sulfurized copper compound and alumina, bound together by two or more binders. The total metal sulfide content other than CuS, was suggested to be below 0.1 wt%. In a related patent (Fish et al., 2013), the preparation of the sorbent became more efficient since the amount of CuS in the total sorbent's mass was significantly reduced (0.75-5 wt%). The preparation method involved the application of a layer of a copper compound on the surface of γ-Al_2O_3 support by dipping or spraying the support material with a slurry of $Cu_2(OH)_2CO_3$. Then the coated support material was dried to avoid bulk decomposition of the copper compounds, and the precursor was sulfurized to form CuS.

An issue of practical concern relates to the accumulation of mercury scavenged from the fluid streams, on the surface of the copper-based sorbent, creating in this way a thin mercury-rich shell, which is brittle and results in the production of mercury-rich particulates when moving saturated beds during sorbent replacement or even during production. In the latter case, the released particulates disrupt the flow of material, causing increases in pressure drop. To overcome this issue as well as achieve a higher level of active component utilization, Kanazirev and Simonetti (2013) developed a sorbent having a core and a shell formed to include a plurality extending therethrough and communicating with the core. The core was produced from CuS and a halide salt through $Cu_2(OH)_2CO_3$ transformation, disposed on transition Al_2O_3. The porous shell comprised of less than 5 wt% of the total mass and contained SiO_2. HgS was formed in the plurality of pores adjacent to the core, and as mercury was scavenged, a mercury-rich layer was formed within the sorbent at the interface between the core and the highly porous shell. As a result, the highly porous shell surrounded and retained the fragile mercury-rich layer, preventing the release of mercury-containing particulates.

Prior methods for producing CuS-based sorbents consisted of a two-step process. The copper precursor (e.g. $Cu_2(OH)_2CO_3$) was first decomposed to CuO, which was then sulfided to form the active CuS component of the sorbent. However, this process requires high temperatures, leading to agglomeration of the active component, thus decreasing its surface area limits and reducing its activity. Hence, Simonetti et al. (2014) proposed the synthesis of a sorbent comprising CuS, formed through the direct sulfidation of $Cu_2(OH)_2CO_3$ with H_2S at 100-150 ºC. Further, Evans et al. (2015) proposed a synthesis route which involved the mixing of particulate CuS, Al_2O_3, and one or more binders. The mixture was shaped and dried under non-oxidizing conditions that mediated sulfate formation. CuS was produced by mixing elemental sulfur and powdered copper metal to react together, avoiding in this way the use of H_2S which is toxic.

Given the extremely low mercury concentration specifications of gas streams entering the LNG plant, the target efficiencies may as high as 99.9% and when the efficiency drops to below 99%, the sorbent might need to be replaced. The reaction of CuS with Hg^0 vapor at 0-300 ºC is spontaneous ($\Delta G<0$). However, Cu_2S, does not react spontaneously with Hg^0 ($\Delta G>0$). Porcheron et al. (2015) found that using sorbents based on a certain type of Al_2O_3 (i.e. referred to as gel Al_2O_3) could improve the Hg^0 sorption capacity. Therefore, they prepared a sorbent comprising of a support essentially based on 100 wt% gel Al_2O_3 and CuS. Al_2O_3 was formed either by producing a gel constituted by a precursor of AlO(OH) or by the rapid dehydration of $Al(OH)_3$ precursor from the Bayer process. The copper precursor (i.e. $Cu(NO_3)_2$) was then introduced by dry impregnation onto the Al_2O_3 support, followed by maturing in a closed vessel saturated with water, calcination in air and finally sulfidation using a gaseous mixture of N_2 and H_2S.

Monolithic structures are particularly attractive in gas separations because the provide substantially uniform flow paths, reducing the pressure drop along the reaction bed. They also possess high thermal stability, good mechanical integrity as well as improved heat or/and mass transfer characteristics. The monolithic or supported extrudates claimed by Porcheron et al. (2014) comprised of at least 90 wt% CuS and had lengths and diameters ranging between 0.5 and 10 mm, as well as a section comprising of at least three lobes with a characteristic radius. The pre-active phase, CuO was deposited on a porous Al_2O_3 support and the mass was then sulfided in-situ or ex-situ to form CuS. The feed to be treated comprised of natural gas, with up to 40% CO_2, and H_2S, at fixed-bed conditions of 30-75 ºC, 150-300 bar and gas hourly space velocity (GHSV) between 4,000 and 20,000 h^{-1}.

As explained previously, to avoid mercury contaminating the gas plant equipment MRUs are preferably installed after the initial separator. However, the gas fed to MRU is often saturated with H_2O and/or hydrocarbons, which, due to the pressure drop through the bed, may accumulate in the pores of the sorbent, thus reducing its performance.

Therefore, O’Rear and Thompson (2017) developed a hydrophobic sorbent that exhibited reduced water uptake and improved mercury removal ability, by filling its pores with a fluid that is immiscible to water, permitting however Hg^0 vapor to enter and react with the adsorption sites of active components. The surface of the sorbent was treated with a hydrophobicity introducing agent such as SiH_4, which alters its surface properties so as to no longer adsorb water. It was explained previously that sorbents impregnated with metals may fail to provide the metal in a single compositional phase which is stable, and even if the metal is present in a stabilized phase (e.g. CuS), some undesirable metal phase may also be present (e.g. $CuSO_4$), hence inhibiting the sorbent’s activity. Therefore, Schmidt et al. (2014) prepared sorbents impregnated with Ag_2S, that is generated by the reaction of SO_2 and hydrogen or H_2S, after Ag_2O loading on Al_2O_3. All silver on the support was present as Ag_2S mono-phase, with the silver content after the conversion being about 15 wt%.

To remove mercury from sulfur-free hydrocarbon streams in the presence of hydrogen, Kanazirev (2009) claimed the use of CuO sorbent supported on Al_2O_3 that is brought in contact with H_2S to form CuS. The CuO sorbent was produced by combining an inorganic halide additive (NaCl or KCl retard copper reduction to a lower valence state) with $Cu_2(OH)_2CO_3$ to produce a mixture, which was then calcined. Using this method, mercury removal occurs through Equation 2.4, while the competing copper reduction reaction (Equation 2.5) is slowed down.

$$2CuO + Hg_{(g)} + 2H_2S_{(g)} \rightarrow HgS + Cu_2S + 2H_2O_{(g)} \tag{2.4}$$

$$2CuS + H_{2(g)} \rightarrow Cu_2S + H_2S \tag{2.5}$$

Finally, it is worth mentioning that the naturally occurring manganese nodules on the floor of bodies of water (e.g. Atlantic and the Pacific Ocean, Lake Michigan) may be of use for mercury abatement (Rollmann, 1982). Apart from manganese, these deposits contain other metals such as iron, cobalt, nickel and copper. After washing to remove salt and mud, the nodules may be preferably dried prior to mixing with sulfur.

2.2.3. Metal Oxides

Transition metals have multiple valence states and are capable of readily forming a redox cycle between the high and low oxidation states. An oxygen vacancy can be generated with the release of lattice oxygen. Reversely, adsorbed oxygen species may form with its restoration. Considerable effort has been devoted to synthesize mesoporous and macroporous single metal oxides with high specific surface area and consequently enhanced number of available sites for reaction (Wang et al., 2017b). Furthermore, with the advent of nanoscience (Bell, 2003) it has been realized that the catalytic activity may be affected by the size and/or shape of metal oxide nanoparticles (Cao et al., 2016). As far as the adsorption process is concerned, two chemical processes are of interest, acidobasic and redox. The role of oxygen vacancies is reflected on the decrease of the surface atoms coordination as well as the modification of electron count. The former factor enhances the activity of the acidic sites close to the vacancy, whilst the latter either improves or inhibits the reactivity (Calatayud et al., 2003).

Metal oxides have been utilized for Hg^0 removal due to their favorable properties, namely their high adsorption capacity, strong metal ion affinity and reusability (Reddy et al., 2012). The latter renders them particularly attractive for natural gas streams treatment. Notable examples of regenerable metal oxides employed at higher temperatures (>150 ºC) for the purification of combustion flue gases are the following: Fe-Ce (Xu et al., 2019), Fe-Mn (Zeng et al., 2017), Ce-Mn (Qu et al., 2015), Zr-Mn (Xie et al., 2013), Fe_2O_3/SiO_2 (Tan et al., 2012), $MnO_x/\gamma\text{-}Al_2O_3$ (Scala et al., 2013; Scala and Cimino, 2015), MnO_x/TiO_2 (Cimino and Scala, 2015), Fe-Mn-Ti (Liao et al., 2015). An appropriate H_2S concentration has been proven to promote Hg^0 removal (Ling et al., 2013; Wang et al., 2018; Xue et al., 2015; Zou et al., 2017) at lower temperatures, by generating active sulfur that reacts, under the presence of oxygen, with Hg^0 to form HgS (Ling et al., 2015).

Pore size, structure volume as well as crystallinity, are the defining properties of metal oxides (Ren et al., 2012) and can be modified depending on the preparation method (Lee and Yoo, 2014). For example, $CuMnO_x/Al_2O_3$ prepared by co-impregnation, withstood 45 days towards Hg^0_{in}=11,600 $\mu g \cdot m^{-3}$ and GHSV=4,000 h^{-1} at room temperature (Zhao et al., 2017). At full scale, sorbents have the form of extrudates, pellets, granules or beads in the range of a few mm. The reduction of a metal oxide may lead to the enlargement of its porosity and pore volume as a result of the shrinkage effect. Yan, (1987b) claimed a sorbent comprising of bismuth and tin, that were mixed together with non-reactive bases such as SiO_2 and Al_2O_3. In another patent (Audeh, 1988a) the preparation of a metal oxide sorbent involved contacting a porous mass of aluminum with an aqueous solution of a soluble mercuric salt to sensitize its surface, followed by drying under a non-oxidizing atmosphere. The synthetic procedure leading to a more efficient porous structure (Ou, 1995) involved mixing the metal oxide and powder substrate (e.g. CuO on Al_2O_3 and

ZnO), shaping the mixture to form an aggregate and then reducing it to convert the metal oxide to its metallic form.

Table 2. 2. *Comparison of commercial metal-oxide sorbents for mercury, carbonyl sulfide and arsine. Experimental conditions: Room temperature and atmospheric pressure,* $Hg^0_{in}=2.3$ *mg·* m^{-3}, $COS_{in}=100$ *ppm,* $AsH_{3in}=100$ *ppm, bed L/D ratio=7/15 (Blankenship and Voight, 2002).*

Adsorbent	*Supplier*	*Composition*	*Pre-treatment*	*Hg^0 (wt%)*	*COS (wt%)*	*AsH_3 (wt%)*
Invention	UCI	55% Fe_2O_3, 27% MnO_2, 15% Al_2O_3	None	2.34	6.22	18.7
T-2552	UCI	6% Ag on Al_2O_3	None	0.23	2.28	3.23
E-315	Calsicat	PbO on Al_2O_3	None	0	4.04	1.05
T-2525	UCI	45% MnO_2 on Al_2O_3	None	0.027	0.28	0.38
T-2550	UCI	17% CuO, 29% MnO_2 on Al_2O_3	None	0.002	5.3	14.9
C28	UCI	52% NiO_2, 29% SiO_2, 10% Al_2O_3	Reduced (2 h-150 ºC, H_2)	0.128	32.1	40.3
G-132D	UCI	55% CuO, 27% ZnO, 15% Al_2O_3	Reduced (2 h-150 ºC, H_2)	0.068	1.52	2.61

Blankenship and Voight (2002) claimed the use of a composite metal oxide sorbent that comprised of 40-65 wt% Fe_2O_3, 20-30 wt% MnO_2 and 10-20 wt% γ-Al_2O_3. The capture mass was prepared through co-precipitation, or decomposition, with intense blending of the components. As shown in Table 2.2, it exhibited far better mercury removal capacity than the commercial competitive metal-oxide sorbents. Hatscher and Hesse (2009) also developed a metal oxide sorbent comprising of Ag_2O on Al_2O_3, with Ag_2O representing up to 10 wt% of the mass, the silver existing essentially as Ag_2O and at least 80% of Al_2O_3 being in the form of θ-Al_2O_3.

Theoretical studies may provide useful information about the removal mechanism at the atomic level. Recently a water-resistant SnO_2/aerogel (Zhang et al., 2019b) was tested for the simultaneous removal of Hg^0 and H_2S. Density functional theory (DFT) calculations were performed on the strongest peak in the XRD spectrum, SnO_2 (110). To elucidate the heterogeneous reaction of Hg^0 and H_2S over the solid sorbent, both Langmuir-Hinshelwood (H-W) and Eley-Rideal (E-R) mechanisms were proposed (Figure 2.4). The first involved the simultaneous adsorption of Hg^0 and H_2S on the sorbent's surface, followed by the reaction with each other to form HgS. The second mechanism involved first the adsorption of H_2S to form active sulfur surface species, which then reacted with Hg^0 to form HgS. According to the authors the E-R mechanism with an energy barrier of 19.91 kJ·mol^{-1} was kinetically more favorable than the L-H mechanism with an energy barrier of 31.20 kJ·mol^{-1}.

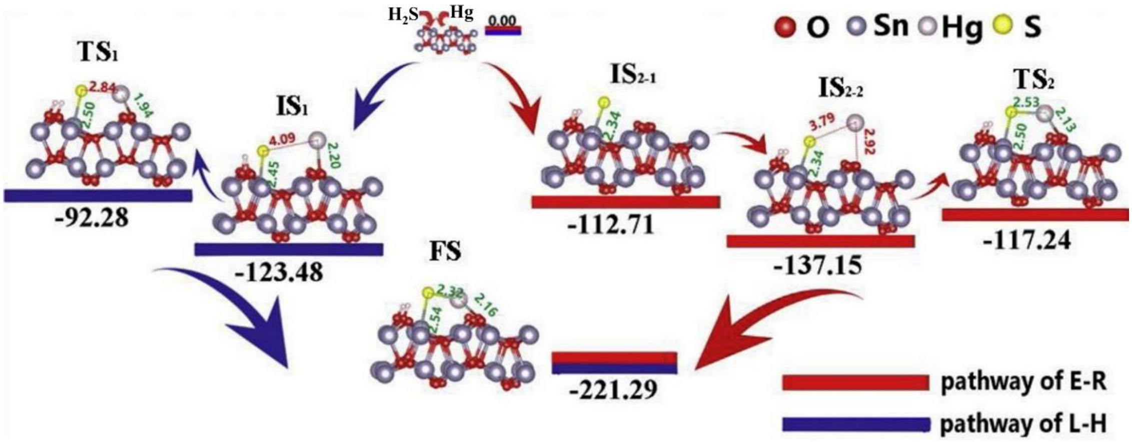

***Figure 2. 4**. Energy and geometrical diagram of the Hg^0 and H_2S adsorption on the SnO_2 (110) surface via the Langmuir-Hinshelwood (H-W) and Eley-Rideal (E-R) mechanisms (Zhang et al., 2019b) .*

Finally, it should be underlined that organomercury compounds (e.g. $(CH_3)_2Hg$) which are more prevalent in liquid hydrocarbons, are unlikely to be removed by conventional sorbents. A patent by Roussel et al. (1990) addressed this concern by using a two-step process. The first step involved the hydrogenation of the dialkylmercury using a nickel-based catalyst and hydrogen. In the second step the reduced Hg^0 was captured by copper sulfide. In a similar process (Rudolf and Bender, 2011) the employed γ-Al_2O_3-based copper sorbent was obtained by impregnating γ-Al_2O_3 with an aqueous solution of copper salt, followed by drying, calcination and conversion of copper to its metallic form by reduction with hydrogen which was introduced together with the hydrocarbon stream. Regeneration was possible at temperatures over 200 °C with inert or hydrogen-comprising gas.

2.2.4. Molecular Sieves

Zeolites are also known as molecular sieves because guest species with appropriate size, shape, and polarity may selectively substitute additional species, such as H_2O, in their pores (Li et al., 2017b). Due to their electrostatic charged framework and abundance of extra-framework cations they are highly hydrophilic. Their water sorption capacity depends not only on the framework type (e.g. zeolite A, X or Y) and extra-framework cations, but also on the defect sites, surface nature, metals in the framework, and coke deposits (Ng and Mintova, 2008). In an efficient sorption process the molecules are selectively retained within the structure forming low-energy bonds. They must be small enough to enter the cavities via the pores, whose properties depend on the type of the zeolite and the charge compensating cations around them (Terrigeol, 2012). In natural gas dehydration process, by replacing some of the drying sorbent with a dual function water and mercury removal sorbent, simultaneous water and mercury removal can be achieved in the same vessel (Stiltner, 2002; Yan, 1994b).

The employment of molecular sieves for mercury removal from natural gas was early reported by Ambrosini et al. (1978) who claimed the use of sulfur-loaded zeolites. To increase the mercury adsorption rate, Chao (1984) developed an ion-exchanged zeolite, in which, part of the cation sites had been exchanged with a copper cation that formed a water-insoluble metal polysulfide compound by getting in contact with polysulfide-forming species. Audeh (1989b) also prepared polysulfide-treated molecular sieves, while in a more recent patent (Cross et al., 2011), the developed molecular sieve further comprised of iron to form FeS after getting in contact with H_2S.

The impregnation of zeolites with silver (Cao et al., 2017; Dong et al., 2009a, b; Liu et al., 2008) leads to the formation of Hg-Ag amalgam (Equation 2.6) alloys with low solubility. After sorption saturation, the Ag-Hg amalgam decomposes to generate Ag^0 and Hg^0 in the heating regeneration process. Mercury, like water, will be regenerated off the sorbent, leaving with the spent regeneration gas.

$$\mathrm{Hg}_{(g)} + \mathrm{Ag} \rightarrow \mathrm{Hg\text{-}Ag} \tag{2.6}$$

The advantage of this approach is that no additional equipment (associated with further increase in pressure drop) is required, and most of the mercury can be recovered through a separate mercury stream. However, to achieve this, secondary mercury removal treatment is needed for the spent regeneration gas. Of course, the regeneration system and the additional size requirements may potentially pose additional capital investment costs (Ruddy et al., 2007).

Markovs (1989) claimed the use of silver-containing zeolitic molecular sieves with pore diameters of at least 3Å for the simultaneous mercury and water removal. The silver containing sorbent was contained within a distinct location in the bed, so that the natural gas stream first contacted the desiccant zone and then passed through the silver containing sorbent. An example of this configuration was a bed containing 42.2 t of 3.2 mm extruded zeolite 4Å pellets in the upper zone. The lower zone contained 3.6 t of 3.2 mm extruded zeolite X pellets with 13.6 wt% silver as zeolite cations. 95% of these were loaded within

0.1 mm of the external surface of the pellets. The bed was regenerated by a heated (315 ºC) non-sorbable gas stream concurrent or counter-current the flow. The use of silver-impregnated molecular sieves was also claimed by Yan (1990b). In his patent, Ag^0 up to 15 wt% was impregnated to zeolite. This was achieved by treatment with an aqueous solution of CH_3CO_2Ag that was subsequently decomposed by heating in the absence of oxygen. This impregnation method was less likely to make the zeolite lose its water absorbing properties than the ion exchange with reduction.

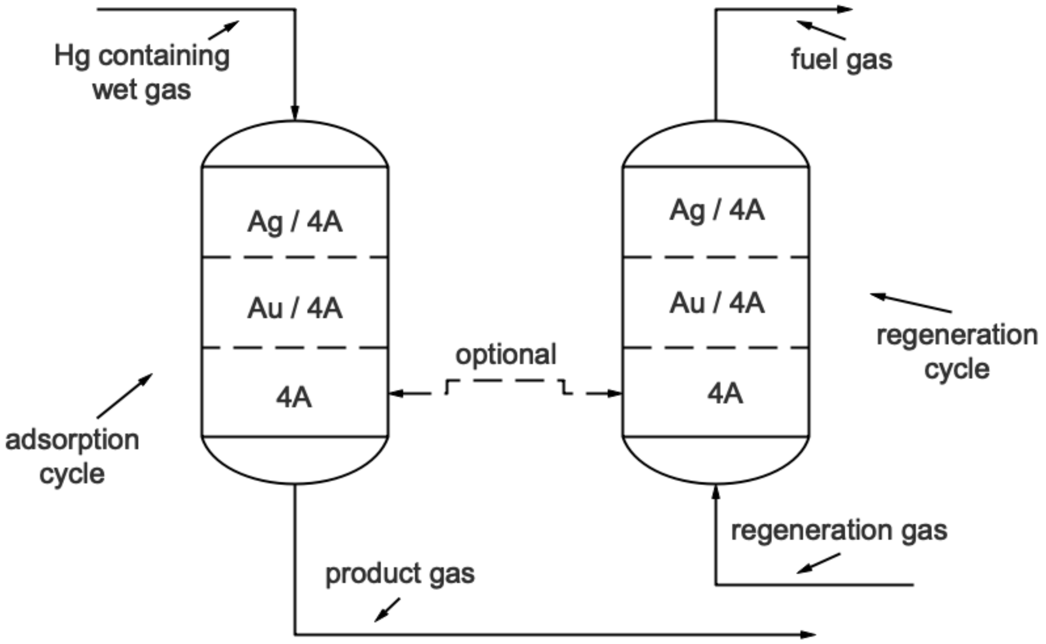

Figure 2. 5. *Composite drier-bed for simultaneous drying and removal of both metallic/inorganic and organic mercury compounds (Yan, 1994a).*

As previously stated organic mercury compounds (e.g. $(CH_3)_2Hg$) may also be present in natural gas environments and are difficult to remove by conventional methods used for elemental/ionic species. To simultaneously remove metallic/ionic and organic mercury, as well as water, Yan (1994a) claimed the use a composite-dryer bed (Figure 2.5) consisting of a first zeolite bed, proximal to the entrance, impregnated with Ag^0 to remove water and metallic/ionic mercury species, and a second zeolite bed impregnated with gold (Rodriguez-Perez et al., 2013) to remove residual water and organic mercury species.

Moreover, with the advent of hydraulic fracturing (Wang et al., 2014b) and horizontal drilling, natural gas may contain small amounts of oxygen (Sutra et al., 2017). In a method conceived to remove both water and mercury from a fluid stream containing natural gas and oxygen (Rastelli et al., 2015), the gas stream is treated in an fixed bed containing molecular sieve crystallites that contain ionic or elemental silver.

The mercury removal efficiency and capacity of silver-based sorbents depend on the valence state, particle size and dispersion of silver particles. In general, the silver loading function is directly related to the adsorption capacity (Khunphonoi et al., 2015). A simple and quick preparation of silver nanoparticles supported on FAU zeolite crystals (zeolite X) was reported by Zaarour et al. (2014) and is based on ultraviolet irradiation. Recently, Sun et al. (2018) showed that the addition of $C_{17}H_{35}CO_2H$ as protective additive is an effective way to produce small nano-scale silver particles (~15 nm) on the surface of Ag/4Å zeolite. The material's characterization showed that after Hg^0 adsorption the silver lattices disappeared from the outer boundary to the interior of the particles, therefore suggesting that Hg^0 firstly reacted with the nano-scale Ag on the surface and then gradually penetrated into the interior. The Hg^0 adsorption capacity reached about 6 $mg \cdot g^{-1}$ and the material remained stable after 5 reuse cycles. To enhance the water resistance properties, the same group in their following study (Zhang et al., 2019a), developed a synthesis protocol utilizing MCM-41 molecular sieve, $(CH_3)_3SiCl$ (TMCS) as an external surface passivator and $C_9H_{23}NO_3Si$ (APTES) for the modification of internal channels (Figure 2.6).

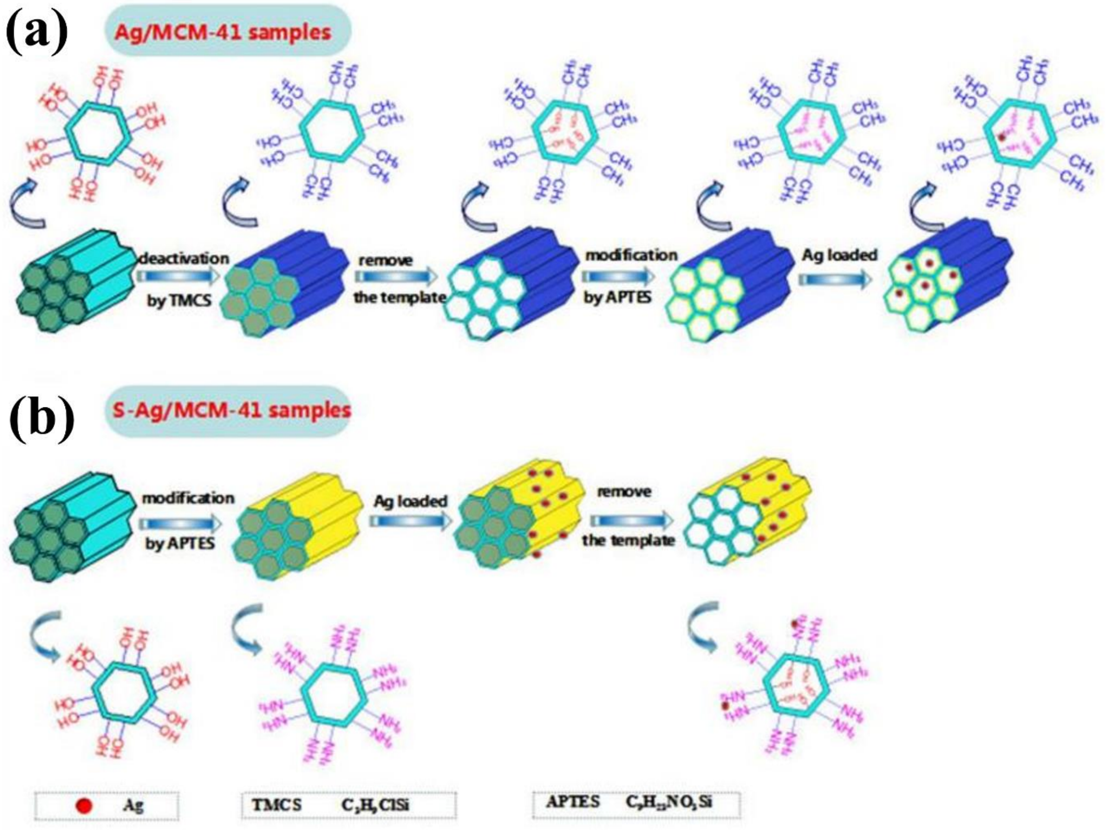

Figure 2. 6. Schematic illustration for the fabrication of a) Ag/MCM-41 and b) S-Ag/MCM-41 (Zhang et al., 2019a).

Two kinds of silver-based sorbents were fabricated: i) Ag/MCM-41 with highly dispersed silver nanoparticles within the inner channels of the mesopores of the molecular sieve, possessing an average diameter of 3 nm, ii) S-Ag/MCM-41 with supported silver nanoparticles on the outside surface of the molecular sieve having an average diameter of 19 nm. Ag/MCM-41 loaded with 1 wt% silver manifested the superior Hg^0 capture capacity (6.64 $mg \cdot g^{-1}$). As it is illustrated in Figure 2.7, the water contained in the gas stream only slightly affected its performance. Its excellent regeneration performance was explained by the confinement effect of mesoporous channels, which prevented the growth and agglomeration of silver nanoparticles.

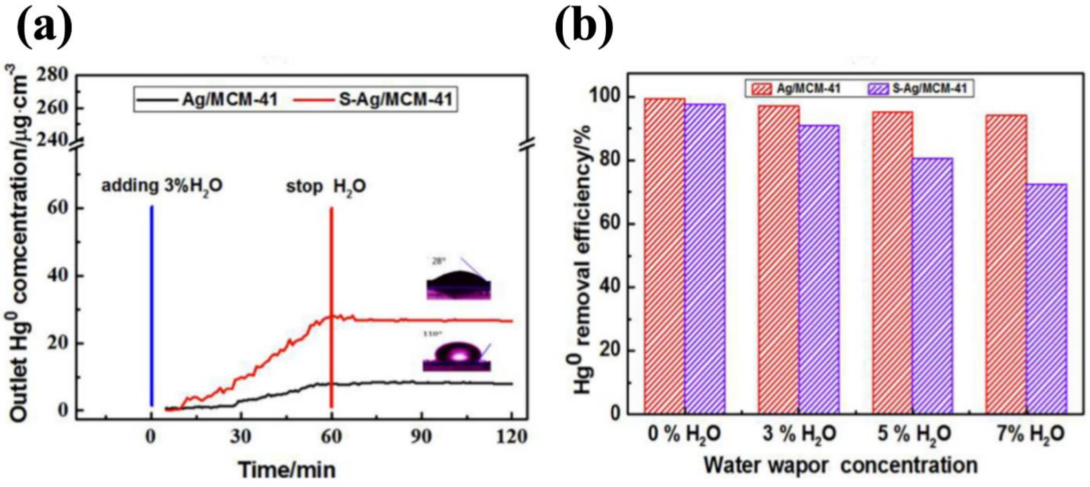

Figure 2. 7. Effects of water vapor on Hg^0 removal efficiency over Ag/MCM-41 and S-Ag/MCM-41. Experimental conditions: Hg^0_{in}=300 $\mu g \cdot m^{-3}$, T=30 °C, sorbent mass=300 mg, GHSV=50,000 h^{-1}, gas mix= CH_4 (Zhang et al., 2019a).

2.2.5. Alternative Materials

Linking ditopic or polytopic organic carboxylates (as well as other similar negatively charged molecules), with metal-containing units, yields crystalline metal-organic frameworks (MOFs) with high porosity and surface areas that exceed those of carbons and zeolites (Furukawa et al., 2013). Their chemical tunability and modularity along with the chemical and thermal stability manifested by many structures, have rendered them attractive for gas separation (Li et al., 2009) and adsorptive removal of hazardous compounds (Khan et al., 2013) including mercury (Yang et al., 2019a; Zhang et al., 2017b, 2016b; Zhao et al., 2018c). Siu and Weston (2016) claimed the use of an MOF comprising of at least one organic ligand consisting of at most one carboxylate group and at least one chalcogen like sulfur. Such organic ligands may be produced with salts of $HSCH_2CO_2H$. A MOF comprising of at least one metal ion like Zr^{4+}, and sulfur content up to 22 wt%, may exhibit a mercury uptake of up to 15 wt%. An example of such MOF is the reaction between $ZrCl_4$, $C_6H_4(CO_2H)_2$ and $HSCH_2CO_2H$, resulting in a product (UiO-66-SH), with 5 wt% sulfur content and 1,400 $m^2 \cdot g^{-1}$ BET specific area. This material exhibited 1 wt% mercury uptake and the incorporation of silver could increase its capacity up to 13 wt%. Currently, however, the employment of MOFs is limited to lab scale applications.

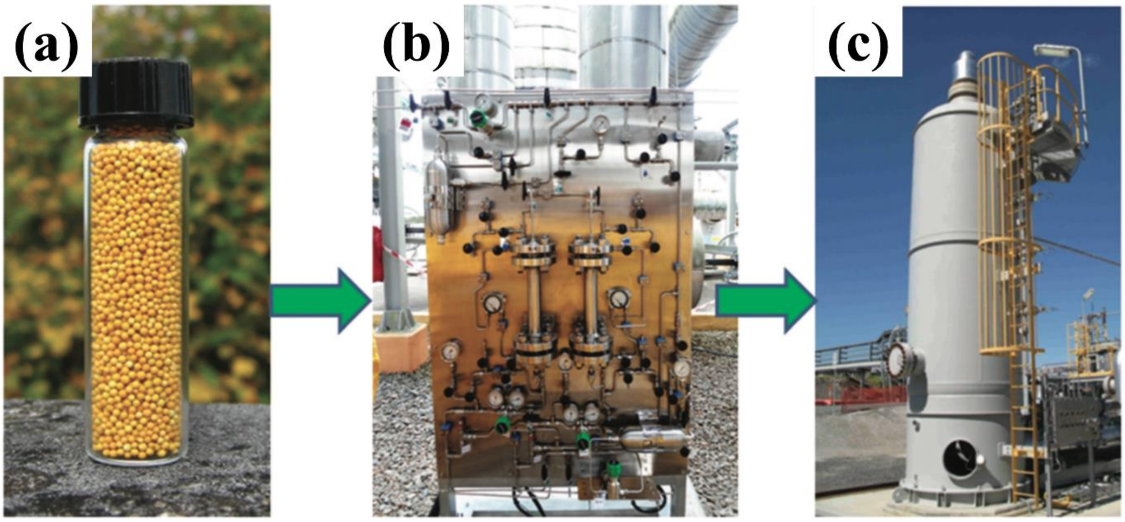

Figure 2. 8. *Application of chlorocuprate(II) SILP a) in lab-scale b) pilot-scale (100 cm^3) and c) full-scale (20 m^3) mercury removal units (Abai et al., 2015).*

On the contrary, ionic liquids (ILs) have already been deployed at full scale. They have attracted considerable attention as reaction solvents due to their non-volatility, thermal stability, non-explosive nature, high polarity, and temperature-dependent miscibility with water (Dai et al., 2017). The immobilization of ILs on different support materials, have rendered them fit for use as heterogeneous catalysts in fixed-beds in industry. In the presence of a physisorbed multilayer of IL, the bulk properties of IL are transferred to the support material (supported ionic liquid phase, SILP) (Campisciano et al., 2017). Room temperature ionic liquids have been successfully employed for capturing oxidized mercury at 160 °C (Ji et al., 2008a, b), with recent studies (Barnea et al., 2013; Cheng et al., 2014a; Cheng et al., 2014b; Li et al., 2016c) indicating their potential at a wide temperature windows.

At ambient temperatures, metal-containing ILs (Abai et al., 2015; Boada et al., 2016) have been successfully utilized to remove metallic, ionic and organic mercury species from hydrocarbon fluids, exhibiting mercury uptake capacities as high as 20 wt%. ILs provide a mild oxidizing environment for Hg^0 to oxidize to highly soluble ionic mercury species, as well as for organomercury to undergo oxidative cleavage to form highly soluble mercury ions, which can then partition with selectivity to the IL. Abai et al. (2017)

claimed the synthesis of ILs that may be described by the formula $[Cat^+][M^+][X^-]$, where $[Cat^+]$ represents one or more organic cationic species, $[M^+]$ represents one or more transition metal cations with oxidation state 2+ or greater, and $[X^-]$ represents one or more anionic species. The ionic liquid may be prepared by adding a salt of the metal cation $[M^+]$ to an ionic liquid having the formula $[Cat^+][X^-]$. For example, $CuCl_2$ may be added to [Bmim]Cl, at an ionic liquid to metal ion ratio of 2:1. The metal salt combines with the chloride of the ionic liquid to form an ionic liquid having the formula $([Bmim]^+)_2([CuCl_4)^{2-})$. The latter may be further impregnated on a solid support (like SiO_2 displayed in Figure 2.8), preferably accounting for 15-25 wt% of the total capture mass. Activated carbon, which is lower cost than silica, was experimented as a solid support for ILs by the same group (Abbas et al., 2016). [Bmim]Cl-coated activated carbon was able to uptake up to 23 $mg \cdot g^{-1}$ and 60 $mg \cdot g^{-1}$ Hg^0 with nitrogen and CH_4 as carrier gas (Figure 2.9), respectively, possibly due to the chemisorption of Hg^0 in the form of $HgCl_2$. $[Bmim]^+$ oxidizes Hg^0 to Hg^{2+} (Equation 2.7). Then Cl^- anions in [Bmim]Cl interact with Hg^{2+} to form $HgCl_2$ (Equation 2.8). The molecular simulation revealed that the anion part of IL plays a major role in Hg^0 adsorption and a possible mechanism may involve the formation of a complex between the imidazolium cation and $HgCl_2$ (Equation 2.9).

$$2[Bmim]^+ + Cl^- + Hg^0 \rightarrow 2[Bmim]Cl^- + Hg^{2+} \tag{2.7}$$

$$2Cl^- + Hg^{2+} \rightarrow HgCl_2 \tag{2.8}$$

$$[Bmim] + HgCl_2 \rightarrow [Bmim]^+ [HgCl_2]^- \tag{2.9}$$

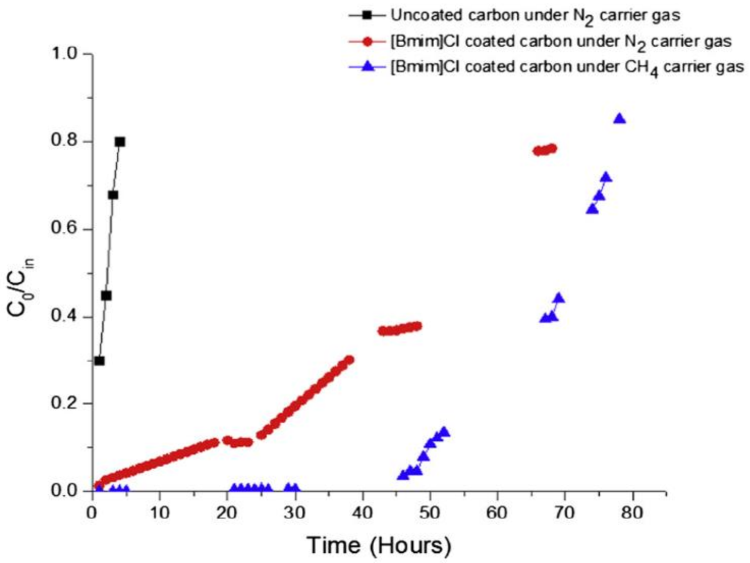

Figure 2. 9. *Hg^0 breakthrough curves of carbon-coated [Bmim]Cl and uncoated carbon under N_2 and CH_4 carrier gases. Experimental conditions: Hg^0_{in}=20 ppm, gas feed=60 $mL \cdot min^{-1}$, room temperature and atmospheric pressure (Abbas et al., 2016).*

Nevertheless, the use of ionic liquids is not free of shortcomings (Warrag et al., 2018). Resynthesizing fresh material is possibly cheaper than recovering the ionic liquid. Furthermore, since the removal process is based on chemisorption, the Hg^0 desorption process is energy intensive. In addition, silica's cost is comparatively high, and carbon-supported materials end up as toxic landfill because there is no recycling method yet (Abbas et al., 2016; 2015).

2.3. Processes

2.3.1. Scrubbing and Complexation

Alternative to fixed-bed reactors, scavenger solutions have been used for mercury removal by utilizing oxidizing, complexing and solvents agents (e.g. HNO_3, RSH and H_2O/CH_3OH, respectively) to produce Hg^{2+} soluble complexes. However, these techniques suffer from low efficiency. Other disadvantages such as increased corrosivity, system contamination and regeneration difficulties (Audeh and Ragonese, 1991; Leppin and Palla, 2002; Miller and Tuckett, 1977; Tarakad and Crawford, 1987; Yan, 1991a) have also been reported in the past. More recently, produced water (Fakhru'l-Razi et al., 2009; Nasiri et al., 2017) as a by-product from hydrocarbon production was employed by O'Rear et al. (2013) in a process where the contaminated natural gas is scrubbed in an absorber with an aqueous solution comprising of a water-soluble sulfur compound, such as Na_2S_x from sulfidic waste water.

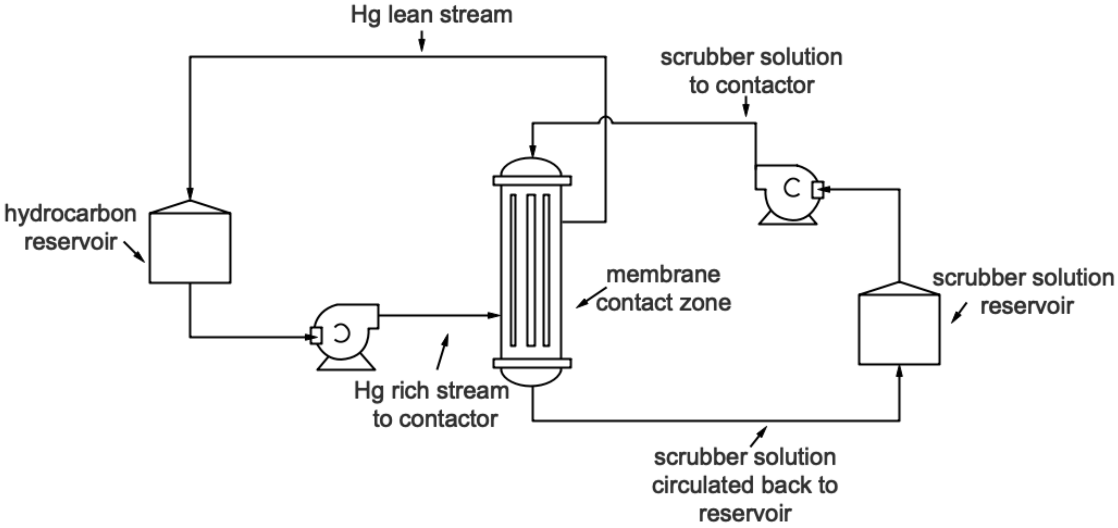

Figure 2. 10. *Mercury removal with the use of a polymeric membrane unit and a scrubbing solution (Hamad et al., 2014).*

Ion-exchange resins (Alexandratos, 2009) can be regenerated by washing with HCl or HNO_3 to remove anion exchanged mercury salts. Thus, polysulfide-resin complexes (Horton, 1986) have been deployed to reduce the mercury content of natural gas. Additionally, polymeric membranes (Lau et al., 2013) which may be applied in acidic gas removal, heavy hydrocarbon recovery, water dehydration as well as nitrogen and helium separation (Scholes et al., 2012) have been used in oxidative membrane gas absorption (Jansen and Feron, 2001; Van Der Vaart et al., 2001). In this method the mercury contaminated-gas phase undergoes membrane absorption in a liquid phase containing an oxidizing agent (e.g. H_2O_2). In the patent of Hamad et al. (2014) the mercury-contaminated fluid is passed on one side of a porous membrane, while flowing a second stream containing a compound (e.g. alkali metal sulfides) that reacts or solubilizes mercury on the other side (Figure 2.10). With this method, non-dispersive contact between the two streams can be achieved, whilst solvent hold-up, emulsion formation, foaming, unloading and flooding are avoided.

2.3.2. Simultaneous Hg and H_2S Removal

H_2S being highly corrosive and toxic, constitutes a serious problem for natural gas industry (Goodwin et al., 2015). Due to the depletion of sweet gas fields, the use of sour fields has become economically viable undertaking (Amott and Mogose, 2015), with the most common technique for acid gas removal being based on amine extraction (Gupta et al., 2016). To remove in a single step both H_2S and mercury traces, Audeh (1988b) claimed a process in which porous granular Al_2O_3 is contacted with an aqueous solution of alkali metal peroxymonosulfate (e.g. $KHSO_5$) that can at the same time convert mercury to its oxide form and H_2S to elemental sulfur. In a related process (Audeh, 1989a), the mercury-contaminated stream is contacted with an aqueous solution of Na_2S_x, and the effluent gas reacts with $CaSO_4$-supported $CoCl_2$ to eventually recover a stream with substantially reduced mercury and H_2S content. A simple process to remove all mercury compounds as well as reduce H_2S to a specific level, was conceived by Carnell and Willis (1999). This made use of a primary bed (e.g. CuS), and three secondary beds (e.g. $Cu_2(OH)_2CO_3$) in series. The gas stream is first passed through the primary sorbent where mercury is eliminated through the formation of HgS, with only a little amount of H_2S being removed. Then a part of the effluent stream is directed through the secondary beds to remove H_2S. The beds get consecutively saturated before the mercury absorption process is completed in the primary bed, allowing the resulting bed after H_2S removal (basic copper carbonate converts to copper sulfide) to be further deployed for mercury removal.

The Claus process is employed to treat high H_2S concentration gas streams (i.e. 50%) and it is subdivided into thermal and catalytic stages (Figure 2.11) (Gupta et al., 2016). In the thermal stage H_2S is partially oxidized under rich conditions (Φ=3) in a Claus furnace (750-1200 °C) to form elemental sulfur. During this reaction one-third of H_2S is burned to form SO_2 (Equation 2.10), which then reacts with the unreacted H_2S to form sulfur (mainly in the form of S_2) (Equation 2.11). The product gases flow into a waste heat boiler to condense sulfur and produce a high temperature and pressure steam for the catalytic stage. In this stage, the remaining H_2S reacts with SO_2 at lower temperatures (200-350 °C) over an Al_2O_3 or TiO_2-based catalyst to produce additional sulfur (mostly in the form of S_8). A typical Claus process including a tail gas clean-up technology may achieve over 99.9% H_2S conversion efficiency.

$$H_2S + 3/2O_2 \rightarrow H_2O + SO_2, \Delta H<0 \tag{2.10}$$

$$2H_2S + SO_2 \rightarrow 3S + 2H_2O, \Delta H>0 \tag{2.11}$$

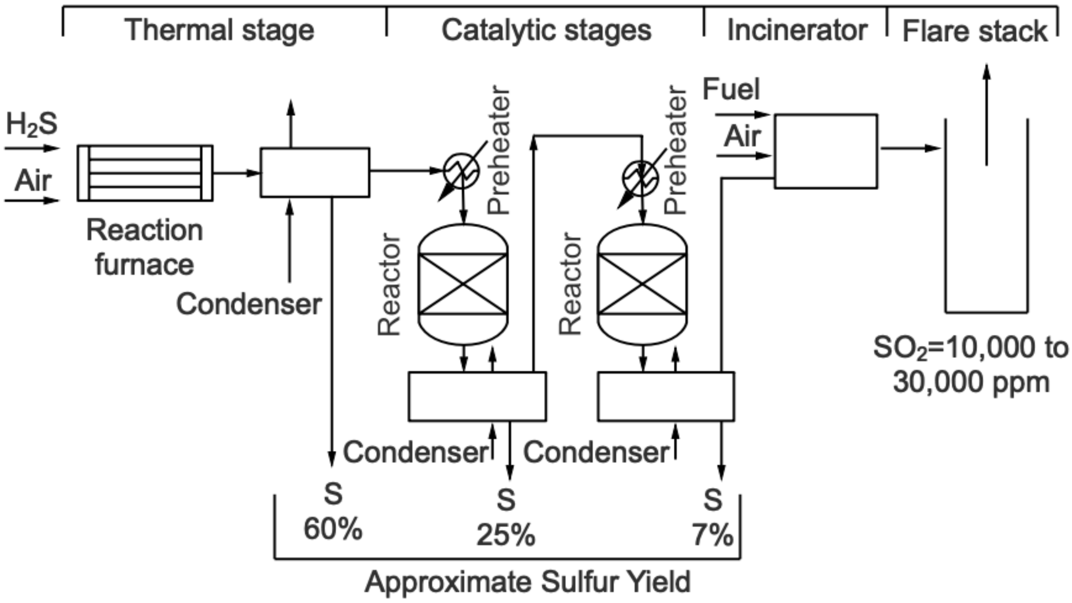

Figure 2. 11*. Process flow diagram of a two-stage Claus process (Stewart and Arnold, 2011).*

Considering the above, Srinivas and Copeland (Srinivas and Copeland, 2006) claimed a process in which H_2S is selectively oxidized in a contaminated gas stream to generate sulfur that reacts with mercury to form HgS, which can be removed along with the remaining sulfur by co-condensation. The advantage of this process is the fact that sulfur and mercury can be removed at the same time in the sulfur condenser. A version of the process is illustrated in Figure 2.12 and includes an amine unit for separating acid gases, thus allowing H_2S to be recycled to the oxidation furnace. The sour gas is mixed with air and heated above sulfur's dew point, before it is directed into the catalytic reactor. The O_2:H_2S ratio is controlled at about 1:2 and depending on the H_2S amount, the mixed metal oxide catalyst is operated at 170-200 °C. The catalyst may comprise of about 0.4-0.6 wt% molybdenum oxide, 4-6 wt% niobium oxide and 4-6 wt% copper, cobalt or iron oxide supported on titania and/or silica. The product gases i.e. sulfur, SO_2, CO_2, H_2O and unreacted H_2S are passed through the sulfur condenser, where HgS condensation takes place at about 130-150 °C. As previously stated, the gas stream may be further treated in an amine unit where H_2S and SO_2 are removed and recycled back to the direct oxidation rector in order to increase sulfur recovery.

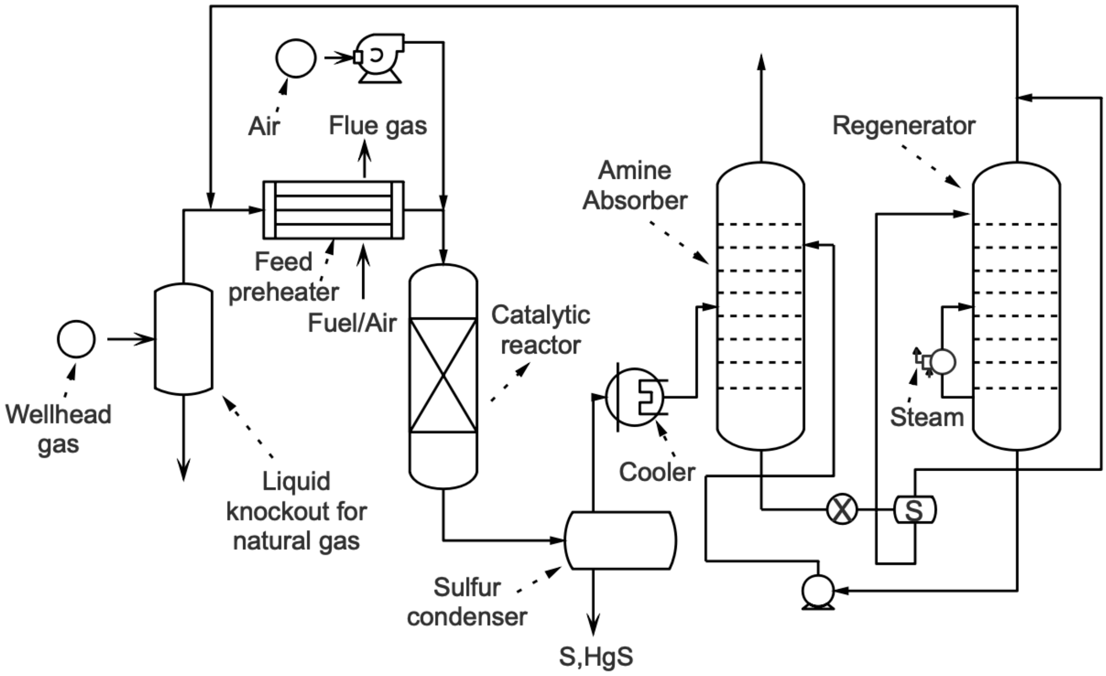

Figure 2. 12*. Simultaneous Hg and H_2S removal: H_2S is selectively oxidized in a contaminated gas stream to generate sulfur that reacts with mercury to form HgS, which is removed along with the remaining sulfur by co-condensation. H_2S is further separated in the amine unit and recycled to improve removal efficiency (Srinivas and Copeland, 2006).*

90% of mercury entering the gas plant may end up in the amine unit. Of this, 70% might partition to the sour gas product stream (i.e. sulfur unit) with the rest staying in the treated sweetened gas stream. The latter is then directed into the gas dehydration unit (e.g. glycol), wherein proportionally 80% can stay in the dry gas and the remaining leaves with the vented moisture stream. Hence, O'Rear et al., (2014) claimed an optimized plant operation (Figure 2.13) involving mercury removal at the amine and/or dehydrator unit, concurrently with the removal of acids and/or water by using mercury-complexing agents, such as $(NH_4)_2S_x$. In this way the extraction of mercury occurs in the aqueous phase through the formation of precipitates (e.g. HgS) or soluble compounds (e.g. HgS_2^{-2}).

Finally, it is worth mentioning that when the MRU is installed upstream of the acid gas removal and dehydration units and downstream of the separator, the mixture temperature may fall undesirably below the dew point of hydrocarbons/water during the operation of absorber unit. This is possibly due to entrainment of droplets from the separator, or mixture cooling down and partial condensing in the line between the separator and absorber. Thus, Bauer (2017) claimed a method in which the gas stream after exiting the separator is warmed to a sufficient extent to avoid the temperature falling below the water dew point in the MRU, and the hydrocarbon dew point in the subsequent acid gas removal unit.

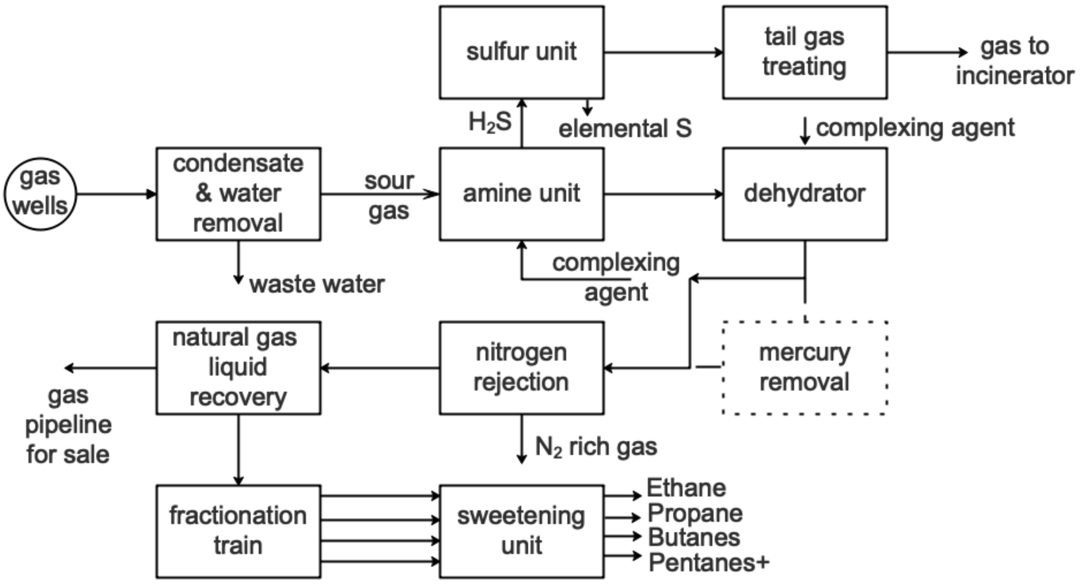

***Figure 2. 13**. Optimized gas processing operations for the simultaneous removal of Hg and H_2S (O'Rear et al., 2014).*

2.3.3. Glycol and Molecular-Sieve Dehydration

Dehydration using glycol is a common method used in the gas processing industry (Kong et al., 2018). As discussed previously, silver-impregnated molecular sieves may also be used to simultaneously remove mercury and water. Mercury can be removed from water via filtration, adsorption or thiol precipitation (Fakhru'l-Razi et al., 2009; Vikrant and Kim, 2019), but the removal from methanol, and glycol solutions is more challenging. At laboratory ambient conditions the solubility of Hg^0 in water-rich MEG was reported up to 60 ppb by Sabri et al. (2015b), and up to 80 ppb by Gallup et al. (2017), who also identified the equilibrium solubility of Hg^0 in water-lean MEG at around 140 ppb. Ezzeldin et al. (2016) studied the mercury speciation in an Egyptian gas plant and reported that the total mercury concentration in water-rich TEG was about 377 ppb at around 50 °C. Furthermore, Sabri et al. (2015a) spiked the industrial MEG, initially devoid of mercury, with Hg^{2+} and found that upon heating, some Hg^{2+} was reduced to Hg^0, with the partition percentage being highly dependent on the salt and organic content of MEG solution (Figure 2.14). Kho and Pham (2019) found that the absorption of $HgCl_2$ into solutions of MEG was comparable to the absorption in pure water (Kho and Pham, 2018), with the interaction between $HgCl_2$ and MEG not yielding organically-bound mercury. Solubilities of both mercury and $HgCl_2$ increase exponentially with temperature, and if Hg^{2+} is present, it will be very soluble in MEG and TEG solutions (Gallup, 2018).

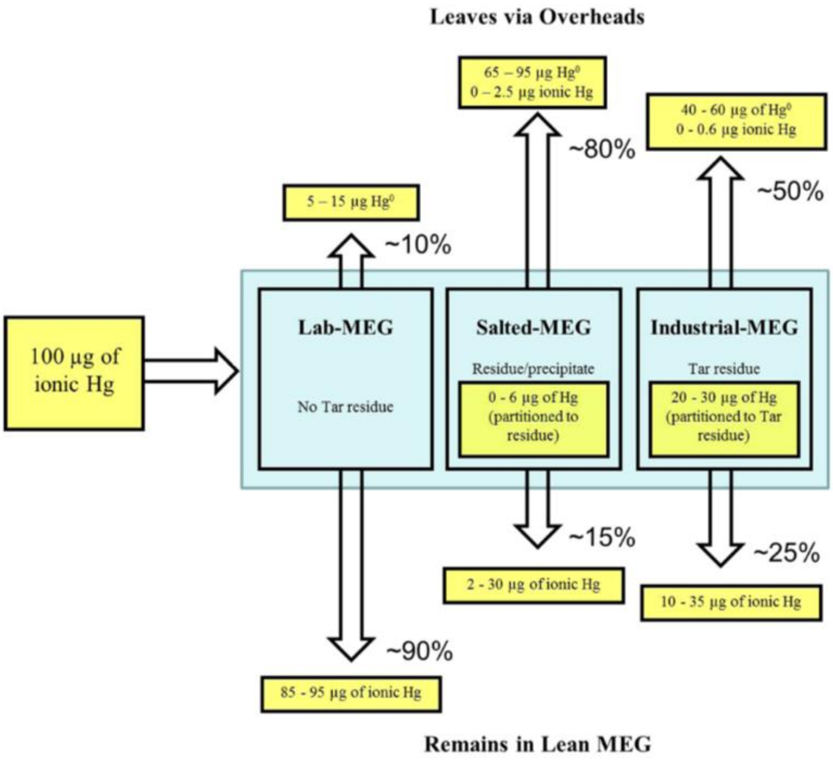

***Figure 2. 14**. Mass balance of mercury during MEG regeneration process (Sabri et al., 2015a).*

To prevent discharging mercury to the environment by waste-water and desorbed gases during the dehydration process with glycol, Carnell (2007) proposed contacting the mercury-contaminated glycol or/and alcohol-containing stream, with a sulfurized metal supported on Al_2O_3. The sulfurized metal may comprise of iron, copper, or nickel possibly with ZnO or $ZnCO_3$ on Al_2O_3 to function as sulfurization promoter and support, respectively. As it can be seen in Figure 2.15, Thompson et al., (2017) added a complexing agent into the recirculated glycol solvent feed (e.g. TEG). Water soluble sulfur species like Na_2S_x was used to extract mercury in the aqueous phase as precipitate, such as HgS or soluble HgS_2^{2-}. The rich glycol stream was fed with the complexing agent to the regenerator, whose overhead contained an absorber to capture mercury, while the regenerated lean glycol steam was recycled back to the dehydration liquid contractor.

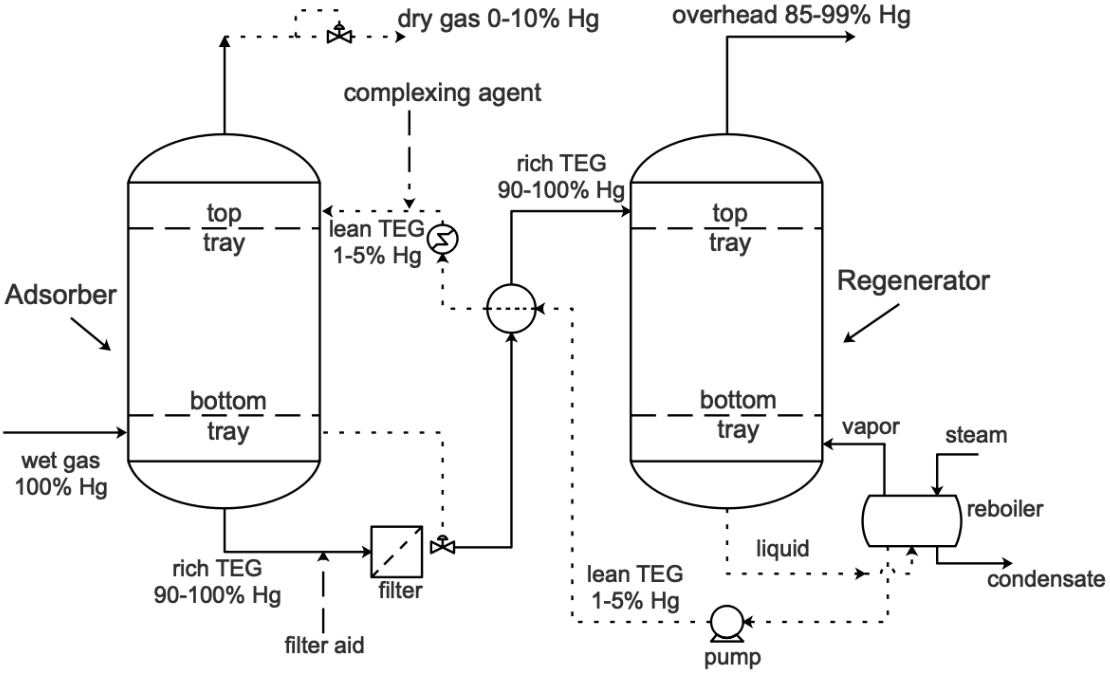

Figure 2. 15. *Glycol dehydration process: Mercury is removed through a system containing a rich glycol filter, while the complexing agent is partially removed with the help of filter aid (Thompson et al., 2017).*

To both achieve sufficient reduction in mercury concentration, avoid re-entry to facilities through recycled regeneration gas and of course dispose mercury in environmental safe manner, Markovs and Maurer (1993) claimed a process using of at least two cyclically regenerated adsorption beds in combination with a condenser. Before entering the condenser, the stream is passed through a chiller to prevent the formation of hydrocarbon hydrates. The spent regeneration gas stream may be further treated (Markovs, 1994) in a desiccant comprising of zeolite to reduce water content below a certain concentration. This allows the mercury-containing effluent stream to be further cooled down without causing the formation of hydrates. Therefore, the removal of a largest portion of mercury is possible. In another version of this process (Markovs et al., 1994), mercury may be removed by using a large cyclically regenerable adsorption bed (e.g. zeolite) in combination with a secondary smaller non-regenerable bed (e.g. metal sulfide). Weekman and Yan (1995) claimed a similar process to recover mercury in liquid form after simultaneously removing residual mercury and water using silver-impregnated zeolites.

It is true that to achieve mercury concentrations lower than 10 ng·Nm^{-3} (i.e. LNG specifications) with non-regenerable methods, large adsorption beds are needed, making the capital and sorbents costs uneconomical. On the other hand, in regenerable methods high volumes of regeneration gas need to be heated and cooled down resulting in oversized regeneration equipment. In both cases, the disposal of mercury sorbent and mercury-laden bed effluent, respectively, need to be conducted in an environmentally safe manner.

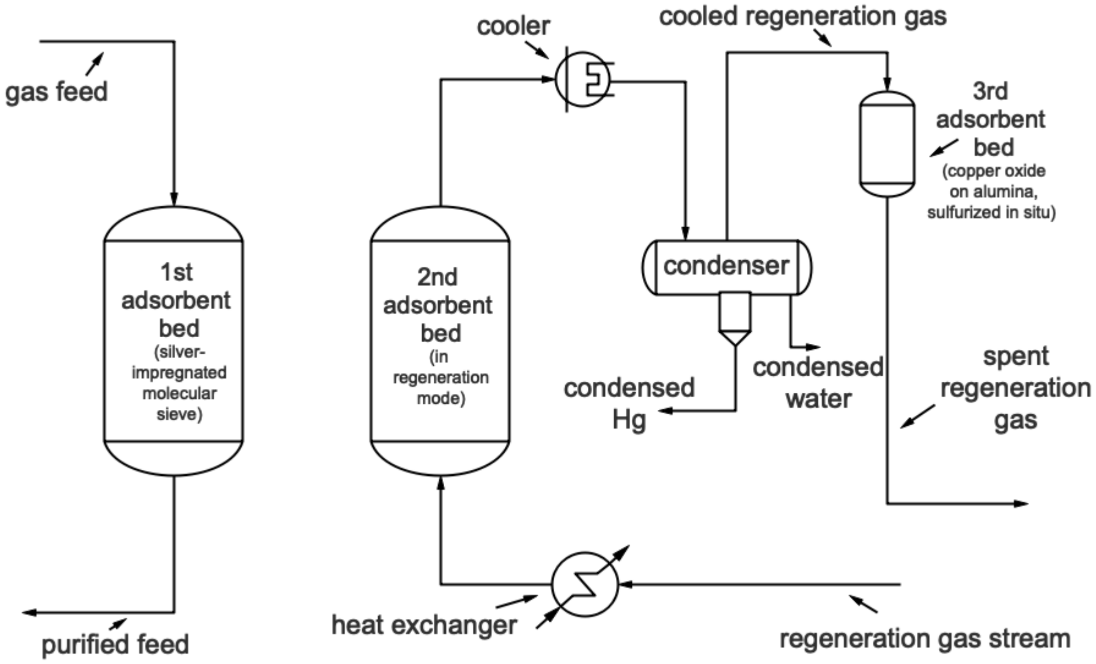

***Figure 2. 16**. Simultaneous Hg and H_2S removal: Sulfur leaching by liquid hydrocarbons is avoided by sulfurizing in-situ a non-regenerable copper oxide-based sorbent* (Mulvaney III et al., 2008).

Thus, Markovs (1999) claimed an optimum process in which the hydrocarbon stream is initially sub-divided into two streams (gaseous and liquid portion). which are then treated separately by adsorption in separate purifying beds (e.g. silver-impregnated zeolites). Then both beds are regenerated sequentially (using a common mercury recovery zone) and after desorption and mercury recovery, the regeneration gas is further purified in a secondary regenerable adsorption bed (e.g. silver-impregnated zeolites), where it can be concentrated and removed at a lower cost. Finally, to avoid sulfur leaching by liquid hydrocarbons Mulvaney III et al. (2008) conceived a process in which the sorbent does not contain elemental sulfur when placed into service, but it is sulfurized in situ while in service after it passes the first adsorption bed comprising of silver-impregnated molecular sieves. The stream is subsequently cooled down to condense out a portion of mercury (Figure 2.16). CuO adsorbs sulfur along with mercury (Equations 2.12 and 2.13) with the rate of sulfur uptake depending on the sulfur amount in the feed.

$$CuO + H_2S \rightarrow CuS + H_2O \qquad (2.12)$$

$$CuS + Hg \rightarrow Cu + HgS \qquad (2.13)$$

2.3.4. Subsurface Methods and Simultaneous Hydrates Treatment

Removal of mercury as close as possible to the production wells is recommended in order to minimize contamination in downstream processes. A subsurface mercury removal method proposed by Jamaluddin and Tibbles (2011), involved placing a sorbent into the vicinity of a producing formation face at a downhole location. The location may be between the formation face and sand screen or gravel pack or part of them or behind them. The granular sorbent may be regenerated downhole by a heated fluid above the reservoir temperature, containing a chemical active component to bind the adsorbed mercury. The subsurface mercury removal (Mock, 2012) apart from injecting a mercury sorbent in the subterranean production formation, can also be achieved by packing part of the wellbore with a sorbent within a drilled length of the wellbore in an annular area around tubing where the produced fluids flow, or fracturing the formation with a fluid-proppant containing sorbent. Yean et al. (2014) claimed an in-situ method for mercury removal from produced fluids by subterranean hydrocarbon-bearing formations which involves, injecting a sufficient amount of a fixing agent (e.g. organic polysulfides) into the formation with produced water (Pichtel, 2016) from the formation. The fixing agent reacts with mercury to form a precipitate or extracts it into the dilution fluid like a water soluble complex.

During transportation, fluids contained in produced hydrocarbons such as crude oil, condensate, formation water and gas, may react under certain temperature and pressure conditions to form solid hydrates which block the pipelines (Chalkidis and Tohidi, 2015; Kinnari et al., 2014). To avoid or prevent their formation thermodynamic (e.g. glycol-based such as MEG) and kinetic (e.g. polymeric compounds) hydrate inhibitors, as well as antiagglomerants (e.g. surfactants) are added prior or during fluids transportation (May et al., 2014; Perrin et al., 2013). O’Rear et al. (2014) claimed a method for concurrent production gas transportation and mercury removal, which involves the simultaneous injection of a complexing agent (e.g. Na_2S_X) and a hydrate inhibitor (e.g. MEG and/or methanol) into the pipeline. The aqueous phase containing the inhibitor, unreacted complexing agent and mercury complexes can be afterwards recovered and re-used. In traditional methods, mercury ions follow the hydrate inhibitor into the reclamation system and they are precipitated in the form of mercury salts, thus requiring the total salts mixture to be treated as hazardous waste. Therefore, Jensen (2016) developed a method in which a sulfide such as Na_2S is added into the rich hydrate inhibitor hydrate stream, at temperatures below 50 °C and pH=6-8, in order to form a salt. The slurry comprising the heavy metal salt is then separated from the hydrocarbon and rich hydrate inhibitor stream, and the remaining hydrate inhibitor can be further recovered from the slurry stream.

2.3.5. Clean Up and Passivation

A method to stabilize Hg^0 in a spent molecular sieve desiccant (Audeh, 1992) involves subjecting the latter to an aqueous solution of $Na_2S_2O_3$, Na_2S_x or $KHSO_5$ in order to trap mercury in the form of an insoluble salt. If $Na_2S_2O_3$ (Equations 2.14 and 2.15) or Na_2S_x (Equations 2.16-2.18) are selected, then an appropriate amount of HCl is also utilized to generate sufficient sulfur to react with Hg^0 and form HgS. However, if $KHSO_5$ (Equation 2.19) is used then HCl is not needed and mercury is fixated in the form of HgO.

$$Na_2S_2O_3 + 2HCl \rightarrow H_2SO_3 + S^0 + 2NaCl \tag{2.14}$$

$$Hg^0 + S^0 \rightarrow HgS \tag{2.15}$$

$$Na_2S_x + HCl \rightarrow NaCl + H_2S_x \tag{2.16}$$

$$H_2S_x \rightarrow H_2S + (x\text{-}1)S^0 \tag{2.17}$$

$$H_2S + Hg^0 \rightarrow H_gS + H_2 \tag{2.18}$$

$$KHSO_5 + Hg^0 \rightarrow KHSO_4 + HgO \tag{2.19}$$

As explained previously, mercury can react with the aluminum coils within the cryogenic heat exchanger to form a soft powdery amalgam. Under normal cryogenic temperatures there is little concern, but at temperatures above 0 °C, corrosion becomes a significant problem. Deriming process (Al Mazrouei et al., 2018) involves contacting the interior surfaces of the heat exchanger with a solvent, at a temperature below the freezing point of mercury. During this process, undesirable deposits in the interior surfaces of the heat exchanger will dissolve and be removed, while a part of mercury present within the heat exchanger will remain in the solid form. To passivate or render non-reactive the accumulated mercury on the cold surfaces of the aluminum heat exchangers, Yan (1988, 1998) suggested contacting the equipment with a flowing stream of sulfur containing gas or liquid solvent (e.g. anhydrous H_2S) when the equipment is in use or is suspended for repair. In a related method (Craig, 1989) mercury may be converted to insoluble HgS that is inert to aluminum, at temperatures below the water's freezing point. To succeed this, the surface is first coated with a condensable solvent like CS_2 that is capable of dissolving H_2S. After contacting the liquid-coated surface with H_2S, SO_2 is applied to the surface so that can react with the already present H_2S. The application of successive reactants causes mercury, in droplet and amalgam form, to be coated on the exterior as HgO or HgS, which prevent further degradation.

Furthermore, Humble and Yan (1989) suggested a deriming process which involves contacting the solid deposits with a solvent like methanol at temperatures lower than -40 °C, where they are dissolved and removed. A substantial amount of any mercury present would be in the solid phase, reducing in this way the threat for corrosion. Wilhelm (1993) claimed the utilization of an oxidizing agent (e.g. HNO_3) along with a non-aqueous solvent (e.g. H_2O/CH_3OH =10/90) and a sequestering agent (e.g. RSH), with the aim of oxidizing and complexing mercury to soluble species. These species would be eventually removed by either an exchange resin bed (complex removal), or through a thermal cycle (complex precipitation) or even via chemical neutralization (complex reduction to elemental mercury). In a non-corrosive method (Lord et al., 2012) to remove water-insoluble forms of mercury from a contaminated solid surface, the latter is subjected at 80-100 °C to a cleaning solution, containing hydrocarbon oil_with up to 5,000 ppm total sulfur.

In general, the use of acid treatment to clean up mercury spills and surface contamination is disfavored because of the safety hazards to workers and the corrosion of steel surfaces present on most downhole tools. Vacuum devices cannot be used because they produce mercury droplets during suction and filtration, extending in this way the contamination. Therefore, Keatch (2018) claimed a method in which the contaminated metal surface is contacted with a solution comprising a metal salt possessing a standard reduction potential of greater than 0.85 (reduction potential of mercury measured at standard conditions) to oxidize mercury contaminant to a soluble mercury salt. For instance, $AgNO_3$ may be used as the metal salt oxidant (Equation 2.20) and the produced $Hg(NO_3)_2$ may be recovered as a solid by the addition of Na_2S precipitating agent to form

HgS (Equation 2.21), which can be further isolated by filtration. The silver particles can be washed and re-dissolved in nitric acid to reconstitute the oxidation agent.

$$Hg^0_{(l)} + 2AgNO_{3\,(aq)} \rightarrow Hg(NO_3)_{2\,(aq)} + 2Ag_{(s)} \quad (2.20)$$

$$Hg(NO_3)_{2\,(aq)} + Na_2S_{(aq)} \rightarrow HgS_{(s)} + 2NaNO_{3\,(s)} \quad (2.21)$$

Processing facilities may operate for extended time periods before detection of mercury in the gas plant as mercury adsorbs on the metallic pipelines used for transportation of fluids from the wells. Chanvanichskul et al. (2017) proposed a methodology to in-situ decontaminate mercury from a pipeline, based on both chemical and mechanical means. As illustrated in Figure 2.17, the method makes use of one chemical and two mechanical pigs. The first pig is designed to be used with the chemical as a pig train, while the second pig removes the residual mercury after the chemical pig train.

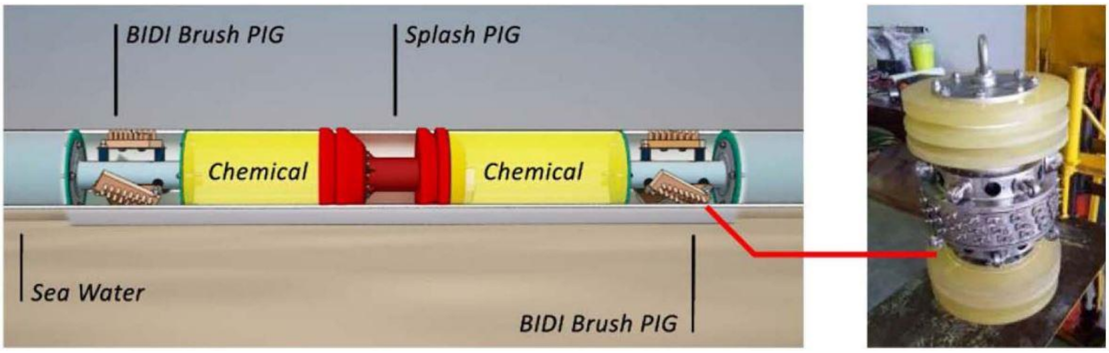

***Figure 2. 17**. In-situ pipeline mercury decontamination by Thailand's PTTEP, combining a chemical and mechanical method (Chanvanichskul et al., 2017).*

In a similar way, O'Rear et al., (2016b) conceived a mercury management scheme based on both chemical and thermal treatments to control mercury accumulated in forms such as Hg^0 and HgS. The thermal treatment relates to the employment of a leading pig equipped with a laser source, an induction coil and a combustor for heating the section of interest. In this way, a portion of Hg^0 is vaporized and a portion of HgS is decomposed as Hg^0 vapor, which is then captured by a gas flow and recovered by condensation downstream of the treated section. The chemical treatment involves the injection of an aqueous sulfidic solution comprising of sulfides (e.g. $(NH_4)_2S$) or polysulfides (e.g. Na_2S_x). Inorganic polysulfides dissolve in water to form HS_x^- or S_x^{2-} anions with x≥2 (Equation 2.22), while inorganic sulfides dissolve to form HS^- or S^{2-} anions (Equation 2.24). Thus, Hg^0 oxidizes to soluble anionic mercury complexes (e.g. HgS_xH^- with x≥2)

(Equation 2.23), and HgS may form soluble complexes (e.g. HgS_xH, HgS_x^{-2} with $x \geq 2$) (Equation 2.25).

$$Na_2S_{2\,(s)} + H_2O_{(aq)} \rightarrow 2Na^+_{(aq)} + OH^-_{(aq)} + HS_2^-{}_{(aq)} \qquad (2.22)$$

$$Hg^0_{(l)} + HS_2^-{}_{(aq)} \rightarrow HgS_2H^-_{(aq)} \qquad (2.23)$$

$$Na_2S_{(s)} + H_2O_{(aq)} \rightarrow 2Na^+_{(aq)} + OH^-_{(aq)} + HS^-_{(aq)} \qquad (2.24)$$

$$HgS_{(s)} + HS^-_{(aq)} \rightarrow HgS_2H^-_{(aq)} \qquad (2.25)$$

2.3.6. Waste Disposal

Incineration, stabilization/solidification, permanent storage, landfills and deep-well injection are the main technologies utilized for mercury disposal. Secondary contamination can be minimized with permanent storage technology (Lee and Lee, 2012). The disposal of mercury-containing waste from oil and gas facilities (Wilhelm, 1999b) (Table 2.3) should be carried out according to the guidelines of the Basel Convention (2011). If buried, some of the inorganic mercury in the landfill may be converted by bacteria into the more toxic form of methylated mercury, which can be then released back into the atmosphere (Randall and Chattopadhyay, 2013). According to the US EPA Land Disposal Restriction program if the mercury content of waste is more than 260 $mg \cdot kg^{-1}$, it must be treated via roasting and retorting to reduce its concentration to less than 0.2 $mg \cdot L^{-1}$, as specified in the toxicity characteristic leaching procedure (TCLP) (Wang et al., 2012). If it is less than 260 $mg \cdot kg^{-1}$ and roasting is selected for treatment, then the mercury concentration should be reduced to 0.2 $mg \cdot L^{-1}$. In case other methods, such as stabilization/solidification (Gesellschaft für Anlagen- und Reaktorsicherheit, 2009; Rodriguez et al., 2012) are used, the threshold value for TCLP is 0.025 $mg \cdot L^{-1}$. In general, the removal of mercury from complex mixtures can be accomplished primarily through chemical and thermal methods (Wilhelm and Mcarthur, 1995; Wilhelm, 1999b). Thermal processes (Bohm and Mussig, 1996) convert, evaporate and condense mercury. Chemical treatment involves reacting elemental, inorganic or organic compounds to a soluble ion, an insoluble inorganic compound or to a solid complex.

Yan (1987a) claimed a process in which the spent sulfur-impregnated activated carbon is rendered non-hazardous for landfill disposal. In this process the spent sorbent is introduced in a fluidized combustion zone (600-1000 °C) along with an alkaline earth material (e.g. limestone) and water to produce steam. The soiled residue is substantially reduced in mercury content and the combustion gases are cooled with the condensed mercury being collected from the cooler. Pornsakulsak and Soponkanabhorn (2007) examined the possibility of metal recovery from spent hydrogen sulfide and mercury sorbents, that comprised of Al_2O_3, $CuCO_3/ZnCO_3$, a cementitious binder and HgS. From the mercury sorbents, 31% of copper and 11% of zinc could be recovered, however, the sorbent had to be pre-treated by vacuum distillation ($[Hg]=4.5\ g{\cdot}kg^{-1}$) before it was processed in the smelting plant for metal recovery, rendering the cost of treating higher than the commercial value of the metals.

Table 2. 3. *Types of mercury-containing waste in oil and gas processing streams (Wilhelm, 1999b).*

Type	***Matrix***	***Mercury species***
Sludge	Water/hydrocarbon	Hg^0, Hg^{2+}, RHgR′, HgS
Cleaning solutions	Water/hydrocarbon solvents	Hg^0, Hg^{2+}, RHgR′
Mercury sorbent	Carbon-sulfur, metal sulfide-alumina, zeolite-silver	Hg^0, RHgR′, HgS (Cu, Al_2O_3), Ag-Hg
Dehydration fluid	Glycol solutions (MEG, TEG)	Hg^0, RHgR′, Hg^{2+}
Sour gas treatment	Amines (MEA, DEA, MDEA)/water	Hg^0, RHgR′, Hg^{2+} (Amines, KCO_3)
Catalysts	Metals, alumina, zeolites	Hg amalgams
Filtration material/debris	Clays, fibers	Hg^0, RHgR′, Hg^{2+}

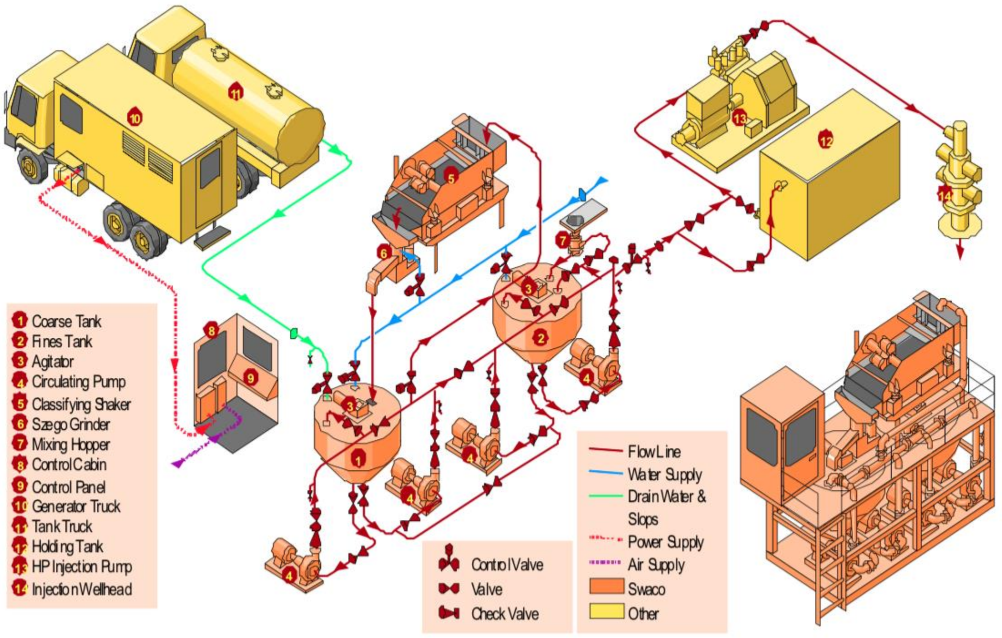

Figure 2. 18. *Mercury-containing waste pre-treatment for disposal via an injection well (Brkic et al., 2003).*

As stated above, one option for disposal is through an injection well (Brkic et al., 2003; Yod-in-Lom and Doyle, 2002), in which the waste material is placed into a secure geologic location. These types of disposal wells are common in oil and gas industry for non-toxic liquid waste. For instance, co-produced water is often re-injected to the original formation. The most important technical consideration for disposal wells is the identification of a suitable formation that will not communicate with water formations in geologic time. The selected geological formations should be covered with impermeable bed rock and cap rock without vertical regional faults, that will prevent the waste from migrating into the aquifer of potable water. Before injection the waste material must be treated (Figure 2.18) to convert it into a form that is injectable and chemically stable.

2.4. Summary

The conclusions drawn from the above discussion can be summarized as follows:

a) The industry's interest on mercury's presence during natural gas production and production is reflected on the increasing number of patents published in the last decade. In fact, the corrosion effects with respect to aluminum and carbon/stainless equipment have been detrimental on several occasions.

b) Metal sulfide technology is the industry's norm for mercury abatement. This type of sorbents can be effective when fitted in MRUs located at the front of gas plants. In this way, all downstream equipment is protected and mercury releases to the environment, through typical natural gas processing operations, are minimized or prevented.

c) The efficient utilization of metal sulfides, however, requires the tuning of shape and size of active phase's particle, as well as the optimization of carrier's porosity. Metal oxides offer the advantage of regeneration and recyclability. Additionally, promising alternative technologies such as SILPs have been already commercialized, although they are not free of shortcomings.

d) The atmospheric mercury emissions from oil and natural gas industry constitute only a very small fraction of the total anthropogenic emissions. In the absence of MRUs, mercury may be released during gas treatment to the environment mainly through the inlet separation, acid gas removal and dehydration processes. Further studies are required to identify the potential impact of unconventional natural gas production with respect to mercury contamination of aquatic ecosystems.

e) Comprehensive speciation studies are required during appraisal and production phases so as to provide effective mitigation treatment. Hg^0, which is the predominant species in natural gas, can be removed by conventional methods, however organic mercury compounds require additional treatment.

f) Reliable detection, sampling and measurement all the way from the hydrocarbon formation through fluid transportation and processing facilities, is required. Mercury is not produced at constant concentration, but rather in the form of plugs and slugs. Regardless of the metallurgy of production, processing and sampling equipment, adsorption always take place.

g) Deep-well injection may be an economically viable and environmentally safe solution for mercury-waste disposal, as long as no communication with water formations in geologic time is ensured.

h) The provision of effective mitigation planning usually depends on the prediction of mercury’s presence in produced fluids. Further research is required to elucidate the behavior of mercury compounds in a variety of geological formations.

Chapter 3. Experimental Methods

3.1. Chapter Overview

The third chapter presents the experimental methods and procedures and it is subdivided into three sections. The first section describes the synthesis of Mn-Ce nano-metal oxides, the 3D-printing of Ti-based support structure as well as its coating. The second section briefly discusses all techniques utilized for the characterization of the developed nanosorbents. These include powder X-ray diffraction (XRD), Brunauer-Emmet-Teller (BET) specific surface area, X-ray photoelectron microscopy (XPS), scanning electron microscopy (SEM), transmission electron and high resolution microcopy (TEM and HRTEM), selected area electron diffraction (SAED), energy dispersive X-ray spectrometry (EDS), microwave plasma atomic emission spectroscopy (MPAES) and thermogravimetry (TG). The third section displays the experimental setup and explains the procedure followed for the conduction mercury removal and sorbent regeneration tests. The bench scale mercury testing rig and sampling system is thoroughly illustrated and the quantitative analysis of mercury by cold-vapor atomic florescence spectroscopy (CVAFS) is analyzed.

3.2. Sorbent Preparation

3.2.1. Synthesis of α-MnO_2 Nanosorbents

For the synthesis of α-MnO_2 nanosorbents, $KMnO_4$ (≥99%), $MnSO_4 \cdot H_2O$ (≥99%), NH_4Cl (≥99.5%) and $Ce(NO_3)_3 \cdot 6H_2O$ (≥99.5%) were purchased from Sigma-Aldrich (Australia), while concentrated HCl (36%), H_2SO_4 (98%) and CH_3CH_2OH (100%) were obtained from Chem-Supply (Australia).

All three α-MnO_2 nanosorbents were prepared by the reduction of $KMnO_4$ through a hydrothermal method according to the literature (Gao et al., 2016; He et al., 2016; Wang et al., 2014a). The two-step synthesis of MnO_2 from $KMnO_4$ in an acidic solution, involves first, the reduction of manganese to Mn^{2+}, and then its oxidation to Mn^{+4} by excess MnO_4^- (Umek et al., 2009). Besides the difference in the hydrothermal reaction conditions and chemical precursors, the same steps were followed for the synthesis of all three morphologies (Figure 3.1). For the synthesis of nanotubes (NTs), 0.66 g $KMnO_4$ and 1.5 mL HCl were added into 75 mL deionized water and kept under stirring until a homogeneous solution was formed. The solution was then transferred to a Teflon-lined stainless-steel autoclave and kept at 150 °C for 10 h. After the hydrothermal treatment was completed, the autoclave was removed and cooled down naturally to room temperature. The product was then washed and centrifuged, before it was vacuum dried overnight.

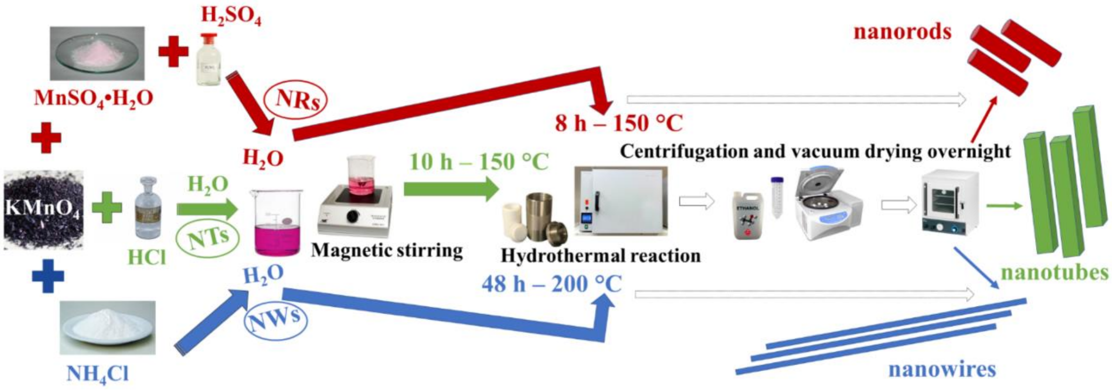

Figure 3. 1*. Schematic of the synthesis process of α-MnO_2 nanotubes, nanorods and nanowires.*

Nanorods (NRs) were prepared as follows: 1.19 g $KMnO_4$ and 0.21 g $MnSO_4 \cdot H_2O$ were dissolved in 35 mL distilled water. Following this, 2.5 mL H_2SO_4 was added with the assistance of magnetic stirring to form a homogeneous solution. The solution was then transferred into a Teflon-lined stainless-steel autoclave and kept at 150 °C for 8 h. Subsequently, the autoclave was taken out and cooled down naturally to room temperature. Then the product was washed and centrifuged, before it was vacuum dried overnight. Finally, nanowires (NWs) were prepared by the addition of 0.25 g $KMnO_4$ and 0.09 g NH_4Cl in 80 mL distilled water. The solution was transferred into a Teflon-lined stainless-steel autoclave and kept at 200 °C for 48 h. Then the product was washed, centrifuged and dried under vacuum overnight.

3.2.2. Decoration of α-MnO_2 Nanotubes with CeO_2 Nanoparticles

Decoration of the α-MnO_2 NTs with CeO_2 nanoparticles was achieved by subjecting them to a second low-temperature hydrothermal method using $Ce(NO_3)_3 \cdot 6H_2O$ as cerium source and $CO(NH_2)_2$ as precipitating agent (Tang et al., 2016). In a typical solution, 500 mg α-MnO_2 NTs, 6 g CH_4N_2O, 100 ml H_2O, 50 ml $CO(NH_2)_2$ and the required amount of $Ce(NO_3)_3 \cdot 6H_2O$ were mixed together to achieve approximately 10, 25 and 35% Ce/Mn atomic weight ratios. The mixture was vigorously stirred under reflux for 2 h at 80 °C. Then the product was dried overnight, followed by calcination in air for 2 h at 350 °C, with a heating rate of 2 $°C \cdot min^{-1}$. The prepared nanosorbents were labeled as MnCe10, MnCe25, MnCe35 reflecting their relative Ce/Mn atomic weight ratios (10, 25 and 35 wt%, respectively) as derived from MPAES. 35 wt% was the maximum Ce/Mn atomic weight ratio obtained from this process. For comparison, pure CeO_2 was synthesized following the aforementioned method in the absence of α-MnO_2 NTs. A physical mixture of α-MnO_2 NTs and CeO_2 was also prepared by grinding the two materials prepared in isolation at 1:1 weight ratio in a pestle and mortar.

3.2.3. 3D-Printing of Ti-Based Alloy and Coating with CeO_2/α-MnO_2 NTs

Selective laser melting (SLM) (Shipley et al., 2018) is a powder bed fusion additive manufacturing (3D-printing) technique in which a laser beam is deployed to build parts through selectively melting areas of powder layers (Figure 3.2). The source powder material is irradiated to melt and produce a liquid pool (melt pool), which then transforms into solid and cools down quickly. When the scanning of the part's cross-section is completed, the building platform is lowered by a pre-defined distance to allow the deposition of a new layer of powder. The process is repeated until the part is completed, and because of the high reactivity of titanium alloys, it is conducted under an inert argon atmosphere. Also, a solid substrate is used for the building of the part so as to prevent material warping as a result of thermal stresses growth.

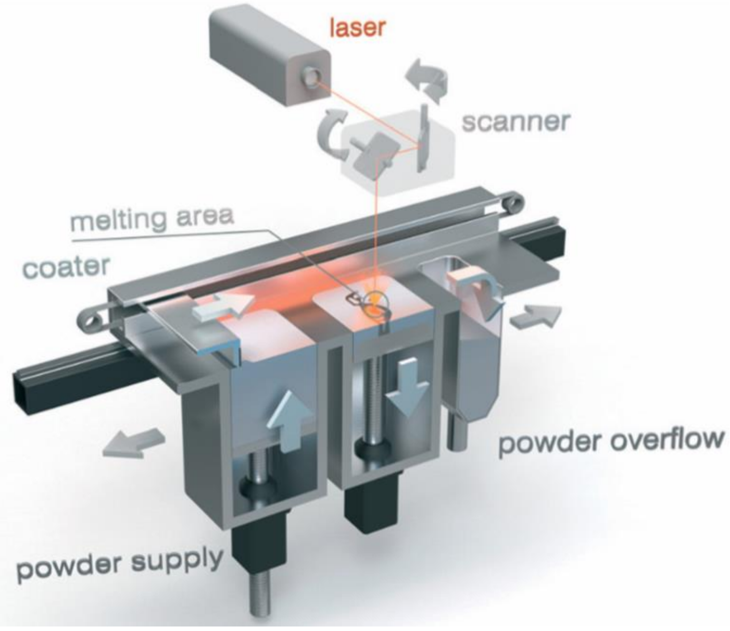

Figure 3. 2. *SLM process as demonstrated by LaserCUSING technology by Concept Laser GmbH (Hurt et al., 2017).*

For the manufacturing of the 3DTi structures a spherical gas atomized Ti-6Al-4V powder (ELI, ASTM Grade 23; TLS Technik GmbH) with a mean particle diameter of 45 μm was used (Table 3.1). A series of square channel tubes (width=0.5 cm, length=5 cm) (Figure 3.3a) with cell-spacings of less than 0.1 cm (Figure 3.3b) were fabricated using SLM 250 HL (SLM Solutions GmbH; flow Ar; oxygen level < 0.1%; chamber temperature: 200 °C) (Xu et al., 2017b). The unit cell of the lattice structure was FCC and BCC with vertical axis struts and no end plates (FBCCZO) and was produced by the optimal conditions: layer thickness: 30 μm, laser power: 173 W, scan speed 710 $mm \cdot s^{-1}$, hatch spacing: 0.12 mm (Mazur et al., 2017).

Table 3. 1. *Composition of Ti-6Al-4V powder (ELI, ASTM Grade 23; TLS Technik GmbH).*

Element	O	N	C	Fe	H	V	Al	Ti
Powder (wt%)	0.1	0.009	0.008	0.17	<0.002	4	6	balance

Table 3. 2. *Weight deposition of MnCe35 after subsequent dip-coating cycles and final calcination followed by sonication.*

Treatment	***C-3DTi weight (g)***	***MnCe35 deposited (mg)***
Initial	4.166	-
1st dip-coating cycle	4.277	111
2nd dip-coating cycle	4.324	47
3rd dip-coating cycle	4.376	52
Calcination and sonication	4.346	-
Total material deposited (mg)		180

The loading of MnCe35 active phase on 3DTi's surface was carried out through dip-coating process. MnCe35 powder (at least 10 wt%) was added into distilled water under rigorous stirring to form a slurry. Subsequently the 3DTi structure was vertically immersed into the wash-coating slurry multiple times. Three coating cycles were carried out, and to ensure good adhesion, after the completion of each cycle the coated structure (C-3DTi) was dried at 150 °C for about 20 min. Finally, the C-3DTi was calcined at 400 °C for 3 h with a heating rate of $2° \cdot min^{-1}$. To assess the coating's stability the treated structure was immersed into an aqueous solution and was sonicated for 15 min. As Table 3.1 displays, some material was lost (30 mg), with the final amount coated being 180 mg (less than 5 wt% of the structure) (Figure 3.3c).

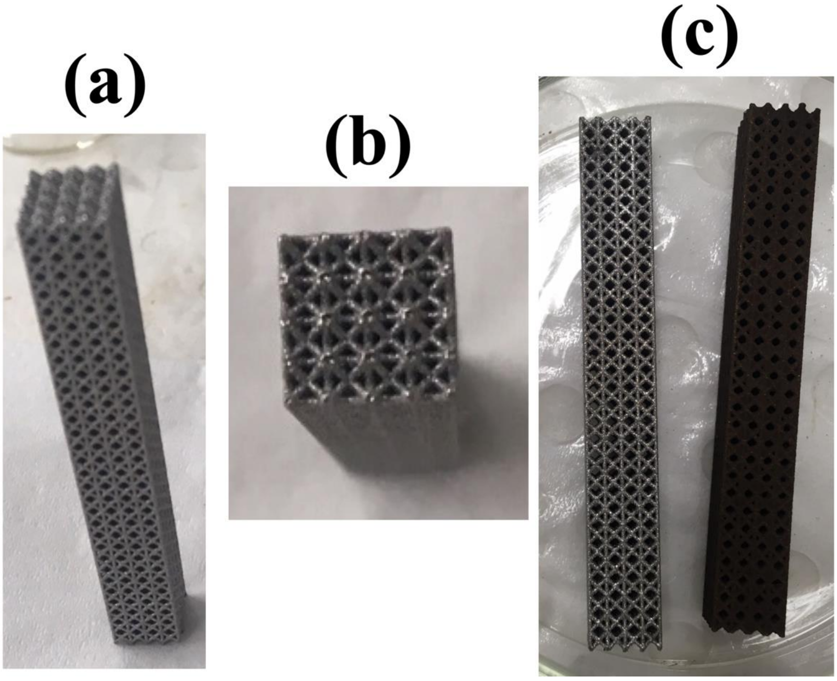

***Figure 3. 3**. a) Side and b) top images of the manufactured 3DTi support structure. c) The 3DTi structure after having been coated with MnCe35 active phase (C-3DTi).*

3.3. Sorbent Characterization

3.3.1. Powder X-Ray Diffraction

Powder XRD was used for the identification of the crystal structure of the synthesized nanomaterials. X-rays are wavelike forms of electromagnetic energy carried by high energy particles, photons, that are produced by the collision of electrons to a metal target (Sardela, 2014). The X-ray beam is generated at high vacuum in the hot cathode tube as emitted electrons, produced by thermionic emission from the filament (cathode), are accelerated due to the high-voltage difference between the cathode and anode. The wavelength of X-rays is in the order of a few angstroms, typically reflecting the inter-atomic distance in crystalline solids (0.15-0.4 nm). When X-rays interact with regularly spaced three-dimensional array of atoms of crystalline solids (Figure 3.4), they are diffracted at specific angles according to Bragg’s law (Equation 3.1), where d_{hkl} is the interplanar spacing between two lattice planes characterized by a set of Miller indices (hkl), θ_{hkl} is the corresponding diffraction angle, λ is the X-ray wavelength and n is the order of diffraction (Zou et al., 2011).

$$n\lambda=2d_{hkl}\sin\theta_{hkl} \tag{3.1}$$

Due to surface effects, nanomaterials have smaller sized crystallites and strains, resulting in significant peak broadening and shift in the peak positions. The alteration of d-spacing as a result of the change of lattice constants under strain, can be identified from the peak positions shift. The crystallite size is calculated by Sherrer's formula (Equation 3.2), where k is Scherrer's constant (~0.9) and β is the full width at half maximum (FWHM) (Leng, 2013d; Waseda et al., 2011).

$$D=(k\lambda)/(\beta\cos\theta) \quad (3.2)$$

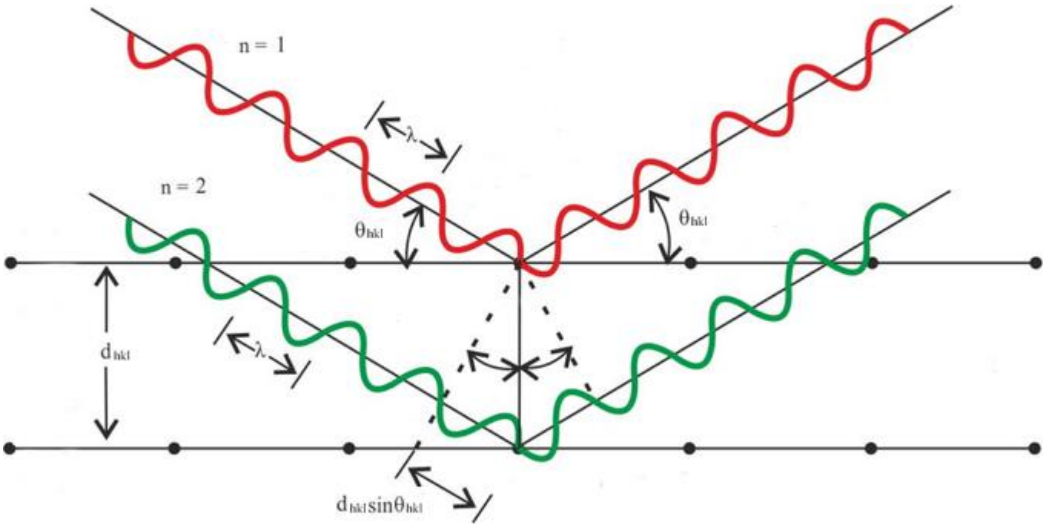

Figure 3. 4. *Bragg's law reflection: The diffracted X-rays exhibit constructive interference when the travel path length difference between the ray paths is an integer multiple of the wavelength (Leng, 2013d).*

XRD was performed on D8 Advance diffractometer (Bruker) which utilized a Ni-filtered Cu K-α radiation source (λ= 0.154 nm). The diffractograms were obtained over a 2θ range of 10-80° with a step size of 0.02° and step time of 1 s per point. The patterns were matched against the international center for diffraction data-powder diffraction file (ICDD-PDF).

3.3.2. BET Specific Surface Area

The determination of the specific surface area of the synthesized nanomaterials was based on the physical adsorption of N_2 on the solid surface, by calculating the adsorbate amount corresponding to a multi-layer coverage, measured by a volumetric or continuous flow procedure. The BET model which was used for this calculation, was built upon the assumptions of a homogeneous surface, limited molecular interactions, local equilibrium, kinetically limited process and infinite adsorption at saturation (Lowell et al., 2004a; b).

The adsorption isotherms were obtained by measuring the amount of gas adsorbed across a wide range of relative pressures (P/P_0) at a constant temperature (at -196 °C for N_2). Conversely, the desorption isotherms were obtained by measuring the amount of gas removed from the surface with pressure reducing.

The variables of BET equation (Equation 3.3) comprise of the partial vapor pressure (P), the saturated vapor pressure (P_0), the volume of the adsorbate gas (V_{ads}) at a relative pressure P/P_0, the volume of a gas adsorbed at STP (V_m) to produce a monolayer on the sample surface, as well as the constant C which is related to the affinity of the solid surface with the adsorbate gas.

$$P/(V_{ads}(P_0-P)) =((C-1)/(V_mC))(P/P_0)+1/(V_mC) \tag{3.3}$$

The plot of $P/(V_{ads}(P_0-P))$ versus the relative pressure (P/P_0) is a straight line with a slope of $(C-1)/(V_mC)$ and intercept of $1/(V_mC)$. The unknown V_m is calculated by the slope and intercept and consequently the specific surface area is derived from Equation 3.4, with N_A representing Avogadro's constant ($6.023\text{x}10^{23}$ mol^{-1}), A_m reflecting the cross sectional of the adsorbate gas molecule (0.162 nm^2 at -196 °C for N_2), W being the weight of the sample and V_l accounting for the liquid molar volume (22,414 $\text{ml}\cdot\text{mol}^{-1}$).

$$\text{BET specific area } (\text{m}^2\cdot\text{g}^{-1}) =(V_mN_AA_m)/(WV_l) \tag{3.4}$$

BET specific surface area was measured through N_2 adsorption-desorption isotherms produced by ASAP 2000 (Micromeritics). The analyzer was set at -196 °C and the samples were degassed at 150 °C under vacuum before the analysis. The specification of isotherms shape, which reflects the porous texture of tested materials, was carried out in line with IUPAC guidelines (Thommes et al., 2015).

3.3.3. X-Ray Photoelectron Spectroscopy

XPS is a semi-quantitative surface spectroscopy technique that was used for the determination of the elemental composition as well as the chemical or electronic state (e.g. oxidation) of elements present in the surface of samples (Haasch, 2014; Leng, 2013a). It is based on the irradiation of the material with monoenergetic X-rays that cause the ejection of electrons according to the photoelectric phenomenon (Figure 3.5). The excited photoelectrons in the near-surface region of the materials are then detected by an energy electron analyzer. The measurement of the kinetic energy (KE) of electrons, and the binding energy (BE) of core level, which reflects the oxidation of elements, is derived from Equation 3.5:

$$\mathrm{BE} = \mathrm{hv}-\mathrm{KE}-\Phi_{spec} \qquad (3.5)$$

where hv is the energy of X-ray quantum (i.e. Al K-$\alpha_{1,2}$=1486.6 eV) and Φ_{spec} is the work function of the spectrometer. The latter is defined as the minimum energy required to remove an electron from the material, leaving it at rest under vacuum.

The spectrometer can be calibrated with metallic samples (e.g. Au, Ag) whose binding energies are known. The depth of information obtained from XPS extends from the surface to about 5-7 nm. Apart from primary ionization electrons (photoelectrons), electrons resulting from the Auger relaxation process (Auger electrons) can be detected. The XPS spectrum is characteristic of each element (except H and He), therefore the surface chemical composition can be identified. XPS was conducted on K-Alpha spectrometer (ThermoFisher Scientific) that used monochromatic Al K-α radiation. The analysis was carried out under ultra-high vacuum at room temperature, and the adventitious carbon peak (C 1s) at 285 eV, was selected as reference for the correction of charging effects. Avantage software (ThermoFisher Scientific) was utilized for fitting the peaks using Smart background.

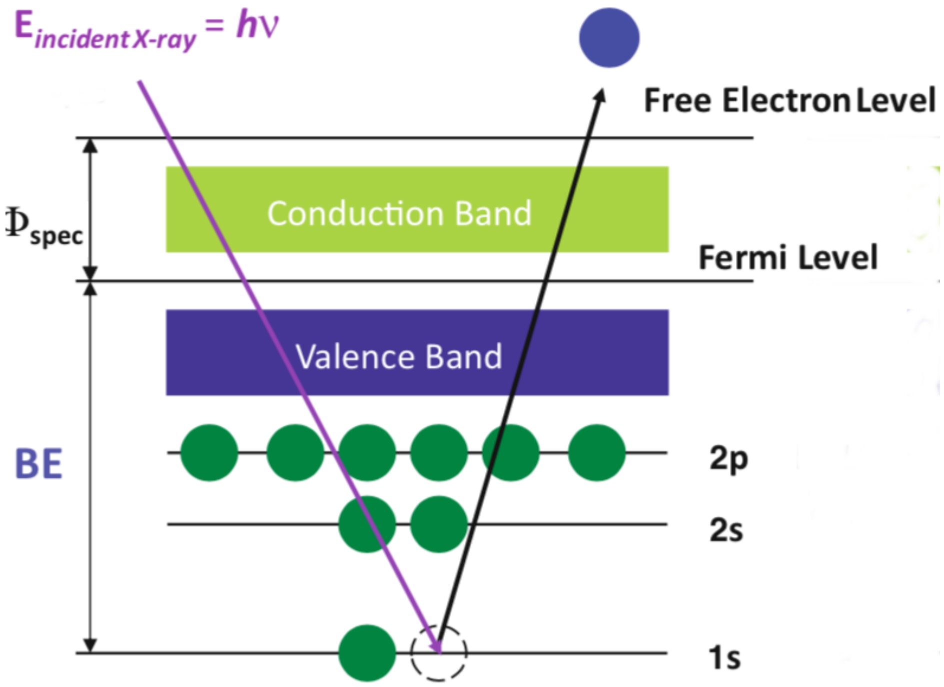

***Figure 3.** 5. Photoelectron emission process (Haasch, 2014).*

3.3.4. Scanning Electron Microscopy

SEM provided valuable information about the morphology of the synthesized nanomaterials. Its principle is based on the interaction of an incident electron beam with the solid specimen, producing a variety of emissions from the specimen including secondary and backscattered electrons, as well as characteristic X-rays (Figure 3.6). The secondary electrons are inelastically scattered, low energy (< 50 eV), abundant and surface-specific, which renders them ideal for imaging topographic features (Reichelt, 2007).

The energy of the incident electron beam ranges from 0.2 to 40 keV. The beam is emitted from an electron gun (e.g. thermionic emitter, field emission gun) and is focused by passing through several condenser lenses. To control the position of the electron on the sample a deflector lens is used, allowing the scanning of its surface in a raster scan pattern. The signal from the resulting secondary electrons is collected, detected, amplified and used to control the intensity of a second electron beam utilized at the cathode ray tube screen, which is controlled simultaneously with the incident electron beam by the same scan generator. A map of the intensity of the secondary electron emission from the scanned area of the specimen is generated as variation in brightness, reflecting the surface morphology of the specimen.

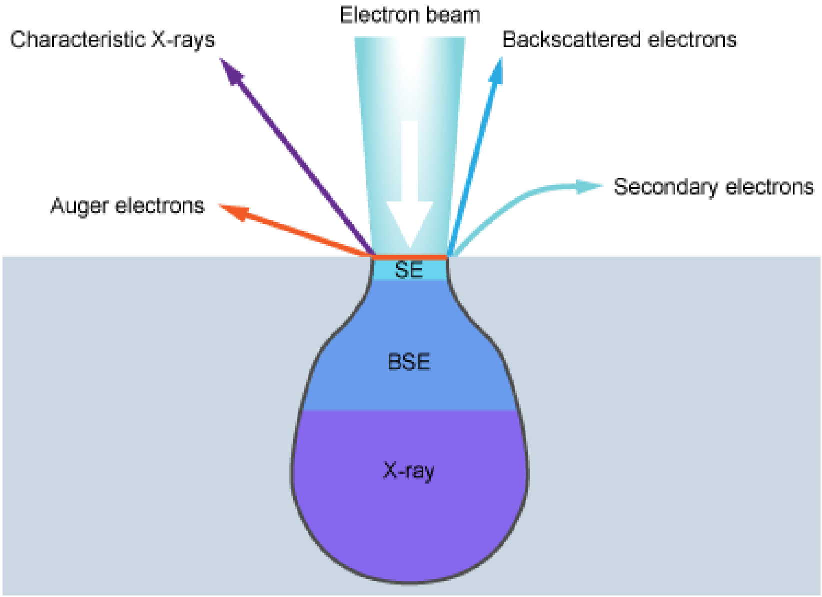

Figure 3. 6*. The interaction zone of electrons and specimen atoms below a specimen surface (AMMRF, 2019a).*

The spatial resolution is strongly dependent on the diameter (spot size) of the electron probe beam at the specimen surface. The effective diameter of the electron source is a key factor in determining the resolution of imaging, with field emission electron guns allowing high-resolution imaging (10 nm effective diameter) (Goldstein et al., 2003; Inkson, 2016). SEM was conducted by Verios 460L (ThermoFischer Scientific) and prior to imaging, the sample powders were first dispersed by ultra-sonication in isopropanol and then were drop-casted onto a gold-coated substrate.

3.3.5. Transmission Electron and High-Resolution Microscopy

TEM was deployed for the characterization of prepared nanomaterials with respect to the grain shape and size, crystallinity and chemical variation. Furthermore, HRTEM enabled the production of images at the atomic scale allowing the visualization of lattice arrangements within the crystalline structure. In TEM, a high-energy (e.g. 100 kV accelerating voltage) electron beam is transmitted through an ultra-thin (e.g. 150 nm) specimen. As a result of its diffraction by the crystalline material lattice, it propagates at different angles. Electromagnetic lenses are employed to focus the diffracted electrons, enabling an image creation on a fluorescent screen that can be recorded. The amplitude and phase of the electron wave can be changed during its transit through, thus both contribute to the image contrast (Inkson, 2016).

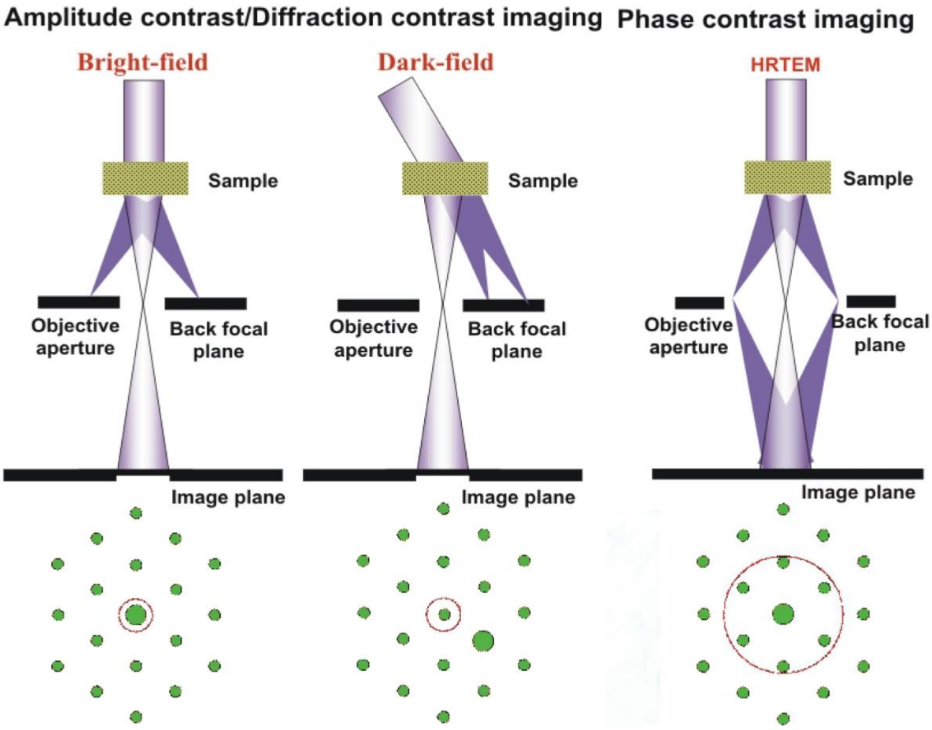

Figure 3. 7*. Different mechanisms of image formation in TEM: bright field, dark field and high-resolution imaging (AMMRF, 2019b).*

In general, three kinds of images can be obtained in TEM depending on the mechanism of image formation: bright field, dark field and high-resolution imaging (Figure 3.7). In bright-field imaging, an aperture is placed in the back focal plane of the objective lens, allowing only the electrons in the transmitted beam to pass and contribute to the resulting image. In dark-field imaging the objective aperture is positioned off-axis from the transmitted beam in order to allow only a diffracted beam to pass, producing in this way images that are particularly useful in examining the grain size in crystalline phases. In high-resolution imaging as previously stated, a large aperture is used, allowing both diffracted and directly transmitted beams to pass. The lattice fringes originate from the interference of the mutually phase-shifted beams from each lattice plane, with the direct beam thereby allowing the identification of lattice plane spacings (Ayache et al., 2010; Fultz and Howe, 2013). TEM was performed on JEM-1010 (JEOL) and HRTEM on the field emission JEM-2100F (JEOL). Before analysis, the sample powders were dispersed in isopropanol by ultra-sonication and subsequently were drop-casted onto a strong carbon-coated copper grid.

3.3.6. Selected Area Electron Diffraction

SAED is a crystallographic technique which was performed with TEM to identify the crystal structure and defects of prepared nanomaterials. It is known that elastically scattered electrons can change direction but do not change their wavelength. Constructive and destructive interference of coherent elastically scattered electrons can generate strong beams of transmitted electrons at specific angles to the incoming electrons, determined by the crystal structure and orientation of the material. The electron diffraction pattern is formed in the back focal plane of the objective lens and is magnified by the projector lenses onto the recording device (Sardela, 2014). In single crystals, atoms are arranged in an ordered lattice, and an electron passing through the single crystal will produce a pattern of spots from which the type of crystal structure (e.g. FCC, BCC), as well as the lattice parameter (i.e. the distance between adjacent (100) planes) can be determined. The formation of the diffraction pattern in polycrystals is analogous to that produced by a beam interacting with a series of single crystals of various orientations. Many spots very close together at various locations result in the formation of a series of concentric rings around the center beam spot, with each one corresponding to a different set of Miller indices (Figure 3.8).

Since in TEM the wavelength of electrons is very small and the Bragg’s angles are also quite small, the Bragg’s equation can be simplified and, therefore, the d-spacing between lattice planes of the crystalline material can be calculated from a SAED pattern using Equation 3.6 (Leng, 2013c; Williams and Carter, 2009):

$$d_{hkl}R = \lambda L \tag{3.6}$$

where L is the distance between the sample and the back focal plane (known as camera length used to record the image), d represents the inter-planar spading for a particular set of reflecting planes (hkl), R refers to the radius of a particular diffraction ring and λ is the wavelength of the electron beam (λL product is known as camera constant).

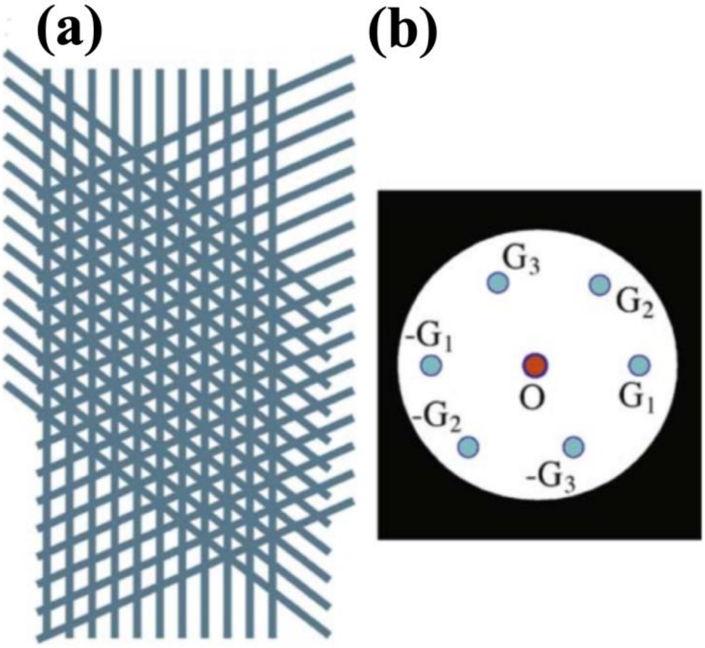

***Figure 3. 8**. a) Fringes in the image corresponding to b) an array of spots in the diffraction pattern, whose spacing may be inversely correlated to the lattice spacings (Williams and Carter, 2009).*

3.3.7. Energy Dispersive X-Ray Spectroscopy

EDS is a qualitative and quantitative technique that provides information about the surface chemical composition of a sample with elements having an atomic number Z>3. An electron beam is focused on the sample either in SEM or TEM and the electrons of the primary beam penetrate and interact with its atoms. An electron is inelastically scattered at an atom of the specimen, exciting a core electron. An electron from a higher orbital fills the empty states in a lower orbital. When the core level electron of high enough atomic number is knocked out, the energy difference is released in the form of photons in the X-ray regime, with characteristic energy that reflects the transition in the respective target atom (Figure 3.9). An energy dispersive detector is deployed for the analysis of X-rays. The displayed signal has the form of a spectrum or histogram of intensity (number of X-rays or X-ray count rate) versus X-ray energy. The energies of the characteristic X-rays allow the elements of the sample to be identified, while their concentrations can be quantified by the intensity of their peaks (Shindo and Oikawa, 2002).

In TEM the beam energies are much higher and the sample should be transparent as well as ultra-thin. The ionization volume in the path of the focused probe is much smaller than in SEM, leading to much better spatial resolution (in the order of nm) due to less scattering of the primary beam by the sample. Since the irradiated volume is much smaller, the number of counts is also smaller (Leng, 2013e). EDS was carried out on both JEM-2100F (JEOL) and Verios 460L (ThermoFischer Scientific) and the samples were prepared as described previously.

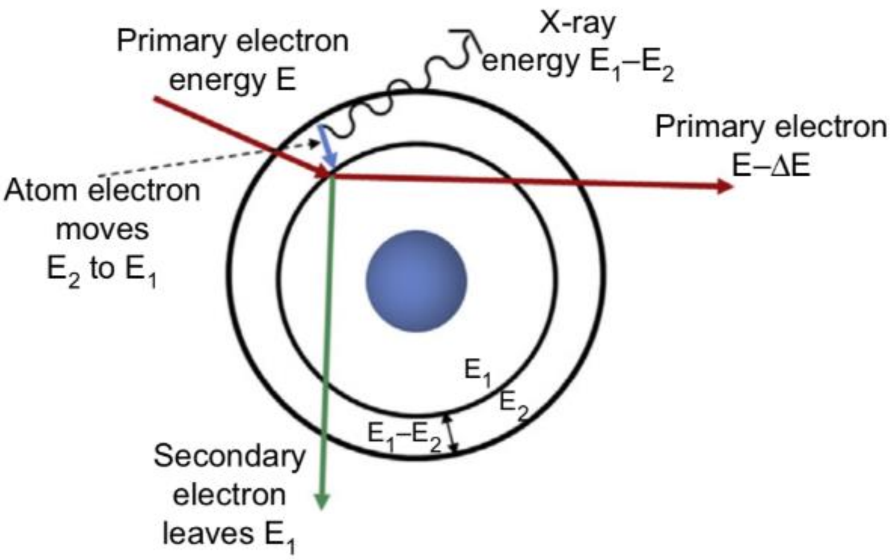

***Figure 3. 9**. Characteristic X-ray generation. An X-ray is generated by an electron that moves to fill the empty electron energy level vacated by the secondary electron (Inkson, 2016).*

3.3.8. Microwave Plasma Atomic Emission Spectroscopy

MPAES is an analytical technique based on atomic emission that was used for the quantitative elemental analysis of prepared samples. The principle of atomic emission relates to the determination of the wavelengths of photons discharged by atoms and molecules as they transit from a higher to a lower energy state (Figure 3.10). The energy transfer is inversely proportional to the wavelength as shown in Equation 3.7, where h is Planck’s constant and c is the velocity of light of the electromagnetic radiation. Hence the wavelength of emitted light is unique to each element as it depends on its electronic structure (Bings et al., 2013).

$$E = hc/\lambda \quad (3.7)$$

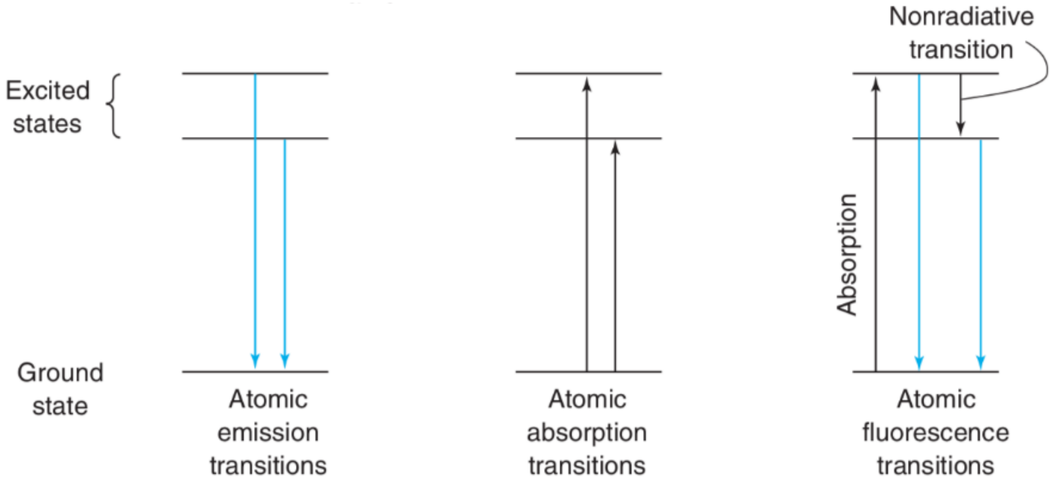

Figure 3. 10*. Principle of different types of atomic spectroscopy (Harris, 2010).*

The intensity of the energy emitted at the chosen wavelength (may be multiple for each element) is proportional to the concentration for a given element. In MPAES, microwave energy is utilized to produce a plasma discharge using N_2, which is subsequently heated to around 4700 °C by a quartz torch. An aerosol is created from the acid-digested liquid sample using a nebulizer and a spray chamber. The aerosol is then introduced to the hot plasma, so that it gets dried, decomposed and atomized. The electrons are promoted to the excited state and the emitted light, from electrons returning to the ground state, is separated into a spectrum with the intensity of each emission line being measured at the detector (Lajunen and Perämäki, 2004). MPAES was conducted on Agilent 4210 (Agilent) and prior to analysis, a certain amount of each powder was dissolved in a nitric acid solution overnight followed by dilution with deionized water.

3.3.9. Thermogravimetric Analysis

TG was utilized to measure the physical or chemical changes of the materials as a function of temperature (heating or cooling at a constant rate). The weight loss or gain is measured during the programmed-heating of the sample, allowing the quantitative measurement any weight change associated with transitions such as oxide phase formation, dehydration or decomposition, which may reflect on the thermodynamics and kinetics of the chemical reactions as well as the final products. The temperature usually reaches to 1200 °C under inert or reactive atmospheres (Le Parlouër, 2013; Leng, 2013b). In our work TG was performed on Pyris 1 analyzer (PelkinElmer), and the temperature was raised from 50 to 850 °C at a rate of 10 °C per min, purged by N_2 atmosphere. To prevent sample weight variation from affecting the peak shape and temperature, the weight of the samples was adjusted to 4-5 mg.

3.4. Mercury Sorption Studies

3.4.1. Mercury Testing Rig and Sampling System

A bench-scale experimental configuration was utilized for the conduction of Hg^0 sorption-desorption tests as well as for the assessment of the sorbents' regeneration capacity (Figure 3.11). Mercury sampling was carried-out by a modified Ontario-Hydro method (ASTM International, 2016a; Linak et al., 2011; López-Antón et al., 2012) and the quantitative analysis, which is discussed in the next section, was performed by CVAFS (Pandey et al., 2011).

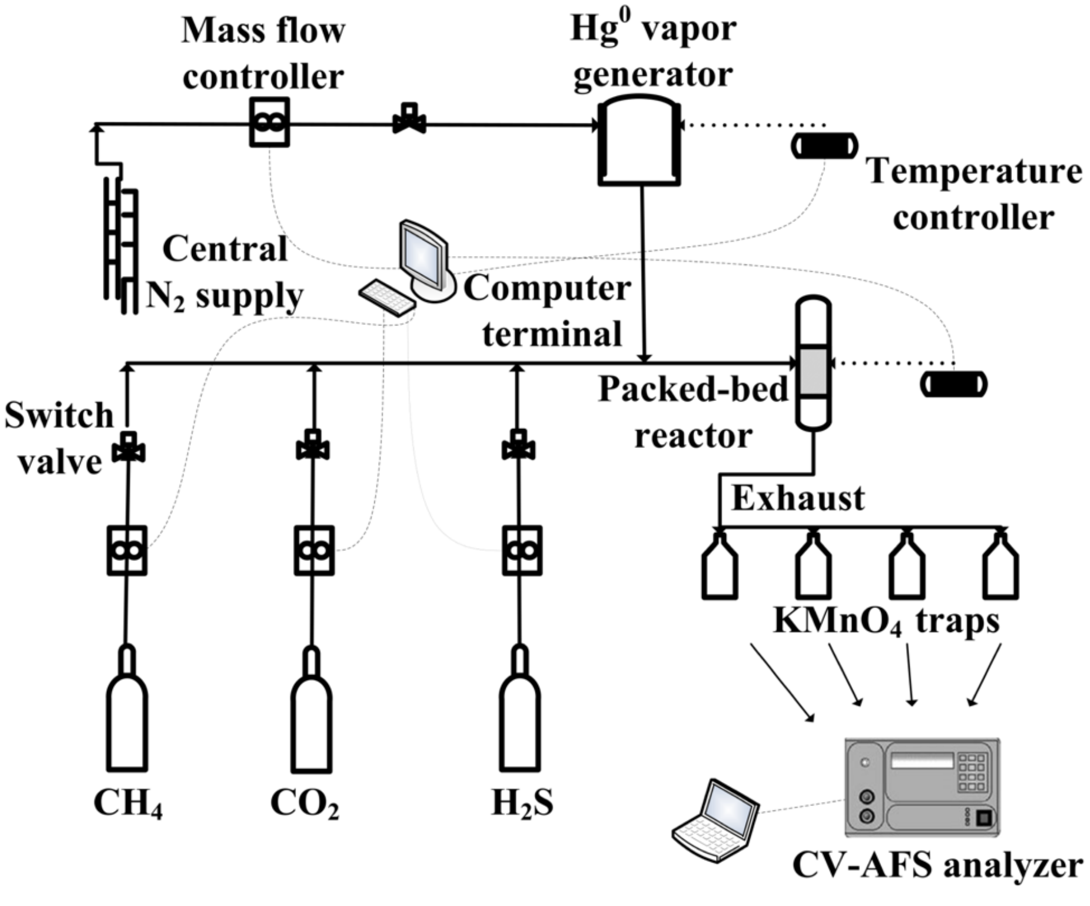

Figure 3. 11. *Schematic diagram of the experimental configuration for the conduction of* Hg^0 *removal tests as well as the sorbent regeneration assessment.*

Hg^0 vapor was produced by a vapor generator (Model 150 Dynacalibrator, VICI Metronics) that consisted of a permeation device (Dynacal, VICI Metronics) that produced a constant inlet mercury concentration (Hg^0_{in}) as a function of temperature at a constant total gas flow. The permeated Hg^0 vapor was delivered to a temperature-controlled, cylindrical quartz reactor (i.d.= 3 mm) with the use of dry N_2 as a carrier gas. Specifically for the evaluation of coated 3D-printed Ti-based support structure, a custom-made Teflon reactor was manufactured as shown in Figure 3.12. The gas mixture was adjusted by utilizing CH_4, CO_2 and H_2S gas cylinders (BOC), as well as a central supply of pure N_2 gas. In each test 50 mg of sorbent was supported on quartz wool within the glass reactor to prevent any material loss.

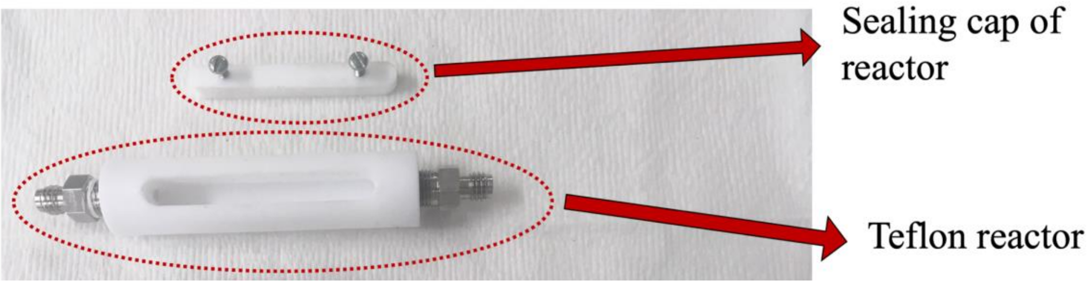

Figure 3. 12. *Custom-made Teflon reactor for the accommodation of the 3D-printed Ti-based support structure.*

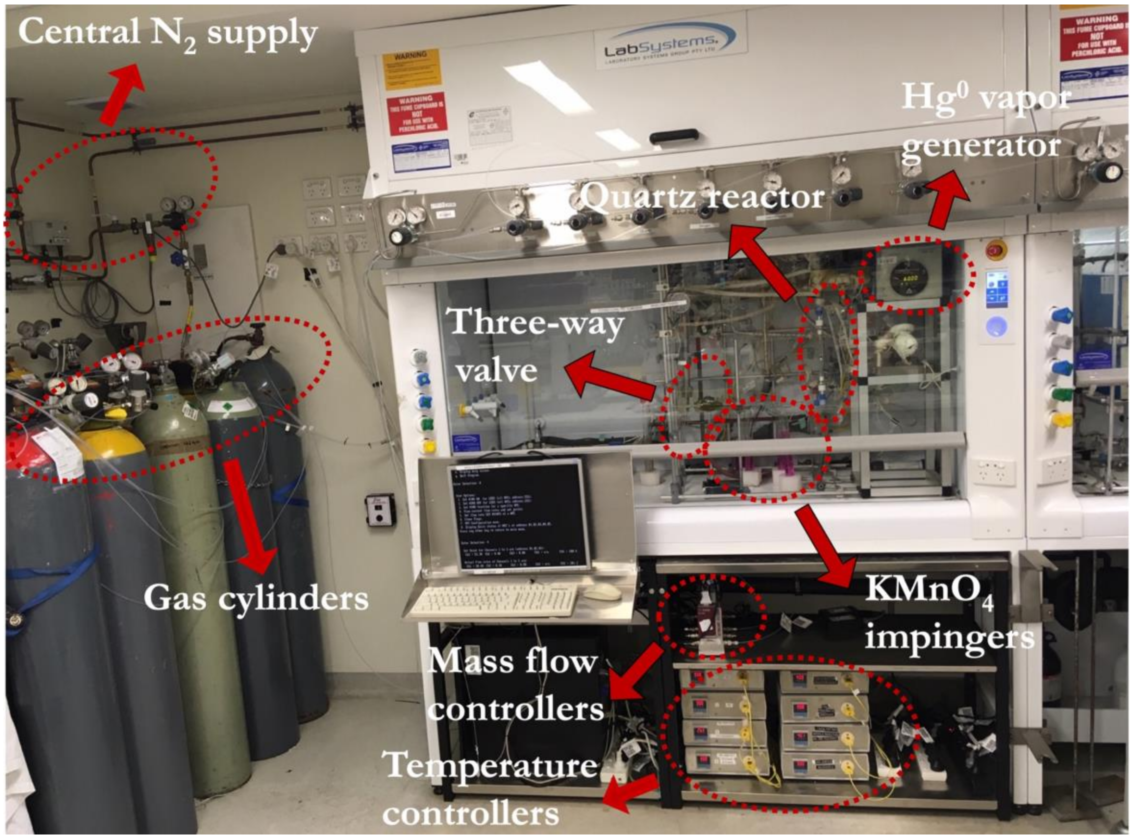

Figure 3. 13. *Photo of the mercury testing rig and sampling system.*

For the continuous sorption (Hg^0 breakthrough) tests, a three-way valve, including one inlet point from the exhaust of the reactor and two outlet points into two sets of impingers was used to switch between traps during mercury sampling at different time intervals

(Figure 3.13). In this way it was ensured that no mercury was lost during the sampling process. The traps, which consisted of acidified $KMnO_4$ solutions (20 mg·L^{-1} in 2 vol% concentrated H_2SO_4), absorbed Hg^0 vapor. The spent sorbents were digested in a reverse aqua-regia (HNO_3/HCl= 3:1) solution to solubilize the adhered mercury (ASTM International, 2017a; Leermakers et al., 2005) and enable its subsequent quantification with CVAFS. The Hg^0 removal efficiency was calculated by Equation 3.8:

$$Hg^0 \text{ removal efficiency (\%)} = (1 - Hg^0_{out}/Hg^0_{in}) \qquad (3.8)$$

3.4.2. Mercury Analysis by Cold Vapor Atomic Fluorescence Spectroscopy

The quantification of collected mercury was carried out by CVAFS (Figure 3.14). The working principle of AFS (ASTM International, 2014b) is based on the absorption of radiation of specific wavelengths by an atomic vapor, followed by the detection of deactivated states through emission in a direction typically orthogonal to the excitation source. As Figure 3.10 shows, both absorption and subsequent emission occur at wavelengths which are characteristic of the atomic species present (see Figure 3.10). In resonance fluorescence, which is the major form of fluorescence measured, the absorption and re-emission radiation is of the same wavelength. The intensity of the fluorescence radiation depends on the excitation source’s intensity, the atoms’ concentration, the quantitative efficiency of the process, the extent of any self-absorption in the atomiser, the analyte’s concentration in the sample as well as the instrument’s optical efficiency. Mercury has significant vapor pressure at room temperature and therefore it can be measured without additional energy (hence the characterization as cold vapor-AFS). Hg^0 vapor can be produced by reduction of the metal with the use of tin(II) chloride. Figure 3.15 depicts a continuous-flow vapor generator whose operation is described by Sánchez-Rodas et al. (2010). Variable-speed multichannel peristaltic pumps are employed to deliver the reductant, blank and sample solutions. An electronically-controlled switching valve alternates between the blank and sample solutions, and two of the liquid streams (either reductant-sample or reductant-blank) are butt-mixed in the sample valve where the reaction occurs. The streams and all gaseous products are continuously and rapidly pumped into a glass-liquid separator, from which the gaseous products are carried by argon through the AFS detector.

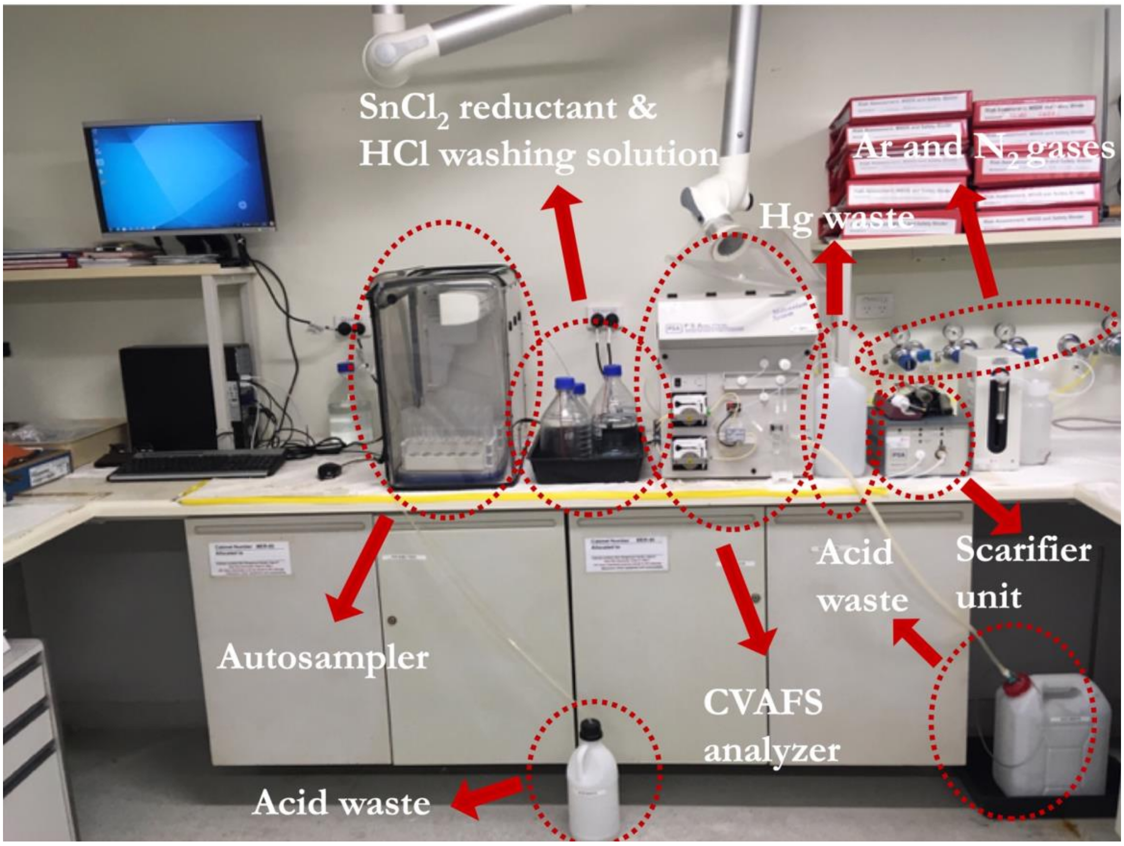

Figure 3. 14. *PS Analytical Millennium Merlin for the quantitative analysis of mercury collected in the impingers.*

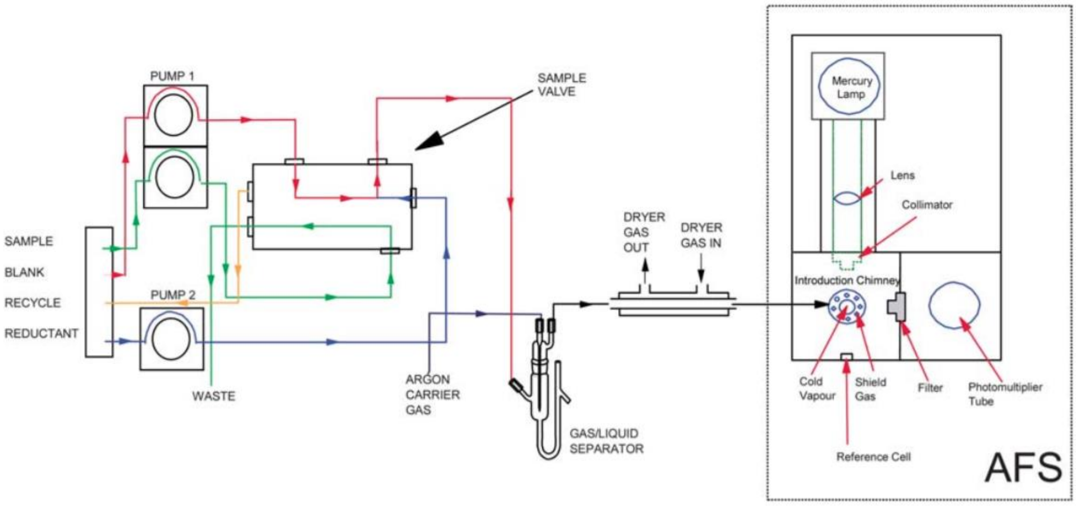

Figure 3. 15. *Schematic diagram of the continuous flow vapor generator and optical configuration of an AFS system for mercury analysis (Sánchez-Rodas et al., 2010).*

An ultra-violet mercury discharge lamp is used as excitation source and the fluorescence light is detected by a photo-multiplier tube light which is positioned perpendicular to the excitation source. A glass chimney, which is shielded with a high flow rate of argon, is used for the introduction of Hg^0 vapor into the optical path and a 253.7 nm interference filter is employed between the introduction chimney and the photo-multiplier tube to keep stray light away from the latter. CVAFS was conducted on Millennium Merlin (PS Analytical), with the use of $SnCl_2 \cdot 2H_2O$ (20 g L^{-1} in 45 vol% concentrated HCl) as reductant.

Chapter 4. α-MnO_2 Nanosorbents

4.1. Chapter Overview

In this chapter the Hg^0 vapor removal ability of α-MnO_2 NTs, NRs and NWs was evaluated in simulated natural gas mixtures. It was shown that NTs exhibited the superior efficiency (~100%) at the temperature range of interest (25-100 °C). The Hg^0 breakthrough (corresponding to 99.5% Hg^0 removal efficiency) at ambient conditions and Hg^0_{in}=870 $\mu g \cdot m^{-3}$, occurred after 48 h, reflecting a Hg^0 uptake of more than 10 $mg \cdot g^{-1}$ (1 wt%). Most importantly, the developed nanosorbent was repeatedly, sufficiently regenerated at the relatively low temperature of 250 °C in a series of seven successive sorption-desorption tests, maintaining its capacity to remove all incoming Hg^0_{in} in each cycle. Interestingly, kinetic studies showed that at least 85% of total adhered Hg^0 could be recovered within the first hour of a 3-h regeneration process. Moreover, the presence of CO_2 and H_2S, did not affect its activity. The thermogravimetric analysis indicated significantly higher dehydration for NTs due to the loss of bound water inside its tunnels, likely suggesting the presence of abundant surface adsorbed oxygen species which are believed to facilitate Hg^0 adsorption. This was also confirmed by X-ray spectroscopy, possibly explaining the enhanced activity of NTs.

---

* Part of the work presented in this chapter has been published in:
Chalkidis, A.*, Jampaiah, D., Hartley, P.G., Sabri, Y.M., Bhargava, S.K. "Regenerable α-*MnO_2 *Nanotubes for Elemental Mercury Removal from Natural Gas".* ***Fuel Processing Technology*** *2019, 193, 317-327 (doi.org/10.1016/j.fuproc.2019.05.034)*

4.2. Background and Rationale

As discussed thoroughly in the second chapter the Hg^0 sorbents developed for the gas processing industry need to be efficient at ambient temperatures, effective at high-mercury concentrations and often reducing gas streams, as well as regenerable at relatively low temperatures. The latter is a desired property as it significantly reduces the cost and landfill of toxic waste, especially when large amounts of mercury are treated. In contrast to sorbents used for mercury removal from flue gases of coal-fired power stations, the tolerance of sorbents in gas processing industry is much smaller, due to the extremely low mercury concentration specifications mentioned earlier. In several studies, mostly related to coal-fired flue gases (Liu et al., 2010; Xu et al., 2018b; Yang et al.,

2007) it has been reported that the Hg^0 removal activity of a sorbent is related to its size, shape, specific surface area, pore volume and pore size distribution. Metal oxides have been extensively studied because they possess high adsorption capacity, strong metal ion affinity and the ability to remove metals in trace concentrations with the possibility of recovery and reuse (Reddy et al., 2012). Among them, manganese oxides (Xu et al., 2017a) are low cost, environmentally friendly and have been tested as sorbents/catalysts for the elimination of various gaseous pollutants including Hg^0 vapor (Li et al., 2018a; Zhang et al., 2015; Zhang et al., 2017a). A particular crystal phase of MnO_2, α-MnO_2 (Li et al., 2017a; Tompsett et al., 2014) consists of 2x2 (4.6x4.6 A) tunnels constructed from double chains of octahedra [MnO_6] with a variety of stabilizing cations (e.g. K^+, Ba^{2+}) being situated inside its tunnels (see Figure 4.2b) (Liu et al., 2019b). Its distinctive properties related to the tunnel cavity, moderately acidic sites and easy release of lattice oxygen have rendered it promising for separation and catalytic applications (Rong et al., 2018).

Xu et al. (Xu et al., 2015) synthesized three different crystallographic phases (α-, β- and γ) of MnO_2 and investigated their Hg^0 vapor removal efficiency. At 150 °C, α-MnO_2 manifested the highest capacity, which was ascribed to its larger surface area and oxidizability. The desorption tests indicated that the interaction forces between the mercury and manganese sites were stronger in the alpha-phase than in the other two phases. The morphological differentiation effect of α-MnO_2 has already been investigated on catalytic applications such as the combustion of dimethyl ether, oxidation of toluene and phenol as well as the decomposition of ozone (Cheng et al., 2017; Jia et al., 2016; Li et al., 2016b; Wang et al., 2015). However, there is no related study examining the abatement of Hg^0 vapor at ambient temperatures, particularly in the absence of oxygen in the gas phase (which has been reported to enhance removal process) (Granite et al., 2000).

The aim of this chapter was to elucidate the morphology effect of α-MnO_2 and at the same time examine its Hg^0 removal capacity as well as its regeneration capacity at conditions pertaining to natural gas processing operations. α-MnO_2 NTs, NRs and NWs were tested for Hg^0 removal in simulated natural gas conditions, with the best performing nanosorbent being further subjected to Hg^0 desorption tests to investigate its regeneration potential. A deeper insight of the causes leading to the activity variations was made possible by the thorough materials characterization.

4.3. Characterization Results

4.3.1. SEM Characterization

The morphology of the synthesized nanostructures samples was first investigated by SEM (Figure 4.1). The lengths and diameters of the nanoparticles are summarized in Table 4.1. All three nanostructures possessed 1D morphologies. The morphology of the first sample (Figures 4.1a and 4.1b) constituted of nanorods with lengths and diameters smaller than 1 μm and 50 nm, respectively. Figure 4.1a illustrates a nanorod-assembled hollow urchin structure. At a higher magnification (Figure 4.1b) the nanostructure's rod-like shape is evident.

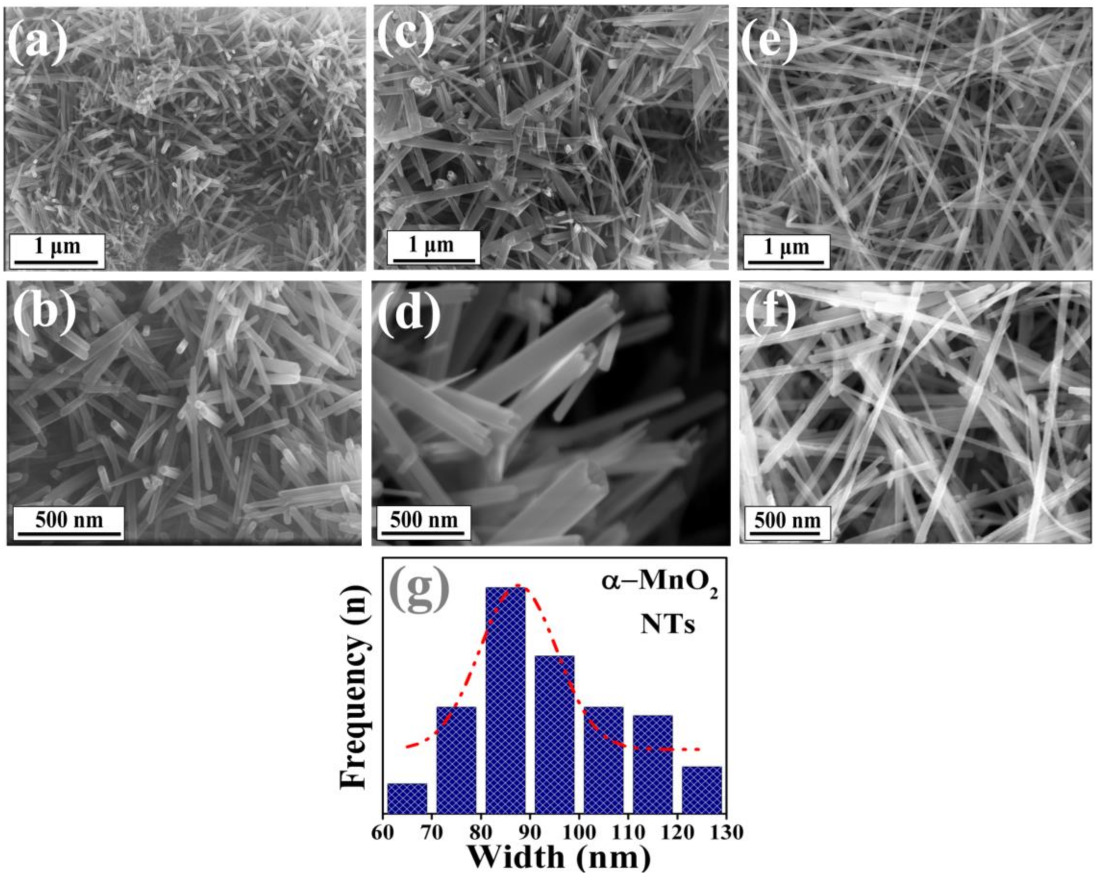

__Figure 4. 1__. SEM images of α-MnO$_2$ NTs (a-b), NRs (c-d) and NWs (e-f). g) Average outer diameter (width) of α-MnO$_2$ NTs.

The second sample (Figures 4.1c and 4.1d) consisted of tetragonal nanotubes with lengths and diameters smaller than 5 μm and 100 nm, respectively. The higher magnification SEM image in Figure 4.1d clearly depicts its tubular-like nanostructure, possessing an average inner diameter at the range of 50 nm. The third sample (Figures 4.1e and 4.1f) was composed of nanowires with lengths over 5 μm and diameters less than 100 nm. The statistical analysis of the dimensions of the tetragonal NTs (most active material), shows an average outer diameter (width) of about 90 nm (Fig. 4.1g).

4.3.2. XRD Analysis

The XRD patterns of α-MnO$_2$ NTs, NRs and NWs, as well as their structural representation, are depicted in Figures 4.2a and 4.2b. The XRD diffractograms of all three nanosorbents corresponded to the body-centered tetragonal α-MnO$_2$ (ICDD-PDF 44-0141, space group I4/m, a=b=9.78 Å, c=2.86 Å) (Jampaiah et al., 2017).

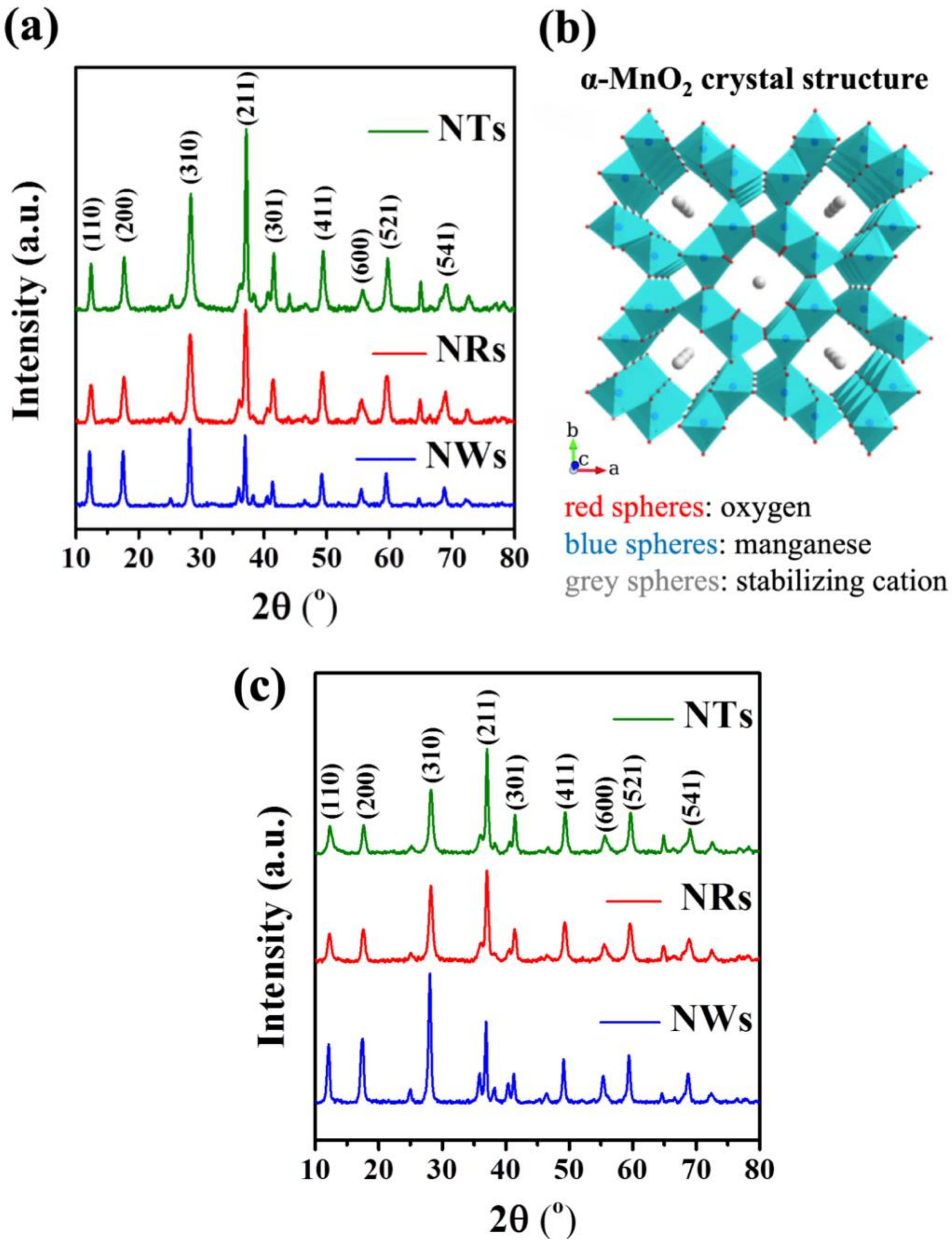

Figure 4. 2. *(a) XRD patterns of fresh α-MnO$_2$ NTs, NRs, and NWs, (b) α-MnO$_2$ 2x2 crystal structure consisting of [MnO$_6$] octahedra, and c) X-ray diffractograms of spent α-MnO$_2$ NTs, NRs, and NWs (Set I).*

The four strongest peaks were observed at 37.5°, 28.8°, 18.1° and 12.8°, and corresponded to the (211), (310), (200) and (110) crystal planes. The absence of any impurities implied the formation of pure phase α-MnO_2 in all cases. Figure 4.2c displays the XRD diffractograms of the three nanosorbents after having been subjected to 14-h sorption experiments (Set I) (discussed later). As it can be observed no change in their nanostructure occurred as a result of their interaction with Hg^0 vapor at the temperature range of 25-100 °C under 75% CH_4/N_2 atmosphere.

4.3.3. TEM, HRTEM and SAED Investigation

The TEM images of α-MnO_2 NTs, NRs and NWs (Figures 4.3a, 4.3d and 4.3g) confirmed the observations made with SEM. Additionally, the obtained data from HRTEM as well as SAED characterization, provided additional information in regard to their crystal structure.

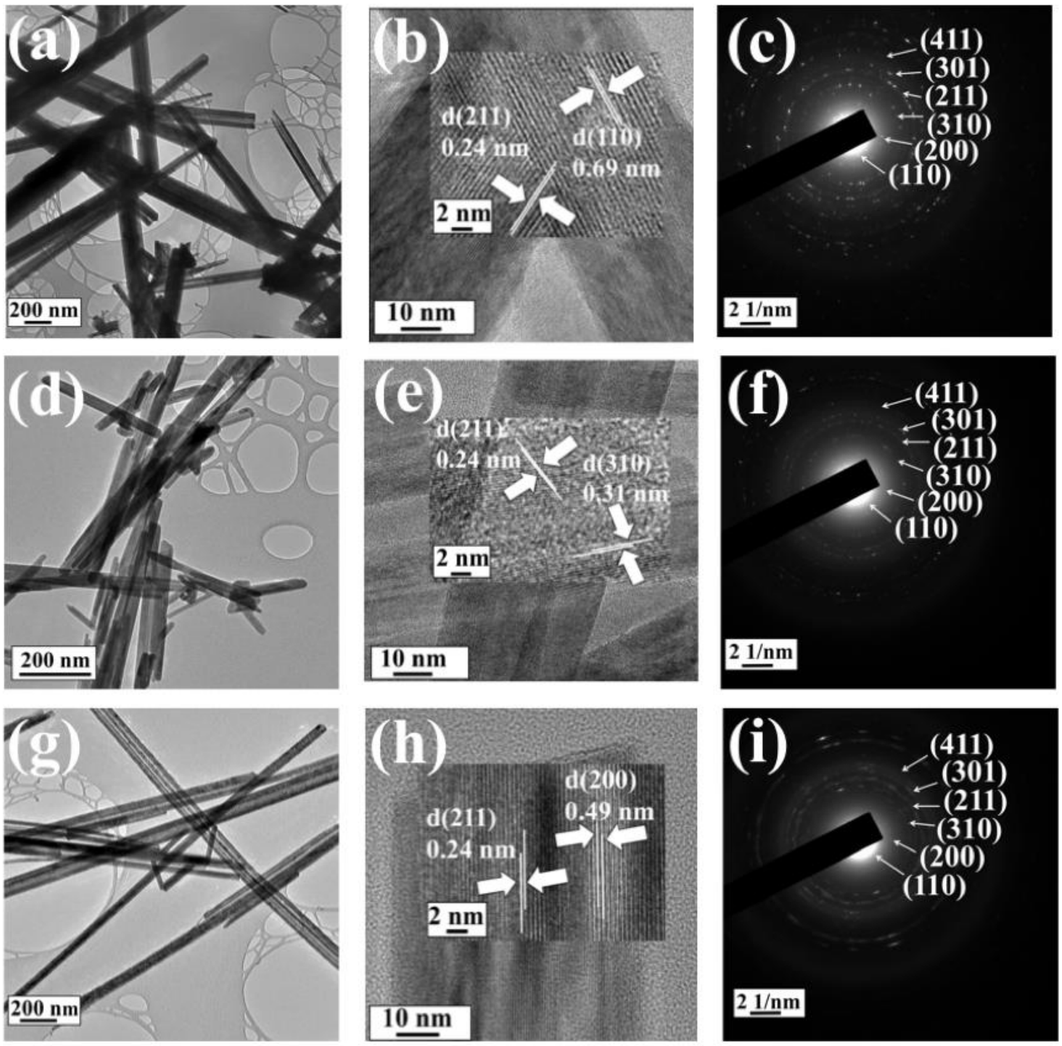

***Figure 4. 3**. TEM (a, d, g), HRTEM (b, e, h) and SAED (c, f, i) images of α-MnO_2 NTs (a-c), NRs (d-f) and NWs (g-i).*

Figure 4.3b displays the exposed crystal planes (110) and (211) for NTs. NRs exposed the (310) and (211) crystal facets (Figure 4.3e), whereas the HR-TEM imaging of NWs (Fig. 4.3h) revealed the (200) and (211) planes. The recorded selected area diffraction patterns (Figures 4.3c, 4.3f and 4.3i) for all three morphologies displayed the (110), (200), (310), (211), (301) and (411) crystal planes that corresponded to lattice spacings of 0.69, 0.49, 0.31, 0.24, 0.21 and 0.18 nm, respectively. Low index surfaces such the (110) plane exposed by NTs, manifest a tendency to have favorable surface coordination for catalytic professes. In their theoretical study (Tompsett et al., 2014) claimed that the enhanced catalytic performance of α-MnO_2 stems from the facile oxygen vacancy formation at its surfaces.

4.3.4. N_2 Adsorption-Desorption Isotherms

The N_2 adsorption-desorption isotherms of α-MnO_2 NTs, NRs, and NWs are shown in Figure 4.4a, while their BET specific surface areas are presented in Table 4.1. All N_2 isotherms corresponded to a Type II isotherm (Thommes et al., 2015) indicating nonporous/macroporous materials. NRs possessed the largest surface area (43.1 $m^2 \cdot g^{-1}$), followed by NWs (40.1 $m^2 \cdot g^{-1}$) and NTs (33.3 $m^2 \cdot g^{-1}$).

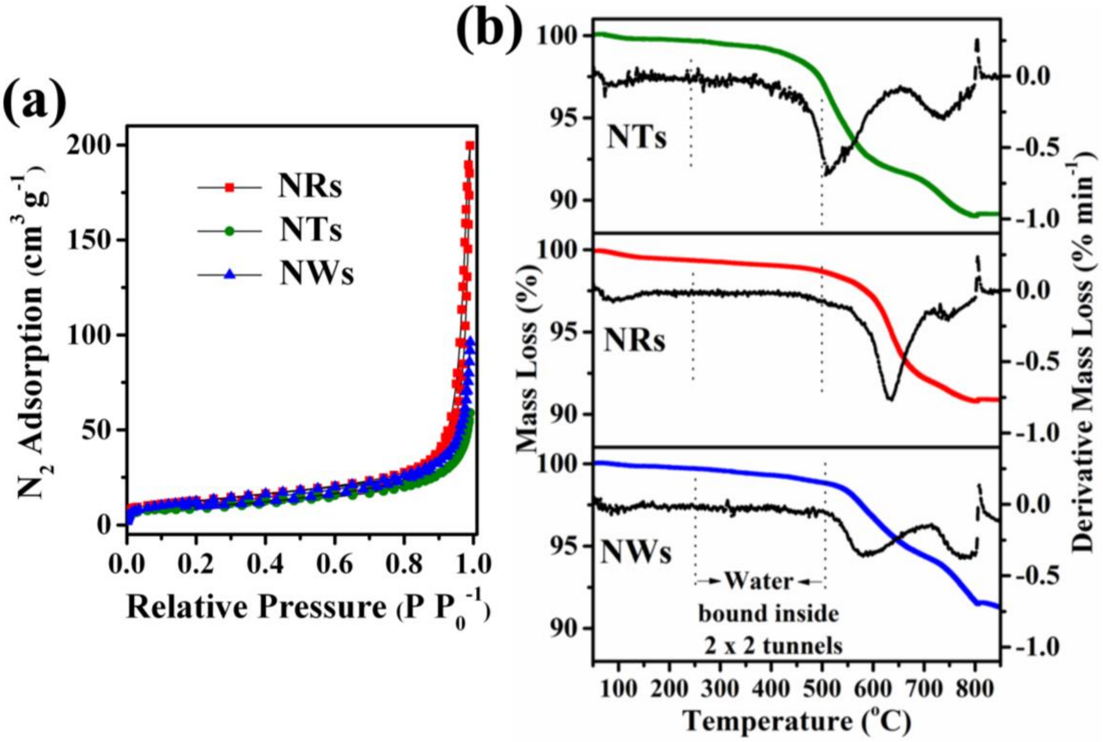

Figure 4. 4. a) N_2 adsorption-desorption isotherms and, b) thermogravimetric profiles of α-MnO_2 NTs, NRs and NWs.

Table 4. 1. *Physical characteristics of α-MnO_2 NTs, NRs and NWs.*

Sample	***Length (μm)***	***Diameter (nm)***	***BET surface area ($m^2 \cdot g^{-1}$)***
NTs	<5	<100	33.3
NRs	<1	<50	43.1
NWs	>5	<100	40.1

4.3.5. TG Profiles

The thermogravimetric profiles of α-MnO_2 NTs, NRs, and NWs are illustrated in Figure 4.4b. According to Gao et al. (Gao et al., 2008) the mass loss can be primarily divided into two segments, which concern the process of dehydration and oxygen evolution, respectively. The dehydration occurred at the temperature range of 50 to 500 °C and included the evaporation of surface-related water (50-250 °C) as well as the bound-water inside the (2x2) tunnels of α-MnO_2 nanostructures (250-500 °C). As shown in Table 4.2, the latter corresponded to a significantly higher mass loss (~2.9%) for NTs in comparison to NRs and NWs. Overall, the dehydration of NTs corresponded to around 3.3% mass loss, compared to 1.3% and 1.2% for NRs and NWs, respectively. This result revealed that the amount of surface oxygen species within NTs was the greatest and may well be related to its Hg^0 removal activity as explained in the next section.

Table 4. 2. *Mass loss due to dehydration of α-MnO_2 NTs, NRs and NWs.*

Sample	***Mass loss (%) (50-250 °C)***	***Mass loss (%) (250-500 °C)***	***Total mass loss (%) (50-500 °C)***
NTs	0.4	2.9	3.3
NRs	0.7	0.6	1.3
NWs	0.3	0.9	1.2

4.3.6. XPS Analysis

XPS was employed to obtain a deeper insight into the surface composition and oxidation state of the three α-MnO_2 morphologies. The Mn 3s, Mn 2p and O 1s XPS spectra of NTs, NRs, and NWs are depicted in Figures 4.5a, 4.5b and 4.5c, respectively. Moreover, the composition of surface oxygen species is presented in Table 4.3.

The magnitude of peak splitting in the Mn 3s XPS spectrum is diagnostic of the manganese oxidation state. This was less or equal to 4.9 eV for all three morphologies (Figure 4.5a), confirming the formation of MnO_2 in all cases. The Mn $2p_{3/2}$ XPS spectra (Figure 4.5b) of all samples displayed a narrow peak maximum at ~642 eV, possessing an identifiable shape, which is also characteristic of MnO_2 and suggests the presence of Mn^{4+} (Biesinger et al., 2011).

The O 1s XPS spectra (Figure 4.5c) of all three nanosorbents comprised of three peaks representing different types of oxygen species (Jampaiah et al., 2016; Jampaiah et al., 2015b). At a lower binding energy ~529.5 eV, the peak was ascribed to the surface lattice oxygen (O_a) of metal oxides. The peak at around 531.5 eV represented the surface adsorbed oxygen and/or hydroxyl groups (O_b), while that one at roughly 533.5 eV was identical to oxygen species from water and/or carbonates (O_c).

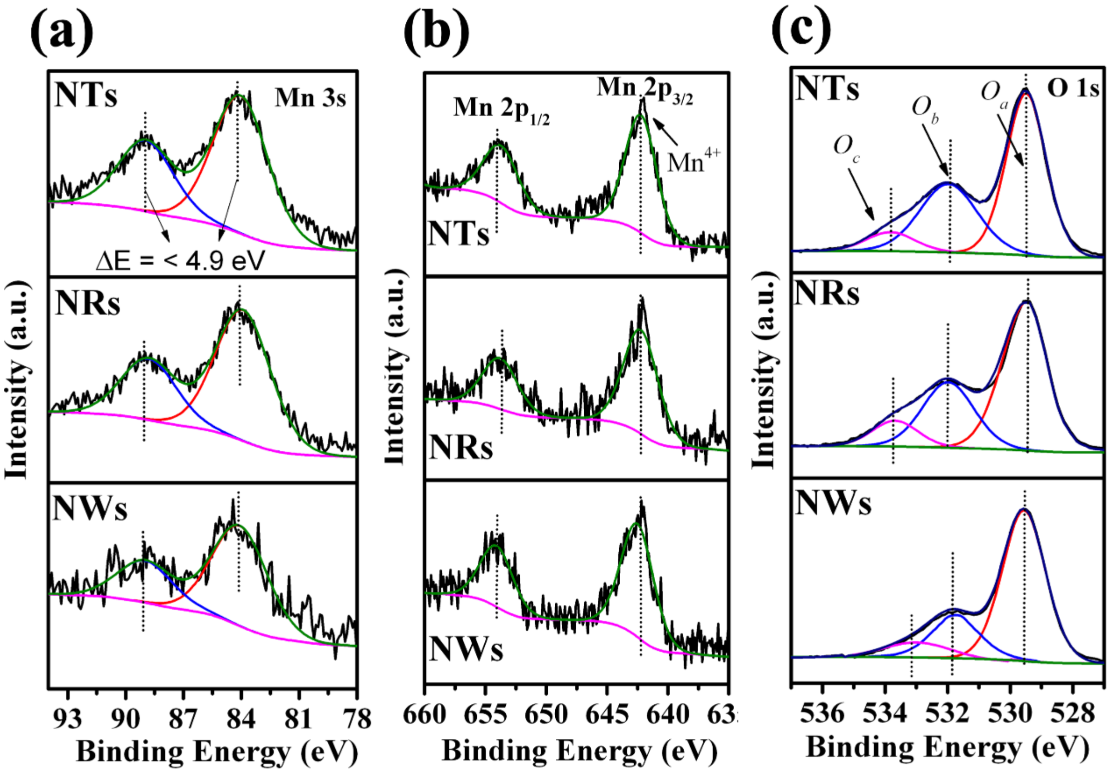

Figure 4. 5*. (a) Mn 3s, (b) Mn 2p and (c) O 1s XPS spectra of α-MnO_2 NTs, NRs and NWs.*

Table 4. 3*. Composition of oxygen species on the surface of α-MnO_2 NTs, NRs and NWs.*

Sample	***O_a (%)***	***O_b (%)***	***O_c (%)***	***O_b + O_c (%)***
NTs	51.1	34.4	14.5	48.9
NRs	55.7	29.7	14.6	44.3
NWs	57.6	23.7	18.7	42.4

As displayed in Table 4.3, the XPS quantitative analysis showed that NTs possessed the highest amount of surface absorbed oxygen (34.4 %) followed by NRs (29.7 %) and NWs (23.7 %). For NTs, the sum of O_b and O_c species accounted for 48.9% of surface oxygen species, while for NRs and NWs this was 44.3% and 42.4%, respectively. This agrees with TG findings and indicates the availability of more surface adsorbed oxygen species for NTs. In fact, the abundance of surface oxygen species has been repeatedly reported to improve Hg^0 removal efficiency, by improving the mobility of surface lattice oxygen and providing the active sites for Hg^0 adsorption on the surface of sorbent/catalyst (Jampaiah et al., 2016; Jampaiah et al., 2015b).

4.4. Hg^0 Removal and Sorbent Regeneration Capacity

4.4.1. Experimental Sequence

The mercury sorption and sorbent regeneration tests were carried out in five steps as displayed in Table 4.4. First the Hg^0 removal efficiency of α-MnO_2 NTs, NRs, and NWs was assessed at three different temperatures (25, 50 & 100 °C) in fixed time periods (14 h) under 75% CH_4/N_2 atmosphere and Hg^0_{in}=290 $\mu g \cdot m^{-3}$. Subsequently, the sorption kinetics was evaluated by obtaining the Hg^0 breakthrough curves at 25°C, 75% CH_4/N_2 atmosphere and Hg^0_{in}=870 $\mu g \cdot m^{-3}$.

Table 4. 4*. Summary of experimental sets and operating conditions with respect to adsorption (ads.) and desorption (des.) processes.*

Set	***Nanosorbent***	***Gas components***	***Operating conditions***
Set I	50 mg α-MnO_2 NTs, NRs & NWs	Ads.: Hg^0 + 75% CH_4/N_2	Ads.: T=25-100 °C, Hg^0_{in}=290 $\mu g \cdot m^{-3}$, t=14 h, GHSV=1.1x10^5 h^{-1}
Set II	50 mg α-MnO_2 NTs, NRs & NWs	Ads.: Hg^0 + 75% CH_4/N_2	Ads.: T=25 °C, Hg^0_{in} =870 $\mu g \cdot m^{-3}$, GHSV=1.1x10^5 h^{-1}
Set III	50 mg α-MnO_2 NTs	Ads.: Hg^0 + 75% CH_4/N_2, Des.: N_2	Ads.: T=25 °C, t=14 h, Hg^0_{in} =870 $\mu g \cdot m^{-3}$, GHSV=1.1x10^5 h^{-1}, Des.: T=250 °C (heat. rate=10 °C·min^{-1}), t=3 h, GHSV=1.1x10^5 h^{-1}
Set IV	50 mg α-MnO_2 NTs	Ads.: Hg^0 + 75% CH_4/N_2, Des.: N_2	Ads.: T= 25 °C, t=14 h, Hg^0_{in}=870 $\mu g \cdot m^{-3}$, GHSV=1.1x10^5 h^{-1}, Des.: T=250 °C (heat. rate=10 °C·min^{-1}), t=90 min, GHSV=1.1x10^5 h^{-1}
Set V	50 mg α-MnO_2 NTs	Ads.: Hg^0 + 75% CH_4 + 12.5% CO_2 + 40 ppm H_2S	Ads.: T=25 °C, t=14 h, Hg^0_{in}=870 $\mu g \cdot m^{-3}$, GHSV=1.1x10^5 h^{-1}

The Hg^0_{in} was almost tripled to get useful results in a short time window. The next experimental set concerned the identification of the optimal regeneration time of the superior sorbent. The desorption tests were conducted at 250 °C under the flow of dry N_2 and lasted 3 h. Once the optimal recovery time was determined, a series of seven successive sorption-desorption cycles was conducted to assess its regenerability potential.

The sorption experiments were conducted in CH_4/N_2 atmosphere, Hg^0_{in}=870 μg·m^{-3}, and lasted 14 h, while the desorption tests were performed at the same conditions as previously. Finally, 12.5% CO_2 and 40 ppm H_2S were introduced to the gas mixture to evaluate their impact on the activity of the superior sorbent at room temperature

4.4.2. Hg^0 Removal Efficiency: Temperature Effect and Kinetics

Figure 4.6a depicts the outcome of Set I. All three nanosorbents manifested excellent removal capacity (>99%) at 25 °C, capturing almost all Hg^0 vapor passing through the reactor bed. When the temperature was raised to 50 °C, their performance was maintained at the same high level. However, their activity differentiation was rendered obvious at 100 °C, where the removal efficiency of both NRs and NWs was reduced to ~90%, whereas that of NTs remained at ~99%.

The results of Set II are displayed in Figures 4.6b and 4.6c. Figure 4.6b displays the Hg^0 breakthrough curve of NRs, NWs, and NTs, whilst Fig. 6c depicts their mercury uptake capacities as a function of the mass of Hg^0 throughput and time. The Hg^0 breakthrough was defined as the time when the Hg^0 removal efficiency dropped below 99.5% (0.5% tolerance) (Abai et al., 2015). This corresponds to a value of Hg^0_{out}/Hg^0_{in}=0.005 in the left y-axis of Figure 4.6b. For NRs this point was observed at around 6 h. However, for NWs the Hg^0 removal efficiency was already around 95% (Hg^0_{out}/Hg^0_{in}=0.05) within 1 h of the beginning of the test and remained at about the same level even after 5 h. After almost 24 h, the removal efficiency of NRs had been reduced to slightly over 90% (Hg^0_{out}/Hg^0_{in}=0.1), while that of NWs was less than 90%. Interestingly, NTs far outreached both NRs and NWs. The Hg^0 breakthrough was observed to occur after 48 h, corresponding to an uptake of over 10 mg Hg^0 per gram of sorbent (1 wt.%). By the end of the third day its removal efficiency had dropped to 96.5% (Hg^0_{out}/Hg^0_{in}=0.035).

It is obvious in Fig. 4.6b that the experiments were conducted up until the Hg^0 removal efficiency dropped to about 90-95%, therefore limiting the information regarding the saturation. This is because the focus of the study was to determine the Hg^0 breakthrough at a very small tolerance (0.5%), which is representative of the requirements of the commercial catalyst/sorbents utilized during natural gas demercuration. As explained in Chapter 2, in gas cleaning operations the target efficiency may be as high as 99.9% and when it drops below 99% the sorbent may need to be replaced (Porcheron et al., 2015). Given this, the Hg^0 breakthrough experiments were considered as complete soon after reaching the breakthrough point, and therefore no further information was obtained about the saturation of nanosorbents.

Taking the above into consideration, it must be underlined that the linear-like curves presented in Figure 4.6c indicate zero-order kinetics (Wdowin et al., 2014) and represent only a part (initial stage) of the reaction's kinetics (Khunphonoi et al., 2015). The mercury uptake capacity may be described by an equation of the type: Q=k*t, which can be determined through the linear fitting of data. The curve with the biggest slope corresponds to the sorbent with the highest Hg^0 uptake rate.

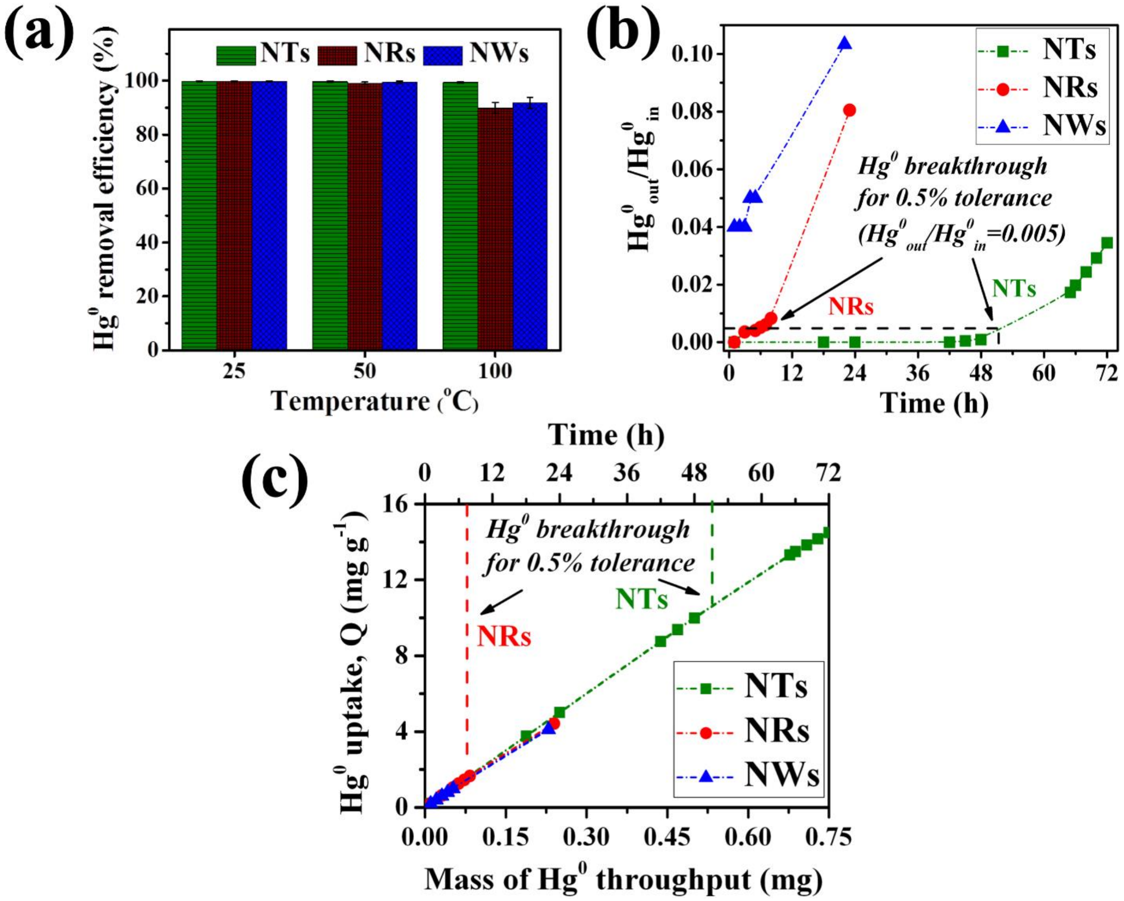

***Figure 4. 6**. a) Set I: Hg^0 vapor removal efficiency of α-MnO_2 NTs, NRs, and NWs at 25-100 °C and 14-h period. b) Set II: Hg^0 breakthrough curves of NTs, NRs and NWs at room temperature and, c) their mercury uptakes as a function of mass of Hg^0 throughput and time.*

4.4.3. Regeneration of α-MnO_2 NTs

In Set III the Hg^0 desorption kinetics of α-MnO_2 NTs, which was previously identified as the superior sorbent, was studied after selecting the regeneration temperature of 250 °C that closely matches the industrial practice (e.g. molecular sieves) (Yan, 1994b). In a series of five successive regeneration cycles the released Hg^0 vapor content was sampled at 1-h intervals with the aim of determining whether the longer regeneration periods resulted in a significantly higher amount of desorbed Hg^0. As Figure 4.7a shows, at least 85% of total desorbed Hg^0 was collected within the first hour of the regeneration test, while the second hour accounted for most of the remaining adhered Hg^0. The amount obtained in the third hour was rather insignificant. Therefore, 90 min was selected as the optimal regeneration period for the next experimental set.

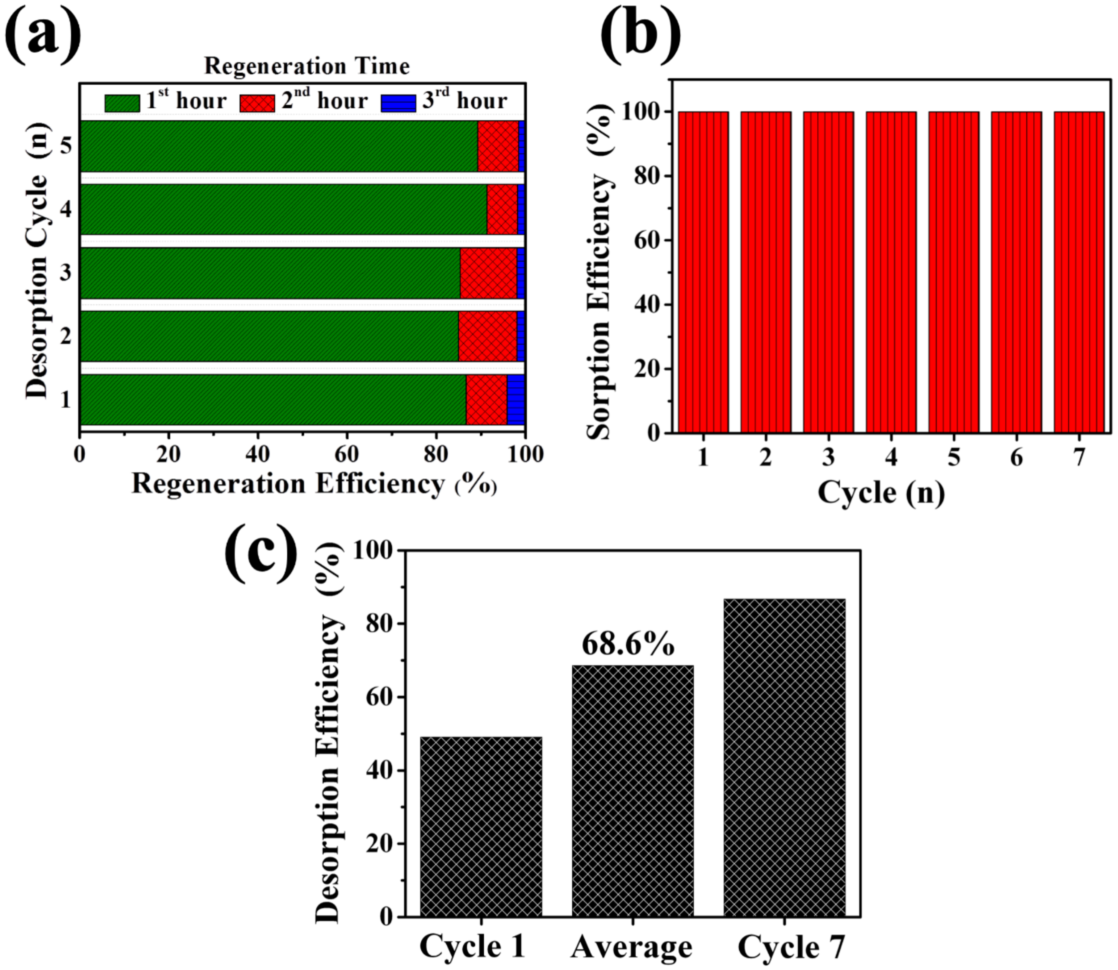

***Figure 4. 7**. (a) Set III: Conduction of a series of five successive Hg^0 regeneration cycles under dry N$_2$ at 250 °C to identify the optimum regeneration time of α-MnO$_2$ NTs. b) Set IV: Implementation of a series of seven successive Hg^0 sorption and, c) desorption cycles to evaluate the regeneration potential of α-MnO$_2$ NTs over the previously identified optimum regeneration time.*

Set IV as previously explained, comprised of a series of seven successive sorption-desorption cycles. The sorption tests were conducted at the same conditions as the Hg^0 breakthrough tests, and the desorption conditions were maintained as previously. Figure 4.7b shows that the Hg^0 removal efficiency of NTs remained at the highest level (~100%) in all cycles with an average ~69% (Figure 4.8c) of adhered Hg^0 in each cycle being desorbed. With the number of cycles and the increasing content of incoming Hg$^0_{in}$ the amount of desorbed Hg^0 increased moderately. However, it is evident that complete regeneration could not be achieved at such a low temperature. The aim of this study was to show that the developed nanosorbent could be sufficiently regenerated at a relatively low temperature, maintaining at the same time its capacity to tolerate a relatively high concentration of Hg^0_{in} vapor (870 $\mu g \cdot m^{-3}$). Indeed, in each cycle the amount of desorbed Hg^0 was high enough to facilitate the sorption of all incoming Hg^0 in the subsequent cycle, at least for the seven-cycle experiment conducted. This suggests that the material was not saturated during the consecutive 14-h sorption experiments. If the regeneration temperature was raised above 250 °C the Hg^0 desorption efficiency would be higher. Hence, given the relatively high Hg^0_{in}, the regeneration potential of NTs may be assessed as promising.

4.4.4. CO_2 and H_2S influence on α-MnO_2 Nanotubes Activity

It was explained in Chapter 2 that natural gas reserves containing acid gases (e.g. CO_2, H_2S) are characterized as sour and their exploitation requires costly processing operations (Goodwin et al., 2015). According to O'Rear et al. (2016a), mercury has been experienced to occur in hydrocarbon fluids well into commercial development, after processes and equipment are in place to handle production, thereby resulting in significant cost overruns. With the aim of simulating a sour gas stream in Set V, first 12.5% CO_2 and then 40 ppm H_2S were introduced into the gas mixture at room temperature in order to evaluate their influence on α-MnO_2 NTs activity over fixed time periods (14 h). Table 4.5 shows that their impact was rather insignificant. Actually, Wang et al. (2018) explained that the presence of H_2S could promote Hg^0 capture by forming active sulfate species that lead to the formation of HgS and HgO on the surface of MnO_2 sorbent, thus enhancing Hg^0 removal efficiency. In this study, however, instead of investigating in detail the effect of acid gases on Hg^0 removal mechanism, the focus was rather placed on confirming that there was no adverse effect due to their presence.

Table 4. 5*. Set V: Effect of CO_2 and H_2S on Hg^0 removal efficiency of α-MnO_2 NTs at ambient conditions*

Gas mixture	***Hg^0 removal efficiency (%)***	***Standard deviation***
Hg^0 + 75% CH_4/N_2	99.9	0.1
Hg^0 + 75% CH_4 + 12.5% CO_2	99.8	0.1
Hg^0 + 75% CH_4 + 12.5% CO_2 + 40 ppm H_2S	99.7	0.1

4.4.5. Mechanism of Hg^0 removal

Zhang et al. (2014) making use of the density functional theory and periodic slab models, attempted to elaborate the mercury adsorption mechanism on MnO_2(110) surface. They deduced that Hg^0 was chemisorbed on the oxygen and manganese sites of MnO_2(110), with the adsorption being more favorable at lower temperatures. In our study, the mercury's presence in spent nanosorbents could not be confirmed through XPS, possibly due to the extra low pressure that caused the removal of gas molecules from the solid surface. However, this was succeeded through the acid digestion of spent nanosorbents, which resulted in a good mass balance. The above observations, along with the fact that the nanosorbent could be regenerated at a relatively low temperature, would suggest that Hg^0 was rather strongly physisorbed on the surface of α-MnO_2 (Equations 4.1-4.2), instead of undergoing oxidation to form HgO (Wang et al., 2019).

$$Hg^0_{(g)} \leftrightarrow Hg^0_{(ads)} \tag{4.1}$$

$$Hg^0_{(ads)} + \alpha\text{-}MnO_{2(surf)} \leftrightarrow Hg(O\text{-}Mn\text{-}O) \tag{4.2}$$

Although NTs possessed the lowest surface area, it exhibited the highest activity. Tompsett et al. (2014) reasoned that the catalytic activity of α-MnO_2 is not only determined by the specific surface area of nanoparticles, but also by the fundamental surface properties (i.e. low defect formation energies). Additionally, one has to consider the impact of stabilizing cation inside the tunnels of α-MnO_2, which has not been yet clarified. Li et al. (2017a) explained, that the depletion of surface K^+, could make the 2x2 tunnels of α-MnO_2 become an open structure, leading in this way to the exposure of sites that are highly active for catalytic oxidation. Also, previous studies (Rong et al., 2018; Xie et al., 2015) have suggested that the exposure of a more active crystal facet, as a result of the morphology tuning, might significantly influence catalytic processes.

In studies related to Hg^0 removal from flue gases at higher temperatures, it has been reported that the abundance of surface adsorbed oxygen species may lead to an increased mobility of lattice oxygen, resulting in this way to higher catalytic activity (Jampaiah et al., 2016; Jampaiah et al., 2015b). Considering the findings of TG and XPS analysis in our work, it is likely that the higher amount of available surface adsorbed oxygen species in NTs facilitated the sorption and bounding of Hg^0 vapor on its surface, leading to its enhanced activity. Consequently, it is expected that the adsorbed Hg^0 can be easily desorbed from the surface after raising moderately the temperature. Indeed, this was observed in our investigation, since a significant amount of the adhered Hg^0 could be desorbed at only 250 °C.

4.4.6. Comparison with Low-Temperature Pure Metal Oxide Sorbents

Table 4.6 presents several pure metal oxide-based sorbents that have been developed for the low- temperature Hg^0 vapor removal from flue gases. Below 100 °C their Hg^0 sorption capacity varied from around 2 to over 5 $mg \cdot g^{-1}$, and some of them could be regenerated at temperatures over 300 °C. Taking a look at recent reviews (Xu et al., 2018b; Yang et al., 2019b), where different types of Hg^0 sorbents are compared, one can realize that α-MnO_2 nanotubes certainly manifested one of the highest reported Hg^0 uptakes among pure metal oxides at ambient temperatures. That, along with its sufficient regeneration ability at a relatively low temperature (250 °C), renders it attractive for use in processes that require low-temperature Hg^0 vapor removal.

Table 4. 6. *Comparison of pure metal oxide Hg^0 vapor sorbents at temperatures below 100 °C.*

Sorbent	*Experimental parameters*	*Hg^0 sorption capacity*	*Regeneration temperature*	*Ref.*
MnO_2/AlO_3	Hg^0_{in}=144 $ng \cdot min^{-1}$, gas mix: Ar, feed=60 $mL \cdot min^{-1}$, T=60 °C	2.4 $mg \cdot g^{-1}$	–	(Granite et al., 2000)
MnO_x/TiO_2	Hg^0_{in}=50-250 $\mu g \cdot m^{-3}$, gas mix: $O_2/NO/NH_3$, GSHV=5.1×10^6 h^{-1}, T= 80 °C	–	320 °C	(Cimino and Scala, 2015)
Ce-Mn binary metal oxide	Hg^0_{in}=1005 $\mu g \cdot m^{-3}$, gas mix: $N_2/O_2/NO/SO_2$, feed=200 $mL \cdot min^{-1}$, T=100 °C	5.6 $mg \cdot g^{-1}$	350 °C	(Qu et al., 2015)
Zr-Mn binary metal oxide	Hg^0_{in}=900 $\mu g \cdot m^{-3}$, gas mix: N_2/O_2, GHSV=3.8×10^5 h^{-1}, T=100 °C	5 $mg \cdot g^{-1}$	350 °C	(Xie et al., 2013)
Mn/γ-Fe_2O_3	Hg^0_{in}=900 $\mu g \cdot m^{-3}$, gas mix: $N_2/O_2/H_2O/SO_2$, feed =12 $L \cdot min^{-1}$, T=100 °C	>2.2 $mg \cdot g^{-1}$	–	(Yang et al., 2011)
α-MnO_2 NTs	Hg^0_{in}=870 $\mu g \cdot m^{-3}$, gas mix: CH_4/ N_2, T=25 °C, GHSV=1.1×10^5 h^{-1}	>10 $mg \cdot g^{-1}$ (0.5% tolerance)	250 °C	this study

During the process Hg^0 can be collected by condensation and after treatment it may be stored permanently or safely disposed of. The United Nations Environment Programme, among others, has published a number of reports over the last years with respect to the technologies (e.g. stabilization/solidification) used for treating Hg^0 and mercury-bearing wastes (see for example the Practical Sourcebook on Mercury Waste Storage and Disposal) (UNEP, 2015b). Although currently the mass production of nanoparticles for commercial applications does not seem attractive, technologies like electrospinning (Zhang and Yu, 2014) constitute promising solutions for the fabrication of functional nanomaterials in the very near future. One way to facilitate low pressure drops along the bed and accommodate high gas flow rates, is to utilize engineered structured supports. This possibility will be further investigated in Chapter 6. Before attempting this, in the next chapter (Chapter 5) the activity of pure α-MnO_2 NTs is considerably improved, by incorporating CeO_2 nanoparticles onto its structure.

Chapter 5. α-MnO_2 Nanotubes Decorated with CeO_2 Nanoparticles

5.1. Chapter Overview

In this chapter the previously identified as superior sorbent, α-MnO_2 NTs, was decorated with CeO_2 nanoparticles and tested for Hg^0 vapor removal in simulated natural gas mixtures at ambient conditions. The ceria-saturate composition, which had a relative Ce/Mn atomic weight ratio of around 35%, exhibited a maximum Hg^0 uptake capacity exceeding 20 $mg \cdot g^{-1}$ (2 wt%), as determined from measurements of mercury breakthrough which corresponded to 99.5% Hg^0 removal efficiency over 96 h of exposure. This represents a significant improvement in the activity of pure metal oxide-based mercury sorbents. Most importantly, the composite nanosorbent was repeatedly regenerated at 350 °C and retained the 0.5% Hg^0 breakthrough threshold. It was projected to be able to sustain 20 regeneration cycles, with the presence of acid gases, CO_2 and H_2S, not affecting its performance. This result is particularly important considering that pure CeO_2 manifests rather poor activity for Hg^0 removal at ambient conditions. The observed synergistic effect in the composite nanomaterial possibly results from the facile oxygen vacancy formation at α-MnO_2 NTs active surfaces, as the result of CeO_2 nanoparticles incorporation.

---

* Part of the work presented in this chapter has been published in:
***Chalkidis, A.**, Jampaiah, D., Amin M.H., Hartley, P.G., Sabri, Y.M., Bhargava, S.K. "CeO_2-Decorated α-MnO_2 Nanotubes: A Highly Efficient and Regenerable Sorbent for Elemental Mercury Removal from Natural Gas". **Langmuir** 2019, 35, 8246-8256 (doi.org/10.1021/acs.langmuir.9b00835)*

5.2. Background and Rationale

Previously the hydrothermally-synthesized α-MnO_2 NTs exhibited a high Hg^0 uptake (1 wt%) and could be repeatedly regenerated at only 250 °C, desorbing around 69% of adhered mercury. Research groups investigating alternative materials such as solid ionic liquid phase adsorbents, have reported even higher Hg^0 uptakes (Abai et al., 2017; Abai et al., 2015; Abbas et al., 2016; Abbas et al., 2015). However, these materials cannot be regenerated and pose environmental threat through dumping of the spent sorbents as toxic waste. Therefore, the aim of this chapter was to examine the possibility of enhancing the

Hg^0 sorption capacity of the developed pure α-MnO_2 NTs, by sustaining, at the same time, its competitive advantage of easy recovery and reuse.

Various studies have involved the incorporation of ceria (CeO_2) into sorbent/catalyst compositions with the aim of enhancing the Hg^0 removal activity, usually at temperatures over 150 °C. This is due to its distinctive properties, related to the reversible Ce^{3+}/Ce^{4+} redox pair, surface acid-base properties, and defects that primarily consist of oxygen vacancies (Montini et al., 2016). Considering this, Qu et al. (2015) prepared a series of Ce-Mn binary metal oxides by a template method and tested them for Hg^0 capture from flue gas. The Hg^0 uptake of $Ce_{0.5}Mn_{0.5}O_y$ reached 5.6 $mg \cdot g^{-1}$ at 100 °C in N_2 and O_2 atmosphere, and the sorbent could be regenerated at 350 °C. MnO_x-CeO_2/TiO_2 prepared by co-impregnation by Reddy et al. (2015) exhibited better sulfur resistance, whereas the same sorbent synthesized by co-deposition-precipitation manifested the highest Hg^0 uptake (17.8 $mg \cdot g^{-1}$) at 175 °C under N_2 atmosphere. The same research group had also reported in the past (He et al., 2011) an even higher Hg^0 uptake (37 $mg \cdot g^{-1}$) by using 20 wt% MnO_x/CeO_2-TiO_2, prepared by wet impregnation. However, the reported materials could not be deemed as suitable for Hg^0 removal under natural gas processing conditions.

As explained in Chapter 4, the effect of catalyst's nanoparticles size and shape may be of great significance (Luo et al., 2018; Rong et al., 2018). Therefore, the target of this chapter was to develop a regenerable Hg^0 vapor sorbent based on nanostructured manganese (Li et al., 2017a; Tompsett et al., 2014) and cerium oxides (Yang et al., 2018a), that is active at ambient conditions for Hg^0 vapor form simulated natural gas mixtures. For this reason, the previously identified as the superior morphology, α-MnO_2 NTs (Zhou et al., 2017), was decorated with different quantities of CeO_2 nanoparticles. The top performing CeO_2-decorated α-MnO_2 NTs sorbent was subsequently subjected to a series of successive sorption-desorption cycles to evaluate its regenerative behavior, whilst also being exposed to acid gases, such as CO_2 and H_2S. As previously, the comprehensive materials characterization provided insights into the mercury removal mechanism.

5.3. Characterization Results

5.3.1. SEM Imaging

SEM was initially employed for the examination of nanosorbents morphology. Previously the tubular-like nanostructure of α-MnO_2 with lengths and widths (external diameter) of less than 5 μm and 90 nm, respectively, was identified. The SEM images of the tetragonal α-MnO_2 NTs decorated with CeO_2 nanoparticles are displayed in Figure 5.1.

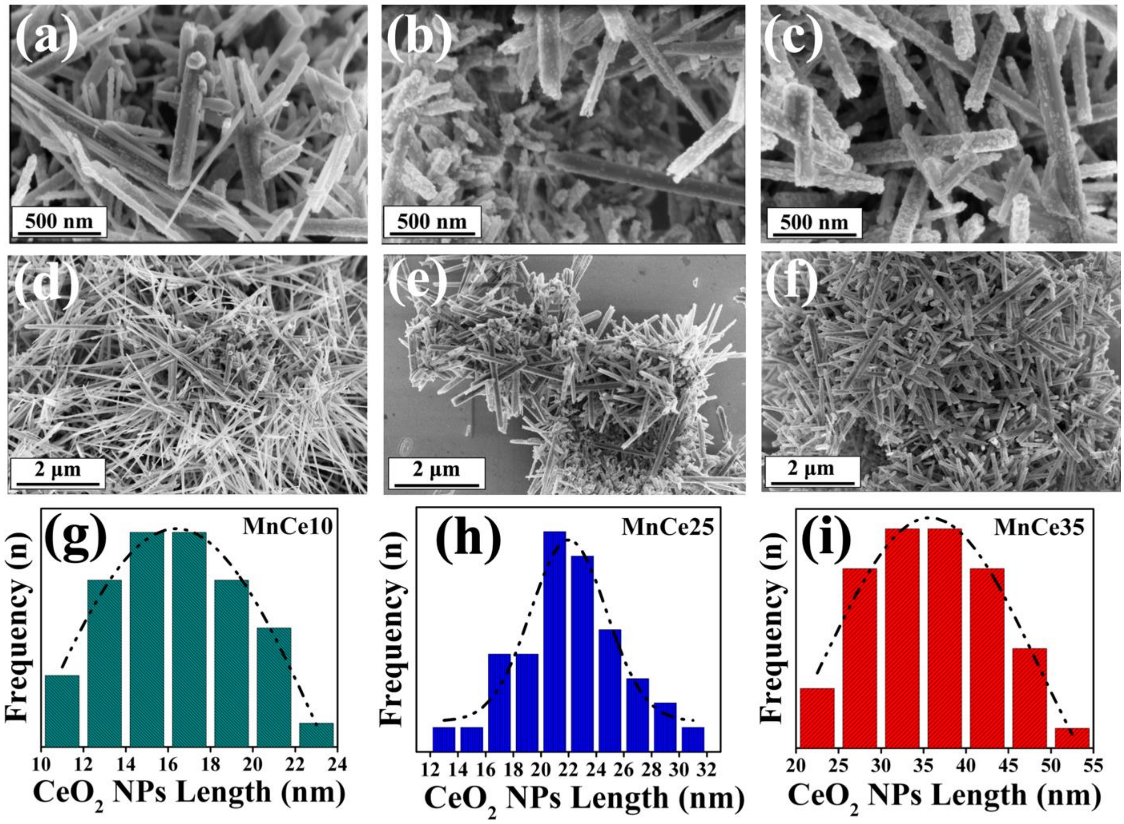

***Figure 5. 1**. SEM images of MnCe10 (a-d), MnCe25 (b-e) and MnCe35 (c-f) as well as length distribution (determined from TEM) of CeO_2 nanoparticles (g, h, i) incorporated on α-MnO_2 NTs.*

In the same figure the length distributions of CeO_2 nanoparticles (as derived from TEM, see Figure 5.5) are also shown. The density of ceria nanoparticles increased with the amount of ceria precursor (cerium(III) nitrate) used during synthesis. The size of the ceria nanoparticles also increased slightly with the amount of ceria precursor content, most probably due to agglomeration process. However, in all cases the distribution onto α-MnO_2 NTs structure was uniform. In Figures 5.1a and 5.1d the average size of ceria nanoparticles was calculated to be around 16 nm (Figure 5.1g), reflecting a relative Ce/Mn atomic weight ratio of around 10%. When the Ce/Mn atomic weight ratio approached 25%, the ceria nanoparticles increased in size to around 22 nm (Figure 5.1h) and started covering a greater area of the surface of α-MnO_2 NTs (Figures 5.1b and 5.1e). At 35% Ce/Mn atomic weight ratio, the decoration approached to a saturation point (Figures 5.1c and 2f), and the average size of ceria nanoparticles reached approximately 35 nm (Figure 5.1i).

5.3.2. EDS Elemental Mapping

The HRTEM-EDS elemental maps of MnCe10, MnCe25 and MnCe35 are shown in Figure 5.2. The accompanying EDS spectra are presented in Figure 5.3a and clearly demonstrate the increasing amount of ceria with the amount of precursor used. This is confirmed for MnCe35, by the presence of multiple peaks assigned to cerium at 0.88, 4.84 and 5.26 keV. Since the powders were loaded on carbon-coated copper grids for analysis, the presence of copper at 8.05 and 8.91 keV, was also expected.

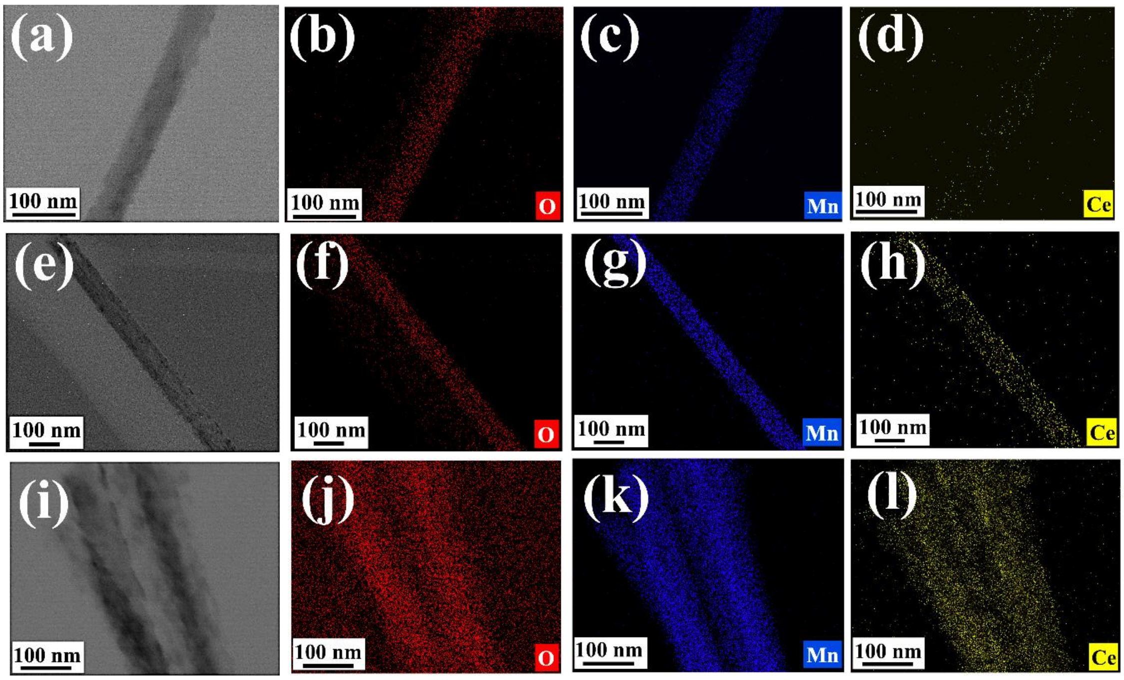

***Figure 5. 2**. HRTEM-EDS elemental mapping of MnCe10 (a-d), MnCe25 (e-h) and MnCe35 (i-l).*

***Table 5. 1**. HRTEM-EDS normalized surface atomic weights of MnCe10, MnCe25, MnCe35.*

Sample	***Mn (%)***	***Ce (%)***	***O (%)***	***K (%)***
MnCe10	42.9	4.7	48.9	3.9
MnCe25	40.4	10.2	45.7	3.7
MnCe35	46.1	17.5	32.1	4.4

The surface elemental atomic composition of MnCe10, MnCe25 and MnCe35 is presented in Table 5.1. The surface Ce/Mn atomic weight ratio was 10.7, 25.2 and 37.7%, respectively. As Table 5.2 demonstrates, these values were in very good agreement with the bulk Ce/Mn atomic weight ratios identified by MPAES (11.5, 24.8 and 35.5% respectively). The cerium coverage (yellow color) in Figures 5.2d, 5.2h, and 5.2l clearly increased in density with the ceria nanoparticle loading. Manganese (blue color in Figures

5.2c, 5.2g and 5.2k) and oxygen (red color in Figures 5.2b, 5.2f and 5.2j), were found to show homogeneous distribution in all samples

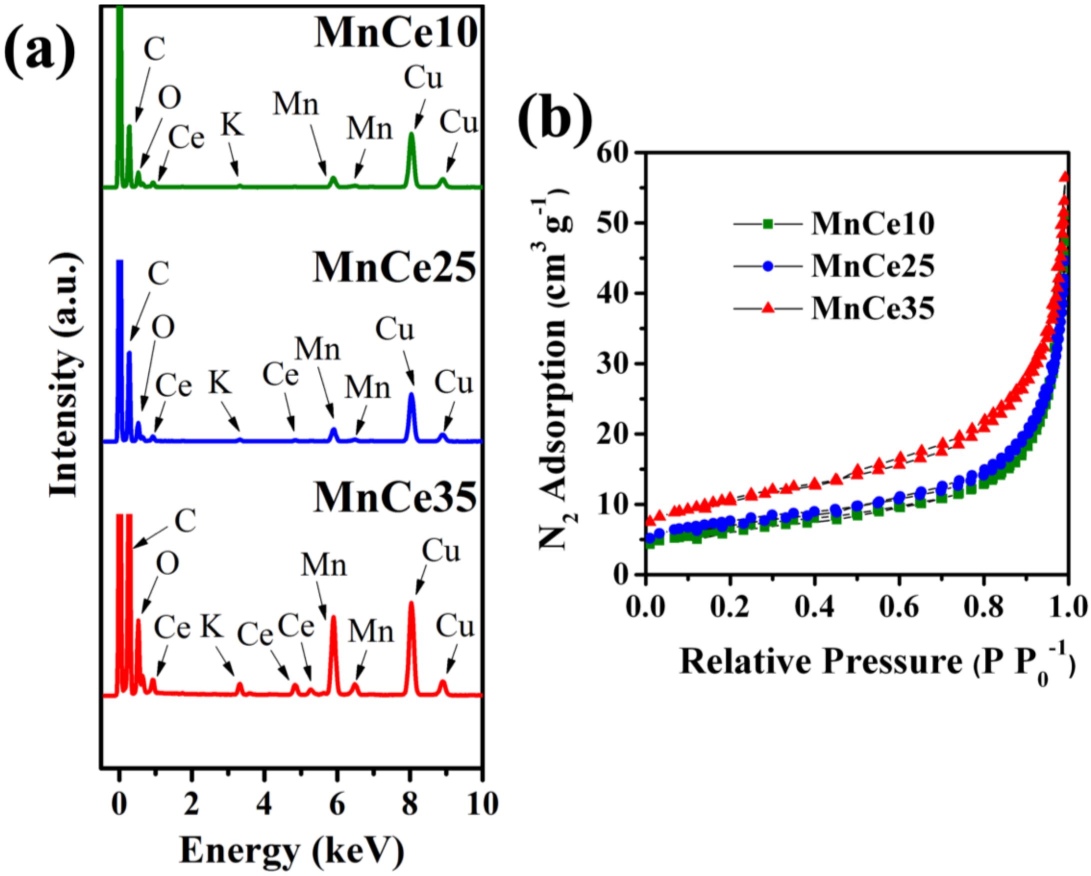

***Figure 5. 3**. a) HRTEM-EDS spectra and b) N_2 adsorption-desorption isotherms of MnCe10, MnCe25 and MnCe35.*

5.3.3. N_2 Adsorption-Desorption Isotherms

Figure 5.3b illustrates the N_2 adsorption-desorption isotherms of pure α-MnO_2 NTs, MnCe10, MnCe25 and MnCe35, respectively. Table 5.2 displays the BET specific areas, as well as the bulk (MPAES) and surface (EDS, XPS) Ce/Mn atomic weight ratios (XPS is discussed in the following section).The N_2 isotherms of all samples corresponded to a Type II isotherm (Thommes et al., 2015) indicating nonporous/macroporous materials. The MnCe35 sorbent possessed the highest surface area (38.1 $m^2 \cdot g^{-1}$) closely followed by MnCe25 (35.7 $m^2 \cdot g^{-1}$), MnCe10 (34.1 $m^2 \cdot g^{-1}$) and pure α-MnO_2 NTs (33.3 $m^2 \cdot g^{-1}$). The higher density of CeO_2 nanoparticles in the MnCe35 sample presumably led to the higher surface area. However, the difference in the specific area values is quite small and hence definitive conclusions should be drawn with caution.

Table 5. 2*. BET specific surface areas and Ce/Mn atomic weight ratios of MnCe10, MnCe25 and MnCe35.*

Sample	***BET specific area ($m^2 \cdot g^{-1}$)***	***Ce/Mn atomic weight ratio (%)***		
		XPS	**MP-AES**	**HRTEM-EDS**
α-MnO_2 NTs	33.3	-	-	-
MnCe10	34.1	11.7	11.5	10.7
MnCe25	35.7	27.6	24.8	25.2
MnCe35	38.1	38.2	35.5	37.7

5.3.4. XRD Analysis

The XRD patterns of CeO_2-decorated α-MnO_2 NTs are presented in Figure 5.4a, while those of pure α-MnO_2 NTs, CeO_2 and their physical mixture are displayed in Figure 5.4b. Essentially, all XRD patterns corresponded to the body-centered tetragonal α-MnO_2 (ICDD-PDF 44-0141) (Jampaiah et al., 2017). However, two peaks, clearly observed at 33.1° and 47.5°, corresponded to (200) and (220) crystal planes of CeO_2 (ICDD-PDF 34-0394, space group Fm3m, a=5.41 Å) (Jampaiah et al., 2015a).

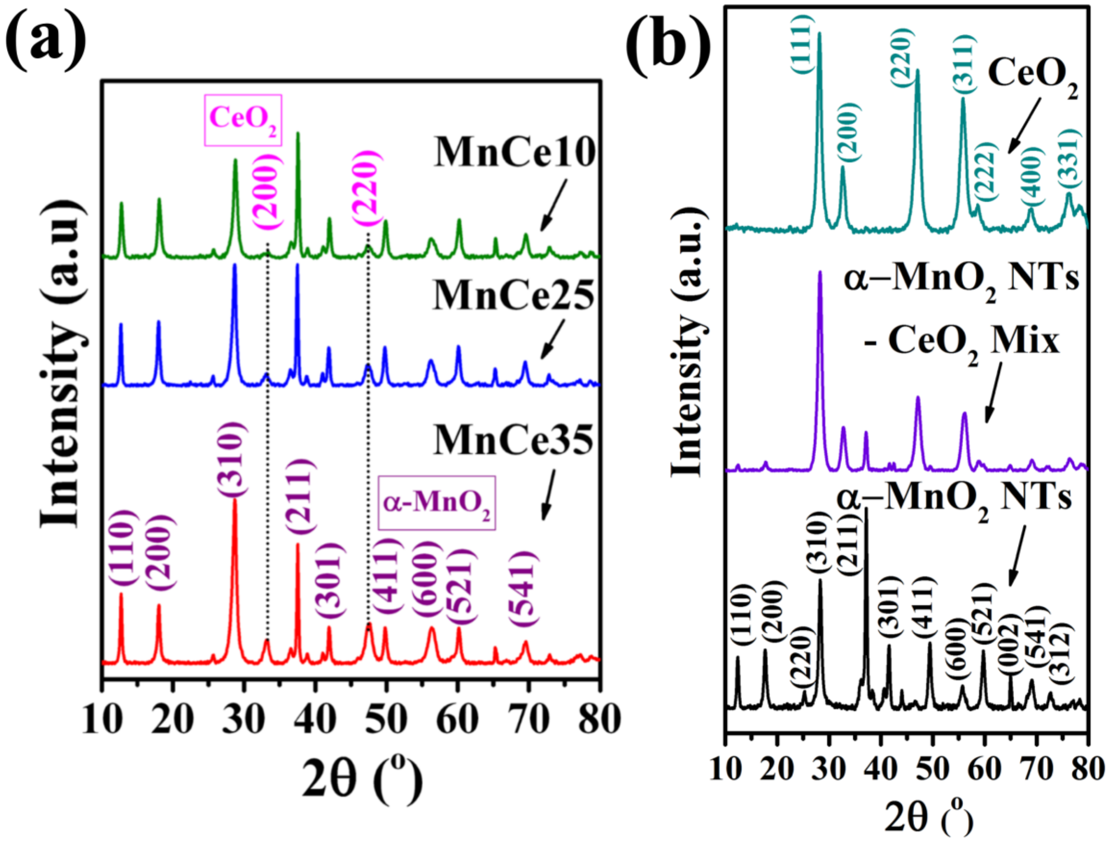

Figure 5. 4*. XRD patterns of a) MnCe10, MnCe25, MnCe35 as well as b) pure α-MnO_2 NTs, CeO_2 and their physical mixture (α-MnO_2 NTs-CeO_2 Mix).*

These were quite faint for MnCe10, however as the amount of CeO_2 decoration increased (i.e. MnCe25 and MnCe35), the peaks could be easily distinguished. As for α-MnO_2, the four strongest peaks in all samples, were evident at 12.8°, 18.1°, 28.8° and 37.5°, and corresponded to (110), (200), (310) and (211) crystal planes, respectively. The X-ray diffractogram of the α-MnO_2 NTs-CeO_2 physical mixture was different to the one of CeO_2-decorated α-MnO_2 NTs. It showed patterns which comprised of peaks reflecting both phases. This observation suggests that the controlled hydrothermal synthesis can result in the production of a composite nanomaterial (CeO_2-decorated α-MnO_2 NTs) with distinctive characteristics.

5.3.5. TEM, HRTEM and SAED Investigation

The TEM images of MnCe10, MnCe25 and MnCe35 are shown in Figures 5.5a, 5.5d and 5.5g, respectively. The exposed crystal facets and their corresponding lattice spacings were identified through HRTEM (Figures 5.5b, 5.5e and 5.5h), and the collected SAED patterns (Figures 5.5c, 5.5f and 5.5i) were correlated with XRD data.

For the CeO_2-decorated nanomaterials, the TEM images confirmed the observations, derived previously from SEM, with respect to CeO_2 nanoparticles' uniformity and size distribution. The size of deposited CeO_2 nanoparticles on α-MnO_2 was slightly smaller for MnCe10 (Figure 5.5a) in comparison to MnCe25 and MnCe35 (Figures 5.5d and 5.5g). The CeO_2 crystal facets, (111) and (200), corresponding to d-spacings of 0.31 and 0.27 nm, could be identified for MnCe10 (Figure 5.5b). For the same sample the α-MnO_2-associated crystal facet (310), corresponding to d-spacing of 0.31 nm, could also be observed. For MnCe25, both CeO_2 (200) and α-MnO_2 (310) crystal planes could be distinguished (Figure 5.5e). When analyzing MnCe35, the CeO_2 (111) and α-MnO_2 (200) crystal facet (with d-spacings of 0.31 and 0.49 nm, respectively) were observed (Figure 5.5h). According to Jiang et al. (2018) the α-MnO_2 catalyst with exposed (200) facets possessed the highest surface acidity, which is considered to be favorable for Hg^0 removal process. Also, it is known that ceria nanoparticles typically expose the most stable (111) facets in order to minimize surface energy (Zhang et al., 2012).

The TEM images of pure CeO_2 as well as its physical mixture with α-MnO_2 NTs are presented in Figures 5.5j and 5.5k, respectively. The CeO_2 particles have irregular shape and its dimensions are well above 100 nm as compared to the smaller nanoparticles incorporated on MnCe10, MnCe25 and MnCe35. Smaller ceria crystal size has been associated with increased oxygen vacancy concentration, and highly activity sorption and oxidation reactivity (Trovarelli and Llorca, 2017). Therefore it is expected that the CeO_2 nanoparticles in the developed Mn-Ce composite nanomaterials would be more active toward Hg^0 sorption than the synthesized separately, control CeO_2 material. In the case of α-MnO_2 NTs-CeO_2 physical mixture, the particles of the two components are segregated, having retained their individual shape and size.

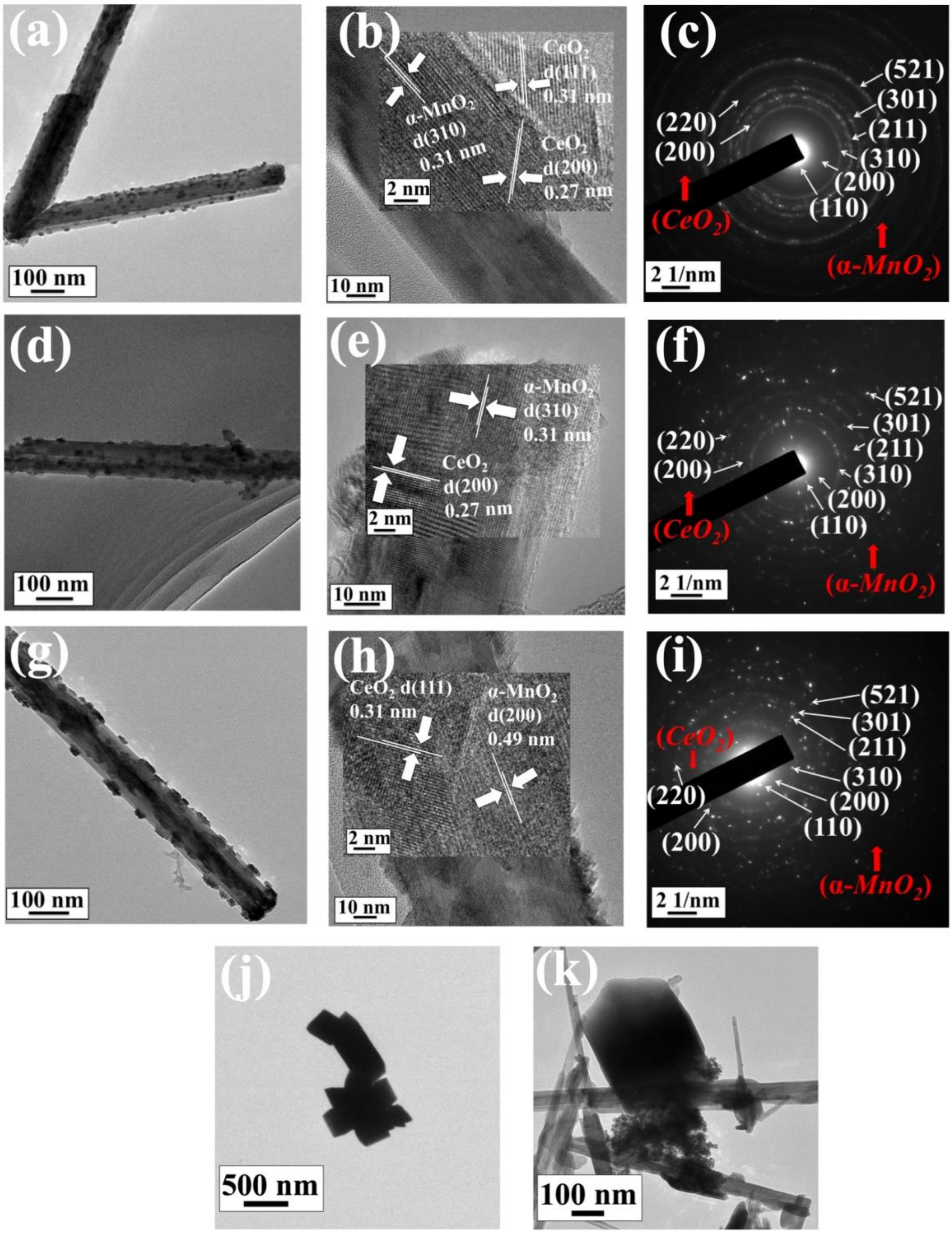

***Figure 5. 5**. TEM (a, d, g), HR-TEM (b, e, h) and SAED (c, f, i) images of MnCe10 (a-c), MnCe25 (d-f) and MnCe35 (g-i). Also, TEM images of* CeO_2 *(j) and α-*MnO_2 *NTs-*CeO_2 *physical mixture (k).*

The obtained SAED patterns (Figures 5.5c, 5.5f and 5.5i) from all samples, displayed α-MnO_2 crystal planes (110), (200), (310), (211), (301) and (521), which corresponded to d-spacings of 0.69, 0.49, 0.31, 0.24, 0.21 and 0.15 nm, respectively (Jampaiah et al., 2017). CeO_2 exposed planes, (111) and (200), as previously stated, reflected d-spacings of 0.27 and 0.31 nm (Jampaiah et al., 2015b) and correlated well with XRD data.

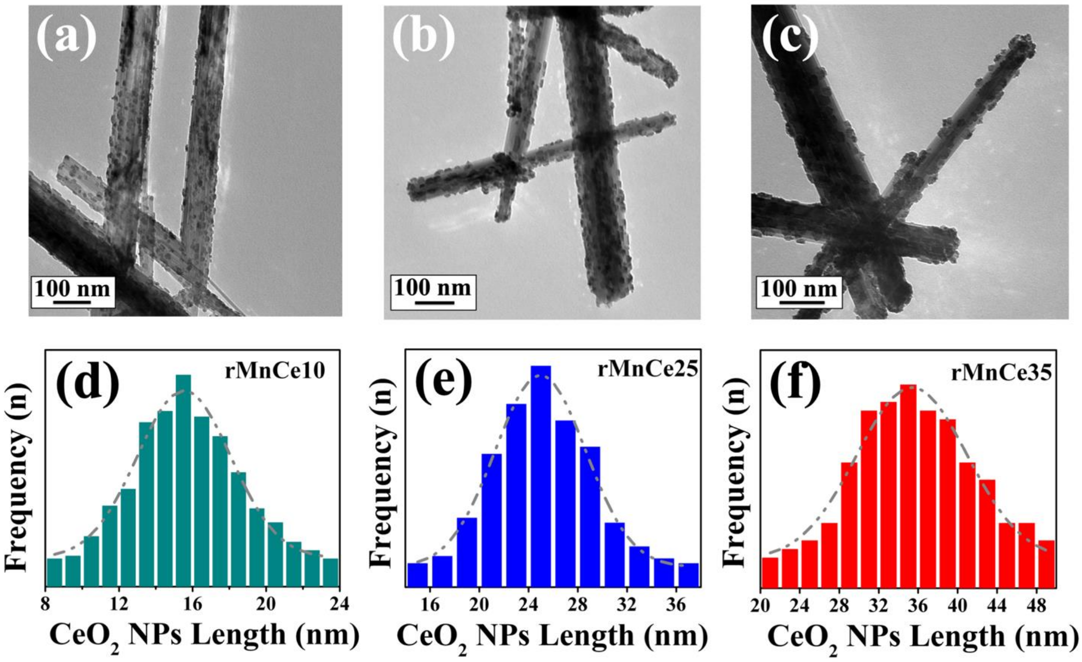

Figure 5. 6. *a), b), c) TEM images and d), e), f) CeO_2 nanoparticle length distribution on MnCe10, MnCe25 and MnCe35, after having been subjected to regeneration process at 350 °C for 90 min under N_2 atmosphere.*

Besides, as it can be confirmed from the TEM images in Figures 5.6c and 5.6f the stability of the interface produced by the decoration α-MnO_2 NTs with CeO_2 nanoparticles, was maintained for MnCe35 (rMnCe35) during the high temperature regeneration process at N_2 atmosphere (discussed later). The same could be argued for the other two samples (rMnCe10-Figures 5.6a and 5.6d, rMnCe25-Figures 5.6b and 5.6e) despite the fact that they have not been subjected to further regeneration tests.

5.3.6. XPS Analysis

XPS was deployed to obtain a deeper insight of the composition and oxidation state of the elements on the surface of nanosorbents. Figures 5.7a, 5.7b, 5.7c and 5.7d depict the Mn 2p, Mn 3s, O 1s and Ce 3d XPS spectra of MnCe10, MnCe20 and MnCe35. Also, Figures 5.7e, 5.7f, 5.7g present the O 1s, Mn2p and Ce 3d XPS spectra of regenerated MnCe35 (rMnCe35) at 350 °C for 90 min under the flow of dry N_2. Finally, Table 5.3

displays the surface concentration of oxygen, manganese and cerium species of all aforementioned samples.

The magnitude of peak splitting (ΔE) in the Mn 3s XPS spectrum is considered as a fingerprint of manganese oxidation state (<4.9 eV for MnO_2) (Jia et al., 2016). As shown in Figure 5.7b this was equal to 4.69 eV for MnCe10, 4.73 eV for MnCe25 and 4.78 eV for MnCe35. Therefore, the average oxidation state (AOS) of manganese, which was estimated according to the formula: AOS(eV)=8.956-1.116xΔE (Zhu et al., 2017a) decreased in the order MnCe10 (3.72) > MnCe25 (3.68) > MnCe35 (3.62), possibly indicating the presence of considerable defect formation at MnCe35 surface.

A narrow peak maximum was seen in the $Mn2p_{3/2}$ XPS spectrum of all nanosorbents (Figure 5.7a). This peak had a distinct asymmetric shape which is also characteristic of MnO_2 (Biesinger et al., 2011). The asymmetrical Mn $2p_{3/2}$ XPS signal at 642 eV region was deconvoluted into three components, centered at about 641.3, 642.4, and 644.5 eV, which were assignable to the surface Mn^{3+} species, Mn^{4+} species and the satellite peaks, respectively (Shi et al., 2012). The binding energies of manganese ions in CeO_2-decorated α-MnO_2 NTs were slightly lower (~0.2 eV) than those of pure α-MnO_2 NTs, possibly suggesting a stronger interaction between manganese and cerium oxide (Jampaiah et al., 2015b).

The Mn^{3+}/Mn^{4+} ratio increased with the amount of decorated CeO_2 nanoparticles onto the surface of α-MnO_2 NTs. As discussed later, the presence of Mn^{3+} in the framework of manganese dioxide may be associated with the generation of oxygen vacancies to maintain the electrostatic balance (Jia et al., 2016). Therefore, by analyzing the Mn^{3+} content, it can be deduced that the generation of oxygen vacancies, possibly induced by CeO_2 introduction, increased in the order: MnCe10 < MnCe25 < MnCe35.

The Ce 3d XPS spectra consisted of eight peaks, u, u′, u″, u‴, v, v′, v″, v‴ that were attributed to four pairs of $3d_{5/2}$ and $3d_{3/2}$ spin-orbit doublets (Wan et al., 2018). Ce^{4+} was associated with u, u″, u‴, v, v″, v‴ peaks while u′ and v′ peaks signified the presence of Ce^{3+} (Govinda Rao et al., 2016; Jampaiah et al., 2016). Therefore, both 3+ and 4+ oxidation states of Ce might have co-existed during adsorption process, with the Ce^{3+}/Ce^{4+} ratio decreasing with increasing CeO_2 decoration. The surface Ce/Mn atomic weight ratio according to XPS analysis, was 11.7% for MnCe10, 27.6% for MnCe25 and 38.2% for MnCe35. These values were consistent with MP-AES and HRTEM-EDS (see Table 5.2), suggesting that the surface and bulk composition were of the same magnitude.

The O 1s XPS spectra of all three sorbents composed of three peaks representing different types of oxygen species (Jampaiah et al., 2015b). At a lower binding energy ~529.3 eV, the peak could be ascribed to the surface lattice oxygen (O_a) of metal oxides. The peak at around 531.4 eV represented the surface adsorbed oxygen and/or hydroxyl groups (O_b), while the one at roughly 533.5 eV was identical to oxygen species from water and/or carbonates (O_c). The peak of O_a in decorated NTs was slightly shifted (0.1-0.2 eV) to a lower binding energy in comparison to pure α-MnO_2 NTs, probably indicating that there was more surface labile active oxygen for Hg^0 sorption after the introduction of CeO_2 (Jampaiah et al., 2015a).

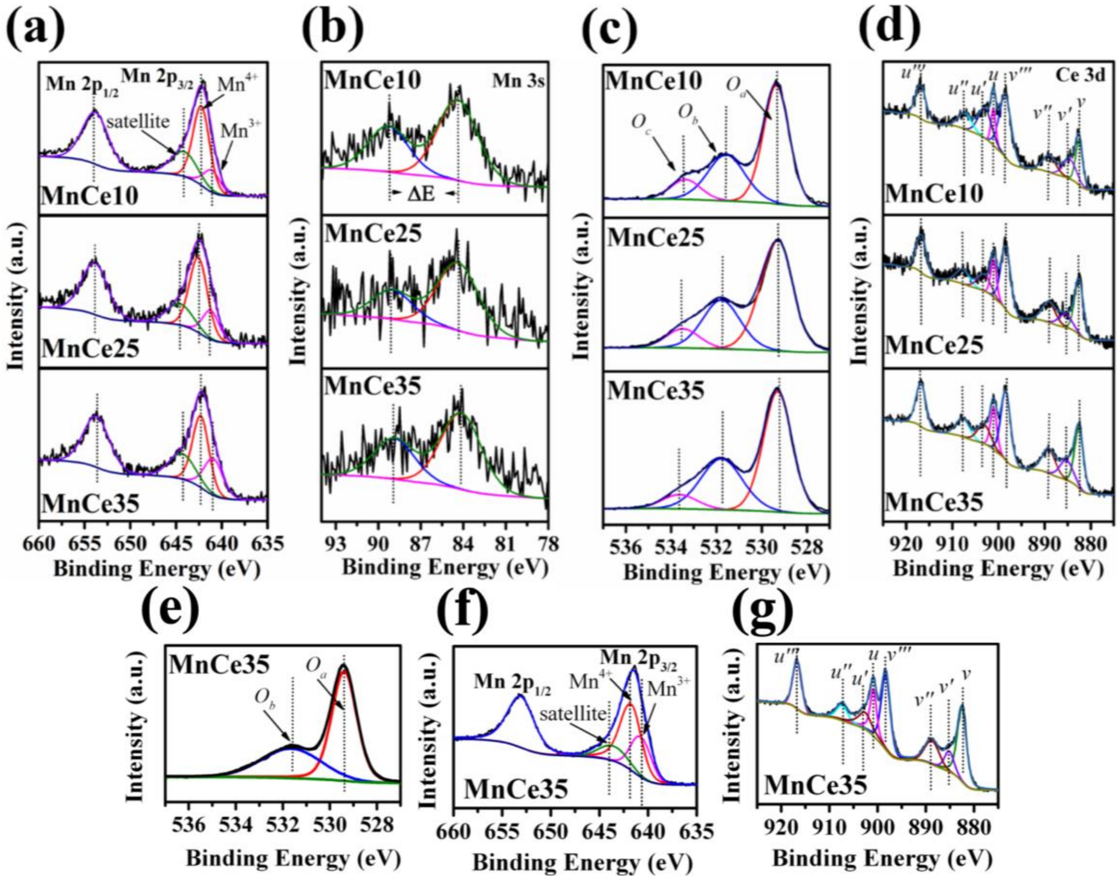

Figure 5. 7. (a) Mn 2p, (b) Mn 3s, (c) O 1s and (d) Ce 3d XPS spectra of fresh MnCe10, MnCe25, MnCe35. e) O 1s, f) Mn 2p and g) Ce 3d XPS spectra of MnCe35 after having been subjected to regeneration process at 350 °C for 90 min under N_2 atmosphere.

MnCe35 possessed the highest ratio of surface adsorbed to lattice oxygen ratio (O_b/O_a=79.9%), followed by MnCe25 (74.2%) and MnC10 (71.2%). The abundance of surface oxygen species has been repeatedly reported to improve Hg^0 removal efficiency, by providing the active sites for Hg^0 adsorption on the surface of sorbent/catalyst. Finally, the O 1s and Mn 2p XPS spectra (Figures 5.7e and 5.7f) of the regenerated MnCe35 (see next sections) revealed that after the high temperature regeneration process under N_2

atmosphere the O_b/O_a and Mn^{3+}/Mn^{4+} ratios were reduced to 62.6 and 55.1%, respectively, possibly indicating, a favorable for Hg^0 removal, correlation between the oxygen vacancies and the surface adsorbed oxygen species.

Table 5. 3. *Surface concentrations of manganese, oxygen and cerium species of MnCe10, MnCe25, MnCe35 and rMnCe35.*

Sample	*O_a (%)*	*O_b (%)*	*O_c (%)*	*O_b/O_a (%)*	*Ce^{3+}/Ce^{4+} (%)*	*Mn^{3+}/Mn^{4+}(%)*
α-MnO_2 NTs	51.1	34.4	14.5	67.3	-	-
MnCe10	50.5	36.3	13.2	71.8	23.3	28.5
MnCe25	50.1	37.2	12.7	74.2	21.6	36.1
MnCe35	49.2	39.3	11.5	79.9	17.1	59.3
rMnCe35	61.5	38.5	-	62.6	18.1	55.1

5.4. Hg^0 Removal and Sorbent Regeneration Capacity

5.4.1. Experimental Sequence

The sorption-desorption tests consisted of three sets (Table 5.4). In Set I, CeO_2 decorated α-MnO_2 NTs with different Ce/Mn atomic weight ratios (MnCe10, MnCe25, MnCe35) were exposed to Hg^0_{in}=870 μg·m^{-3} at room temperature under a CH_4/N_2 atmosphere and GHSV=1.1x10^5 h^{-1} to identify the Hg^0 uptake up to a 0.5% Hg^0 breakthrough threshold.

Table 5. 4. *Summary of experimental sets and operating conditions with respect to adsorption (ads.) and desorption (des.) processes.*

Set	*Nanosorbent*	*Gas components*	*Operating conditions*
Set I	50 mg MnCe10, MnCe25, MnCe35	Ads.: Hg^0 + 75% CH_4/N_2	Ads.: T=25 °C, Hg^0_{in}=870μg·m^{-3}, GHSV=1.1x10^5 h^{-1}
Set II	50 mg pure α-MnO_2 NTs, CeO_2, α-MnO_2 NTs-CeO_2 Mix	Ads.: Hg^0 + 75% CH_4/N_2	Ads.: T=25 °C, Hg^0_{in} =870 μg·m^{-3}, GHSV=1.1x10^5 h^{-1}, t=14 h
Set III	50 mg MnCe35	Des.: N_2	Ads.: T=25 °C, t=14 h, Hg^0_{in} =870 μg·m^{-3}, GHSV=1.1x10^5 h^{-1} , Des.: T=350 °C (heat. rate=10 °C·min^{-1}), t=90 min, GHSV=1.1x10^5 h^{-1}
Set IV	50 mg MnCe35	Ads.: Hg^0 + 75% CH_4 + 12.5% CO_2 + 40 ppm H_2S	Ads.: T=25 °C, t=14 h, Hg^0_{in}=870 μg·m^{-3}, GHSV=1.1x10^5 h^{-1}

For comparison purposes, in Set II pure α-MnO_2 NTs, CeO_2 and their physical mixture (α-MnO_2 NTs-CeO_2 Mix) were tested under the same conditions at fixed-time experiments (14 h). Subsequently, in Set III the superior sorbent was subjected to a series of seven successive sorption-desorption cycles to evaluate its regeneration potential. The sorption process was conducted under the same conditions and lasted 14 h. The desorption process lasted 90 min and was carried out at 350 °C under dry N_2 atmosphere (GHSV=$1.1x10^5$ h^{-1}) and a heating rate of 10°C·min^{-1}. Finally, in Set IV 12.5% CO_2 and 40 ppm H_2S were introduced to the gas mixture to evaluate their impact on the activity of the superior sorbent at room temperature.

5.4.2. Removal Efficiency of MnCe10, MnCe25 and MnCe35

The Hg^0 breakthrough curves of MnCe10, MnCe25, MnCe35, are depicted in Figure 5.8a, which includes the tested in previous chapter, α-MnO_2 NTs. The Hg^0 adsorption performance of pure α-MnO_2 NTs, which was used here as a benchmark, was already superior to most metal oxides reported in the literature (Xu et al., 2018b; Yang et al., 2019b). Again it must be highlighted that as Hg^0 breakthrough was considered the point in the process when the Hg^0 removal efficiency dropped below 99.5% (0.5% tolerance). This point in Figure 5.8a corresponds to a value of Hg^0_{out}/Hg^0_{in}=0.005. This extremely low tolerance was purposely set due to the excellent Hg^0 sorption performance of the developed nanosorbents as well as for easy comparison with alternative materials proposed specifically for Hg^0 capture from natural gas (Abai et al., 2015). In the gas processing industry the target efficiencies may be as high as 99.9%, and when the efficiency drops below 99%, the capture mass is no longer effective and needs to be replaced (Porcheron et al., 2015). As stated in Chapter 1, this is because the maximum allowable concentration of mercury-contaminated gas stream entering the cryogenic section in LNG plants is 10 ng·m^{-3}.

Remarkably, even with the stringency of mercury tolerance, the MnCe10 sorbent retained activity for almost 72 h, extending the breakthrough time relative to α-MnO_2 NTs by roughly a day. This improvement in mercury sorption capacity is significantly high from the industrial application point of view, since such a sorbent could remain active for a longer period, thereby reducing the requirement for regeneration/replacement operations. Following the 72-h period, the Hg^0 sorption capacity of MnCe10 reached 15 mg·g^{-1} (1.5 wt% or 15 mg Hg^0 per gram of sorbent), being greatly promoted by the modest presence of nanostructured CeO_2. The Hg^0 removal efficiency further increased with the deployment of MnCe25, reaching the 0.5% tolerance level after 88 h. Impressively, the CeO_2-saturated sorbent, MnCe35, was still active after more than 96 h, having captured more than 20 mg·g^{-1} (2 wt%), achieving a two-day operating time extension relative to pure α-MnO_2 NTs, for the 0.5% Hg^0 breakthrough threshold.

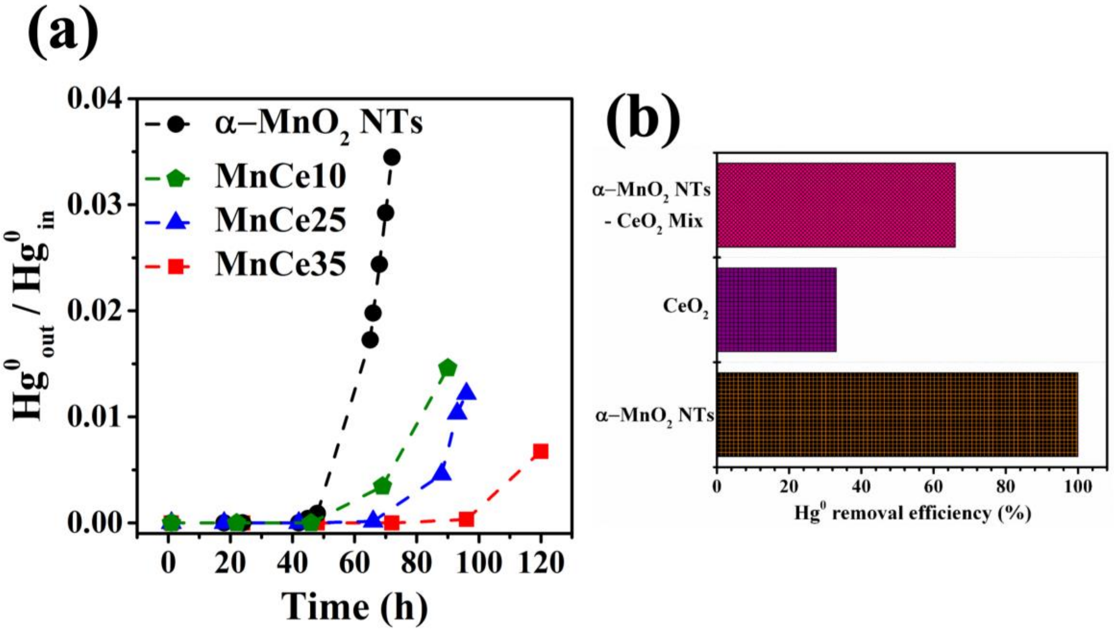

***Figure 5. 8**. a) Set I: Hg^0 breakthrough curves of pure α-MnO_2 NTs, MnCe10, MnCe25, and MnCe35. b) Set II: Hg^0 removal efficiency of pure α-MnO_2 NTs and CeO_2 as well as their physical mixture (α-MnO_2 NTs-CeO_2 Mix).*

In order to compare these results with realistic control materials, in Set II pure CeO_2 as well as CeO_2 physically mixed with α-MnO_2 NTs were tested over a 14-h period (Figure 5.8b) at room temperature. The performance of both was significantly lower than that of pure α-MnO_2 NTs or the composite Mn-Ce materials. This result indicates that the Hg^0 sorption enhancement of the developed MnCe10, MnCe25, and MnCe35 was due to the synergistic effects of the Mn-Ce composite, and was attributed to the chemical rather than the physical interaction between CeO_2 and MnO_2 (physical mixture) as well as the control of the Ce and Mn content, their oxidation states and ratios. This result also indicates that the shape and size control may have a great impact on a sorbent's activity.

5.4.3. Regeneration of MnCe35

The superior sorbent, MnCe35, was subjected in Set III to a series of seven successive sorption-desorption cycles to assess its regeneration potential, the results of which are presented in Figure 5.9. The optimum regeneration conditions for pure α-MnO_2 NTs was previously found to be 90 min at 250 °C, possibly indicating a weaker interaction between the adhered Hg^0 on active Mn-O sites. As expected, the embodiment of CeO_2 strengthened the Hg^0 interaction on the active sites of MnCe35 and only a small amount of adhered Hg^0 could be desorbed at 250 °C, in contrast to pure α-MnO_2 NTs. Consecutive sorption-desorption experiments were then performed at both 300 and 350 °C. In the latter case, the amount of recovered mercury was significant, in agreement with previous reports (Qu et al., 2015).

Figures 5.9a and 5.9b show that on average ~66% of Hg^0 undergoing sorption in each cycle, was desorbed upon the completion of each of the successive sorption-desorption cycles. With the number of cycles, the amount of desorbed Hg^0 moderately increased, as a result of the increasing Hg^0_{in}. The average Hg^0 desorption efficiency reported, reflects the nanosorbent's ability to desorb enough Hg^0 in each cycle facilitating 100% Hg^0 removal in the subsequent cycle, at least for the seven-cycle experiment conducted in this work. It should be noted that the sorption cycles during regeneration experiments lasted only 14 h, while the Hg^0 breakthrough was previously found to occur at about 96 h. This suggests that the material was not saturated with mercury during these experiments, and further that a lower Hg^0_{in} concentration in the gas stream would likely result in a lower saturation, and consequently an increased number of possible regeneration cycles with 100% Hg^0 removal efficiency. The opposite could be argued for a higher Hg^0_{in} concentration or if the sorption tests were extended for longer times.

To project the maximum number of regeneration cycles (Figure 5.9c) which might be achieved for MnCe35 and given the 0.5% Hg^0 breakthrough threshold (tolerance), the following assumptions were made. As previously shown, on average ~96 μg Hg^0 (equivalent to ~66% of Hg^0_{in} per cycle) was desorbed in each regeneration cycle. This amount of desorbed Hg^0 was assumed to be constant in our calculations. Second, since the Hg^0 removal efficiency was maintained at close to 100% over the seven regeneration cycles, it was also assumed to be stable in our calculations. Of course, this assumption is an over-simplification since in reality, the mercury removal efficiency is expected to drop after extended sorption-desorption cycling. Our projection of maximum regeneration cycles serves the purpose of highlighting the very limited tolerance of sorbents used in natural gas industry in contrast to other applications such as coal-fired power plants.

Considering the above, MnCe35 could undergo a staggering 20 regeneration cycles before its removal efficiency dropped by only 0.5%. Given the amount of used nanosorbent (only 50 mg), the 0.5% Hg^0 breakthrough threshold corresponded to a capacity of 1 mg per 50 mg sorbent, as shown on the X-axis of Figure 5.9c. Even with such a small amount of nanosorbent, the number of regeneration cycles is expected to increase proportionally with either decreasing the threshold limit to <99.5% or decreasing the Hg^0_{in} concentration.

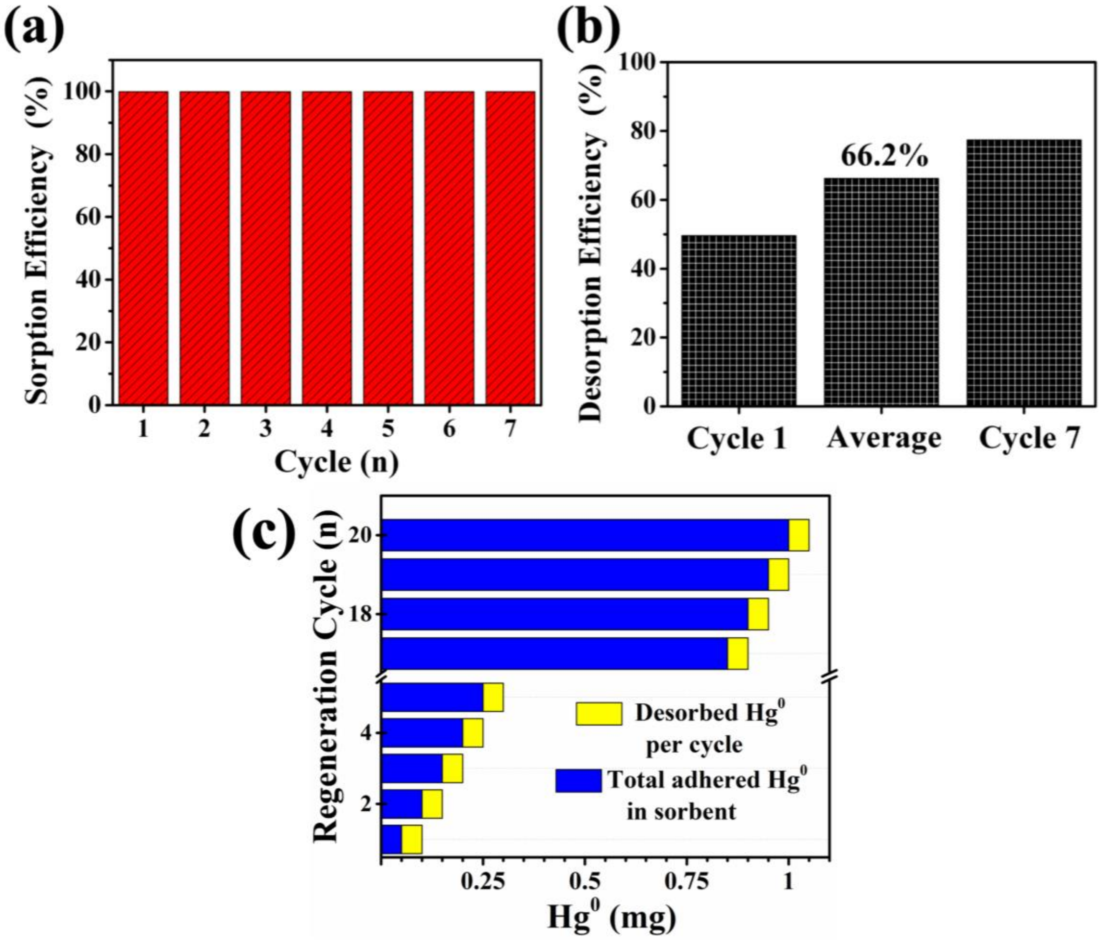

Figure 5. 9. *Regeneration behaviour of MnCe35 over a series of seven successive* Hg^0 *sorption-desorption cycles, a) sorption and b) desorption process. c) Projected maximum regeneration cycles for MnCe35. Average* Hg^0 *desorption per cycle ~66% of* Hg^0_{in} *per cycle (~96 µg* Hg^0*). Maximum* Hg^0 *uptake= 2 wt% (0.5% tolerance).*

5.4.4. CO_2 and H_2S influence on MnCe35

In Set IV first 12.5% CO_2 and then 40 ppm H_2S were added to the methane gas mixture to evaluate the behavior of MnCe35 under real life conditions in which gas resources often contain significant amounts of acid gases (Amott and Mogose, 2015; Goodwin et al., 2015).

Table 5. 5. *Set IV: Effect of acid gases,* CO_2 *and* H_2S *on the* Hg^0 *removal efficiency of MnCe35 at ambient conditions.*

Gas Mixture	***Hg^0 removal efficiency (%)***	***Standard deviation***
Hg^0 + 75% CH_4/N_2	99.9	0.1
Hg^0 + 75% CH_4 + 12.5% CO_2	99.9	0.1
Hg^0 + 75% CH_4 + 12.5% CO_2 + 40 ppm H_2S	99.9	0.1

As shown in Table 5.5 there was no adverse effect on the nanosorbent's performance, at least for the 14-h period of the tests. Ceria-supported manganese oxides have been used previously for the simultaneous Hg and H_2S removal (Chytil et al., 2017), and considering that MnCe35 showed no poisoning from H_2S, it is safe to claim that the developed nanosorbent can be effectively deployed in sour gas environments.

5.4.5. Mechanism of Hg^0 removal

Mn^{4+} species in mixed-valence $MnO_{x,}$ favor Hg^0 removal as they constitute the active sites for Hg^0 oxidation at higher temperatures (> 150 °C). In processes following the Mars-Maessen mechanism, the reduction of Mn^{4+} to Mn^{3+} or even to Mn^{2+} provides the lattice oxygen during the metal transfer process, for the oxidation of the surface adsorbed Hg^0 (Xu et al., 2017a). However, there are only a few studies focusing on the role of valence effect of MnO_2, especially at room temperature processes. Additionally, the role of defects such as oxygen and cation vacancies on α-MnO_2 has been rarely studied (Li et al., 2017a; Tompsett et al., 2014). In the previous chapter it was mentioned that according to the theoretical study of Zhang et al. (2014) Hg^0 undergoes chemisorption on MnO_2(110), especially on oxygen active sites, in a process favored at lower temperatures. Recently, Wang et al. (2019) attempted to theoretically investigate the role of different types of oxygen species on Hg^0 removal by MnO_2, concluding that the surface chemisorbed oxygen promoted Hg^0 oxidation, which is in agreement with our study. As evidenced by XPS, MnCe35 possessed the largest amount of surface adsorbed oxygen species (O_b), explaining partly its superior activity.

The process of oxygen defect formation at MnO_2 surfaces, may play a critical role in its activity (Zhu et al., 2017a). Tompsett et al. (2014) underwent theoretical studies and explained that the enhanced activity of α-MnO_2 compared to other crystal phases, may be attributed to the facile oxygen formation at its exposed surfaces. A process which incorporates oxygen vacancy formation (Yang et al., 2018b; Zhu et al., 2017a) and can be observed through XPS, relates to the reduction of Mn^{4+}/Mn^{3+} ratio in order to maintain electrostatic balance (Lin et al., 2016) as follows (Equation 5.1):

$$–Mn^{4+}–O^{2-}–Mn^{4+}– \rightarrow –Mn^{3+}–\square– Mn^{3+}– +1/2O_2 \qquad (5.1)$$

Indeed, the presence of a higher Mn^{3+}/Mn^{4+} ratio for MnCe35, which was derived from the analysis of Mn2p and Mn3s XPS spectra, might imply the existence of a higher oxygen vacancy content for Hg^0 sorption. As in the case of Ce-doped MnO_2 (Zhu et al., 2017b) the generation of oxygen vacancies can be ascribed to the incorporation of CeO_2 nanoparticles. Additionally, the decoration of α-MnO_2 NTs with CeO_2 may result in the weakening of Mn-O bonds (Zhu et al., 2018a) consequently increasing the mobility of surface oxygen species. This was confirmed by HRTEM, where CeO_2 (200) and (111) crystal planes were clearly observed, indicating that cerium participated in the formation of interface structure, in contrast to what was observed in α-MnO_2 NTs-CeO_2 physical mixture. The XRD patterns of the latter indicated that CeO_2 possibly hindered α-MnO_2 phase, adversely affecting its activity, as confirmed by sorption tests.

Judging from the weak performance of pure CeO_2, it could be argued that the oxygen vacancies of α-MnO_2 (Equations 5.2-5.3) played a far more critical role in active sites than the oxygen vacancy defect sites of CeO_2 (Equations 5.2-5.4). The fact that MnCe35 could be adequately regenerated at higher temperature (350 °C) in comparison to pure α-MnO_2 NTs (250 °C) indicates a higher desorption activation energy, and thus a stronger interaction with the nanocomposite's solid surface.

$$Hg^0_{(gas)} \leftrightarrow Hg^0_{(ads)} \tag{5.2}$$

$$Hg^0_{(ads)} + \alpha\text{-}MnO_{2(surf)} \leftrightarrow Hg(O\text{-}Mn\text{-}O) \tag{5.3}$$

$$Hg^0_{(ads)} + CeO_{2(surf)} \leftrightarrow Hg(O\text{-}Ce\text{-}O) \tag{5.4}$$

Consequently, the modification of a certain morphology of α-MnO_2 by means of ceria nanoparticles decoration, can significantly improve its Hg^0 removal activity at room temperature. This is exciting given that there are many studies reporting Mn-Ce composite materials for Hg^0 removal, however operating at high temperatures (> 150 ºC).

5.4.6. Comparison with Sorbents Prepared for Natural Gas Demercuration

Table 5.6 presents the available alternative materials, recently proposed for natural gas demercuration. Considering the extensive literature review in Chapter 2, CeO_2-decorated α-MnO_2 NTs possesses certain advantages which are related to its high selectivity, Hg^0 vapor uptake and regenerability, that render it environmentally and economically promising for utilization in several industrial processes requiring low temperature Hg^0 removal. The next step (Chapter 6) investigates its incorporation in an engineered structure support that could be deployed at production scale operations.

***Table 5. 6**. Comparison of sorbents developed for Hg^0 removal from natural gas streams.*

Sorbent	***Experimental conditions***	***Hg^0 uptake***	***Hg^0 breakthrough tolerance***	***Regeneration temperature***	***Ref.***
10 wt.% [N_{4441}]Cl-$CuCl_2$ SILP on silica	Hg^0_{in}=2,000 µg·m^{-3}, gas mix=N_2, feed=600 mL·min^{-1}, T=25 °C	25 mg·g^{-1}	0.5%	–	(Abai et al., 2015)
Sulfonated carbon (SC 600)	Hg^0_{in}=50 µg·m^{-3}, gas mix= He, feed=500 mL·min^{-1}, T=50 °C	5.5 mg·g^{-1}	–	–	(Kumar Reddy et al., 2016)
C-AgNPs/4A-zeolite	Gas mix=CH_4, GHSV=4.2x10^4 h^{-1}, T=30 °C	6 mg·g^{-1}	–	250 °C	(Sun et al., 2018)
CeO_2-decorated α-MnO_2 NTs	Hg^0_{in}=870 µg·m^{-3}, gas mix=N_2/CH_4, GHSV=1.1x10^5 h^{-1}, T=25 °C	> 20 mg·g^{-1}	0.5%	350 °C	this study

Chapter 6. Outlook and Challenges: Coating 3D-Printed Structures with CeO_2-Decorated α-MnO_2 Nanotubes

6.1. Chapter Overview

In the final chapter the previously developed MnCe35 nanocomposite is loaded on an 3D-printed Ti-based support structure (3DTi) with the aim of demonstrating its applicability at full scale operations. Monolithic structures are advantageous in gas separations because they provide substantially uniform flow paths which result in the reduction of the pressure drop across the fixed-bed reactor. Also they possess high thermal stability, good mechanical integrity as well as improved heat or/and mass transfer characteristic. 3DTi was manufactured by selective laser melting (SLM) with Ti-6Al-4V alloy powder as the source material. A simple dip-coating process resulted in the loading of less than 5 wt% of MnCe35 on its surface, which was high enough to allow it capture almost 100% of Hg^0 vapor in a preliminary 7-h test at ambient conditions. The materials characterization with XRD, SEM and EDS helped identify the areas which require further research with respect to the optimization of the coating process as well as the improvement of the mercury removal capacity. Taking into account the results in this chapter, the current challenges and future research work are thoroughly discussed in the epilogue.

6.2. Background and Rationale

The active material used in catalytic and adsorption processes is often structured into beads, granules, spheres or pellets using binders and processing techniques like extrusion or spray drying. These materials are packed together within a unit as a packed bed, in which tortuous flow results in large pressure drops (Rezaei and Webley, 2009). In engineered structures the active materials are coated into substrates such as metal or ceramic monoliths, which provide substantially uniform flow paths that reduce the pressure drop (Brody et al., 2018; Govender and Friedrich, 2017; Ide et al., 2018; Kreutzer et al., 2006). Monolithic structures are generally characterized by high thermal stability, good mechanical integrity as well as improved heat or/and mass transfer characteristics (Gu and Balakotaiah, 2016; Rezaei and Webley, 2010). They are advantageous in multiphase reactions (Roy et al., 2004) and can be prepared through direct extrusion (Akhtar et al., 2014) or as previously stated by attaching an active layer to the support structure via wash-coating, dip-coating or crystal growth among other methods (Mehla et al., 2019; Meille, 2006; Montebelli et al., 2014; Sonström et al., 2011).

Nevertheless, slurry coating sacrifices the catalyst utilization efficiency as a result of the large amount of catalyst loading. It also requires careful control of slurry's viscosity to ensure good adherence. Alternatively, nanostructure array-based monolithic catalysts (Ren et al., 2015; Weng et al., 2017), have been developed by in situ growing hierarchically arranged arrays of various types of nanostructures onto bare-channeled monolithic substrates. In general, the challenge in shaping monolithic contactors lies in the compromise between the active phases coating, the heat and/or mass transfer properties, and cell density which is expressed in terms of cells per square inch (cpsi) (Rezaei et al., 2011). To achieve higher sorption/catalytic activity a higher active phase content per unit volume is desirable, however as a consequence of the thicker walls the reaction kinetics tend to be slower. Moreover, structure shapes characterized by high-cell-density offer larger surface area and allow maximum active phase loading, but the trade-off is the significantly higher pressure drop through the narrow channels.

3D-printing (Ruiz-Morales et al., 2017) also known as additive manufacturing (Hurt et al., 2017) provides much higher level of freedom in operation, allowing to generate a wide variety of structures. In the last years 3D-printing, has become popular in both catalytic (Azuaje et al., 2017; Michorczyk et al., 2016; Minas et al., 2016; Tubío et al., 2016) and adsorption processes (Couck et al., 2018; Couck et al., 2017; Nguyen et al., 2018; Thakkar et al., 2017; Thakkar et al., 2016). Compared to the conventional extrusion technique the 3D-printing technique offers substantial benefits which relate to the precise fabrication of configurations with controllable channel size, wall thickness, and density.

Manganese and/or cerium oxide-based monolithic catalysts have been utilized for the cleaning of automotive exhaust gases (González-Velasco et al., 2003), the selective catalytic reduction of NO_x (Feng et al., 2016; Liu et al., 2017; Liu et al., 2015; Xu et al., 2012), as well as CO (Barbato et al., 2016; Gómez et al., 2013) and VOCs oxidation (Aguero et al., 2011; Azalim et al., 2013; Barbero et al., 2008; Hernández-Garrido et al., 2015; Park et al., 2014). Fewer studies have been published with respect to Hg^0 vapor abatement. Izquierdo et al. (2011) coated a honeycomb-structured carbon monolith with carbon-supported Au nanoparticles for the capture of Hg^0 at 120 °C and GHSV=53,000 h^{-1}. TPD showed that the amalgamated mercury could be desorbed at temperatures as low as 220 °C (Ballestero et al., 2013). The same sorbent was effective for mercury capture under oxycoal conditions (Gómez-Giménez et al., 2015; Gómez-Giménez et al., 2017) with O_2 inhibiting its activity and CO_2 not causing any impact. More recently, a copper-based monolithic mercury sorbent was developed for use in the dry syngas purification unit of an oxy-fuel IGCC power generation system at 220 °C and 0.98 MPa (Akiho and Kobayashi, 2019). The honeycomb was pre-sulfided with H_2S and could be regenerated at 280 °C. Additionally, $MnO_x/\gamma\text{-}Al_2O_3$ (Scala et al., 2013; Scala and Cimino, 2015) was supported as a thin layer (40 μm) into a cordierite honeycomb monolith. The sorbent was effective up to 300 °C and could be regenerated at 500 °C, with CO_2 moderately inhibiting mercury capture. TiO_2 has been successfully employed in the past as a support for MnO_x or/and CeO_2 active phases for the oxidation/adsorption of Hg^0 vapor (He et al., 2011; 2013; Li et al., 2012a; Li et al., 2012b). Its selection as a support as opposed to Al_2O_3 or ZrO_2, is based on the fact that in the presence of SO_2 and O_2 it can be weakly and reversibly sulfated.

It has been reported that the formation of a compact TiO_2 layer on Ti-6Al-4V by oxidation, enhances its corrosion resistance, making it attractive for employment in oil and gas applications (Lin et al., 2017). Given this as well as its high strength-to-weight ratio, the aforementioned titanium alloy (Xu et al., 2017b) was utilized in our study for the 3D-printing (SLM) of a support structure that can accommodate on its surface the MnCe35 active phase. The characterization of the coated (C-3DTi) and uncoated structure (3DTi) through XRD, SEM and EDS helped us identify the direction of future research, which is the subject of discussion in the final section.

6.3. Assessment of the 3D-Printed Ti-Based Structure as a Support for MnCe35

6.3.1. XRD Analysis

Figure 6.1 presents the X-ray diffractograms of the 3DTi and C-3DTi samples. The XRD pattern of MnCe35 powder has been also included to help the reader evaluate the efficiency of the coating process. Depending on the thermochemical processing Ti-6V-Al may attain an equiaxed α (HCP) or/and intergranular β (BCC) microstructure, with each one possessing different mechanical characteristics (Yang et al., 2016). During SLM process, as a result of the rapid solidification and cooling rates, β (BCC) phase of Ti-6Al-4V alloy transforms into HCP α (HCP). Indeed, the XRD pattern of 3DTi in Figure 6.1 shows that the body centred cubic (BCC) β-phase was not clearly detected. If it was present, β-Ti peaks would appear at 2θ=39.5º and 57º, corresponding to reflections of (110) and (200) planes (Chen et al., 2017). On the contrary the XRD peaks observed are typical of the hexagonal closed-packed α (HCP) structure of Ti (Yang et al., 2016). The peaks at 35.5º, 38.6º, 40.6º, 53.3º, 63.5º, 71º and 76.8º correspond to the (100), (002), (101), (102), (110), (103) and (112) planes, respectively, of α-Ti (ICDD-PDF 44-1294). By comparing the diffractograms of 3DTi, C-3DTi and MnCe35 one can identify the XRD peaks of the coated Ti alloy, which correspond to the Mn-Ce nanocomposite loaded on its surface. It is very interesting that both (200) and (220) crystal planes of ceria nanoparticles can be easily distinguished on C-3DTi's XRD pattern.

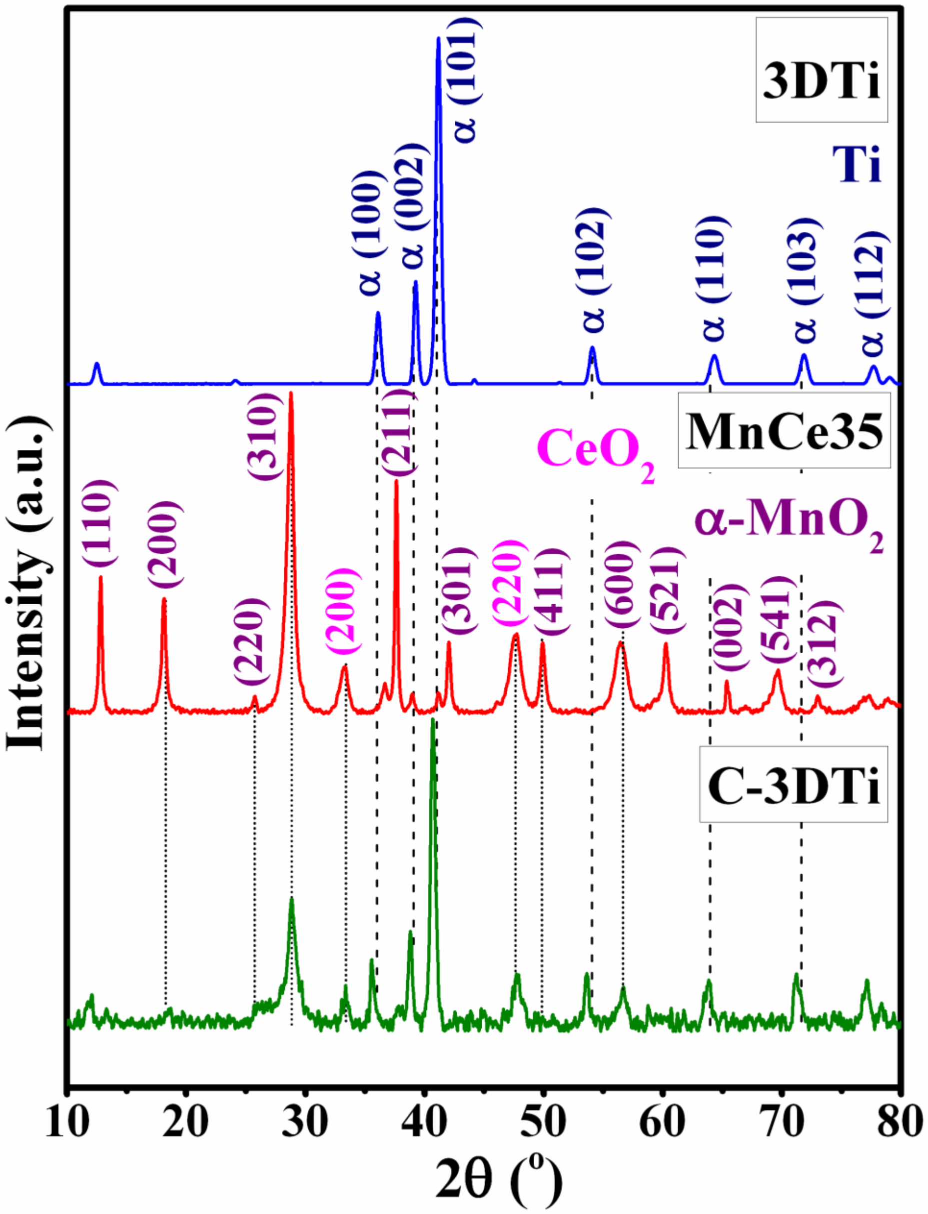

***Figure 6. 1**. X-ray diffractograms of the 3DTi and C-3DTi samples as well as the MnCe35 powder used for coating.*

6.3.2. SEM Imaging

Figure 6.2 illustrates the SEM images of the 3DTi support structure. Figure 6.2a shows that the honeycomb-like structure presents a fully interconnected open-pore architecture. The channels of the monolithic support structure have a shape of isosceles triangle with a base of about 500 μm. It is evident in low magnifications images (Figures 6.2b, 6.2c and 6.2d) that aggregates of non-melted Ti-6Al-4V globules were present on the printed sample (3DTi). These loosely-bound surface particles may be deleterious to the mechanical properties of the support structure. To improve the surface quality, future work is recommended to include methods (e.g. chemical etching) (Song et al., 2019) that will remove the weakly-bonded particles.

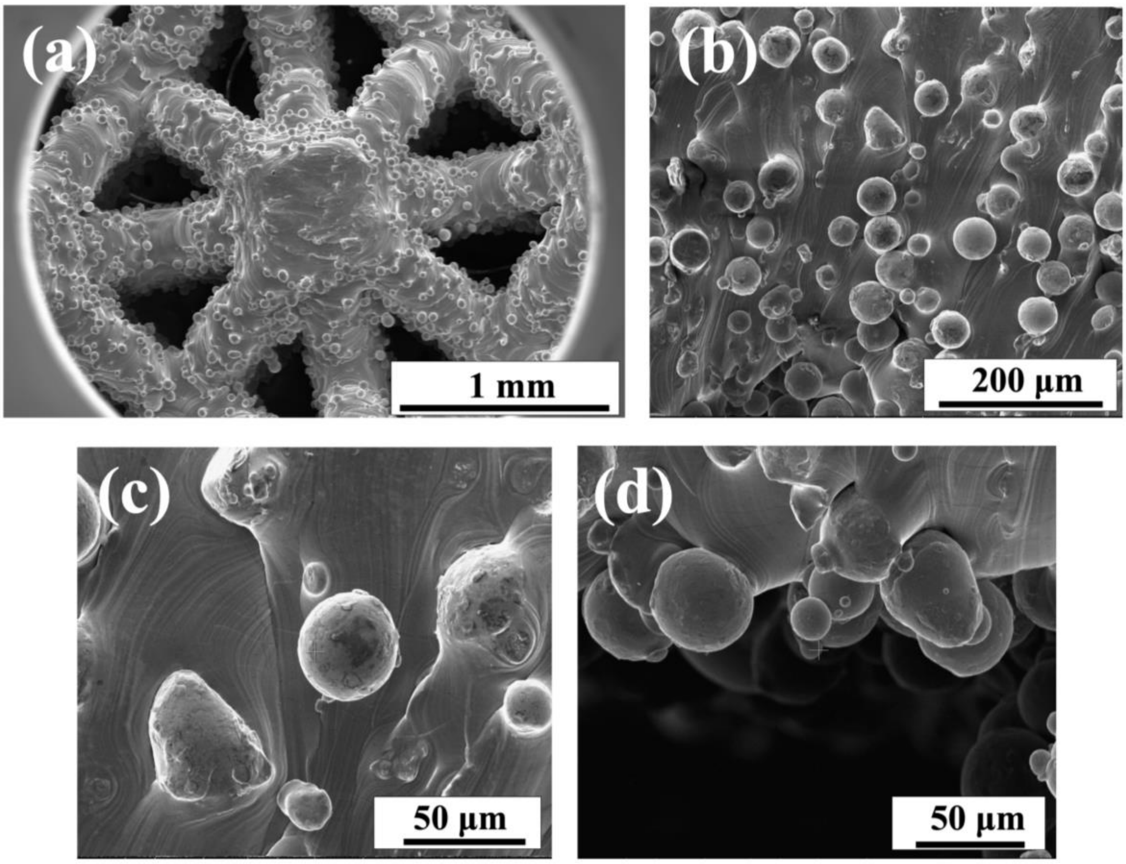

***Figure 6. 2**. SEM images of the 3DTi support structure at different magnifications.*

Figure 6.3 displays SEM images of the support structure after having been coated with the Mn-Ce nanocomposite (C-3DTi). The low-magnification image in Figure 6.3a presumably shows the initiation of a nucleation and agglomeration process regarding the surface weakly-bound particles. It is possible that during the coating process a TiO_2 layer started forming on the surface of C-3DTi. The EDS analysis presented in the next section, indicates a significant increase in the amount of oxygen in the coated support, while the composition of titanium was considerably lower. Actually, the formation on TiO_2 layer has been reported to provide chemical inertness (e.g. corrosion resistance). However, it is obvious from the higher-magnification images that this process is only at a very early stage and most importantly it was not intended. Despite the fact that agglomeration has taken place, the pores of the channels have not been affected, being still capable to facilitate the gas flow through C-3DTi.

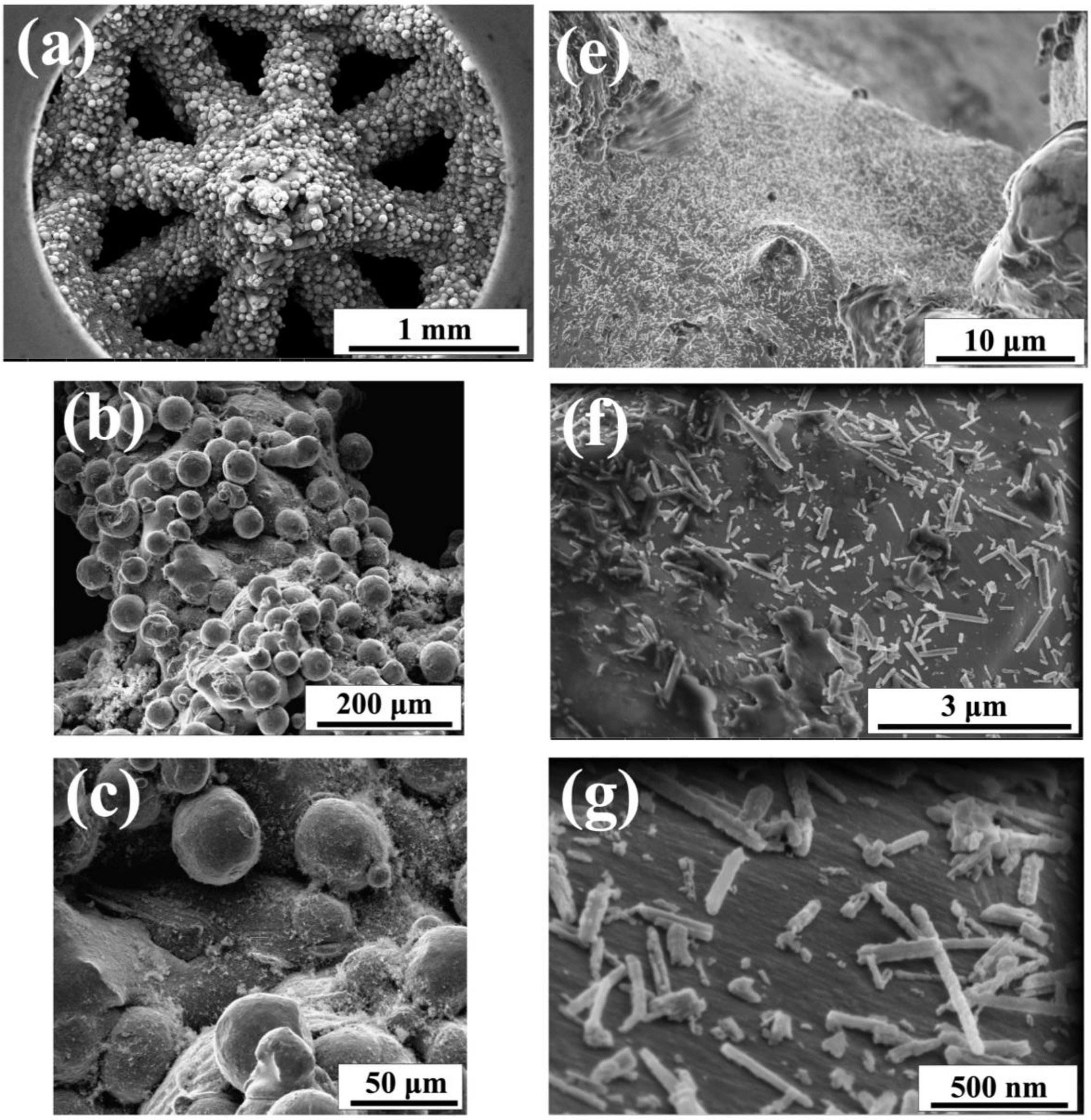

***Figure 6. 3**. SEM images of the C-3DTi sorbent at different magnifications.*

As the magnification of the images increases (Figures 6.3b and 6.3c) it becomes obvious that there are several sections covered by the CeO_2-decorated α-MnO_2 nanotubes, although it is rather clear that the coverage is neither full nor homogenous. At the highest magnification (Figures 6.3.e, 6.3f and 6.3g) the decorated nanotubes can be readily distinguished. Most importantly, it can be observed that the shape and size of MnCe35 nanostructure is maintained, ensuring in this way that the unique properties of the Mn-Ce nanosorbent (as manifested in Chapter 5), can be still exploited. An interesting topic for further research would be the investigation of the effect of TiO_2 formation as well as the optimization of MnCe35 layer, so that more active phase can be loaded without affecting the pressure drop in the reactor as a result of pores blocking.

6.3.3. EDS Elemental Mapping

To evaluate the coating process as well as compare the composition of the 3D-printed support structure with the nominal composition given for the Ti-6Al-4V powder, SEM-EDS was performed on both uncoated and coated samples. Figure 6.4 displays the ESD elemental spectrum of 3DTi and C-3DTi and Table 6.1 presents the quantitative analysis results. Furthermore, Figures 6.5 and 6.6 illustrate the respective surface elemental mapping.

Table 6. 1. *SEM-EDS normalized surface atomic weights of 3DTi and C-3DTi.*

Sample	***Ti (%)***	***Al (%)***	***V (%)***	***O (%)***	***Mn (%)***	***K (%)***	***Ce (%)***
3DTi	86.7	4.8	4.2	4.3	-	-	-
C-3DTi	48.7	2.5	2.4	33.5	8.2	0.4	4.3

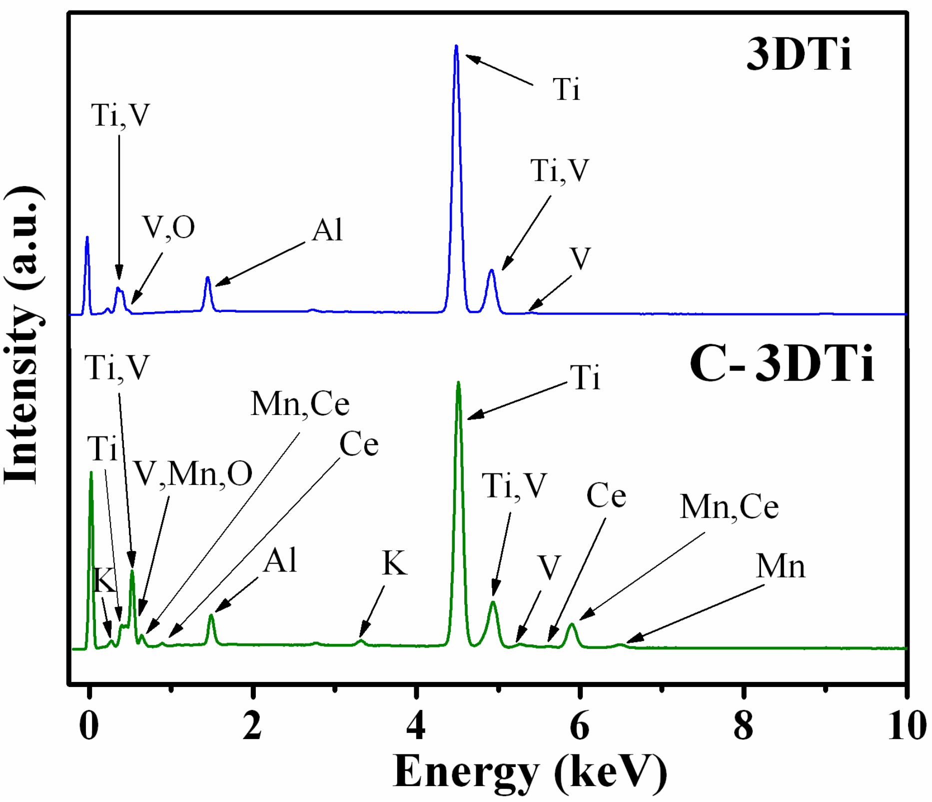

Figure 6. 4. *SEM-EDS elemental spectrum of both 3DTi and C-3DTi structures.*

The peaks at 4.51 and 1.49 keV in the spectrum of 3DTi, clearly confirm the presence of titanium and aluminium, respectively. The overlapping peaks at about 4.94 and 0.45 keV can be attributed to both vanadium and titanium. The surface oxygen composition was quite higher (4.3 wt%) than that in the source powder (0.1 wt%), which is up to certain extend expected, given the nature of the manufacturing process. The surface concentration of vanadium is around as much as indicated in Ti-6Al-4V powder, while that of aluminium is less than 6 wt%. As it is shown in Figures 6.5b, 6.5c and 6.5d, the presence of aluminum, vanadium and titanium is uniform and homogenous. Apart from the peaks attributed to titanium, aluminium and vanadium, the EDS spectrum of C-3DTi suggests the presence of manganese, cerium and potassium, proving that the coating process was successful. The peak at 6.49 keV can be ascribed to manganese, those at 5.61 and 0.88 keV can be attributed to cerium, while that at 3.59 keV to potassium. Peak overlapping between manganese and cerium was observed at around 5.75 and 0.65 keV.

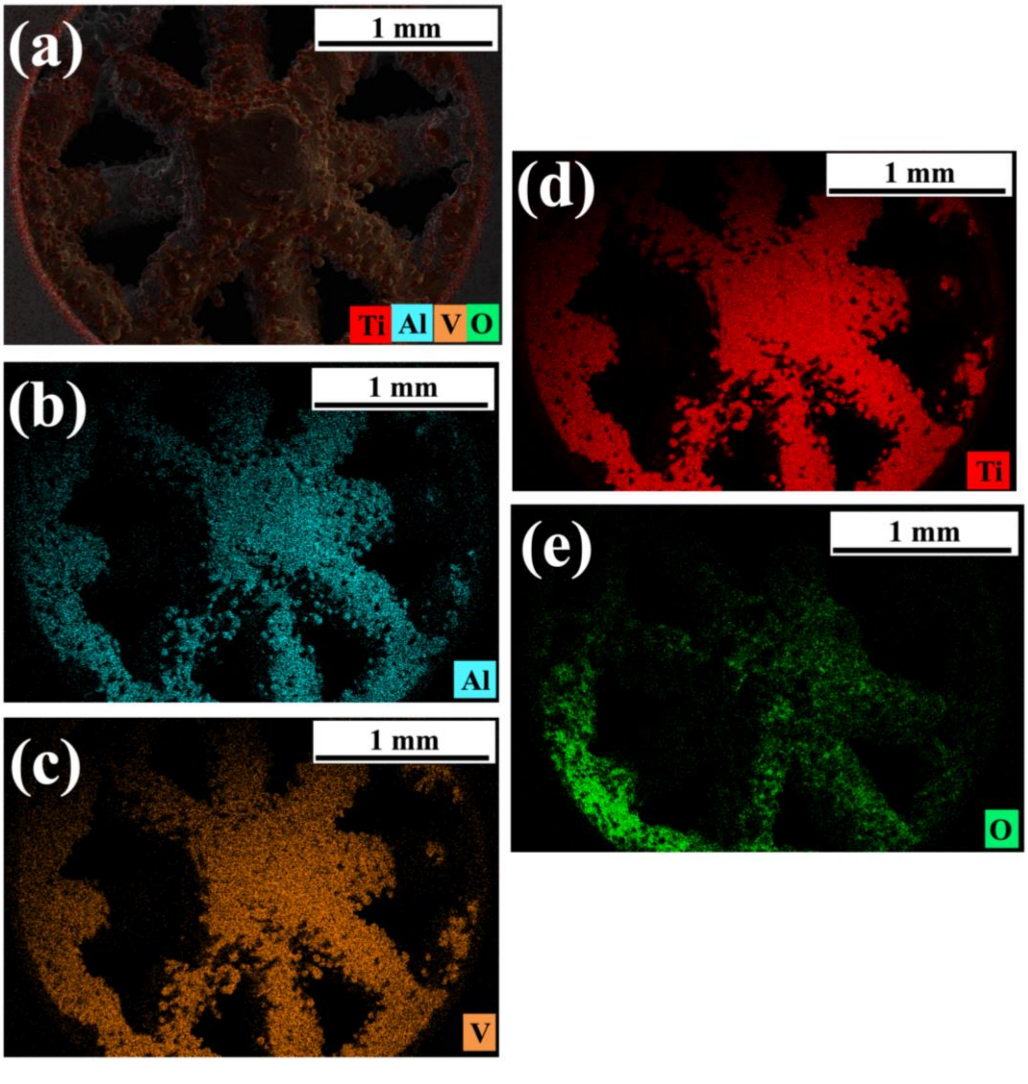

Figure 6. 5. *SEM-EDS elemental mapping of the 3DTi support structure.*

The most interesting observation with respect to the examination of C-3DTi, relates to the significant reduction in the surface elemental composition of titanium (48.7%), accompanied by a considerable increase in oxygen's concentration (33.5%). As previously assumed, this is may be due to the deposition process of MnCe35, which caused the formation TiO_2. Both manganese and cerium were detected at a weight ratio of almost 2:1. The presence of potassium (0.4 wt%) can be explained by the fact that $KMnO_4$ was used as the source material for the production of α-MnO_2.

Figure 6.6a shows that the coverage of MnCe35 on the surface of C-3DTi is not uniform. There are sections where the concentration of MnCe35 is considerably higher, which is something that was also underlined in the previous section. Of course the black sections on the mages are the result of the orientation of X-ray beam during analysis, given that the support structure has a honeycomb-like shape. To optimize the coating process, future research work should focus on increasing the amount of coated material as well as improving the coverage uniformity, without compromising the gas flow rate through the channels.

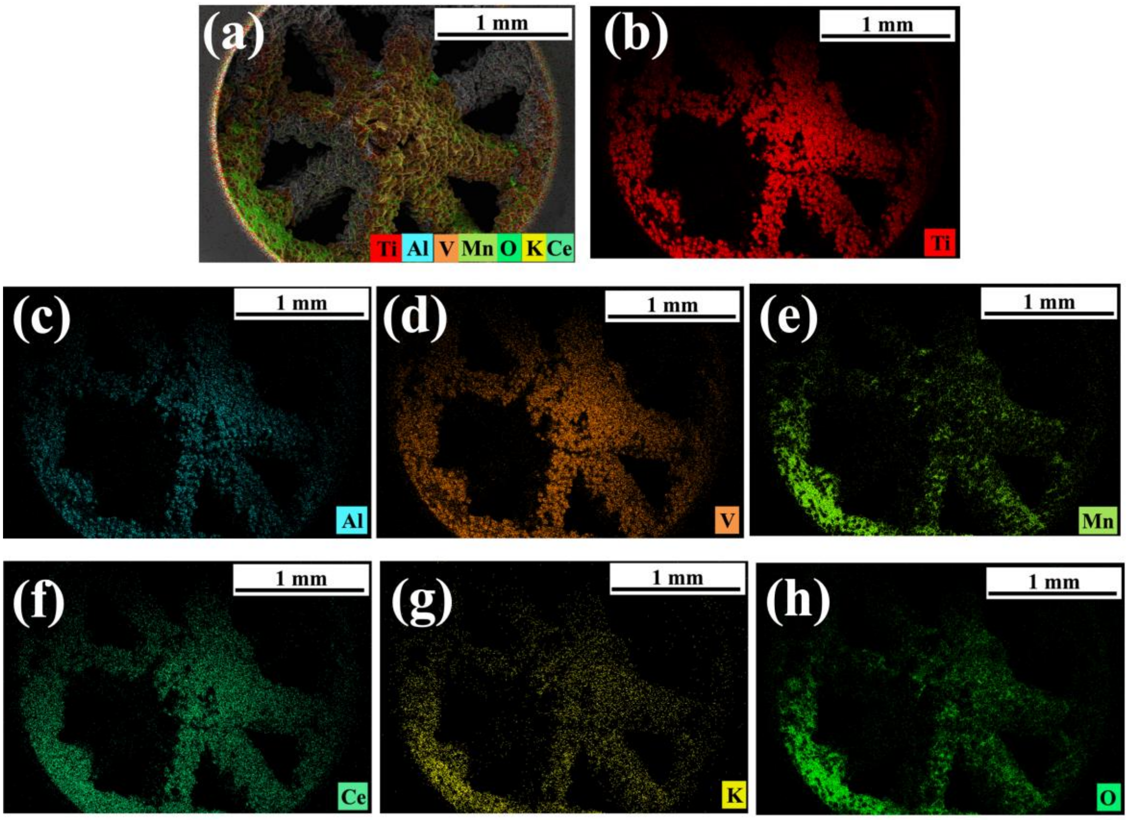

Figure 6. 6. *SEM-EDS elemental mapping of C-3DTi sorbent.*

6.3.4. Mercury Removal Efficiency

To assess the potential of C-3DTi for mercury capture, a preliminary test was conducted under the conditions described in Table 6.2 (Set I). The aim of this experiment was to show that the coated-support structure does not only perform substantially better than the uncoated, but it also possesses highly advantageous properties for application at full scale. As explained in the background section of this chapter, these properties are related to its mechanical integrity, improved heat or/and mass transfer characteristics and its ability to facilitate high gas flow rates with low pressure drops in the reactor.

Table 6. 2. *Experimental conditions for the assessment of the mercury removal efficiency of pure (3DTi) and coated (C-3DTi) 3D-printed Ti-based support structure.*

Set	***Nanosorbent***	***Gas components***	***Operating conditions***
Set I	3DTi, C-3DTi	Hg^0/N_2	T=25 °C, Hg^0_{in}=290 $\mu g \cdot m^{-3}$, total gas flow rate= 200 $ml \cdot min^{-1}$

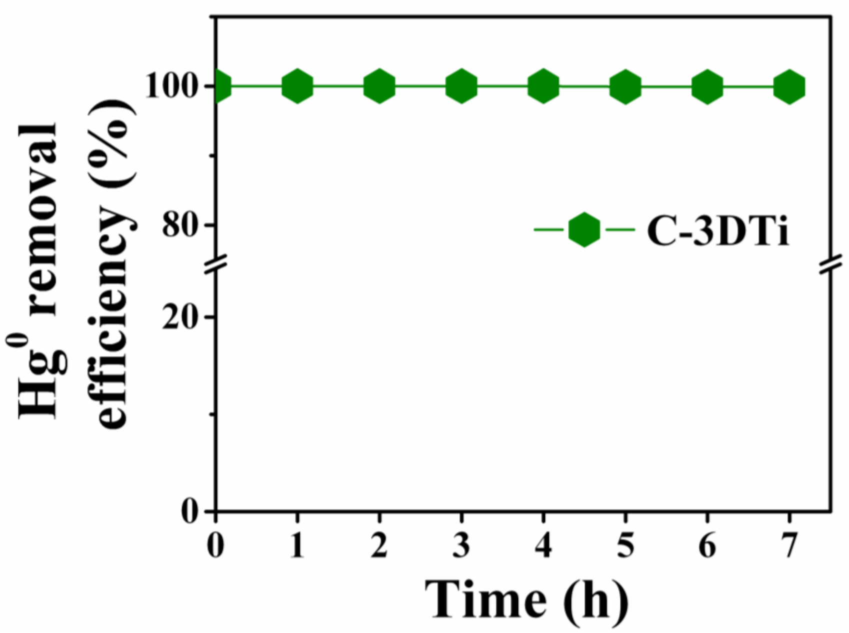

Figure 6. 7.*Mercury removal efficiency of C-3DTi under the conditions specified in Table 6.2.*

The 3DTi structure, which was tested at the same conditions as the C-3DTi sorbent, could not really capture any worth-mentioning amount of mercury. TiO_2, Al_2O_3 and V_2O_5 have all been extensively used in the design of commercial catalysts for the oxidation of Hg^0 vapor at temperatures above 150 °C, but they only possess very low adsorption capacity at room temperature conditions. Besides, the presumably induced by the coating process TiO_2 formation on the surface of the support structure, is unlikely to lead to any substantial activity. On the contrary the C-3DTi sorbent manifested an excellent Hg^0 removal capacity in the preliminary 7-h test. Figure 6.7. shows that it maintained almost 100% Hg^0 removal efficiency under the flow of dry N_2 gas. It should be reminded, to utilize the tetragonal tubular 3D-printed sorbent, a custom-made reactor (see Chapter 3) was manufactured from Teflon so as to ensure no interference with the gaseous mercury as well as full contact with the gas stream, which was not possible to achieve with the cylindrical quartz reactor employed for all previous experiments.

6.4. Summary and Future Work

The objective of this thesis was the development of regenerable sorbents for the removal of Hg^0 vapor from natural gas streams at ambient conditions. In comparison to the available, both conventional and alternative sorbents, metal oxides offer advantageous properties, including high sorption capacity, strong metal-ion affinity and most importantly, capacity for regeneration and reuse. Among the plethora of sorbents/catalysts developed for the abatement of Hg^0 in combustion flue gases at temperatures higher than 150 °C, MnO_x and CeO_2 have been proven to exhibit an excellent synergistic effect. However, the flue gas conditions differ from those pertaining to natural gas processing operations, which require regenerable and room-temperature efficient sorbents with very small Hg^0 breakthrough tolerances at high-mercury concentration gas streams and reducing conditions. In the last years with the advance of nanoscience it has been realized that the shape and size of sorbents/catalysts particles may play a defining role in their activity. Considering this, as well as the previous studies regarding the abatement of mercury in flue gases, the focus of this work was placed on the examination of certain properties at nanoscale that could render MnO_x and CeO_2 attractive for natural gas demercuration.

First, a specific crystal structure of MnO_2, α-MnO_2, was selected for investigation because of its tunnel cavity, moderately acidic sites and easy release of lattice oxygen. Among, the different nanomorphologies synthesized and tested, nanotubes (of about 50 and 90 nm internal and external diameter, respectively) manifested a particularly promising performance. The nanosorbent exhibited a mercury uptake of 1 wt% at 0.5% Hg^0 breakthrough tolerance, and was repeatedly, sufficiently regenerated at only 250 °C without being affected by common acid gases like CO_2 and H_2S. This outcome confirmed previous reports with respect to the effects of nanocatalysts' shape. XPS and TG analysis of the prepared materials revealed that a possible explanation may be related to the abundance of surface adsorbed oxygen species on the surface of α-MnO_2 NTs, which are believed to facilitate Hg^0 bonding through relatively strong physical sorption.

Given that recently proposed alternative materials (i.e. immobilized ionic liquids) have manifested better sorption capacities, the next step was to enhance the capacity of the developed nanosorbent by sustaining at the same time its regeneration ability, which is its major competitive advantage. After experimenting with different synthesis methods to accommodate CeO_2, it was found out that nanoparticles (~35 nm) of the latter can be incorporated onto α-MnO_2 NTs by a low-temperature post hydrothermal method, which leads to the formation of a highly active interface. The ceria saturated Mn-Ce nanocomposite manifested twice the mercury uptake of pure α-MnO_2 NTs, and could still be adequately regenerated at the relatively low temperature of 350 °C. XPS analysis indicated that a possible explanation for its enhanced activity may be related to the generation of oxygen vacancies at the active α-MnO_2 surfaces, as a result of the CeO_2 nanoparticles introduction. The fact that the nanocomposite was sufficiently regenerated at a higher temperature than the pure α-MnO_2, suggested a stronger bonding of the adhered Hg^0. Also, tests conducted with the control materials (CeO_2 nanoparticles and α-MnO_2-CeO_2 physical mixture) indicated that the oxygen vacancies of α-MnO_2 played a far more critical role in the active sites than the oxygen vacancy defect sites of CeO_2. This is based on the fact that pure CeO_2 exhibited much lower mercury uptakes. This outcome is particularly important given that in most studies which utilized Mn-Ce composite materials for Hg^0 removal, the operating temperatures were at least 150 ºC.

The last section of this thesis discussed the feasibility of employing the developed Mn-Ce nanosorbent at full scale. For this, the synthesized powder material was loaded onto a 3D-printed Ti-based support structure through a simple dip-coating process. It is known that such engineered monolithic structures offer advantageous properties, as they can accommodate high gas flow rates with small increases in pressure drop across the bed. A titanium alloy (Ti-6Al-4V) was selected as the source material for the manufacturing (SLM process) of the honeycomb-like tetragonal tubular support, because of its corrosion resistance and high strength to weight ratio. Besides, TiO_2 has been reported to be favourable over Al_2O_3 and ZrO_2 supports in the design of composite catalysts, due to the fact that it is not irreversibly sulfated when SO_2 and O_2 are present in the gas reaction. Although the active phase (CeO_2/α-MnO_2) which was loaded by a simple dip-coating process, constituted less than 5wt% of the sorbent’s mass, the coated structure captured almost 100% Hg^0 in a preliminary 7-h test. This is particularly exciting considering the vast opportunities that additive manufacturing offers.

The question that is always raised when nanomaterials are proposed for specific applications, relates to the development of an economically viable procedure for their synthesis at large scale. Despite the fact that currently such methods are not widely deployed, techniques such as electrospinning are considered to be promising. Therefore the scope of future work, at least as far as the nanomaterials preparation procedure is concerned, concerns the investigation of synthesis methods that could potentially result in materials with the desirable properties. Furthermore, another aspect of this work that requires further research, regards the elucidation of Hg^0 removal mechanism. It is true, that the characterization methods employed in this study provided some useful indications, but there is no doubt that a vigorous investigation is required. For example, it is known that nanocatalysts exposing more active crystal facets may be favourable in several applications (e.g. oxidation reactions). Indeed, HRTEM analysis in our work showed that such correlations may be established if the research objective is directed on this subject.

Although the potential impact of CO_2 and H_2S acid gases was addressed, it is true that this study focused rather on proving that there was no adverse effect on the performance of the tested nanosorbents under the specified conditions. However, previous studies have reported that H_2S, for instance, may promote Hg^0 removal process by interacting with mercury to form HgS. Therefore, it is recommended that future research should possibly involve extended tests in the presence of higher H_2S concentrations. Additionally, water vapor must be included in the gas mixture, since it is known to play an inhibitory role. This is actually the reason why sulfur-impregnated carbons are replaced by metal sulfides when they are utilized in MRUs located at the front of the gas plants, where the inlet gas stream is wet. Hence, the effect of water vapor must be verified, and the tolerance of the developed nanosorbent should be determined. To improve its activity modifiers such as hydrophobic agents could be possibly utilized.

Finally, as explained in the this chapter, one may construct directly the desired monolithic sorbent or produce a support structure that can be modified at a later stage by making use of post-treatment methods (e.g. washcoating). In the first case the challenge is to produce the desired material in a controllable way. In the second case the aim is to develop an optimized coating process without comprising the fundamental advantageous properties offered by the use of the honeycomb-like support (e.g. uniform flow path). Without rejecting the first case scenario, our challenge most probably relates to the second case. The optimal support to active phase ratio should be identified, without compromising the support’s inherent advantages. Moreover, the regeneration ability of the coated structured sorbent must be investigated. In any case, other engineered structures produced by different materials and methods should be compared in order to determine the extent of the support's effect on the sorbent's performance.

References

Abai, M., Atkins, M.P., Cheun, K.Y., Holbrey, J.D., Nockemann, P., Seddon, K.R., Srinivasan, G., Zou, Y., 2017. Process for removing metals from hydrocarbons. U.K. Patent 2547364 A.

Abai, M., Atkins, M.P., Hassan, A., Holbrey, J.D., Kuah, Y., Nockemann, P., Oliferenko, A.A., Plechkova, N.V., Rafeen, S., Rahman, A.A., Ramli, R., Shariff, S.M., Seddon, K.R., Srinivasan, G., Zou, Y., 2015. An ionic liquid process for mercury removal from natural gas. Dalton Trans. 44, 8617-8624.

Abbas, T., Gonfa, G., Lethesh, K.C., Mutalib, M.I.A., Abai, M.B., Cheun, K.Y., Khan, E., 2016. Mercury capture from natural gas by carbon supported ionic liquids: Synthesis, evaluation and molecular mechanism. Fuel 177, 296-303.

Abbas, T., Kallidanthiyil Chellappan, L., Mutalib, M.I.A., Cheun, K.Y., Nasir Shah, S., Nazir, S., Hassan, A., Abai, M.B., Khan, E., 2015. Stability and performance of physically immobilized ionic liquids for mercury adsorption from a gas stream. Ind. Eng. Chem. Res. 54, 12114-12123.

Abbott, J., Openshaw, P.J., 2002. Mercury removal technology and its application. In: 81st GPA Annual Convention. Dallas, TX, United States.

Abu El Ela, M., Mahgoub, I.S., Nabawi, M.H., Abdel Azim, M., 2007. Mercury monitoring and removal at gas processing facilities. In: SPE Europec/EAGE Annual Conference and Exhibition. London, United Kingdom.

Achazhiyath Edathil, A., Banat, F., Kumar Reddy, K.S., Srinivasakannan, C., Shoaibi, A., 2018. Alginate-pyrolyzed porous carbon as efficient gas phase elemental mercury scavenger. J. Nat. Gas Sci. Eng. 55, 165-173.

Adriano, D.C., 2001. Mercury. In: Trace elements in terrestrial environments: Biogeochemistry, bioavailability, and risks of metals (2nd ed.), Springer-Verlag, New York, NY, United States, pp. 411-458.

Aguero, F.N., Barbero, B.P., Almeida, L.C., Montes, M., Cadús, L.E., 2011. MnO_x *supported on metallic monoliths for the combustion of volatile organic compounds. Chem. Eng. J. 166, 218-223.*

Akhtar, F., Andersson, L., Ogunwumi, S., Hedin, N., Bergström, L., 2014. Structuring adsorbents and catalysts by processing of porous powders. J. Eur. Ceram. Soc. 34, 1643-1666.

Akiho, H., Kobayashi, M., 2019. Development of reusable mercury sorbents for an oxy-fuel IGCC power generation system. Fuel 253, 1385-1391.

Al Mazrouei, R., Salmeen, H., Agung, M., 2018. Criteria of bypassing main cryogenic heat exchanger de-riming procedure. In: Abu Dhabi International Petroleum Exhibition & Conference. Abu Dhabi, United Arab Emirates.

Al-Faqeer, F., 2007. Method and apparatus for removing mercury from natural gas. U.S. Patent 2007/0246401.

Al-Sawafi, K., Al-Jabri, H., 2017. Optimization of mercury removal unit MRU location in gas processing facilities. In: Abu Dhabi International Petroleum Exhibition & Conference. Abu Dhabi, United Arab Emirates.

Alcheikhhamdon, Y., Hoorfar, M., 2016. Natural gas quality enhancement: A review of the conventional treatment processes, and the industrial challenges facing emerging technologies. J. Nat. Gas Sci. Eng. 34, 689-701.

Alexandratos, S.D., 2009. Ion-exchange resins: A retrospective from industrial and engineering chemistry research. Ind. Eng. Chem. Res. 48, 388-398.

Ambrosini, R.F., Anderson, R.A., Fornoff, L.L., Manchanda, K.D., 1978. Selective adsorption of mercury from gas streams. U.S. Patent 4,101,631.

Amott, N., Mogose, S., 2015. Typical process challenges and configurations for sour gas mega projects. In: SPE Kuwait Oil and Gas Show and Conference. Mishref, Kuwait.

AMMRF, 2019a. Scanning electron microscope training module (MyScope). Australian Microscopy & Microanalysis Research Facility, Australia.

AMMRF, 2019b. Transmission electron microscope training module (MyScope). Australian Microscopy & Microanalysis Research Facility, Australia.

Ariya, P.A., Amyot, M., Dastoor, A., Deeds, D., Feinberg, A., Kos, G., Poulain, A., Ryjkov, A., Semeniuk, K., Subir, M., Toyota, K., 2015. Mercury physicochemical and biogeochemical transformation in the atmosphere and at atmospheric interfaces: A review and future directions. Chem. Rev. 115, 3760-3802.

ASTM International, 2014a. D5954-98: Standard test method for mercury sampling and measurement in natural gas by atomic absorption spectroscopy. West Conshohocken, PA, United States.

ASTM International, 2014b. D6350-14: Standard test method for mercury sampling and analysis in natural gas by atomic fluorescence spectroscopy. West Conshohocken, PA, United States.

ASTM International, 2016. D6784-16: Standard test method for elemental, oxidized, particle-bound and total mercury in flue gas generated from coal-fired stationary sources (Ontario Hydro method). West Conshohocken, PA, United States.

ASTM International, 2017a. D5198-17: Standard practice for nitric acid digestion of solid waste. West Conshohocken, PA, United States.

ASTM International, 2017b. D7482-17: Standard practice for sampling, storage, and handling of hydrocarbons for mercury analysis. West Conshohocken, PA, United States.

Audeh, C.A., 1988a. Process for preparing particulate aluminum metal for adsorbing mercury from natural gas. U.S. Patent 4,771,030.

Audeh, C.A., 1988b. Process for removing hydrogen sulfide and mercury from gases. U.S. Patent 4,786,483.

Audeh, C.A., 1989a. Process for removing residual mercury from treated natural gas. U.S. Patent 4,834,953.

Audeh, C.A., 1989b. Use of polysulfide treated molecular sieves to remove mercury from liquefied hydrocarbons. U.S. Patent 4,877,515.

Audeh, C.A., 1992. Fixation of elemental mercury present in spent molecular sieve desiccant for disposal. U.S. Patent 5,173,286.

Audeh, C.A., Hoffman, B.E., 1992a. Mercury removal from gaseous hydrocarbons. U.S. Patent 5,141,724.

Audeh, C.A., Hoffman, B.E., 1992b. Simultaneous dehydration and removal of residual impurities from gaseous hydrocarbons. U.S. Patent 5,120,515.

Audeh, C.A., Kirker, G.W., 1993. Dual function mercury trap/particulate filter beds. U.S Patent 5,209,773.

Audeh, C.A., Ragonese, F.P., 1991. Removal of mercury from natural gas utilizing a polysulfide scrubbing solution. U.S. Patent 5,034,203.

Avellan, A., Stegemeier, J.P., Gai, K., Dale, J., Hsu-Kim, H., Levard, C., O'Rear, D., Hoelen, T.P., Lowry, G.V., 2018. Speciation of mercury in selected areas of the petroleum value chain. Environ. Sci. Technol. 52, 1655-1664.

Ayache, J., Beaunier, L., Boumendil, J., Ehret, G., Laub, D., 2010. The different observation modes in electron microscopy (SEM, TEM, STEM). In: Sample preparation handbook for transmission electron microscopy: Methodology (1st ed.), Springer-Verlag, New York, NY, United States, pp. 33-55.

Azalim, S., Brahmi, R., Agunaou, M., Beaurain, A., Giraudon, J.M., Lamonier, J.F., 2013. Washcoating of cordierite honeycomb with Ce–Zr–Mn mixed oxides for VOC catalytic oxidation. Chem. Eng. J. 223, 536-546.

Azuaje, J., Tubío, C.R., Escalante, L., Gómez, M., Guitián, F., Coelho, A., Caamaño, O., Gil, A., Sotelo, E., 2017. An efficient and recyclable 3D printed α-Al_2O_3 catalyst for the multicomponent assembly of bioactive heterocycles. Appl. Catal. A: Gen. 530, 203-210.

Baageel, O.M., 2010. Gas plant solves Hg problems with copper-sulfate absorbent. Oil Gas J. 108, 51-55.

Ballestero, D., Gomez-Gimenez, C., Garcia-Diez, E., Juan, R., Rubio, B., Izquierdo, M.T., 2013. Influence of temperature and regeneration cycles on Hg capture and efficiency by structured Au/C regenerable sorbents. J. Hazard. Mater. 260, 247-254.

Barbato, P.S., Di Benedetto, A., Landi, G., Lisi, L., 2016. Structuring CuO/CeO_2 catalyst as option to improve performance towards CO-PROX. Top. Catal. 59, 1371-1382.

Barbero, B.P., Costa-Almeida, L., Sanz, O., Morales, M.R., Cadus, L.E., Montes, M., 2008. Washcoating of metallic monoliths with a MnCu catalyst for catalytic combustion of volatile organic compounds. Chem. Eng. J. 139, 430-435.

Barnea, Z., Sachs, T., Chidambaram, M., Sasson, Y., 2013. A novel oxidative method for the absorption of Hg(0) from flue gas of coal fired power plants using task specific ionic liquid scrubber. J. Hazard. Mater. 244-245, 495-500.

The Basel Convention, 2011. Technical guidelines for the environmentally sound management of wastes consisting of elemental mercury and wastes containing or contaminated with mercury. Basel, Switzerland.

Bauer, H., 2017. Method for treating a hydrocarbon-rich gas mixture containing mercury and acid gases. U.S. Patent 9,550,143 B2.

Beckers, F., Rinklebe, J., 2017. Cycling of mercury in the environment: Sources, fate, and human health implications: A review. Crit. Rev. Environ. Sci. Technol. 47, 693-794.

Bell, A.T., 2003. The impact of nanoscience on heterogeneous catalysis. Science 299, 1688.

Berdugo, V., Bjoroy, R.P., Richards, J., Macwilliam, D., Riding, M., Ross, B., 2005. Removing mercury from the workplace: A case history of the decommissioning and recycling of mercury-contaminated equipment. In: SPE Asia Pacific Health, Safety and Environment Conference and Exhibition. Kuala Lumpur, Malaysia.

Bessone, J.B., 2006. The activation of aluminium by mercury ions in non-aggressive media. Corros. Sci. 48, 4243-4256.

Biesinger, M.C., Payne, B.P., Grosvenor, A.P., Lau, L.W.M., Gerson, A.R., Smart, R.S.C., 2011. Resolving surface chemical states in XPS analysis of first row transition metals, oxides and hydroxides: Cr, Mn, Fe, Co and Ni. Appl. Surf. Sci. 257, 2717-2730.

Bingham, M.D., 1991. Field detection and implications of mercury in natural gas. SPE Prod. Eng. 5, 120-124.

Bings, N.H., Bogaerts, A., Broekaert, J.A.C., 2013. Atomic spectroscopy. Anal. Chem. 85, 670-704.

Blankenship, S.A., Voight, R.W., 2002. Adsorbent for the removal of trace quantities from a hydrocarbon stream and process for its use. U.S. Patent 6,383,981 B1.

Bloom, N.S., 2000. Analysis and stability of mercury speciation in petroleum hydrocarbons. Fresenius J. Anal. Chem. 366, 438-443.

Boada, R., Cibin, G., Coleman, F., Diaz-Moreno, S., Gianolio, D., Hardacre, C., Hayama, S., Holbrey, J.D., Ramli, R., Seddon, K.R., Srinivasan, G., Swadzba-Kwasny, M., 2016. Mercury capture on a supported chlorocuprate(II) ionic liquid adsorbent studied using operando synchrotron X-ray absorption spectroscopy. Dalton Trans. 45, 18946-18953.

Bohm, J., Mussig, S., 1996. Treatment of mercury contaminated waste in a two stage process, pre-treatment, volume reduction and subsequent high temperature oxidation. In: SPE Health, Safety and Environment in Oil and Gas Exploration and Production Conference. New Orleans, LA, United States.

Bomba, J., Chin, D., Kak, A., Meng, W., 2018. Flow assurance engineering in deepwater offshore - past, present, and future. In: Offshore Technology Conference. Houston, TX, United States.

Bouyssiere, B., Baco, F., Savary, L., Lobinski, R., 2000. Analytical methods for speciation of mercury in gas condensates: Critical assessment and recommendations. Oil Gas Sci. Technol.- Rev. IFP 55, 639-648.

Bouyssiere, B., Baco, F., Savary, L., Lobiñski, R., 2002. Speciation analysis for mercury in gas condensates by capillary gas chromatography with inductively coupled plasma mass spectrometric detection. J. Chromatogr. A 976, 431-439.

Branco, V., Caito, S., Farina, M., Teixeira Da Rocha, J., Aschner, M., Carvalho, C., 2017. Biomarkers of mercury toxicity: Past, present, and future trends. J. Toxicol. Environ. Health B Crit. Rev. 20, 119-154.

Brkic, V., Omrcen, I., Omrcen, B., 2003. Disposal of mercury sulfide and residual ash by deep well injection. In: SPE/EPA/DOE Exploration and Production Environmental Conference. San Antonio, TX, United States.

Brody, J.F., Wooler, B., Altera, F.J., Tindall, P.J., Du, Y., 2018. Self-supporting structures having active materials. U. S. Patent 2018/0169617 A1.

Brombach, C.C., Pichler, T., 2019. Determination of ultra-low volatile mercury concentrations in sulfur-rich gases and liquids. Talanta 199, 277-284.

BP plc, 2018. BP Statistical review of world energy. London, United Kingdom.

Budnik, L.T., Casteleyn, L., 2018. Mercury pollution in modern times and its socio-medical consequences. Sci. Total Environ. 654, 720-734.

Cachia, M., Bouyssière, B., Carrier, H., Garraud, H., Caumette, G., Le Hécho, I., 2017. Development of a high-pressure bubbling sampler for trace element quantification in natural gas. Energy Fuels 31, 4294-4300.

Calabrese, E.J., Iavicoli, I., Calabrese, V., Cory-Slechta, D.A., Giordano, J., 2018. Elemental mercury neurotoxicity and clinical recovery of function: A review of findings, and implications for occupational health. Environ. Res. 163, 134-148.

Calatayud, M., Markovits, A., Menetrey, M., Mguig, B., Minot, C., 2003. Adsorption on perfect and reduced surfaces of metal oxides. Catal. Today 85, 125-143.

Camargo, C.L.M., De Resende, N.S., De Oliveira, A.G., Salim, V.M.M., Tavares, F.W., 2014. Investigation of adsorption-enhanced reaction process of mercury removal from simulated natural gas by mathematical modeling. Fuel 129, 129-137.

Camargo, C.L.M., Oliveira, A.G., Resende, N.S., Biscaia, E.C., Secchi, A.R., Tavares, F.W., Salim, V.M.M., 2015. Modelling of Hg^0 *removal from gaseous streams and its fixation in hydroxyapatite-based adsorbents modified with copper sulphide. Adsorpt. Sci. Technol. 33, 175-190.*

Camargo, C.L.M., Salim, V.M.M., Tavares, F.W., Resende, N.S.D., 2018. Phenomenological modeling for elemental mercury capture on hydroxyapatite-based adsorbents: An experimental validation. Fuel 225, 509-518.

Cameron, C., Courty, P., Boitiaux, J.P., Varin, P., Leger, G., 1993. Method of eliminating mercury or arsenic from a fluid in the presence of a mercury and/or arsenic recovery mass. U.S. Patent 5,245,106.

Campisciano, V., Giacalone, F., Gruttadauria, M., 2017. Supported ionic liquids: A versatile and useful class of materials. Chem. Rec. 17, 918-938.

Candler, J.E., Leuterman, A.J.J., Wong, S.Y.L., Stephens, M.P., 1992. Sources of mercury and cadmium in offshore drilling discharges. SPE Drill. Eng. 7, 279-283.

Cao, S., Tao, F.F., Tang, Y., Li, Y., Yu, J., 2016. Size- and shape-dependent catalytic performances of oxidation and reduction reactions on nanocatalysts. Chem. Soc. Rev. 45, 4747-4765.

Cao, T., Zhou, Z., Chen, Q., Li, Z., Xu, S., Wang, J., Xu, M., Bisson, T., Xu, Z., 2017. Magnetically responsive catalytic sorbent for removal of Hg^0 *and NO. Fuel Process. Technol. 160, 158-169.*

Carnell, P.J.H., 2007. Removal of mercury compounds from glycol. U.S. Patent 2007/0134143 A1.

Carnell, P.J.H., Openshaw, P.J., 2004. Mercury distribution on gas processing plants. In: 83rd GPA Annual Convention. San Antonio, TX, United States.

Carnell, P.J.H., Row, V.A., 2007. A re-think of the mercury removal problem for LNG plants. In: 15th International Conference & Exhibition on Liquefied Natural Gas (LNG 15). Barcelona, Spain.

Carnell, P.J.H., Willis, E.S., 1999. Removal of sulphur together with other contaminants from fluids. U.S. Patent 6,007,706.

Chalkidis, A., Tohidi, B., 2015. Effect of hold up on the hydrate stability zone. In: Offshore Technology Conference Houston, TX, United States.

Chanvanichskul, C., Punpruk, S., Silakorn, P., Thammawong, C., Pornnimitthum, S., Kumseranee, S., 2017. In situ mercury decontamination for pipeline decommissioning in the Gulf of Thailand. In: Abu Dhabi International Petroleum Exhibition & Conference. Abu Dhabi, United Arab Emirates.

Chao, C.C., 1984. Adsorbent compositions. U.S. Patent 4,474,896.

Charoensawadpong, P., Chatwarodom, P., Manit, P., Atibodhi, N., Yongmanitchai, M., Hayook, C., Sujijantararat, K., Suwanvesh, K., 2018. Unlocking field potential from high mercury wells: New opportunities, challenges and solutions. In: Offshore Technology Conference Asia. Kuala Lumpur, Malaysia.

Chemrak, M.A., Benderdouche, N., Bestani, B., Benallou, M.B., Cagnon, B., 2018. Removal of mercury from natural gas by a new activated adsorbent from olive stones. Can. J. Chem. Eng. 96, 241-249.

Chen, C.Y., Driscoll, C.T., Eagles-Smith, C.A., Eckley, C.S., Gay, D.A., Hsu-Kim, H., Keane, S.E., Kirk, J.L., Mason, R.P., Obrist, D., Selin, H., Selin, N.E., Thompson, M.R., 2018. A critical time for mercury science to inform global policy. Environ. Sci. Technol. 52, 9556-9561.

Chen, L.Y., Huang, J.C., Lin, C.H., Pan, C.T., Chen, S.Y., Yang, T.L., Lin, D.Y., Lin, H.K., Jang, J.S.C., 2017. Anisotropic response of Ti-6Al-4V alloy fabricated by 3D printing selective laser melting. Mater. Sci. Eng. A 682, 389-395.

Cheng, G., Bai, B., Zhang, Q., Cai, M., 2014a. Hg^0 *removal from flue gas by ionic liquid/*H_2O_2*. J. Hazard. Mater. 280, 767-773.*

Cheng, G., Yu, L., He, B., Sun, M., Zhang, B., Ye, W., Lan, B., 2017. Catalytic combustion of dimethyl ether over α*-*MnO_2 *nanostructures with different morphologies. Appl. Surf. Sci. 409, 223-231.*

Cheng, G., Zhang, Q., Bai, B., 2014b. Removal of Hg^0 *from flue gas using Fe-based ionic liquid. Chem. Eng. J. 252, 159-165.*

Chevron Australia, 2015. Gorgon gas development and Jansz feed gas pipeline: Best practice pollution control design report. Perth, WA, Australia.

Chytil, S., Kure, M., Lødeng, R., Blekkan, E.A., 2017. Performance of Mn-based H_2S *sorbents in dry, reducing atmosphere – manganese oxide support effects. Fuel 196, 124-133.*

Cimino, S., Scala, F., 2015. Removal of elemental mercury by MnO_x catalysts supported on TiO_2 or Al_2O_3. Ind. Eng. Chem. Res. 55, 5133-5138.

Clarkson, T.W., Magos, L., Myers, G.J., 2003. The toxicology of mercury—current exposures and clinical manifestations. N. Engl. J. Med 349, 1731.

Clegg, R.E., 2010. Measurements of the interface between 5083 aluminium and liquid mercury using impedance spectroscopy. Corros. Sci. 52, 4028-4034.

Coade, R., Coldham, D., 2006. The interaction of mercury and aluminium in heat exchangers in a natural gas plants. Int. J. Press. Vesssel. Pip. 83, 336-342.

Couck, S., Cousin-Saint-Remi, J., Van Der Perre, S., Baron, G.V., Minas, C., Ruch, P., Denayer, J.F.M., 2018. 3D-printed SAPO-34 monoliths for gas separation. Micropor. Mesopor. Mat. 255, 185-191.

Couck, S., Lefevere, J., Mullens, S., Protasova, L., Meynen, V., Desmet, G., Baron, G.V., Denayer, J.F.M., 2017. CO_2, CH_4 and N_2 separation with a 3DFD-printed ZSM-5 monolith. Chem. Eng. J. 308, 719-726.

Couling, D.J., Nguyen, H.V., Green, W.H., 2012. Screening of metal oxides and metal sulfides as sorbents for elemental mercury at elevated temperatures. Fuel 97, 783-795.

Cousins, M.J., 2012. Mercury removal. U.S. Patent 8,177,983 B2.

Cousins, M.J., Logan, R., Young, C.J., 2012. Absorbents. U.S. Patent 8,197,695 B2.

Craig, H.L.J., 1989. Conversion of aluminum-mercury amalgam and incidental mercury in contact with aluminum alloy surfaces to harmless compounds. U.S. Patent 4,830,829.

Cross, J.B., Hays, J.M., Schmidt, R., Katdare, V.Y., 2011. Removal of heavy metals from hydrocarbon gases. U.S. Patent 7,901,486 B2.

Dai, C., Zhang, J., Huang, C., Lei, Z., 2017. Ionic liquids in selective oxidation: Catalysts and solvents. Chem. Rev. 117, 6929-6983.

Dejong, G.J., Vos, H.J., 1980. Process for removing mercury from a gas. U.S. Patent 4,196,173.

Denny, P.J., 1991. Mercury removal. E.U. Patent 0 480 603 A2.

Diamantopoulou, I., Skodras, G., Sakellaropoulos, G.P., 2010. Sorption of mercury by activated carbon in the presence of flue gas components. Fuel Process. Technol. 91, 158-163.

Doll, B., Knickerbocker, B.M., Nucci, E., 2012. Industry response to the UN global mercury treaty negotiations focus on oil and gas. In: International Conference on Health, Safety and Environment in Oil and Gas Exploration and Production. Perth, WA, Australia.

Dong, J., Xu, Z., Kuznicki, S.M., 2009a. Magnetic multi-functional nano composites for environmental applications. Adv. Funct. Mater. 19, 1268-1275.

Dong, J., Xu, Z., Kuznicki, S.M., 2009b. Mercury removal from flue gases by novel regenerable magnetic nanocomposite sorbents. Environ. Sci. Technol. 43, 3266-3271.

Driscoll, C.T., Mason, R.P., Chan, H.M., Jacob, D.J., Pirrone, N., 2013. Mercury as a global pollutant: Sources, pathways, and effects. Environ. Sci. Technol. 47, 4967-4983.

Eckersley, N., 2010. Advanced mercury removal technologies. Hydrocarb. Process. 89, 29-35.

Eckersley, N., 2013. Mercury treatment options for natural gas plants. In: 92nd GPA Annual Convention. San Antonio, TX, United States.

El-Feky, A.A., El-Azab, W., Ebiad, M.A., Masod, M.B., Faramawy, S., 2018. Monitoring of elemental mercury in ambient air around an Egyptian natural gas processing plant. J. Nat. Gas Sci. Eng. 54, 189-201.

Environment Canada, 2007. Mercury in crude oil refined in Canada. Ottawa, ON, Canada.

Esdaile, L.J., Chalker, J.M., 2018. The mercury problem in artisanal and small-scale gold mining. Chem. Eur. J.

Evans, M.J., Lunn, M.D.G., Partridge, M.G., Young, C.J., 2015. Method for preparing a sorbent. U.K. Patent 2522332 A.

Ezzeldin, M.F., Gajdosechova, Z., Masod, M.B., Zaki, T., Feldmann, J., Krupp, E.M., 2016. Mercury speciation and distribution in an Egyptian natural gas processing plant. Energy Fuels 30, 10236-10243.

Fakhru'l-Razi, A., Pendashteh, A., Abdullah, L.C., Biak, D.R., Madaeni, S.S., Abidin, Z.Z., 2009. Review of technologies for oil and gas produced water treatment. J. Hazard. Mater. 170, 530-551.

Faramawy, S., Zaki, T., Sakr, A.a.E., 2016. Natural gas origin, composition, and processing: A review. J. Nat. Gas Sci. Eng. 34, 34-54.

Feng, W., Borguet, E., Vidic, R.D., 2006a. Sulfurization of a carbon surface for vapor phase mercury removal – ii: Sulfur forms and mercury uptake. Carbon 44, 2998-3004.

Feng, W., Borguet, E., Vidic, R.D., 2006b. Sulfurization of carbon surface for vapor phase mercury removal – i: Effect of temperature and sulfurization protocol. Carbon 44, 2990-2997.

Feng, X., Cao, Y., Lan, L., Lin, C., Li, Y., Xu, H., Gong, M., Chen, Y., 2016. The promotional effect of Ce on CuFe/beta monolith catalyst for selective catalytic reduction of NO_x *by ammonia. Chem. Eng. J. 302, 697-706.*

Fields, C.A., Borak, J., Louis, E.D., 2017. Mercury-induced motor and sensory neurotoxicity: Systematic review of workers currently exposed to mercury vapor. Crit. Rev. Toxicol. 47, 811-844.

Fish, A., Challis, L.J., Cousins, M.J., Feaviour, M.R., Wagland, A.M., Pollington, S.D., Stitt, E.H., 2013. Sorbent. U.S. Patent 2013/0053234 A1.

Frech, W., Baxter, D.C., Bakke, B., Snell, J., Thomassen, Y., 1996. Highlight. Determination and speciation of mercury in natural gases and gas condensates. Anal. Commun. 33, 7H-9H.

Frech, W., Baxter, D.C., Dyvik, G., Dybdahl, B., 1995. On the determination of total mercury in natural gases using the amalgamation technique and cold vapour atomic absorption spectrometry. J. Anal. At. Spectrom. 10, 769-775.

Fukuda, N., Takaoka, M., Doumoto, S., Oshita, K., Morisawa, S., Mizuno, T., 2011. Mercury emission and behavior in primary ferrous metal production. Atmospheric Environ. 45, 3685-3691.

Fultz, B., Howe, J., 2013. The TEM and its optics. In: Transmission electron microscopy and diffractometry of materials (4th ed.), Springer-Verlag, Berlin, Germany, pp. 59-115.

Furukawa, H., Cordova, K.E., O'Keeffe, M., Yaghi, O.M., 2013. The chemistry and applications of metal-organic frameworks. Science 341, 1230444.

Gajdosechova, Z., Boskamp, M.S., Lopez-Linares, F., Feldmann, J., Krupp, E.M., 2015. Hg speciation in petroleum hydrocarbons with emphasis on the reactivity of Hg particles. Energy Fuels 30, 130-137.

Galbreath, K.C., Zygarlicke, C.J., 1996. Mercury speciation in coal combustion and gasification flue gases. Environ. Sci. Technol. 30, 2421-2426.

Galbreath, K.C., Zygarlicke, C.J., 2000. Mercury transformations in coal combustion flue gas. Fuel Process. Technol. 65-66, 289-310.

Gallup, D.L., 2018. The behavior of mercury in water, alcohols, monoethylene glycol and triethylene glycol ii. Elemental mercury solubility in alcohols, ethers and acetone; gas plant mercury distribution; and speciation in monoethylene glycol solution. Fluid Phase Equil. 477, 58-61.

Gallup, D.L., O'Rear, D.J., Radford, R., 2017. The behavior of mercury in water, alcohols, monoethylene glycol and triethylene glycol. Fuel 196, 178-184.

Gammie, D.J., Yan, T.Y., 1991. Natural gas treating system including mercury trap. U.S. Patent 4,982,050.

Gao, J., Jia, C., Zhang, L., Wang, H., Yang, Y., Hung, S.-F., Hsu, Y.-Y., Liu, B., 2016. Tuning chemical bonding of MnO_2 through transition-metal doping for enhanced CO oxidation. J. Catal. 341, 82-90.

Gao, T., Glerup, M., Krumeich, F., Nesper, R., Fjellvåg, H., Norby, P., 2008. Microstructures and spectroscopic properties of cryptomelane-type manganese dioxide nanofibers. J. Phys. Chem. C 112, 13134-13140.

Gaulier, F., Gibert, A., Walls, D., Langford, M., Baker, S., Baudot, A., Porcheron, F., Lienemann, C.-P., 2015. Mercury speciation in liquid petroleum products: Comparison between on-site approach and lab measurement using size exclusion chromatography with high resolution inductively coupled plasma mass spectrometric detection (SEC-ICP-HR MS). Fuel Process. Technol. 131, 254-261.

Gesellschaft für Anlagen- und Reaktorsicherheit, 2009. Technologies for the stabilization of elemental mercury and mercury-containing wastes. Köln, Germany.

Goldstein, J.I., Newbury, D.E., Echlin, P., Joy, D.C., Lyman, C.E., Lifshin, E., Sawyer, L., Michael, J.R., 2003. The SEM and its modes of operation. In: Scanning electron microscopy and x-ray microanalysis (3rd ed.) Springer-Verlag, New York, NY, United States, pp. 21-60.

Gómez, L.E., Boix, A.V., Miró, E.E., 2013. Co/ZrO_2, Co/CeO_2 and MnCoCe structured catalysts for COPrOx. Catal. Today 216, 246-253.

Gómez-Giménez, C., Ballestero, D., Juan, R., Rubio, B., Izquierdo, M.T., 2015. Mercury capture by a regenerable sorbent under oxycoal combustion conditions: Effect of SO_2 and O_2 on capture efficiency. Chem. Eng. Sci. 122, 232-239.

Gómez-Giménez, C., Izquierdo, M.T., De Las Obras-Loscertales, M., De Diego, L.F., García-Labiano, F., Adánez, J., 2017. Mercury capture by a structured Au/C regenerable sorbent under oxycoal combustion representative and real conditions. Fuel 207, 821-829.

Gonzalez-Raymat, H., Liu, G., Liriano, C., Li, Y., Yin, Y., Shi, J., Jiang, G., Cai, Y., 2017. Elemental mercury: Its unique properties affect its behavior and fate in the environment. Environ. Pollut. 229, 69-86.

González-Velasco, J.R., Gutiérrez-Ortiz, M.A., Marc, J.L., Botas, J.A., González-Marcos, M.P., Blanchard, G., 2003. Pt/$Ce_{0.68}Zr_{0.32}O_2$ washcoated monoliths for automotive emission control. Ind. Eng. Chem. Res. 42, 311-317.

Goodwin, M.J., Musa, O.M., Steed, J.W., 2015. Problems associated with sour gas in the oilfield industry and their solutions. Energy Fuels 29, 4667-4682.

Govender, S., Friedrich, H., 2017. Monoliths: A review of the basics, preparation methods and their relevance to oxidation. Catalysts 7.

Govinda Rao, B., Jampaiah, D., Venkataswamy, P., Reddy, B.M., 2016. Enhanced catalytic performance of manganese and cobalt co-doped CeO_2 catalysts for diesel soot oxidation. ChemistrySelect 1, 6681-6691.

Granite, E.J., Pennline, H.W., Hargis, R.A., 2000. Novel sorbents for mercury removal from flue gas. Ind. Eng. Chem. Res. 39, 1020-1029.

Grant, C.J., Weimer, A.B., Marks, N.K., Perow, E.S., Oster, J.M., Brubaker, K.M., Trexler, R.V., Solomon, C.M., Lamendella, R., 2015. Marcellus and mercury: Assessing potential impacts of unconventional natural gas extraction on aquatic ecosystems in Northwestern Pennsylvania. J. Environ. Sci. Health A Tox. Hazard. Subst. Environ. Eng. 50, 482-500.

Gras, R., Luong, J., Shellie, R.A., 2015. Direct measurement of trace elemental mercury in hydrocarbon matrices by gas chromatography with ultraviolet photometric detection. Anal. Chem. 87, 11429-11432.

Grice, K.J., Vanorman, L.D., 2008. Evaluation of several portable mercury vapor monitors and their response to concentrations of mercury vapor in the presence of interference *compounds in a simulated oil processing environment. In: SPE International Conference on Health, Safety, and Environment in Oil and Gas Exploration and Production. Nice, France.*

Griffin, M.J., Kabir, K.M., Coyle, V.E., Kandjani, A.E., Sabri, Y.M., Ippolito, S.J., Bhargava, S.K., 2016. A nanoengineered conductometric device for accurate analysis of elemental mercury vapor. Environ. Sci. Technol. 50, 1384-1392.

Gu, T., Balakotaiah, V., 2016. Impact of heat and mass dispersion and thermal effects on the scale-up of monolith reactors. Chem. Eng. J. 284, 513-535.

Guieze, P., Martin, B., Schroeder, R., 2010. In-line mercury detector for hydrocarbon and natural gas. U.S. Patent 2010/0253933 A1.

Guijarro, M.I., Mendioroz, S., Munoz, V., 1994. Impact of the preparation conditions in the sulfur distribution of a new sulfurized porous adsorbent. Ind. Eng. Chem. Res. 33, 375-381.

Gupta, A.K., Ibrahim, S., Al Shoaibi, A., 2016. Advances in sulfur chemistry for treatment of acid gases. Prog. Energy Combust. Sci. 54, 65-92.

Gustin, M.S., 2011. Exchange of mercury between the atmosphere and terrestrial ecosystems. In: Environmental chemistry and toxicology of mercury (1st ed.). Editors: Liu, G., Cai, Y., O'Driscoll. N. John Wiley & Sons, Hoboken, NJ, United States, pp. 423-451.

Gworek, B., Bemowska-Kalabun, O., Kijenska, M., Wrzosek-Jakubowska, J., 2016. Mercury in marine and oceanic waters-a review. Water Air Soil Pollut. 227, 371.

Haasch, R.T., 2014. X-ray photoelectron spectroscopy (XPS) and auger electron spectroscopy (AES), In: Practical materials characterization (1st ed.). Editor: Sardela, M. Springer-Verlag. New York, NY, United States, pp. 93-132.

Hamad, F., Bahamdan, A.A., Al-Mulhim, A.N., Rashwan, A.K., Fadhel, B.A., 2014. Method for removing mercury from a gaseous or liquid stream. U.S. Patent 8,641,890 B2.

Han, L., Meng, H., Wang, J., Hu, Y., Bao, W., Chang, L., Wang, H., 2016. Application of spent H_2S scavenger of iron oxide in mercury capture from flue gas. Ind. Eng. Chem. Res. 55, 5100-5107.

Harfoushian, J.H., 2013. Quantification of low levels of mercury in gas reservoirs using advanced sampling and analysis techniques. In: SPE Annual Technical Conference and Exhibition. New Orleans, LA, United States.

Harris, D.C., 2010. Atomic spectroscopy. In: Quantitative chemical analysis, W. H. Freeman and Company, New York, NY, United States, pp. 479-501.

Hatscher, S., Hesse, M., 2009. Absorption composition and process for removing mercury. U.S. Patent 2009/0200207 A1.

Hazen, R.M., Golden, J., Downs, R.T., Hystad, G., Grew, E.S., Azzolini, D., Sverjensky, D.A., 2012. Mercury (Hg) mineral evolution: A mineralogical record of supercontinent assembly, changing ocean geochemistry, and the emerging terrestrial biosphere. Am. Mineral. 97, 1013-1042.

He, J., Reddy, G.K., Thiel, S.W., Smirniotis, P.G., Pinto, N.G., 2011. Ceria-modified manganese oxide/titania materials for removal of elemental and oxidized mercury from flue gas. J. Phys. Chem. C 115, 24300-24309.

He, J., Reddy, G.K., Thiel, S.W., Smirniotis, P.G., Pinto, N.G., 2013. Simultaneous removal of elemental mercury and NO from flue gas using CeO_2 modified MnO_x/TiO_2 materials. Energy Fuels 27, 4832-4839.

He, W., Yang, W., Wang, C., Deng, X., Liu, B., Xu, X., 2016. Morphology-controlled syntheses of alpha-MnO_2 for electrochemical energy storage. Phys. Chem. Chem. Phys. 18, 15235-15243.

Hernández-Garrido, J.C., Gaona, D., Gómez, D.M., Gatica, J.M., Vidal, H., Sanz, O., Rebled, J.M., Peiró, F., Calvino, J.J., 2015. Comparative study of the catalytic performance and *final surface structure of Co_3O_4/La-CeO_2 washcoated ceramic and metallic honeycomb monoliths. Catal. Today 253, 190-198.*

Horton, R.L., 1986. Removal of mercury from gases. U.S. Patent 4,591,490.

Hower, J.C., Senior, C.L., Suuberg, E.M., Hurt, R.H., Wilcox, J.L., Olson, E.S., 2010. Mercury capture by native fly ash carbons in coal-fired power plants. Prog. Energy Combust. Sci. 36.

Hrncevic, L., Simon, K., Kristafor, Z., Malnar, M., 2010. Long-lasting experience in environmental protection during sour gas reservoir exploitation. In: SPE Deep Gas Conference and Exhibition. Manama, Bahrain.

Humble, J.D., Yan, T.Y., 1989. Process for the low temperature deriming of cryogenic heat exchangers. U.S. Patent 4,813,986.

Hurt, C., Brandt, M., Priya, S.S., Bhatelia, T., Patel, J., Selvakannan, P.R., Bhargava, S., 2017. Combining additive manufacturing and catalysis: A review. Catal. Sci. Technol. 7, 3421-3439.

Ide, M.S., Skoulidas, A.I., Camisa, J.A., Wu, J.J., Allen, J.W., O'Neal, E.J., 2018. Metal monolith for use in a reverse flow reactor. U. S. Patent 2018/0333703 A1.

Ikealumba, W.C., Wu, H., 2014. Some recent advances in liquefied natural gas (LNG) production, spill, dispersion, and safety. Energy Fuels 28, 3556-3586.

Inkson, B.J., 2016. Scanning electron microscopy (SEM) and transmission electron microscopy (TEM) for materials characterization. In: Materials characterization using nondestructive evaluation (NDE) methods (1st ed.). Editors: Hübschen, G., Altpeter, I., Tscuncky, R. Herrmann. H.G. Woodhead Publishing, Cambridge, MA, United States, pp. 17-43.

International Gas Union, 2018. IGU world LNG report. Barcelona, Spain.

Izquierdo, M.T., Ballestero, D., Juan, R., Garcia-Diez, E., Rubio, B., Ruiz, C., Pino, M.R., 2011. Tail-end Hg capture on Au/carbon-monolith regenerable sorbents. J. Hazard. Mater. 193, 304-310.

Jamaluddin, A.K.M., Tibbles, R.J., 2011. Apparatus and methods for removing mercury from formation effluents. U.S. Patent 2011/0253375 A1.

Jampaiah, D., Ippolito, S.J., Sabri, Y.M., Reddy, B.M., Bhargava, S.K., 2015a. Highly efficient nanosized Mn and Fe codoped ceria-based solid solutions for elemental mercury removal at low flue gas temperatures. Catal. Sci. Technol. 5, 2913-2924.

Jampaiah, D., Ippolito, S.J., Sabri, Y.M., Tardio, J., Selvakannan, P.R., Nafady, A., Reddy, B.M., Bhargava, S.K., 2016. Ceria-zirconia modified MnO_x catalysts for gaseous elemental mercury oxidation and adsorption. Catal. Sci. Technol. 6, 1792-1803.

Jampaiah, D., Tur, K.M., Ippolito, S.J., Sabri, Y.M., Tardio, J., Bhargava, S.K., Reddy, B.M., 2013. Structural characterization and catalytic evaluation of transition and rare earth metal doped ceria-based solid solutions for elemental mercury oxidation. RSC Adv. 3, 12963-12974.

Jampaiah, D., Tur, K.M., Venkataswamy, P., Ippolito, S.J., Sabri, Y.M., Tardio, J., Bhargava, S.K., Reddy, B.M., 2015b. Catalytic oxidation and adsorption of elemental mercury over nanostructured CeO_2-MnO_x catalyst. RSC Adv. 5, 30331-30341.

Jampaiah, D., Velisoju, V.K., Venkataswamy, P., Coyle, V.E., Nafady, A., Reddy, B.M., Bhargava, S.K., 2017. Nanowire morphology of mono- and bidoped alpha-MnO_2 catalysts for remarkable enhancement in soot oxidation. ACS Appl. Mater. Interfaces 9, 32652-32666.

Jansen, A.E., Feron, P.H.M., 2001. Method for absorbing gaseous oxidizable or reducible constituents through a membrane. U.S. Patent 6,197,269 B1.

Jensen, K., 2016. System and method for removal of heavy metals ions from a rich hydrate inhibitor system. U.S. Patent 9,376,358 B2.

Ji, L., Thiel, S.W., Pinto, N.G., 2008a. Pyrrolidinium imides: Promising ionic liquids for direct capture of elemental mercury from flue gas. Water Air Soil Pollut. 8, 349-358.

Ji, L., Thiel, S.W., Pinto, N.G., 2008b. Room temperature ionic liquids for mercury capture from flue gas. Ind. Eng. Chem. Res. 47, 8396-8400.

Jia, J., Zhang, P., Chen, L., 2016. The effect of morphology of α-MnO_2 *on catalytic decomposition of gaseous ozone. Catal. Sci. Technol. 6, 5841-5847.*

Jiang, H., Wang, Y., Zhou, J., Chen, Y., Zhang, M., 2018. Morphology control of manganese-based catalysts for low-temperature selective catalytic reduction of NO_x*. Mater. Lett. 233, 250-253.*

Jubin, C., 2017. Challenge of mercury removal for natural gas processing. In: 96th GPA Midstream Annual Convention. San Antonio, TX, United States.

Jubin, C., Ducreux, O., 2014. Mercury removal units operation at front-end location. In: Abu Dhabi International Petroleum Exhibition and Conference. Abu Dhabi, United Arab Emirates.

Junio-Ramirez, E., 2004. Assessing the health status and mercury in urine of workers on an offshore facility (platform) in the Philippines. In: SPE International Conference on Health, Safety, and Environment in Oil and Gas Exploration and Production. Calgary, AB, Canada.

Kabir, K.M.M., Ippolito, S.J., Kandjani, A.E., Sabri, Y.M., Bhargava, S.K., 2017a. Nano-engineered surfaces for mercury vapor sensing: Current state and future possibilities. Trends Anal. Chem. 88, 77-99.

Kabir, K.M.M., Sabri, Y.M., Myers, L., Harrison, I., Boom, E., Coyle, V.E., Ippolito, S.J., Bhargava, S.K., 2017b. Investigating the cross-interference effects of alumina refinery process gas species on a SAW based mercury vapor sensor. Hydrometallurgy 170, 51-57.

Kanazirev, V.I., 2009. Removal of mercury from fluids by supported metal oxides. U.S. Patent 2009/0155148 A1.

Kanazirev, V.I., Simonetti, D.A., 2013. Protected adsorbents for mercury removal and method of making and using same. U.S. Patent 2013/0139526 A1.

Keatch, R., 2018. Method for mercury decontamination. U. S. Patent 9,903,006 B2.

Khalifa, M., Lue, L., 2017. A group contribution method for predicting the solubility of mercury. Fluid Phase Equil. 432, 76-84.

Khan, N.A., Hasan, Z., Jhung, S.H., 2013. Adsorptive removal of hazardous materials using metal-organic frameworks (MOFs): A review. J. Hazard. Mater. 244-245, 444-456.

Kho, F., Pham, G.H., 2018. Absorption kinetics of mercury (II) chloride into water and aqueous sodium chloride solution. Fuel Process. Technol. 174, 78-87.

Kho, F., Pham, G.H., 2019. Absorption kinetics of mercury(II) chloride into mono-ethylene glycol (MEG) solution. Fuel Process. Technol. 185, 46-55.

Khunphonoi, R., Khamdahsag, P., Chiarakorn, S., Grisdanurak, N., Paerungruang, A., Predapitakkun, S., 2015. Enhancement of elemental mercury adsorption by silver supported material. J. Environ. Sci. 32, 207-216.

Kidd, K., Clayden, M., Jardine, T., 2011. Bioaccumulation and biomagnification of mercury through food webs, In: Environmental chemistry and toxicology of mercury (1st ed.). Editors: Liu, G., Cai, Y., O'Driscoll. N. John Wiley & Sons, Hoboken, NJ, United States, pp. 455-499.

Kim, K.H., Kabir, E., Jahan, S.A., 2016. A review on the distribution of Hg in the environment and its human health impacts. J. Hazard. Mater. 306, 376-385.

Kinnari, K., Hundseid, J., Li, X., Askvik, K.M., 2014. Hydrate management in practice. J. Chem. Eng. Data 60, 437-446.

Kirk, J.L., Muir, D.C., Gleason, A., Wang, X., Lawson, G., Frank, R.A., Lehnherr, I., Wrona, F., 2014. Atmospheric deposition of mercury and methylmercury to landscapes and waterbodies of the Athabasca oil sands region. Environ. Sci. Technol. 48, 7374-7383.

Kong, Z.Y., Mahmoud, A., Liu, S., Sunarso, J., 2018. Revamping existing glycol technologies in natural gas dehydration to improve the purity and absorption efficiency: Available methods and recent developments. J. Nat. Gas Sci. Eng. 56, 486-503.

Korpiel, J.A., Vidic, R.D., 1997. Effect of sulfur impregnation method on activated carbon uptake of gas-phase mercury. Environ Sci. Technol. 31, 2319-2325.

Koulocheris, V., Louli, V., Panteli, E., Skouras, S., Voutsas, E., 2018. Modelling of elemental mercury solubility in natural gas components. Fuel 233, 558-564.

Kozin, L.F., Hansen, S.C., 2013a. Amalgam solubility. In: Mercury handbook: Chemistry, applications and environmental impact (1st ed.). The Royal Society of Chemistry, Cambridge, United Kingdom, pp. 36-49.

Kozin, L.F., Hansen, S.C., 2013b. Chemical properties of mercury. In: Mercury handbook: Chemistry, applications and environmental impact (1st ed.). The Royal Society of Chemistry, Cambridge, United Kingdom, pp. 80-127.

Kozin, L.F., Hansen, S.C., 2013c. Physicochemical properties of metallic mercury. In: Mercury handbook: Chemistry, applications and environmental impact (1st ed.). The Royal Society of Chemistry, Cambridge, United Kingdom, pp. 1-35.

Kreutzer, M.T., Kapteijn, F., Moulijn, J.A., 2006. Shouldn't catalysts shape up?: Structured reactors in general and gas–liquid monolith reactors in particular. Catal. Today 111, 111-118.

Krupp, R., 1988. Physicochemical aspects of mercury metallogenesis. Chem. Geol. 69, 345-356.

Kumar Reddy, K.S., Al Shoaibi, A., Srinivasakannan, C., 2015. Sulfur-leaching facts from sulfur-impregnated porous carbons in the mercury removal process. Energy Fuels 29, 4488-4491.

Kumar Reddy, K.S., Prabhu, A., Al Shoaibi, A., Srinivasakannan, C., 2016. Application of sulfonated carbons for mercury removal in gas processing. Energy Fuels 30, 3227-3232.

Laine, P., Vickery, J.H.J., Buhlman, J.L., 2018. Mercury-in-gas sampling system. U.S. Patent 2018/0246015 A1.

Lajunen, L.H.J., Perämäki, P., 2004. Plasma atomic emission spectrometry. In: Spectrochemical analysis by atomic absorption and emission (2nd ed.). The Royal Society of Chemistry, Cambridge, United Kingdom, pp. 202-256.

Lan, X., Talbot, R., Laine, P., Torres, A., Lefer, B., Flynn, J., 2015. Atmospheric mercury in the Barnett shale area, Texas: Implications for emissions from oil and gas processing. Environ. Sci. Technol. 49, 10692-10700.

Larsson, T., Frech, W., Björn, E., Dybdahl, B., 2007. Studies of transport and collection characteristics of gaseous mercury in natural gases using amalgamation and isotope dilution analysis. Analyst 132, 579-586.

Lau, C.H., Li, P., Li, F., Chung, T.-S., Paul, D.R., 2013. Reverse-selective polymeric membranes for gas separations. Prog. Polym. Sci. 38, 740-766.

Le Parlouër, P., 2013. Thermal analysis and calorimetry techniques for catalytic investigations. In: Calorimetry and thermal methods in catalysis (1st ed.). Editors: Auroux, A. Springer-Verlag, Berlin, Germany pp. 51-101.

Lee, D.W., Yoo, B.R., 2014. Advanced metal oxide (supported) catalysts: Synthesis and applications. J. Ind. Eng. Chem. 20, 3947-3959.

Lee, K.J., Lee, T.G., 2012. A review of international trends in mercury management and available options for permanent or long-term mercury storage. J. Hazard. Mater. 241-242, 1-13.

Lee, S.-H., Park, Y.-O., 2003. Gas-phase mercury removal by carbon-based sorbents. Fuel Process. Technol. 84, 197-206.

Leeper, J.E., 1980. Mercury - LNG's problem. Hydrocarb. Process. 59, 237-240.

Leermakers, M., Baeyens, W., Quevauviller, P., Horvat, M., 2005. Mercury in environmental samples: Speciation, artifacts and validation. Trends Anal. Chem. 24, 383-393.

Leng, Y., 2013a. Electron spectroscopy for surface analysis. In: Materials characterization (2nd ed.). Wiley-VCH Verlag GmbH & Co. KGaA, Weinheim, Germany, pp. 221-251.

Leng, Y., 2013b. Thermal analysis. In: Materials characterization (2nd ed.). Wiley-VCH Verlag GmbH & Co. KGaA, Weinheim, Germany, pp. 333-365.

Leng, Y., 2013c. Transmission electron microscopy. In: Materials characterization (2nd ed.). Wiley-VCH Verlag GmbH & Co. KGaA, Wenheim, Germany, pp. 83-126.

Leng, Y., 2013d. X-ray diffraction methods. In: Materials characterization (2nd ed.). Wiley-VCH Verlag GmbH & Co. KGaA, Weinheim, Germany, pp. 47-82.

Leng, Y., 2013e. X-ray spectroscopy for elemental analysis. In: Materials characterization (2nd ed.). Wiley-VCH Verlag GmbH & Co. KGaA, Weinheim, Germany, pp. 191-219.

Leppin, D., Palla, N., 2002. Mercury removal from gaseous process streams. U.S. Patent 6,475,451 B1.

Lewis, L., 1995. Measurement of mercury in natural gas streams. In: 74th GPA Annual Convention. San Antonio, TX, United States.

Li, H., Wu, C.Y., Li, Y., Li, L., Zhao, Y., Zhang, J., 2012a. Role of flue gas components in mercury oxidation over TiO_2 *supported* MnO_x*-*CeO_2 *mixed-oxide at low temperature. J. Hazard. Mater. 243, 117-123.*

Li, H., Wu, C.Y., Li, Y., Zhang, J., 2012b. Superior activity of MnO_x*-*CeO_2*/*TiO_2 *catalyst for catalytic oxidation of elemental mercury at low flue gas temperatures. Appl. Catal. B: Environ. 111-112, 381-388.*

Li, H., Zhao, J., Zhang, W., Yang, J., Wang, J., Zhang, M., Yang, Z., Li, L., Shih, K., 2018a. NH_3 *inhibits mercury oxidation over low-temperature* MnO_x*/*TiO_2 *SCR catalyst. Fuel Process. Technol. 176, 124-130.*

Li, H., Zhu, L., Wang, J., Li, L., Shih, K., 2016a. Development of nano-sulfide sorbent for efficient removal of elemental mercury from coal combustion fuel gas. Environ. Sci. Technol. 50, 9551-9557.

Li, H., Zhu, W., Yang, J., Zhang, M., Zhao, J., Qu, W., 2018b. Sulfur abundant S/FeS_2 *for efficient removal of mercury from coal-fired power plants. Fuel 232, 476-484.*

Li, J., Qu, Z., Qin, Y., Wang, H., 2016b. Effect of MnO_2 *morphology on the catalytic oxidation of toluene over Ag/*MnO_2 *catalysts. Appl. Surf. Sci. 385, 234-240.*

Li, J.-R., Kuppler, R.J., Zhou, H.-C., 2009. Selective gas adsorption and separation in metal–organic frameworks. Chem. Soc. Rev. 38, 1477-1504.

Li, K., Chen, J., Peng, Y., Lin, W., Yan, T., Li, J., 2017a. The relationship between surface open cells of α*-*MnO_2 *and co oxidation ability from a surface point of view. J. Mater. Chem. A 5, 20911-20921.*

Li, N., Wei, H., Duan, Y., Tang, H., Zhao, S., Hu, P., Ren, S., 2018c. Experimental study on mercury adsorption and adsorbent regeneration of sulfur-loaded activated carbon. Energy Fuels 32, 11023-11029.

Li, X., Zhang, L., Zhou, D., Liu, W., Zhu, X., Xu, Y., Zheng, Y., Zheng, C., 2016c. Elemental mercury capture from flue gas by a supported ionic liquid phase adsorbent. Energy Fuels 31, 714-723.

Li, Y., Li, L., Yu, J., 2017b. Applications of zeolites in sustainable chemistry. Chem 3, 928-949.

Li, Y.H., Lee, C.W., Gullett, B.K., 2003. Importance of activated carbon's oxygen surface functional groups on elemental mercury adsorption. Fuel 82, 451-457.

Liao, Y., Xiong, S., Dang, H., Xiao, X., Yang, S., Wong, P.K., 2015. The centralized control of elemental mercury emission from the flue gas by a magnetic rengenerable Fe-Ti-Mn spinel. J. Hazard. Mater. 299, 740-746.

Liao, Y., Xu, H., Liu, W., Ni, H., Zhang, X., Zhai, A., Quan, Z., Qu, Z., Yan, N., 2019. One step interface activation of ZnS using cupric ions for mercury recovery from nonferrous smelting flue gas. Environ. Sci. Technol. 53, 4511-4518.

Lim, W., Choi, K., Moon, I., 2013. Current status and perspectives of liquefied natural gas (LNG) plant design. Ind. Eng. Chem. Res. 52, 3065-3088.

Lin, C.-C., Yee, N., Barkay, T., 2011a. Microbial transformations in the mercury cycle. In: Environmental chemistry and toxicology of mercury (1st ed.). Editors: Liu, G., Cai, Y., O'Driscoll. N. John Wiley & Sons, Hoboken, NJ, United States, pp. 155-191.

Lin, C.-J., Singhasuk, P., Pehkonen, S.O., 2011b. Atmospheric chemistry of mercury. In: Environmental chemistry and toxicology of mercury (1st ed.). Editors: Liu, G., Cai, Y., O'Driscoll. N. John Wiley & Sons, Hoboken, NJ, United States, pp. 113-153.

Lin, N., Liu, Q., Zou, J., Li, D., Yuan, S., Wang, Z., Tang, B., 2017. Surface damage mitigation of Ti6Al4V alloy via thermal oxidation for oil and gas exploitation application: Characterization of the microstructure and evaluation of the surface performance. RSC Adv. 7, 13517-13535.

Lin, T., Yu, L., Sun, M., Cheng, G., Lan, B., Fu, Z., 2016. Mesoporous α-MnO_2 microspheres with high specific surface area: Controlled synthesis and catalytic activities. Chem. Eng. J. 286, 114-121.

Linak, W.P., Ryan, J.V., Ghorishi, B.S., Wendt, J.O.L., 2011. Issues related to solution chemistry in mercury sampling impingers. J. Air Waste Manage. Assoc. 51, 688-698.

Ling, L., Fan, M., Wang, B., Zhang, R., 2015. Application of computational chemistry in understanding the mechanisms of mercury removal technologies: A review. Energ. Environ. Sci. 8, 3109-3133.

Ling, L., Han, P., Wang, B., Zhang, R., 2013. Theoretical prediction of simultaneous removal efficiency of ZnO for H_2S and Hg^0 in coal gas. Chem. Eng. J. 231, 388-396.

Ling, L.H., Kasim, A., 2017. Optimization of mercury health surveillance program for offshore workers. In: SPE Asia Pacific Health, Safety, Security, Environment and Social Responsibility Conference. Kuala Lumpur, Malaysia.

Liu, B.-T., Huang, C.-J., Ke, Y.-X., Wang, W.-H., Kuo, H.-L., Lin, D., Lin, V., Lin, S.-H., 2017. Enhanced selective catalytic reduction of NO over Mn-Ce catalysts with the acetic-acid-chelated titania support at low temperature. Appl. Catal. A: Gen. 538, 74-80.

Liu, G., Li, Y., Cai, Y., 2011. Adsorption of mercury on solids in the aquatic environment. In: Environmental chemistry and toxicology of mercury (1st ed.). Editors: Liu, G., Cai, Y., O'Driscoll. N. John Wiley & Sons, Hoboken, NJ, United States, pp. 367-387.

Liu, Q., 2013. Mercury concentration in natural gas and its distribution in the Tarim basin. Sci. China Earth Sci. 56, 1371-1379.

Liu, W., Vidic, R.D., Brown, T.D., 2000. Impact of flue gas conditions on mercury uptake by sulfur-impregnated activated carbon. Environ. Sci. Technol. 34, 154-159.

Liu, W., Vidić, R.D., Brown, T.D., 1998. Optimization of sulfur impregnation protocol for fixed-bed application of activated carbon-based sorbents for gas-phase mercury removal. Environ. Sci. Technol. 32, 531-538.

Liu, W., Xu, H., Liao, Y., Quan, Z., Li, S., Zhao, S., Qu, Z., Yan, N., 2019a. Recyclable CuS sorbent with large mercury adsorption capacity in the presence of SO_2 from non-ferrous metal smelting flue gas. Fuel 235, 847-854.

Liu, X., Jiang, S., Li, H., Yang, J., Yang, Z., Zhao, J., Peng, H., Shih, K., 2019b. Elemental mercury oxidation over manganese oxide octahedral molecular sieve catalyst at low flue gas temperature. Chem. Eng. J. 356, 142-150.

Liu, Y., Bisson, T.M., Yang, H., Xu, Z., 2010. Recent developments in novel sorbents for flue gas clean up. Fuel Process. Technol. 91, 1175-1197.

Liu, Y., Kelly, D.J.A., Yang, H., Lin, C.C.H., Kuznicki, S.M., Xu, Z., 2008. Novel regenerable sorbent for mercury capture from flue gases of coal-fired power plant. Environ. Sci. Technol. 42, 6205-6210.

Liu, Y., Xu, J., Li, H., Cai, S., Hu, H., Fang, C., Shi, L., Zhang, D., 2015. Rational design and in situ fabrication of MnO_2*@*$NiCo_2O_4$ *nanowire arrays on Ni foam as high-performance monolith de-*NO_x *catalysts. J. Mater. Chem. A 3, 11543-11553.*

López-Antón, M.A., Díaz-Somoano, M., Ochoa-González, R., Martínez-Tarazona, M.R., 2012. Analytical methods for mercury analysis in coal and coal combustion by-products. Int. J. Coal Geol. 94, 44-53.

Lopez-Anton, M.A., Rumayor, M., Díaz-Somoano, M., Martínez-Tarazona, M.R., 2015. Influence of a CO_2*-enriched flue gas on mercury capture by activated carbons. Chem. Eng. J. 262, 1237-1243.*

Lord, C.J., Lambertsson, L.T., Björn, E.L., Frech, W., 2012. Method for removing mercury contamination from solid surfaces. U.S. Patent 2012/0073601 A1.

Lothongkum, A.W., Suren, S., Chaturabul, S., Thamphiphit, N., Pancharoen, U., 2011. Simultaneous removal of arsenic and mercury from natural-gas-co-produced water from the Gulf of Thailand using synergistic extractant via HFSLM. J. Membrane Sci. 369, 350-358.

Lowell, S., Shields, J.E., Thomas, M.A., Thommes, M., 2004a. Adsorption mechanism. In: Characterization of porous solids and powders: Surface area, pore size and density (1st ed.). Springer-Verlag, Dordrecht, Netherlands, pp. 15-57.

Lowell, S., Shields, J.E., Thomas, M.A., Thommes, M., 2004b. Surface area analysis from the langmuir and bet theories. In: Characterization of porous solids and powders: Surface area, pore size and density (1st ed.). Springer-Verlag, Dordrecht, Netherlands, pp. 58-81.

Lund, D.L., 1996. Wyoming operator solves mercury exposure problems. Oil Gas J. 94, 70-77.

Luo, J., Meng, X., Crittenden, J., Qu, J., Hu, C., Liu, H., Peng, P., 2018. Arsenic adsorption on α*-*MnO_2 *nanofibers and the significance of (1 0 0) facet as compared with (1 1 0). Chem. Eng. J. 331, 492-500.*

Lynch, S.P., 1981. Liquid-metal embrittlement in an Al 6%Zn 3%Mg alloy. Acta Metall. 29, 325-340.

Lynch, S.P., 2008. Failures of structures and components by metal-induced embrittlement. J. Fail. Anal. Prev. 8, 259-274.

Mac Kinnon, M.A., Brouwer, J., Samuelsen, S., 2018. The role of natural gas and its infrastructure in mitigating greenhouse gas emissions, improving regional air quality, and renewable resource integration. Prog. Energy Combust. Sci. 64, 62-92.

Makkuni, A., Varma, R.S., Sikdar, S.K., Bhattacharyya, D., 2007. Vapor phase mercury sorption by organic sulfide modified bimetallic iron-copper nanoparticle aggregates. Ind. Eng. Chem. Res. 46, 1305-1315.

Malaysian Ministry of Human Resources, 2011. Guidelines on mercury management in oil & gas industry. Putrajaya, Malaysia.

Manelius, T., Aguedach, I., 2018. Efficient condensate mercury removal offshore. In: Offshore Technology Conference. Houston, TX, United States.

Markovs, J., 1989. Purification of fluid streams containing mercury. U.S. Patent 4,874,525.

Markovs, J., 1994. Removal of mercury impurity from natural gas. U.S. Patent 5,281,258.

Markovs, J., 1999. Process for the removal and recovery of mercury from hydrocarbon streams. U.S. Patent 5,989,506.

Markovs, J., Clark, K., 2005. Optimized mercury removal in gas plants. In: 84th GPA Annual Convention. San Antonio, TX, United States.

Markovs, J., Maurer, R.T., 1993. Recovery of liquid mercury from process streams. U.S. Patent 5,271,760.

Markovs, J., Maurer, R.T., Zarchy, A.S., Holmes, E.S., 1994. Removal of mercury from process streams. U.S. Patent 5,354,357.

Marsh, K.N., Bevan, J.W., Holste, J.C., Mcfarlane, D.L., Eliades, M., Rogers, W.J., 2016. Solubility of mercury in liquid hydrocarbons and hydrocarbon mixtures. J. Chem. Eng. Data 61, 2805-2817.

Matviya, T.M., Gebhard, R.S., Greenbank, M., 1987. Mercury adsorbent carbon molecular sieves and process for removing mercury vapor from gas streams. U.S. Patent 4,786,483.

May, E.F., Wu, R., Kelland, M.A., Aman, Z.M., Kozielski, K.A., Hartley, P.G., Maeda, N., 2014. Quantitative kinetic inhibitor comparisons and memory effect measurements from hydrate formation probability distributions. Chem. Eng. Sci. 107, 1-12.

Mazur, M., Leary, M., Mcmillan, M., Sun, S., Shidid, D., Brandt, M., 2017. Mechanical properties of Ti6Al4V and AlSi12Mg lattice structures manufactured by selective laser melting (SLM). In: Laser additive manufacturing. Editor: Brandt, M. Woodhead Publishing, Cambridge, MA, United States, pp. 119-161.

Mehla, S., Das, J., Jampaiah, D., Periasamy, S., Nafady, A., Bhargava, S.K., 2019. Recent advances in preparation methods for catalytic thin films and coatings. Catal. Sci. Technol.

Meille, V., 2006. Review on methods to deposit catalysts on structured surfaces. Appl. Catal. A: Gen. 315, 1-17.

Michorczyk, P., Hędrzak, E., Węgrzyniak, A., 2016. Preparation of monolithic catalysts using 3D printed templates for oxidative coupling of methane. J. Mater. Chem. A 4, 18753-18756.

Miedaner, M.M., Migdisov, A.A., Williams-Jones, A.E., 2005. Solubility of metallic mercury in octane, dodecane and toluene at temperatures between 100 °C and 200 °C. Geochim. Cosmochim. Acta 69, 5511-5516.

Mikos-Szymanska, M., Rusek, P., Borowik, K., Rolewicz, M., Bogusz, P., Gluzinska, J., 2018. Characterization of drilling waste from shale gas exploration in central and eastern Poland. Environ. Sci. Pollut. Res. Int. 25, 35990-36001.

Miller, A.J., Tuckett, W.F., 1977. Removal of mercury from gas streams using hydrogen sulfide and amines. U.S. Patent 4,044,098.

Minas, C., Carnelli, D., Tervoort, E., Studart, A.R., 2016. 3D printing of emulsions and foams into hierarchical porous ceramics. Adv. Mater. 28, 9993-9999.

Mock, J.M., 2012. In situ process for mercury removal. U.S. Patent 2012/0073811 A1.

Mohibul Kabir, K.M., Jampaiah, D., Kandjani, A.E., Mullett, M., Tardio, J., Sabri, Y.M., Bhargava, S.K., 2019. Cold vapor integrated quartz crystal microbalance (CV-QCM) based detection of mercury ions with gold nanostructures. Sens. Actuator B-Chem. 290, 453-458.

Mojammal, A.H.M., Back, S.-K., Seo, Y.-C., Kim, J.-H., 2019. Mass balance and behavior of mercury in oil refinery facilities. Atmos. Pollut. Res. 10, 145-151.

Mokhatab, S., Mak, J.Y., Valappil, J.V., Wood, D.A., 2014. LNG fundamentals. In: Handbook of liquefied natural gas (1st ed.). Gulf Professional Publishing, Cambridge, MA, United States, pp. 1-54.

Mokhatab, S., Poe, W.A., Mak, J.Y., 2019. Mercury removal. In: Handbook of natural gas transmission and processing: Principles and practices (4th ed.), Gulf Professional Publishing, Cambridge, MA, United States, pp. 349-359.

Montebelli, A., Visconti, C.G., Groppi, G., Tronconi, E., Cristiani, C., Ferreira, C., Kohler, S., 2014. Methods for the catalytic activation of metallic structured substrates. Catal. Sci. Technol. 4, 2846-2870.

Montini, T., Melchionna, M., Monai, M., Fornasiero, P., 2016. Fundamentals and catalytic applications of CeO_2*-based materials. Chem. Rev. 116, 5987-6041.*

Mulvaney Iıı, R.C., Clark, K.R., Kanazirev, V.I., Rastelli, H., 2008. Process for removal of mercury from gas stream. U.S. Patent 2008/0041227 A1.

Nasiri, M., Jafari, I., Parniankhoy, B., 2017. Oil and gas produced water management: A review of treatment technologies, challenges, and opportunities. Chem. Eng. Comm. 204, 990-1005.

Nédez, C., Boitiaux, J.-P., Cameron, C.J., Didillon, B., 1996. Optimization of the textural characteristics of an alumina to capture contaminants in natural gas. Langmuir 12, 3927-3931.

Neff, J.M., 2008. Estimation of bioavailability of metals from drilling mud barite. Integr. Environ. Assess. Manag. 4, 184-193.

Nelson, D.R., 1994. Mercury attack of brazed aluminum heat exchangers in cryogenic gas service. In: 73rd GPA Annual Convention. New Orleans, LA, United States.

Nengkoda, A., Al-Hinai, Z.M., 2009. Understanding of mercury corrosion attack on stainless steel material at gas wells: Case study. In: International Petroleum Technology Conference. Doha, Qatar.

Nengkoda, A., Awwami, M., Cai, X., Mufleh, J., Harbi, B., Haas, M., Jarri, A., Marriott, R., Bernard, F., Clark, P., Qureshi, A., 2014. The importance of elemental sulphur, mercury and condensate identification in sour gas field development project: Case study. In: Offshore Technology Conference Asia. Kuala Lumpur, Malaysia.

Ng, E.-P., Mintova, S., 2008. Nanoporous materials with enhanced hydrophilicity and high water sorption capacity. Micropor. Mesopor. Mat. 114, 1-26.

Nguyen, D.T., Aines, R.D., Baker, S.E., Bourcier, W.L., Duoss, E.B., Oakdale, J.S., Smith, M.M., Smith, W.L., Stolaroff, J.K., Ye, C., 2018. Composite 3D-printed reactors for gas absorption, purification and reaction. U. S. Patent 2018/0272268 A1.

Nishino, H., Aibe, T., Noguchi, K., 1985. Process for removal of mercury vapor and adsorbent therefor. U.S. Patent 4,500,327.

Norwegian Oil and Gas Association, 2016. Recommended guidelines for identification, assessment, control and follow-up of mercury exposure. Stavanger, Norway.

O'Rear, D.J., Cooper, R.E., Sheu, F.R., Belue, J.T., 2014. Process, method, and system for removing mercury from fluids. U.S. Patent 8,790,427 B2.

O'Rear, D.J., Cooper, R.E., Sheu, F.R., Belue, J.T., 2014 Process, method, and system for removing heavy metals from fluids. U.S. Patent 2014/0066683 A1.

O'Rear, D.J., Cooper, R.E., Wang, W., Yean, S., 2016a. Process for mercury removal. U.S. Patent 2016/0003023 A1.

O'Rear, D.J., Cooper, R.E., Yean, S., Gallup, D.L., Young, L.A., 2013. Process, method, and system for removing mercury from fluids. U.S. Patent 2013/0306312 A1.

O'Rear, D.J., Grice, K., Pradhan, V., Dassey, A.J., Hakam, A., Tiwary, A., 2016b. Process, method, and system for removing mercury from pipelines. WIPO Patent 2016/154394 A1.

O'Rear, D.J., Thompson, J.A., 2017. Hydrophobic adsorbents and mercury removal processes therewith. U.S. Patent 2017/0354951 A1.

Obrist, D., Kirk, J.L., Zhang, L., Sunderland, E.M., Jiskra, M., Selin, N.E., 2018. A review of global environmental mercury processes in response to human and natural perturbations: Changes of emissions, climate, and land use. Ambio 47, 116-140.

Oekon, J.R., Suyanto, 1985. Operating history of Arun liquefied natural gas plant. J. Petrol. Tech. 37, 863-867.

Otani, Y., Kanaoka, C., Emi, H., Uchijima, I., Nishino, H., 1988. Removal of mercury vapor from air with sulfur-impregnated adsorbents. Environ. Sci. Technol. 22, 708-711.

Ou, D.Y.O., 1995. Mercury removal by dispersed-metal adsorbents. U.S. Patent 5,463,167.

Pandey, S.K., Kim, K.-H., Brown, R.J.C., 2011. Measurement techniques for mercury species in ambient air. Trends Anal. Chem. 30, 899-917.

Pang, X.-Q., Jia, C.-Z., Wang, W.-Y., 2015. Petroleum geology features and research developments of hydrocarbon accumulation in deep petroliferous basins. Pet. Sci. 12, 1-53.

Park, S.M., Jeon, S.W., Kim, S.H., 2014. Formaldehyde oxidation over manganese–cerium–aluminum mixed oxides supported on cordierite monoliths at low temperatures. Catal. Lett. 144, 756-766.

Parker, M.E., Smith, J.P., 2004. Environmental significance of mercury in drilling discharges. In: SPE International Conference on Health, Safety, and Environment in Oil and Gas Exploration and Production. Calgary, AB, Canada.

Pavlish, J.H., Hamre, L.L., Zhuang, Y., 2010. Mercury control technologies for coal combustion and gasification systems. Fuel 89, 838-847.

Pavlish, J.H., Sondreal, E.A., Mann, M.D., Olson, E.S., Galbreath, K.C., Laudal, D.L., Benson, S.A., 2003. Status review of mercury control options for coal-fired power plants. Fuel Process. Technol. 82, 89-165.

Perrin, A., Musa, O.M., Steed, J.W., 2013. The chemistry of low dosage clathrate hydrate inhibitors. Chem. Soc. Rev. 42, 1996-2015.

Phannenstiel, L.L., Mckinley, C., Sorensen, J.C., 1976. Mercury in natural gas. In: American Gas Association - Operation Section Transmission Conference. Las Vegas, NV, United States.

Pichtel, J., 2016. Oil and gas production wastewater: Soil contamination and pollution prevention. Appl. Environ. Soil. Sci. 2016, 1-24.

Pojtanabuntoeng, T., Saiwan, C., Sutthiruangwong, S., Gallup, D.L., 2011. Effect of mercury on corrosion in production wells in Gulf of Thailand. Corros. Eng. Sci. Techn. 46, 547-553.

Polishuk, I., Nakonechny, F., Brauner, N., 2016. Predicting phase behavior of metallic mercury in liquid and compressed gaseous hydrocarbons. Fuel 174, 197-205.

Polishuk, I., Vilk, A., Chorążewski, M., 2017. Predicting phase behavior of metallic mercury in liquid and compressed gaseous hydrocarbons ii: Further examination of CP-PC-SAFT in the light of new data. Fuel 203, 686-689.

Porcheron, F., Barthelet, K., Baudot, A., Daudin, A., Lelias, M.A., Gelie, Y., Nicolaos, A., 2015. Performance trapping mass and use thereof in heavy metal trapping. U.S. Patent 2015/0034561 A1.

Porcheron, F., Barthelet, K., Baudot, A., Daudin, A., Schweitzer, J.M., Gazarian, J., 2014. Shaping capture masses for the purification of a liquid or gas feed containing heavy metals. U.S. Patent 2014/0308189 A1.

Pornsakulsak, L., Soponkanabhorn, T., 2007. Metal recovery from spent mercury and H_2S *absorbents. In: SPE Asia Pacific Health, Safety, and Security Environment Conference and Exhibition. Bangkok, Thailand.*

Pudasainee, D., Seo, Y.-C., Sung, J.-H., Jang, H.-N., Gupta, R., 2017. Mercury co-beneficial capture in air pollution control devices of coal-fired power plants. Int. J. Coal Geol. 170, 48-53.

Qu, Z., Xie, J., Xu, H., Chen, W., Yan, N., 2015. Regenerable sorbent with a high capacity for elemental mercury removal and recycling from the simulated flue gas at a low temperature. Energy Fuels 29, 6187-6196.

Quan, Z., Huang, W., Liao, Y., Liu, W., Xu, H., Yan, N., Qu, Z., 2019. Study on the regenerable sulfur-resistant sorbent for mercury removal from nonferrous metal smelting flue gas. Fuel 241, 451-458.

Qureshi, A., Macleod, M., Sunderland, E., Hungerbühler, K., 2011. Exchange of elemental mercury between the oceans and the atmosphere. In: Environmental chemistry and toxicology of mercury (1st ed.). Editors: Liu, G., Cai, Y., O'Driscoll. N. John Wiley & Sons, Hoboken, NJ, United States, pp. 389-421.

Randall, P.M., Chattopadhyay, S., 2013. Mercury contaminated sediment sites-an evaluation of remedial options. Environ. Res. 125, 131-149.

Rastelli, H., Gorawara, J.K., Simonetti, D.A., 2015. Process for the removal of mercury from hydrocarbon streams containing oxygen. U.S. Patent 2015/0159094 A1.

Reddy, B.M., Durgasri, N., Kumar, T.V., Bhargava, S.K., 2012. Abatement of gas-phase mercury—recent developments. Catal. Rev. 54, 344-398.

Reddy, G.K., He, J., Thiel, S.W., Pinto, N.G., Smirniotis, P.G., 2015. Sulfur-tolerant Mn-Ce-Ti sorbents for elemental mercury removal from flue gas: Mechanistic investigation by XPS. J. Phys. Chem. C 119, 8634-8644.

Reddy, K.S.K., Shoaibi, A.A., Srinivasakannan, C., 2018. Mercury removal using metal sulfide porous carbon complex. Process Saf. Environ. 114, 153-158.

Regnell, O., Watras, C.J., 2019. Microbial mercury methylation in aquatic environments: A critical review of published field and laboratory studies. Environ. Sci. Technol. 53, 4-19.

Reichelt, R., 2007. Scanning electron microscopy. In: Science of microscopy (1st ed.). Editors: Hawkes, P.W., Spence, J.C.H. Springer-Verlag, New York, NY, United Sates, pp. 133-272.

Ren, Y., Ma, Z., Bruce, P.G., 2012. Ordered mesoporous metal oxides: Synthesis and applications. Chem. Soc. Rev. 41, 4909-4927.

Ren, Z., Guo, Y., Gao, P.-X., 2015. Nano-array based monolithic catalysts: Concept, rational materials design and tunable catalytic performance. Catal. Today 258, 441-453.

Rezaei, F., Mosca, A., Hedlund, J., Webley, P.A., Grahn, M., Mouzon, J., 2011. The effect of wall porosity and zeolite film thickness on the dynamic behavior of adsorbents in the form of coated monoliths. Sep. Purif. Technol. 81, 191-199.

Rezaei, F., Webley, P., 2009. Optimum structured adsorbents for gas separation processes. Chem. Eng. Sci. 64, 5182-5191.

Rezaei, F., Webley, P., 2010. Structured adsorbents in gas separation processes. Sep. Purif. Technol. 70, 243-256.

Rhodes, E.F., Openshaw, P.J., Carnell, P.J.H., 1999. Fixed-bed technology purifies rich gas with H_2S*, Hg. Oil Gas J. 97, 58-63.*

Rios, J.A., Coyle, D.A., Durr, C.A., Frankie, B.M., 1998. Removal of trace mercury contaminants from gas and liquid streams in the LNG and gas processing industry. In: 77th GPA Annual Convention. Dallas, TX, United States.

Rodriguez, O., Padilla, I., Tayibi, H., Lopez-Delgado, A., 2012. Concerns on liquid mercury and mercury-containing wastes: A review of the treatment technologies for the safe storage. J. Environ. Manage. 101, 197-205.

Rodriguez-Perez, J., Lopez-Anton, M.A., Diaz-Somoano, M., Garcia, R., Martinez-Tarazona, M.R., 2013. Regenerable sorbents for mercury capture in simulated coal combustion flue gas. J. Hazard. Mater. 260, 869-877.

Rollmann, L.D., 1982. Sorbent for removing metals from fluids. U.S. Patent 4,338,288.

Rong, S., Zhang, P., Liu, F., Yang, Y., 2018. Engineering crystal facet of α*-*MnO_2 *nanowire for highly efficient catalytic oxidation of carcinogenic airborne formaldehyde. ACS Catal. 8, 3435-3446.*

Roussel, M., Courty, P., Boitiaux, J.P., Cosyns, J., 1990. Process for removing mercury and possibly arsenic in hydrocarbons. U.S. Patent 4,911,825.

Row, V.A., 2012. Desulphurization and mercury removal from natural gases. Presentation at the GasTech Centre of Technical Excellence. London, United Kingdom.

Row, V.A., Humphrys, M., 2011. The impact of mercury on gas processing plant assets and its removal. In: GPA Europe Spring Conference. Copenhagen, Denmark.

Roy, S., Bauer, T., Al-Dahhan, M., Lehner, P., Turek, T., 2004. Monoliths as multiphase reactors: A review. AIChE J. 50, 2918-2938.

Ruddy, T., Pennybaker, K., Goethe, A., 2007. State of mercury removal technology. In: 86th GPA Annual Convention. San Antonion, TX, United States.

Rudolf, P., Bender, M., 2011. Method for removing mercury from hydrocarbon streams. U.S. Patent 2011/0005975 A1.

Rufford, T.E., Smart, S., Watson, G.C.Y., Graham, B.F., Boxall, J., Diniz Da Costa, J.C., May, E.F., 2012. The removal of CO_2 *and* N_2 *from natural gas: A review of conventional and emerging process technologies. J. Petrol. Sci. Eng. 94-95, 123-154.*

Ruhland, D., Nwoko, K.C., Perez, M., Feldmann, J., Krupp, E.M., 2018. AF4-UV-MALS-ICP-MS/MS, SPICP-MS and STEM-EDX for the characterization of metal-containing nanoparticles in gas condensates from petroleum hydrocarbon samples. Anal. Chem.

Ruiz-Morales, J.C., Tarancón, A., Canales-Vázquez, J., Méndez-Ramos, J., Hernández-Afonso, L., Acosta-Mora, P., Marín Rueda, J.R., Fernández-González, R., 2017. Three dimensional printing of components and functional devices for energy and environmental applications. Energ. Environ. Sci. 10, 846-859.

Ryzhov, V.V., Mashyanov, N.R., Ozerova, N.A., Pogarev, S.E., 2003. Regular variations of the mercury concentration in natural gas. Sci. Total Environ. 304, 145-152.

Sabri, Y.M., Ippolito, S.J., Tardio, J., Abd Hamid, S.B., Bhargava, S.K., 2015a. Mercury migration and speciation study during monoethylene glycol regeneration processes. Ind. Eng. Chem. Res. 54, 5349-5355.

Sabri, Y.M., Ippolito, S.J., Tardio, J., Morrison, P.D., Bhargava, S.K., 2015b. Studying mercury partition in monoethylene glycol (MEG) used in gas facilities. Fuel 159, 917-924.

Sainal, M.R., Shafawi, A., Hj. Mohamed, A.J., 2007a. Mercury removal system for upstream application: Experience in treating mercury from raw condensate. In: E&P Environmental and Safety Conference. Galveston, TX, Unted States.

Sainal, M.R., Tg Mat, T.M.U., Shafawi, A.B., Mohamed, A.J., 2007b. Mercury removal project: Issues and challenges in managing and executing a technology project. In: SPE Annual Technical Conference and Exhibition. Anaheim, CA, United States.

Salva, C.A., Gallup, D.L., 2010. Mercury removal process is applied to crude oil of southern Argentina. In: SPE Latin American and Caribbean Petroleum Engineering Conference. Lima, Peru.

Sánchez-Rodas, D., Corns, W.T., Chen, B., Stockwell, P.B., 2010. Atomic fluorescence spectrometry: A suitable detection technique in speciation studies for arsenic, selenium, antimony and mercury. J. Anal. Atom. Spectrom. 25, 933-946.

Sardela, M.R., 2014. X-ray diffraction and reflectivity. In: Practical materials characterization (1st ed.). Editor: Sardela, M. Springer-Verlag, New York, NY, United States, pp. 1-41.

Sayed, A.E.-R., Ashour, I., Gadalla, M., 2017. Integrated process development for an optimum gas processing plant. Chem. Eng. Res. Des. 124, 114-123.

Scala, F., Anacleria, C., Cimino, S., 2013. Characterization of a regenerable sorbent for high temperature elemental mercury capture from flue gas. Fuel 108, 13-18.

Scala, F., Cimino, S., 2015. Elemental mercury capture and oxidation by a regenerable manganese-based sorbent: The effect of gas composition. Chem. Eng. J. 278, 134-139.

Schmidt, R., Hughes, M.A., Hays, J.M., Morton, R.W., Nelson, J.M., 2014. Supported silver sulfide sorbent. U.S. Patent 8,690,991 B2.

Scholes, C.A., Stevens, G.W., Kentish, S.E., 2012. Membrane gas separation applications in natural gas processing. Fuel 96, 15-28.

Selin, N.E., 2009. Global biogeochemical cycling of mercury: A review. Annu. Rev. Environ. Resour. 34, 43-63.

Selin, N.E., 2018. A proposed global metric to aid mercury pollution policy. Science 360, 607-609.

Shafawi, A., Ebdon, L., Foulkes, M., Stockwell, P., Corns, W., 1999. Determination of total mercury in hydrocarbons and natural gas condensate by atomic fluorescence spectrometry. Analyst 124, 185-189.

Shafawi, A., Ebdon, L., Foulkes, M., Stockwell, P., Corns, W., 2000. Preliminary evaluation of adsorbent-based mercury removal systems for gas condensate. Anal. Chim. Acta 415, 21-32.

Shah, M.S., Tsapatsis, M., Siepmann, J.I., 2017. Hydrogen sulfide capture: From absorption in polar liquids to oxide, zeolite, and metal-organic framework adsorbents and membranes. Chem. Rev. 117, 9755-9803.

Shah, P., Strezov, V., Nelson, P.F., 2010. Speciation of mercury in coal-fired power station flue gas†. Energy Fuels 24, 205-212.

Shi, F., Wang, F., Dai, H., Dai, J., Deng, J., Liu, Y., Bai, G., Ji, K., Au, C.T., 2012. Rod-, flower-, and dumbbell-like MnO_2: Highly active catalysts for the combustion of toluene. Appl. Catal. A: Gen. 433-434, 206-213.

Shindo, D., Oikawa, T., 2002. Energy dispersive x-ray spectroscopy. In: Analytical electron microscopy for materials science (1st ed.). Springer-Verlag, Tokyo, Japan, pp. 81-102.

Shipley, H., Mcdonnell, D., Culleton, M., Coull, R., Lupoi, R., O'Donnell, G., Trimble, D., 2018. Optimisation of process parameters to address fundamental challenges during selective laser melting of Ti-6Al-4V: A review. Int. J. Mach. Tool. Manu. 128, 1-20.

Silva, T.L.S., Morales-Torres, S., Castro-Silva, S., Figueiredo, J.L., Silva, A.M.T., 2017. An overview on exploration and environmental impact of unconventional gas sources and treatment options for produced water. J. Environ. Manage. 200, 511-529.

Simonetti, D.A., Kanazirev, V.I., Traynor, T.J., 2014. Method of removing mercury from a fluid stream using high capacity copper adsorbents. U.S. Patent 8,876,952 B2.

Siu, P.W., Weston, M.H., 2016. Porous polymers for the abatement and purification of electronic gas and the removal of mercury from hydrocarbon streams. U.S. Patent 2016/0160348 A1.

Smit, C.J., Meijer, H., Hendriks, E.M., 2004. Mercury, the volatile surprise in gas processing. In: 83rd GPA Annual Convention. San Antonio, TX, United States.

Snell, J.P., Frech, W., Thomassen, Y., 1996. Performance improvements in the determination of mercury species in natural gas condensate using an on-line amalgamation trap or solid-phase micro-extraction with capillary gas chromatography–microwave-induced plasma atomic emission spectrometry. Analyst 121, 1055-1060.

Sompongchaiyakul, P., Bureekul, S., Sombatjinda, S., 2018. Impact of natural gas exploration and production on mercury concentrations in surface sediment of the Gulf of Thailand. In: Abu Dhabi International Petroleum Exhibition & Conference. Abu Dhabi, United Arab Emirates.

Song, P., Hu, C., Pei, X., Sun, J., Sun, H., Wu, L., Jiang, Q., Fan, H., Yang, B., Zhou, C., Fan, Y., Zhang, X., 2019. Dual modulation of crystallinity and macro-/microstructures of 3D printed porous titanium implants to enhance stability and osseointegration. J. Mater. Chem. B 7, 2865-2877.

Sonström, P., Halbach, B., Tambou Djakpou, S., Ritz, B., Ahrenstorf, K., Grathwohl, G., Weller, H., Bäumer, M., 2011. Foam, fleece and honeycomb: Catalytically active coatings from colloidally prepared nanoparticles. Catal. Sci. Technol. 1, 830-838.

Špirić, Z., Mashyanov, N.R., 2000. Mercury measurements in ambient air near natural gas processing facilities. Fresenius J. Anal. Chem. 366, 429-432.

Srinivas, G., Copeland, R.J., 2006. Process for the simultaneous removal of sulfur and mercury. U. S. Patent 7,060,233.

Srivastava, R.K., Hutson, N., Martin, B., Princiotta, F., Staudt, J., 2006. Control of mercury emissions from coal-fired electric utility boilers. Environ. Sci. Technol. 40, 1385-1393.

Staun, C., Vaughan, J., Lopez-Anton, M.A., Rumayor, M., Martínez-Tarazona, M.R., 2018. Geochemical speciation of mercury in bauxite. Appl. Geochem. 93, 30-35.

Stewart, M., Arnold, K., 2011. Gas sweetening. In: Gas sweetening and processing field manual (1st ed.). Gulf Professional Publishing, Boston, MA, United States, pp. 1-140.

Stiltner, J., 2002. Mercury removal from natural gas and liquid streams. In: 81st GPA Annual Convention. Dallas, TX, United States.

Streets, D.G., Horowitz, H.M., Jacob, D.J., Lu, Z., Levin, L., Ter Schure, A.F.H., Sunderland, E.M., 2017. Total mercury released to the environment by human activities. Environ. Sci. Technol. 51, 5969-5977.

Sugier, A., Villa, F.L., 1978. Process for removing mercury from a gas or a liquid by absorption on a copper sulfide containing solid mass. U.S. Patent 4,094,777.

Sun, H., Zhao, S., Ma, Y., Wu, J., Liang, P., Yang, D., Zhang, H., 2018. Effective and regenerable Ag/4A zeolite nanocomposite for Hg^0 removal from natural gas. J. Alloy Compd. 762, 520-527.

Suresh Kumar Reddy, K., Al Shoaibi, A., Srinivasakannan, C., 2014a. Elemental mercury adsorption on sulfur-impregnated porous carbon – a review. Environ. Technol. 35, 18-26.

Suresh Kumar Reddy, K., Al Shoaibi, A., Srinivasakannan, C., 2014b. Gas-phase mercury removal through sulfur impregnated porous carbon. J. Ind. Eng. Chem. 20, 2969-2974.

Sutra, E., Spada, M., Burgherr, P., 2017. Chemicals usage in stimulation processes for shale gas and deep geothermal systems: A comprehensive review and comparison. Renew. Sust. Energ. Rev. 77, 1-11.

Svoboda, K., Hartman, M., Syc, M., Pohorely, M., Kamenikova, P., Jeremias, M., Durda, T., 2016. Possibilities of mercury removal in the dry flue gas cleaning lines of solid waste incineration units. J. Environ. Manage. 166, 499-511.

Syversen, T., Kaur, P., 2012. The toxicology of mercury and its compounds. J. Trace Elem. Med. Biol. 26, 215-226.

Tagliabue, M., Farrusseng, D., Valencia, S., Aguado, S., Ravon, U., Rizzo, C., Corma, A., Mirodatos, C., 2009. Natural gas treating by selective adsorption: Material science and chemical engineering interplay. Chem. Eng. J. 155, 553-566.

Tan, Z., Su, S., Qiu, J., Kong, F., Wang, Z., Hao, F., Xiang, J., 2012. Preparation and characterization of Fe_2O_3–SiO_2 composite and its effect on elemental mercury removal. Chem. Eng. J. 195-196, 218-225.

Tang, W., Yao, M., Deng, Y., Li, X., Han, N., Wu, X., Chen, Y., 2016. Decoration of one-dimensional MnO_2 with Co_3O_4 nanoparticles: A heterogeneous interface for remarkably promoting catalytic oxidation activity. Chem. Eng. J. 306, 709-718.

Tao, H., Murakami, T., Tominaga, M., Miyazaki, A., 1998. Mercury speciation in natural gas condensate by gas chromatography-inductively coupled plasma mass spectrometry. J. Anal. At. Spectrom. 13, 1085-1093.

Tarakad, R.R., Crawford, D.B., 1987. Removal of mercury from gases. U.S Patent 4,693,731.

Terrigeol, A., 2012. Molecular sieves contaminants: Effects, consequences and mitigation. In: GPA Europe Annual Conference. Berlin, Germany.

Thakkar, H., Eastman, S., Al-Mamoori, A., Hajari, A., Rownaghi, A.A., Rezaei, F., 2017. Formulation of aminosilica adsorbents into 3D-printed monoliths and evaluation of their CO_2 *capture performance. ACS Appl. Mater. Interfaces 9, 7489-7498.*

Thakkar, H., Eastman, S., Hajari, A., Rownaghi, A.A., Knox, J.C., Rezaei, F., 2016. 3D-printed zeolite monoliths for CO_2 *removal from enclosed environments. ACS Appl. Mater. Interfaces 8, 27753-27761.*

Thomas, D.J., Langley, N.P., Last, N.C., Travis, R.J., 2017. Mercury sensor for detecting, differentiating, and measuring organic and inorganic mercury compounds U.S. Patent 9,791,428 B2, Oct. 17.

Thommes, M., Kaneko, K., Neimark, A.V., Olivier, J.P., Rodriguez-Reinoso, F., Rouquerol, J., Sing, K.S.W., 2015. Physisorption of gases, with special reference to the evaluation of surface area and pore size distribution (IUPAC technical report). Pure Appl. Chem. 87, 1051-1069.

Thompson, J.A., Chinn, D., Hatakeyama, E.S., Owen, R.O., 2017. Process, method and system for removal of mercury in a gas dehydration process. U.S. Patent 2017/0355920 A1.

Tompsett, D.A., Parker, S.C., Islam, M.S., 2014. Surface properties of α*-*MnO_2*: Relevance to catalytic and supercapacitor behaviour. J. Mater. Chem. A 2, 15509-15518.*

Trefry, J.H., Smith, J.P., 2003. Forms of mercury in drilling fluid barite and their fate in the marine environment: A review and synthesis. In: SPE/EPA/DOE Exploration and Production Environmental Conference. San Antonio, TX, United States.

Trefry, J.H., Trocine, R.P., Mcelvaine, M.L., Rember, R.D., Hawkins, L., 2003. Concentrations of total mercury and methylmercury in sediment adjacent to offshore drilling sites. In: SPE/EPA/DOE Exploration and Production Environmental Conference. San Antonio, TX, United States.

Trovarelli, A., Llorca, J., 2017. Ceria catalysts at nanoscale: How do crystal shapes shape catalysis? ACS Catal. 7, 4716-4735.

Tubío, C.R., Azuaje, J., Escalante, L., Coelho, A., Guitián, F., Sotelo, E., Gil, A., 2016. 3D printing of a heterogeneous copper-based catalyst. J. Catal. 334, 110-115.

Umek, P., Gloter, A., Pregelj, M., Dominko, R., Jagodič, M., Jagličić, Z., Zimina, A., Brzhezinskaya, M., Potočnik, A., Filipič, C., Levstik, A., Arčon, D., 2009. Synthesis of 3D hierarchical self-assembled microstructures formed from α*-*MnO_2 *nanotubes and their conducting and magnetic properties. J. Phys. Chem. C 113, 14798-14803.*

UNEP, 2015. Practical sourcebook on mercury waste storage and disposal. Nairobi, Kenya.

UNEP, 2018. Global mercury assessment 2018: Sources, emissions, releases and environmental transport. Nairobi, Kenya.

US EPA, 2001. Mercury in petroleum and natural gas: Estimation of emissions from production, processing and combustion. Research Triangle Park, NC, United States.

US EPA, 2007. Treatment technologies for mercury in soil, waste, and water. Cincinnati, OH, United States.

Van Der Vaart, R., Akkerhuis, J., Feron, P., Jansen, B., 2001. Removal of mercury from gas streams by oxidative membrane gas absorption. J. Membrane Sci. 187, 151-157.

Van Hal, R.E.G., Sieben, V., Floquet, C., Lee, V., 2018. Systems and methods for detection of mercury in hydrocarbon-containing fluids using optical analysis of slug flow. U.S. Patent 2018/0059088 A1.

Vengosh, A., Jackson, R.B., Warner, N., Darrah, T.H., Kondash, A., 2014. A critical review of the risks to water resources from unconventional shale gas development and hydraulic fracturing in the United States. Environ. Sci. Technol. 48, 8334-8348.

Vikrant, K., Kim, K.-H., 2019. Nanomaterials for the adsorptive treatment of Hg(II) ions from water. Chem. Eng. J. 358, 264-282.

Vost, E.E., Amyot, M., O'Driscoll, N.J., 2011. Photoreactions of mercury in aquatic systems. In: Environmental chemistry and toxicology of mercury (1st ed.). Editors: Liu, G., Cai, Y., O'Driscoll. N. John Wiley & Sons, Hoboken, NJ, United States, pp. 193-218.

Wan, Q., Yao, Q., Duan, L., Li, X., Zhang, L., Hao, J., 2018. Comparison of elemental mercury oxidation across vanadium and cerium based catalysts in coal combustion flue gas: Catalytic performances and particulate matter effects. Environ. Sci. Technol. 52, 2981-2987.

Wang, F., Shen, B., Yang, J., Singh, S., 2017a. Review of mercury formation and capture from CO_2*-enriched oxy-fuel combustion flue gas. Energy Fuels 31, 1053-1064.*

Wang, J., Feng, X., Anderson, C.W., Xing, Y., Shang, L., 2012. Remediation of mercury contaminated sites - a review. J. Hazard. Mater. 221-222, 1-18.

Wang, J.-G., Yang, Y., Huang, Z.-H., Kang, F., 2014a. MnO_2*/polypyrrole nanotubular composites: Reactive template synthesis, characterization and application as superior electrode materials for high-performance supercapacitors. Electrochim. Acta 130, 642-649.*

Wang, Q., Chen, X., Jha, A.N., Rogers, H., 2014b. Natural gas from shale formation – the evolution, evidences and challenges of shale gas revolution in United States. Renew. Sust. Energ. Rev. 30, 1-28.

Wang, Y., Arandiyan, H., Scott, J., Bagheri, A., Dai, H., Amal, R., 2017b. Recent advances in ordered meso/macroporous metal oxides for heterogeneous catalysis: A review. J. Mater. Chem. A 5, 8825-8846.

Wang, Y., Indrawirawan, S., Duan, X., Sun, H., Ang, H.M., Tadé, M.O., Wang, S., 2015. New insights into heterogeneous generation and evolution processes of sulfate radicals for phenol degradation over one-dimensional α-MnO_2 *nanostructures. Chem. Eng. J. 266, 12-20.*

Wang, Z., Liu, J., Yang, Y., Liu, F., Ding, J., 2019. Heterogeneous reaction mechanism of elemental mercury oxidation by oxygen species over MnO_2 *catalyst. Proc. Combust. Inst. 37, 2967-2975.*

Wang, Z., Liu, J., Yang, Y., Miao, S., Shen, F., 2018. Effect of the mechanism of H_2S *on elemental mercury removal using the* MnO_2 *sorbent during coal gasification. Energy Fuels 32, 4453-4460.*

Warrag, S.E.E., Fetisov, E.O., Van Osch, D.J.G.P., Harwood, D.B., Kroon, M.C., Siepmann, J.I., Peters, C.J., 2018. Mercury capture from petroleum using deep eutectic solvents. Ind. Eng. Chem. Res. 57, 9222-9230.

Waseda, Y., Matsubara, E., Shinoda, K., 2011. Diffraction from polycrystalline samples and determination of crystal structure. In: X-ray diffraction crystallography: Introduction, examples and solved problems (1st ed.). Springer-Verlag, Berlin, Germany, pp. 107-167.

Washburn, S.J., Blum, J.D., Johnson, M.W., Tomes, J.M., Carnell, P.J., 2018. Isotopic characterization of mercury in natural gas via analysis of mercury removal unit catalysts. ACS Earth Space Chem. 2, 462-470.

Wdowin, M., Wiatros-Motyka, M.M., Panek, R., Stevens, L.A., Franus, W., Snape, C.E., 2014. Experimental study of mercury removal from exhaust gases. Fuel 128, 451-457.

Weekman, V.W., Yan, T.Y., 1995. Regenerative mercury removal process. U.S. Patent 5,419,884.

Wei, Y., Yu, D., Tong, S., Jia, C.Q., 2015. Effects of H_2SO_4 *and* O_2 *on* Hg^0 *uptake capacity and reversibility of sulfur-impregnated activated carbon under dynamic conditions. Environ. Sci. Technol. 49, 1706-1712.*

Weng, J., Lu, X., Gao, P.-X., 2017. Nano-array integrated structured catalysts: A new paradigm upon conventional wash-coated monolithic catalysts? Catalysts 7, 253-277.

Wilcox, J., Rupp, E., Ying, S.C., Lim, D.-H., Negreira, A.S., Kirchofer, A., Feng, F., Lee, K., 2012. Mercury adsorption and oxidation in coal combustion and gasification processes. Int. J. Coal Geol. 90-91, 4-20.

Wilhelm, M., Mcarthur, A., 1995. Removal and treatment of mercury contamination at gas processing facilities. In: SPE/EPA Exploration and Production Environmental Conference. Houston, TX, United States.

Wilhelm, M.S., Mcarthur, A., D., K.R., 1993. Methods to combat liquid metal embrittlement in cryogenic aluminum heat exchangers. In: 73rd GPA Annual Convention. New Orleans, LA, United States.

Wilhelm, S.M., 1993. Process and solution for transforming insoluble mercury metal into a soluble compound. U.S. Patent 4,238,488.

Wilhelm, S.M., 1999a. Avoiding exposure to mercury during inspection and maintenance operations in oil and gas processing. Process Saf. Progr. 18, 178-188.

Wilhelm, S.M., 1999b. Generation and disposal of petroleum processing waste that contains mercury. Environ. Prog. 18, 130-143.

Wilhelm, S.M., 2001. Estimate of mercury emissions to the atmosphere from petroleum. Environ. Sci. Technol. 35, 4704-4710.

Wilhelm, S.M., 2009. Risk analysis for operation of aluminum heat exchangers contaminated by mercury. Process Saf. Progr. 28, 259-266.

Wilhelm, S.M., Bloom, N., 2000. Mercury in petroleum. Fuel Process. Technol. 63, 1-27.

Wilhelm, S.M., Liang, L., Kirchgessner, D., 2006. Identification and properties of mercury species in crude oil. Energy Fuels 20, 180-186.

Williams, D.B., Carter, C.B., 2009. Phase-contrast images. In: Transmission electron microscopy: A textbook for materials science (2nd ed.). Springer-Verlag, New york, NY, United States, pp. 389-405.

Worthington, M.J.H., Kucera, R.L., Albuquerque, I.S., Gibson, C.T., Sibley, A., Slattery, A.D., Campbell, J.A., Alboaiji, S.F.K., Muller, K.A., Young, J., Adamson, N., Gascooke, J.R., Jampaiah, D., Sabri, Y.M., Bhargava, S.K., Ippolito, S.J., Lewis, D.A., Quinton, J.S., Ellis, A.V., Johs, A., Bernardes, G.J.L., Chalker, J.M., 2017. Laying waste to mercury: Inexpensive sorbents made from sulfur and recycled cooking oils. Chem. Eur. J. 23, 16219-16230.

Wu, S., Oya, N., Ozaki, M., Kawakami, J., Uddin, M.A., Sasaoka, E., 2007. Development of iron oxide sorbents for Hg^0 removal from coal derived fuel gas: Sulfidation characteristics of iron oxide sorbents and activity for COS formation during Hg^0 removal. Fuel 86, 2857-2863.

Xie, J., Qu, Z., Yan, N., Yang, S., Chen, W., Hu, L., Huang, W., Liu, P., 2013. Novel regenerable sorbent based on Zr-Mn binary metal oxides for flue gas mercury retention and recovery. J. Hazard. Mater. 261, 206-213.

Xie, Y., Yu, Y., Gong, X., Guo, Y., Guo, Y., Wang, Y., Lu, G., 2015. Effect of the crystal plane figure on the catalytic performance of MnO_2 for the total oxidation of propane. CrystEngComm 17, 3005-3014.

Xu, H., Qu, Z., Zhao, S., Mei, J., Quan, F., Yan, N., 2015. Different crystal-forms of one-dimensional MnO_2 nanomaterials for the catalytic oxidation and adsorption of elemental mercury. J. Hazard. Mater. 299, 86-93.

Xu, H., Yan, N., Qu, Z., Liu, W., Mei, J., Huang, W., Zhao, S., 2017a. Gaseous heterogeneous catalytic reactions over Mn-based oxides for environmental applications: A critical review. Environ. Sci. Technol. 51, 8879-8892.

Xu, H., Zhang, Q., Qiu, C., Lin, T., Gong, M., Chen, Y., 2012. Tungsten modified MnO_x*–*CeO_2/ZrO_2 *monolith catalysts for selective catalytic reduction of* NO_x *with ammonia. Chem. Eng. Sci. 76, 120-128.*

Xu, T., Wang, L.A., Wang, X., Li, T., Zhan, X., 2018a. Heavy metal pollution of oil-based drill cuttings at a shale gas drilling field in Chongqing, Xhina: A human health risk assessment for the workers. Ecotoxicol. Environ. Saf. 165, 160-163.

Xu, W., Hussain, A., Liu, Y., 2018b. A review on modification methods of adsorbents for elemental mercury from flue gas. Chem. Eng. J. 346, 692-711.

Xu, W., Lui, E.W., Pateras, A., Qian, M., Brandt, M., 2017b. In situ tailoring microstructure in additively manufactured Ti-6Al-4V for superior mechanical performance. Acta Mater. 125, 390-400.

Xu, Y., Luo, G., Pang, Q., He, S., Deng, F., Xu, Y., Yao, H., 2019. Adsorption and catalytic oxidation of elemental mercury over regenerable magnetic Fe–Ce mixed oxides modified by non-thermal plasma treatment. Chem. Eng. J. 358, 1454-1463.

Xue, L., Liu, T., Guo, X., Zheng, C., 2015. Hg oxidation reaction mechanism on Fe_2O_3 *with* H_2S*: Comparison between theory and experiments. Proc. Combust. Inst. 35, 2867-2874.*

Yamada, J., Kobayashi, K., Shibuya, T., Kawasaki, M., Nakayama, T., Maruta, H., Kobayashi, A., 2017. Occurrence of particulate mercury in flowback fluids after well workover. In: SPE/IATMI Asia Pacific Oil & Gas Conference and Exhibition. Jakarta, Indonesia.

Yan, Q., Han, Z., Wang, S., 2017. Geochemical characteristics of mercury in oil and gas. IOP Conf. Ser.: Earth Environ. Sci. 63.

Yan, T.Y., 1987a. Recovery of mercury and heat energy from waste using fluidized beds. U.S. Patent 4,701,212.

Yan, T.Y., 1987b. Removal of mercury from natural gas and liquid hydrocarbons utilizing downstream guard chamber. U.S. Patent 4,709,118.

Yan, T.Y., 1988. Clean up and passivation of mercury in gas liquefaction plants. U.S. Patent 4,764,219.

Yan, T.Y., 1989. Process for removing mercury vapor and chemisorbent composition therefor. U.S. Patent 4,814,152.

Yan, T.Y., 1990a. Removal of mercury from natural gas. U.S. Patent 4,895,708.

Yan, T.Y., 1990b. Simultaneous removal of mercury and water from fluids. U.S. Patent 4,892,567.

Yan, T.Y., 1991a. Reaction of trace mercury in natural gas with dilute polysulfide solutions in a packed column. Ind. Eng. Chem. Res. 30, 2592-2595.

Yan, T.Y., 1991b. Removal of mercury from natural gas and liquid hydrocarbons utilizing silver on alumina adsorbent. U.S. Patent 5,053,209.

Yan, T.Y., 1994a. Method for simultaneously drying and removing metallic and organic mercury from fluids. U.S Patent 5,322,628.

Yan, T.Y., 1994b. A novel process for Hg removal from gases. Ind. Eng. Chem. Res. 33, 3010-3014.

Yan, T.Y., 1998. Passivation of mercury contaminants in process systems. Chem. Eng. Comm. 165, 217-225.

Yang, H., Xu, Z., Fan, M., Bland, A.E., Judkins, R.R., 2007. Adsorbents for capturing mercury in coal-fired boiler flue gas. J. Hazard. Mater. 146, 1-11.

Yang, J., Yu, H., Yin, J., Gao, M., Wang, Z., Zeng, X., 2016. Formation and control of martensite in Ti-6Al-4V alloy produced by selective laser melting. Mater. Des. 108, 308-318.

Yang, J., Zhu, W., Qu, W., Yang, Z., Wang, J., Zhang, M., Li, H., 2019a. Selenium functionalized metal-organic framework MIL-101 for efficient and permanent sequestration of mercury. Environ. Sci. Technol.

Yang, S., Guo, Y., Yan, N., Qu, Z., Xie, J., Yang, C., Jia, J., 2011. Capture of gaseous elemental mercury from flue gas using a magnetic and sulfur poisoning resistant sorbent Mn/gamma-Fe_2O_3 at lower temperatures. J. Hazard. Mater. 186, 508-515.

Yang, W., Adewuyi, Y.G., Hussain, A., Liu, Y., 2019b. Recent developments on gas–solid heterogeneous oxidation removal of elemental mercury from flue gas. Environ. Chem. Lett. 17, 19-47.

Yang, W., Li, C., Wang, H., Li, X., Zhang, W., Li, H., 2018a. Cobalt doped ceria for abundant storage of surface active oxygen and efficient elemental mercury oxidation in coal combustion flue gas. Appl. Catal. B: Environ. 239, 233-244.

Yang, Y., Jia, J., Liu, Y., Zhang, P., 2018b. The effect of tungsten doping on the catalytic activity of α-MnO_2 nanomaterial for ozone decomposition under humid condition. Appl. Catal. A: Gen. 562, 132-141.

Yang, Z., Li, H., Feng, S., Li, P., Liao, C., Liu, X., Zhao, J., Yang, J., Lee, P.H., Shih, K., 2018c. Multiform sulfur adsorption centers and copper-terminated active sites of nano-CuS for efficient elemental mercury capture from coal combustion flue gas. Langmuir 34, 8739-8749.

Yao, Y., Velpari, V., Economy, J., 2014. Design of sulfur treated activated carbon fibers for gas phase elemental mercury removal. Fuel 116, 560-565.

Yean, S., Gallup, D.L., Young, L.A., Cooper, R.E., Zielinski, M.B., Emanuele, M.A., Llewellyn, B.C., O'Rear, D.J., 2014. In-situ method and system for removing heavy metals from produced fluids. U.S. Patent 2014/0158353 A1.

Yeo, Z.Y., Chew, T.L., Zhu, P.W., Mohamed, A.R., Chai, S.-P., 2012. Conventional processes and membrane technology for carbon dioxide removal from natural gas: A review. J. Nat. Gas. Chem. 21, 282-298.

Yod-in-Lom, W., Doyle, B.A., 2002. Deep well injection of mercury contaminated sludge in the Gulf of Thailand. In: SPE International Conference on Health, Safety and Environment in Oil and Gas Exploration and Production. Kuala Lumpur, Malaysia.

Zaarour, M., El Roz, M., Dong, B., Retoux, R., Aad, R., Cardin, J., Dufour, C., Gourbilleau, F., Gilson, J.P., Mintova, S., 2014. Photochemical preparation of silver nanoparticles supported on zeolite crystals. Langmuir 30, 6250-6256.

Zaferani, S., Pérez-Rodríguez, M., Biester, H., 2018. Diatom ooze-a large marine mercury sink. Science 361, 797.

Zeng, X., Xu, Y., Zhang, B., Luo, G., Sun, P., Zou, R., Yao, H., 2017. Elemental mercury adsorption and regeneration performance of sorbents $FeMnO_x$ enhanced via non-thermal plasma. Chem. Eng. J. 309, 503-512.

Zettlitzer, M., Scholer, H.F., Eiden, R., Falter, R., 1997. Determination of elemental, inorganic and organic mercury in north German gas condensates and formation brines. In: International Symposium on Oilfield Chemistry. Houston, TX, Unted States.

Zhang, A., Zhang, Z., Chen, J., Sheng, W., Sun, L., Xiang, J., 2015. Effect of calcination temperature on the activity and structure of MnO_x/TiO_2 adsorbent for Hg^0 removal. Fuel Process. Technol. 135, 25-33.

Zhang, B., Liu, J., Zheng, C., Chang, M., 2014. Theoretical study of mercury species adsorption mechanism on MnO_2(110) surface. Chem. Eng. J. 256, 93-100.

Zhang, C.L., Yu, S.H., 2014. Nanoparticles meet electrospinning: Recent advances and future prospects. Chem. Soc. Rev. 43, 4423-4448.

Zhang, D., Du, X., Shi, L., Gao, R., 2012. Shape-controlled synthesis and catalytic application of ceria nanomaterials. Dalton Trans. 41, 14455-14475.

Zhang, H., Sun, H., Zhang, D., Zhang, W., Chen, S., Li, M., Liang, P., 2019a. Nanoconfinement of Ag nanoparticles inside mesoporous channels of MCM-41 molecule sieve as a *regenerable and H_2O resistance sorbent for Hg^0 removal in natural gas. Chem. Eng. J. 361, 139-147.*

Zhang, H., Zhang, D., Wang, J., Xu, W., Yang, D., Jiao, T., Zhang, W., Liang, P., 2019b. Simultaneous removal of Hg(0) and H_2S at a high space velocity by water-resistant SnO_2/carbon aerogel. J. Hazard. Mater. 371, 123-129.

Zhang, L., Wang, S.X., Wu, Q.R., Wang, F.Y., Lin, C.J., Zhang, L.M., Hui, M.L., Yang, M., Su, H.T., Hao, J.M., 2016a. Mercury transformation and speciation in flue gases from anthropogenic emission sources: A critical review. Atmos. Chem. Phys. 16, 2417-2433.

Zhang, S., Zhao, Y., Yang, J., Zhang, Y., Sun, P., Yu, X., Zhang, J., Zheng, C., 2017a. Simultaneous NO and mercury removal over MnO_x/TiO_2 catalyst in different atmospheres. Fuel Process. Technol. 166, 282-290.

Zhang, X., Shen, B., Shen, F., Zhang, X., Si, M., Yuan, P., 2017b. The behavior of the manganese-cerium loaded metal-organic framework in elemental mercury and NO removal from flue gas. Chem. Eng. J. 326, 551-560.

Zhang, X., Shen, B., Zhu, S., Xu, H., Tian, L., 2016b. UIO-66 and its Br-modified derivates for elemental mercury removal. J. Hazard. Mater. 320, 556-563.

Zhao, H., Mu, X., Zheng, C., Liu, S., Zhu, Y., Gao, X., Wu, T., 2018a. Structural defects in 2D MoS_2 nanosheets and their roles in the adsorption of airborne elemental mercury. J. Hazard. Mater. 366, 240-249.

Zhao, J., Li, H., Yang, Z., Zhu, L., Zhang, M., Feng, Y., Qu, W., Yang, J., Shih, K., 2018b. Dual roles of nano-sulfide in efficient removal of elemental mercury from coal combustion flue gas within a wide temperature range. Environ. Sci. Technol. 52, 12926-12933.

Zhao, L., Huang, Y., Chen, H., Zhao, Y., Xiao, T., 2017. Study on the preparation of bimetallic oxide sorbent for mercury removal. Fuel 197, 20-27.

Zhao, S., Mei, J., Xu, H., Liu, W., Qu, Z., Cui, Y., Yan, N., 2018c. Research of mercury removal from sintering flue gas of iron and steel by the open metal site of MIL-101(Cr). J. Hazard. Mater. 351, 301-307.

Zhao, S., Pudasainee, D., Duan, Y., Gupta, R., Liu, M., Lu, J., 2019. A review on mercury in coal combustion process: Content and occurrence forms in coal, transformation, sampling methods, emission and control technologies. Prog. Energy Combust. Sci. 73, 26-64.

Zheng, Y., Jensen, A.D., Windelin, C., Jensen, F., 2012. Review of technologies for mercury removal from flue gas from cement production processes. Prog. Energy Combust. Sci. 38, 599-629.

Zhou, J., Qin, L., Xiao, W., Zeng, C., Li, N., Lv, T., Zhu, H., 2017. Oriented growth of layered-MnO_2 nanosheets over α-MnO_2 nanotubes for enhanced room-temperature HCHO oxidation. Appl. Catal. B: Environ. 207, 233-243.

Zhu, G., Zhu, J., Jiang, W., Zhang, Z., Wang, J., Zhu, Y., Zhang, Q., 2017a. Surface oxygen vacancy induced α-MnO_2 nanofiber for highly efficient ozone elimination. Appl. Catal. B: Environ. 209, 729-737.

Zhu, G., Zhu, J., Li, W., Yao, W., Zong, R., Zhu, Y., Zhang, Q., 2018a. Tuning the K^+ concentration in the tunnels of α-MnO_2 to increase the content of oxygen vacancy for ozone elimination. Environ. Sci. Technol. 52, 8684-8692.

Zhu, L., Wang, J., Rong, S., Wang, H., Zhang, P., 2017b. Cerium modified birnessite-type MnO_2 for gaseous formaldehyde oxidation at low temperature. Appl. Catal. B: Environ. 211, 212-221.

Zhu, S., Zhang, Z., Žagar, D., 2018b. Mercury transport and fate models in aquatic systems: A review and synthesis. Sci. Total Environ. 639, 538-549.

Zou, S., Liao, Y., Xiong, S., Huang, N., Geng, Y., Yang, S., 2017. H_2S-modified Fe–Ti spinel: A recyclable magnetic sorbent for recovering gaseous elemental mercury from flue gas as a co-benefit of wet electrostatic precipitators. Environ. Sci. Technol. 51, 3426-3434.

Zou, X., Hovmöller, S., Oleynikov, P., 2011. Fundamental crystallography. In: Electron crystallography: Electron microscopy and electron diffraction (1st ed.). Oxford University Press, Oxford, United Kingdom, pp. 21-61.